BULGARIAN CHEMICAL COMMUNICATIONS

2010 Volume 42/ Number 2

Journal of the Chemical Institutes
of the Bulgarian Academy of Sciences
and of the Union of Chemists in Bulgaria

Bulgarian Chemical Communications, Volume 42, Number 2 (pp. 79–102) 2010

Kinetics of chemical reactions and phase transitions at changing temperature: General reconsiderations and a new approach

I. Gutzow[1]*, S. Todorova[2], N. Jordanov[1]

[1] *Institute of Physical Chemistry, Bulgarian Academy of Sciences, Acad. G. Bonchev St., Block 11, 1113 Sofia, Bulgaria*
[2] *Institute of Geophysics, Bulgarian Academy of Sciences, Acad. G. Bonchev St., Block 3, 1113 Sofia, Bulgaria*

Received October 1, 2009

An extended analysis is given and a new approach developed on the possibilities to describe in terms of classical kinetic models, developed for isothermal conditions, the kinetics of chemical reactions or processes of phase transition, of structural relaxation and of vitrification in terms of non-isothermal kinetics. The main question investigated is to determine to which extent both the kinetic models involved and the activation energies, determining and limiting the process investigated, can be established by a single cooling or heating run, performed e.g. in a DTA or in a DSC calorimetric device. As a first possibility existing isoconversional methods of non-isothermal analysis are considered and in particular the usually disregarded method of cooling run experimentation, which, it is shown is a necessity and can give excellent results in analyzing processes of melt crystallization and of topochemical reaction kinetics, e.g. when relative activities of nucleants or catalyzers are involved. However, in the framework of isoconversional methods it is impossible to determine both absolute values of activation energies and unambiguously to decide upon possible mechanisms of reactions.

A general method is thus developed, based on Ozawa's concepts, in which the Avrami equation is introduced as a general intermediate algorithm of change, describing both homogeneous reaction kinetics (with power coefficients $n \leq 1$) and topochemical reactions and phase transitions (at $n = 1, 2, 3, 4$). It is shown how analytical and geometrical considerations can be exploited to determine in terms of the employed Avrami algorithm both kinetic models and activation energies in a new and more appropriate generalized Ozawa-type analysis.

The theoretical results obtained are illustrated with examples from nucleation and growth kinetics in polymer melt crystallization, in supersaturated aqueous solutions, in devitrification of glasses and in glass transition and in electrolytical metal deposition at galvanostatic conditions.

Key words: Non-isothermal kinetics, isoconversional analysis, topochemical reactions, Avrami equation, Ozawa method, phase transitions.

1. INTRODUCTION

With the very beginning of thermal analysis, both by DTA and DSC methods, efforts were made to derive approaches, permitting the analysis and determination of both kinetic reaction models and the respective activation energies.

Here first the Kissinger procedure [1], developed end of the 1950-ties, has to be mentioned. In plotting peak reaction temperatures T_{max} *vs*. linear heating rates q, this author calculated activation energies; moreover from the form of the obtained transition rate/temperature curves Kissinger tried to determine the reaction order, i.e. the anticipated reaction model. Kissinger's procedure, described in present-day terms, is analyzed in details in [2] in both its merits and shortcomings. It is essential, that with Kissinger's paper the analysis of non-isothermal reaction kinetics was opened in terms of isoconversional approaches: at the peak, i.e. at the maximum reaction rate temperature, T_{max}, a constant degree of conversion, α, was anticipated or proven to exist.

The isoconversional methods are in principle less informative than methods of analysis, in which the whole course of the non-isothermal transition kinetics is used in order to determine both anticipated models of reaction, of phase transition or change and the corresponding activation energies. The first and very widely used method in this way was indicated by Ozawa beginning of the 1970-ties [3, 4]. It was performed in the framework of the Kolmogorov-Avrami overall crystallization model (see [5, 6 and 7]).

In the present paper an attempt is made to employ and further specify Ozawa's method so as to develop a general approach, applicable to chemical reaction kinetics of any order, to topochemical reactions, to phase transitions and relaxation processes in undercooled melts, in crystalline and amorphous solids, in glasses.

* To whom all correspondence should be sent:
E-mail: igutzow@ipc.bas.bg

In developing our approach, we first show, that Avrami equation, derived originally and modified (see [7]) to follow the overall kinetics of crystallization at various phase transitions (in melt crystallization of compact volumes [6], in solid state reactions [8, 9], in the crystallization of finely dispersed materials like glassy semolina or powders [10] brought to micro-dimensions, two-dimensional nucleation, in thin layers [7] etc.) can also be used to describe with sufficient accuracy the kinetics of homogeneous reactions. It is especially shown here, that Avrami dependence can be applied to processes, which according to van't Hoff's classical schemes [11] of homogeneous reactions kinetics are classified as first, second and third order reactions. It is also demonstrated how reaction models, summarized in Garner's book (see [12]), and proposed by authors like Roginskii [13] and Erofeev (see [8]) for solid state decompositions and reaction kinetics can be described with this same dependence. Non-isothermal relaxation kinetics in viscoelastic bodies, i.e. vitrification and devitrification is also analyzed in the present contribution employing Avrami equation. In Section 3 it is shown, that the broad applicability of Avrami equation is determined by the circumstance, that this dependence is the particular case of a very general kinetic relation, following directly from the so called phenomenological equation of the thermodynamics of irreversible processes (see [7]). In this way Avrami form of this general dependence is used here only as a convenient algorithm in describing isothermal reaction kinetics and in transforming it from isothermal to non-isothermal applications

In our treatment, we consider all cases in terms of a non-isothermal variant of the integral form of Avrami equation. A simple procedure to deter-mine the reaction model based essentially on the value of Avrami power index n and an unambi-guous procedure to calculate also the corresponding activation energies is derived. It is shown here, that the Avrami power index n (originally expected to be n = 1, 2, 3, 4, see [6]) can have also non-integer, fractional values, corresponding to physically unexpected and interesting applications.

Thus we continue efforts, initiated by Kissinger [1] and by other authors, like Coats and Redfern [14, 15] in non-isothermal chemical reaction kinetics, and by Henderson [16], Gutzow [17] and Gutzow and Dobreva [18, 19] and Colmenero *et al*. [20] in analyzing processes of overall crystallization and nucleation at increasing or decreasing temperatures (i.e. at increasing supersaturation) in electrolytic phase deposition [17, 18], in polymer crystallization [19, 20] or in glass transitions. This lastly mentioned type of processes, as they are described in [7, 21–23]) can be considered as a non-isothermal kinetic process of structural freezing. Thus we anticipate here in fact not only chemical reaction kinetics, but we are even more interested in structural changes, their relaxation and in phase transition processes, taking place in condensed matter (see also [7, 22, 24, 25]).

The present contribution is organized in the following way:

In Section 2 we summarize basic relations, necessary for our analysis. Then in Section 3 the properties of the Avrami kinetic equation are analyzed in the new general, thermodynamically based form necessary here. It is shown, how this general approach can be used to describe practically any known case of isothermal or non-isothermal change in a new way. This description is done in such a form as to define by the value of Avrami power index n the reaction type and by a generalization of Ozawa's procedure – the temperature dependence of the activation energy $U(T)$ in non-isothermal processes. To the possible non-isothermal approaches with Avrami equation are destined Sections 4, 5 and 6. There we employ two isoconversional methods and derive an analytical and geometrical approach to enlarge in Section 7 the classical non-isothermal method of analysis proposed by Ozawa in [3, 4]. In Section 5, the analysis of several examples of reaction kinetics and phase transitions is given in terms of $U(T)$ dependences and considered in order to demonstrate both the possibilities and the limitations of existing and of the newly developed methods. Here we analyze crystallization process in general, chemical reactions and overall crystallization in polymer and simple melts, in glass-forming systems, in aqueous solutions and in electrolytic phase deposition. In Section 6 we describe isoconversional approximations and in Section 7 enlarge Ozawa's method of analysis. In Section 8 we apply the previously formalism developed to the kinetics of non-isothermal glass relaxation, i.e. to glass transitions, vitrification and to glass stabilization. In doing so we use the results and approaches of the kinetic theory of vitrification, initially formulated by Vol'kenstein and Ptizyn [21, 22] and then developed in a generic way by one of the present authors [23–25] on the basis of the thermodynamics of irreversible processes (see [7], [23], [25] and literature cited here in Section 10). In Section 9 a comparison with experimental results is given and lastly, in Section 10 several necessary conclusions are drawn. In Appendixes 1, 2, 3 several mathematical details are discussed.

2. SEVERAL BASIC KINETIC RELATIONS

Since van't Hoff's times the order of a reaction in chemical kinetics is determined by the way rate of change (at isothermal conditions) of the concentration dc_A/dt of one of the components (A, B, C) in the reaction system depends on the sum of the stochiometric coefficients ($a + b + c + \ldots$) in the expression

$$\frac{dC_A}{dt} = K(T)[A]^a[B]^b[C]^c .. \qquad (1)$$

Here [A], [B], [C] … indicate the concentrations of the components A, B, C, … in the reaction mixture and $K(T)$ is the temperature dependent reaction constant [11]. In homogeneous reactions (taking place in gaseous or liquid phases) the coefficients a, b, c,…. are as a rule integer numbers. More generally reactions of first, second or third order in chemical kinetics are called chemical or physical changes, following a time dependence of the type

$$\frac{dC}{dt} = K(T)C^m, \text{ with } m = 1, 2, 3, \ldots . \qquad (2)$$

Here C indicates the concentration of any structurally significant unit of the system. The transition of Eqn. (2) to more general formulations is usually done in defining C *via*

$$C = \frac{\xi - \xi_e(T)}{\xi_0 - \xi_e(T)} \qquad (3)$$

as the change of a physically significant internal parameter [7, 24, 25] from its momentary value, ξ, to its equilibrium value, $\xi_e(T)$. The initial value of ξ (at time $t = 0$) is indicated in Eqn. (3) with ξ_0. In considering phase transitions or topochemical reaction kinetics the rate of overall conversion (or phase transition), α, is defined *via* the provision

$$\alpha = \frac{V - V_i(T)}{V_0 - V_i(T)} \equiv C , \qquad (4)$$

when the notations of Eqns. (2), (3) are considered. Here V_t indicates the momentary value of the volume transformed (e.g. crystallized) at time t at the temperature T, V_0 is the initial and $V_i(T)$ its end value of V in the isothermal crystallization process investigated. This definition of α is particularly used in deriving and employing the Kolmogorov-Avrami equation [6, 7], to be discussed in the following Section 3 in details.

In terms of the still non-reacted, non-changed molar part $(1–\alpha)$ of the reaction participants van't Hoff's equation (2) can be written as

$$d\alpha/dt = K(T)(1–\alpha)F(\alpha) \qquad (5)$$

For first, second and third order homogeneous reaction kinetics the reaction model function $F(\alpha)$ in Eqn. (5) has the values

$$F(\alpha) = (1–\alpha)^p, \quad \text{with } p = 0, 1, 2 \qquad (6)$$

In considering solid state reactions as a case of heterogeneous, topochemical reaction kinetics, Roginskii and Shultz [13] (see also further similar proposals summarized in [8, 9, 12]) indicated as a realistic general possibility of reaction rate equations these to which $F(\alpha)$ in Eqn. (5) is defined in the form

$$F(\alpha) = \alpha^{2/3} \qquad (7)$$

This indicates, that in topochemical reactions not the volume V, but the surface area $S \approx V^{2/3}$ of the products formed is reaction determining.

To similar $F(\alpha)$-values in Eqn. (5) leads also Erofeev's topochemical reaction kinetics [8, 9, 26], which he formulated also in terms of the already mentioned Avrami equation. In its integral form, this equation gives the time dependence of α at constant temperature, T, as

$$\alpha = 1–\exp[–K_A(T)t^n] \qquad (8)$$

Here, according to Erofeev [8, 9, 26] the value of the integer power index $n = 1, 2, 3, 4$ depends (in analogy with Avrami's initial formulations, see [6, 7]) on the way in which the new interface, S, is formed via nucleation and growth processes in the reacting volume. This same Eqn. (8), as one of us has earlier shown [10, 27], describes also fairly well with values of $n = 1$ to 3 the overall crystallization process in an ensemble of equal spheres of radius R, each one of them crystallizing from the surface to its own volume. This model of crystallization of more or less finely dispersed materials was initially formulated by Mampel [28] in a way, leading to complicated, non-soluble integral dependences. They are, however, as also the results in [10, 27], of particular significance in DTA and DSC thermoanalysis, where usually fine-grained samples have to be investigated. This is one of the possibilities which the Avrami equation gives as a convenient algorithm in reaction kinetics. Further possibilities in this respect are indicated in Section 3.

According to Eqn. (8) the rate of change and conversion is given by

$$\frac{d\alpha}{dt} = nK_A(T)t^{n-1}\exp\left[-K_A(T)t^n\right] =$$

$$= nK_A(T)(1-\alpha)\ t^{n-1} \qquad (9a)$$

Thus we arrive at a simple relation, which is of general significance in the following analysis in Section 4: we can write Eqn. (9a) also as

$$\frac{d\alpha}{dt} = n(1-\alpha)\left[-\ln(1-\alpha)\right]^{\frac{n-1}{n}}\left[K_A(T)\right]^{\frac{1}{n}} =$$

$$= (1-\alpha)F(\alpha)K^*(T) \qquad (9b)$$

Observing that with Eqn. (8) we have $t^{n-1} = \left[-\ln(1-\alpha)\right]^{\frac{n-1}{n}} K_A^{2/3}(T)$ we can write Eqn. (9) also in the general form of Eqn. (5) with $K^*(T) = n\left[K_A(T)\right]^{1/n}$ and with a reaction model function, which for any power index n in Eqn. (8) is to be written as

$$F(\alpha) \equiv F_n(\alpha) = \left[-\ln(1-\alpha)\right]^{\frac{n-1}{n}} \qquad (10)$$

As far as in our notations always the coefficient of conversion has values $0 \le \alpha \le 1$, it is evident that for $n = 3$, Eqn. (10) gives by a simple expansion of the logarithm in a good approximation the $F(\alpha)$ value indicated with Eqn. (7) for the Roginskii-Schultz topochemical kinetics. More general and more precise, it can be shown (see [8, 26] and the mathematical procedure described there) that the Avrami Eqn. (8) leads to rate dependences of the type

$$\frac{d\alpha}{dt} = K^*(T)(1-\alpha)^r \alpha^s \qquad (11)$$

They can be also represented in the form of our Eqn. (5), however, with

$$F(\alpha) = F_n^E(\alpha) = (1-\alpha)^{r-1}\alpha^s \qquad (12)$$

and with r and s values, corresponding to concrete n-values [8, 26] in Avrami equation, as this is given on Table 1, taken from [8].

Table 1. Avrami and Erofeev power indeces in Eqns. (8), (11) and (12).

Avrami power index, n in Eqn. (8)	Erofeev power index			
	Eqn. (11)		Eqn. (12)	
	r	s	$(r-1)$	s
1	1	0	0	0
2	0.774	1/2	–0.226	1/2
3	0.700	2/3	–0.300	2/3
4	0.665	3/4	–0.335	3/4

The essential point, to be mentioned here is, that the kinetic Eqn. (5) is in fact one of the possible forms of a general growth and development dependences (see [29, 30]), determining the rate of change by the present status (here indicated by the value of $(1-\alpha)$) of the system and by an additional correction function, $F(\alpha)$, determined by the concrete model or mechanism of the expected change. This model approach considered initially for isothermal regimes and conditions is to be transformed here to non-isothermal kinetics of reaction and change.

For the particular forms of the $F(\alpha)$-function different integral forms of Eqn. (5) follow. Thus for first, second and third order homogeneous reactions after integration of Eqn. (5) with the indicated values of p in Eqn. (6) and the additional condition $\alpha = 0$ at $t = 0$ it follows

$$\alpha = 1-\exp[-K_A(T)t] \qquad (13)$$

$$\alpha = 1-[1+K(T)t]^{-1} \qquad (14)$$

$$\alpha = 1-[1+2K(T)t^{-1/2}] \qquad (15)$$

Thus for first order reaction kinetics follows directly Avrami Eqn. (8) with $n = 1$.

The integration of the kinetic rate equations of the type (5) with fractional values of the power index, as given by Eqn. (7), leads to mathematically implicit dependences. Thus for $\alpha^{1/2}$ we obtain the complicated expression (see [31] p. 32)

$$\alpha = \left\{1-\left(1+\sqrt{\alpha}\right)\exp\left[-K(T)^{1/2}t\right]\right\}^2 \qquad (16)$$

which, as it is obvious from Fig. 1, can be conveniently and with sufficient accuracy approximated by an Avrami-type dependence with $n = 2$. The integration of Eqn. (9) leads directly to the corresponding Avrami Eqn. (8). In Section 3 it is shown, that Eqns. (14), (15) can be also written in the form of the Avrami equation, however, with fractional values of the power index n.

Thus it is turns out, that quite differing kinetic dependences, corresponding to the general kinetic relation Eqn. (5) having various $F(\alpha)$-values, can be represented in their integral form by Avrami equation simply by varying the value of the power index n. In this way seemingly different dependences can be, as discussed in the following Section 3, represented in a relatively uniform way and characterized by a distinct number: the value of the power index n. These properties of Avrami equation give, according to the main idea of the present contribution, also a more easy way to analyze kinetic changes at different mechanisms (i.e. at differing $F(\alpha)$-values in Eqns. (5) and (6)) at non-isothermal conditions, and especially at increasing or decreasing cooling (heating) rates q

$$dT = qdt \qquad (17)$$

taking place with a constant value of q. As far as Eqn. (17) is fulfilled, it is easy to change the argu-

ment from time, t, to temperature, T, in both the differential and the integral kinetic dependences, so far introduced above.

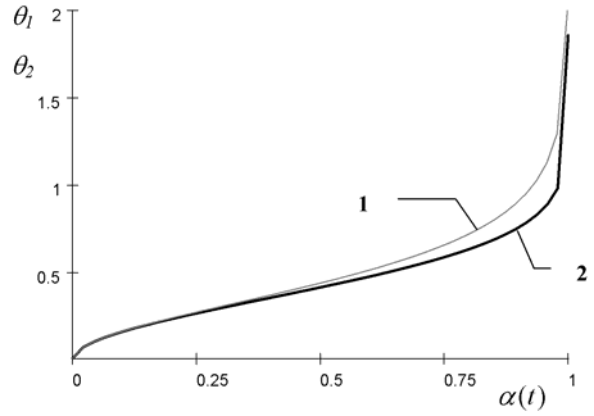

Fig. 1. Approxination of the implicit $\alpha(t)$-dependence, Eqn. (16) with an Avrami-type dependence (Eqn. (8)) with $n = 2$. On the ordinate is plotted $\theta_1 = \dfrac{t}{\sqrt{K(T)}}$ *vs.* $\alpha(t)$ on the ordinate for Eqn. (16) as (**1**) and $\theta_2 = \dfrac{t}{\left(\dfrac{\ln(2)}{K(t)^{1/2}}\right)}$ for Eqn. (8) as (**2**). According to Eqns. (22) and (16) in Section 3, θ_1 and θ_2 are reduced times in respect to the corresponding half transition times, $\tau_{0.5}$, for both dependences.

From a more general point of view Eqn. (5) with the additional specifications, provided by $F(\alpha)$ (Eqns. (6), (7), (12)) is a general form of one of possible equations of steady growth and development [29, 30].

When additional structural specifications are connected with the process investigated, $F(\alpha)$ indicates the way this specifications are transformed, either steadily decreasing the rate of general change (Eqn. (6) or determining a maximum (Eqn. (7)) as seen on Fig. 2. At $F(\alpha) = 1$ as this is for first order kinetics of change we consider unrestricted growth proper, dependent only on the depletion of the concentration of the initial components, $(1–\alpha)$. In Eqns. (7) and (9) the build-up of a new interphase surface determines a maximum value in the $d\alpha/dt$-course. In nucleation and growth processes the nature of both the $F(\alpha)$ and the $K(T)$-functions are determined by the interplay of the activation energies of these two processes (see Section 4).

In describing relaxation processes in glasses (Section 8) we have to discuss cases, when the change of $K(T)$ is dependent on the depletion of the active constituents of the system. Thus there $K(T)$ has in fact the significance of a time dependent resistance, changing with the advancement of the process of structural relaxation [30] and with the alteration of activation energies it causes.

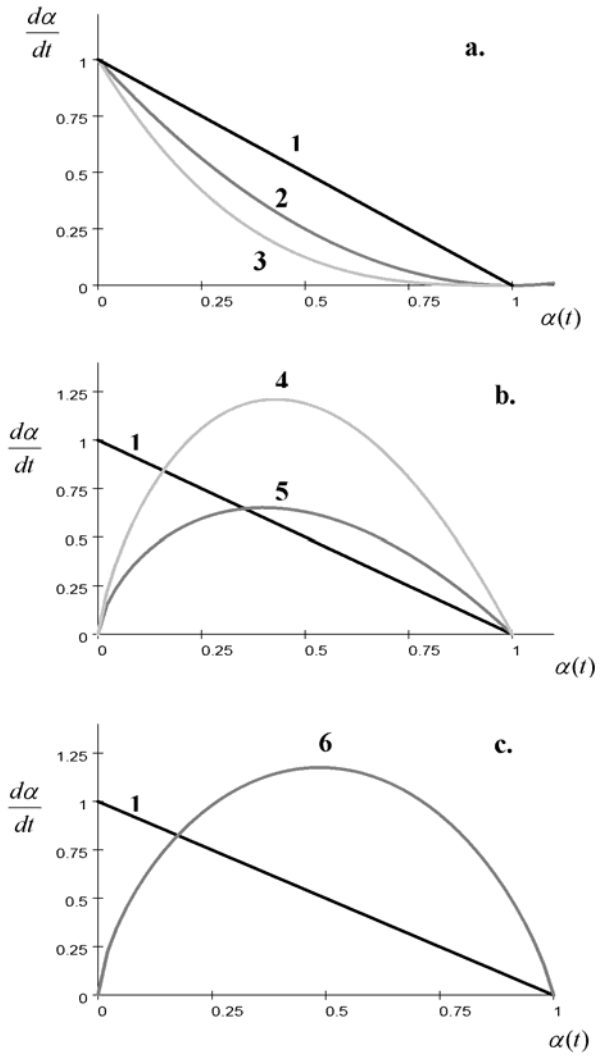

Fig. 2. Rate of transition dependences for various kinetic mechanisms.
a. Homogenous reaction kinetics (Eqns. (5) and (6)). 1 - first order; 2 - second order; 3 - third order reaction;
b. Topochemical reaction mechanisms: 1 - first order; 4, 5 - Roginskii type dependences: according to Eqn. (7) with $\alpha^{2/3}$ and $\alpha^{3/4}$;
c. Avrami-type rate dependences, Eqn. (9): 1 - with $F(\alpha) = 1$; 6 - with $n = 3$ and $d\alpha/dt$, according to Eqn. (9).

3. PROPERTIES OF THE AVRAMI EQUATION AS A GENERAL KINETIC DEPENDENCE

The general reaction and crystallization dependence given here as Eqn. (8), usually attributed to Avrami is initially derived by Kolmogorov [5] (for the special case $n = 3$) and than by Avrami [6] more generally in the framework of a crystallization model and as the result of a long history of development of ideas, summarized in [7]. Also on crystallization models are based the already mentioned derivations of Mampel [28] and Gutzow *et al.*

[10] and even Erofeev's applications of this equation to solid state reactions [32], summarized in [8].

There are, however, also other ways of deriving and analyzing Eqn. (8), which we are still denoting here as Avrami dependence, which are based on broader premises. Here first has to be mentioned an attempt by Kazeev [33] to postulate dependences equivalent to Eqn. (8) as following from the theory of physicochemical similarity for reaction kinetics and change, taking place under distinct constraints. In a more recent series of papers by Gutzow *et al*. [30, 34, 35] it was shown, that rate dependences of the type, given here with Eqn.(5) with time dependent $F(\alpha)$-values follow in cases, when the rate of change ($d\alpha/dt$, or $d\xi/dt$, see Eqn. (3)) of the process is determined by a time-changing activation energy $U(T,t)$. In this sense as a result of the analysis in [34, 35] Eqns. (5), (6) having values of the Avrami power index $n < 1$, can be also written as

$$\frac{d\xi}{dt} = \frac{1}{\tau_0(T)}\frac{n}{t^b}(1-\xi) \qquad (18)$$

i.e. as changes, determined by a time dependent relaxation time $\tau^* = \tau_0(T)/t^b$. To Eqn. (18) correspond integral forms of the type

$$(\xi - \xi_0) = (\xi_0 - \xi_{in})\exp\left[-\left(\frac{t}{\tau_0^*}\right)^{1-b}\right] \qquad (19)$$

usually referred to as fractional or stretched-exponent relaxation dependences (see the historic background given in [34] and the original publications of R. Kohlrausch [36], F. Kohlrausch, [37] and Boltzmann [38] for this formula). According to these general considerations a value $n > 1$ in Eqn. (8) corresponds to kinetic barriers, $U(T, t)$ decreasing with time, while $n < 1$ suits models with time increasing values of the barrier. In terms of Eqn. (18) the relaxation time $\tau^* = \tau_0 t^b$ gives at $n = 1$, a constant value of the activation energy $U(T,t) = U(T) = U_0 = const$. At $b = 0$ Eqn. (19) thus gives dependences, corresponding to first order reactions and to Maxwell's classical solution of the kinetics of relaxation (see [7, 39])

$$(\xi - \xi_0) = (\xi_0 - \xi_{in})\exp\left(-\frac{t}{\tau^{\#}(T)}\right) \qquad (20)$$

According to the initial derivations of Avrami, the power index n in Eqns. (8), (9) has to have only integer values $n \geq 1$ (1 to 4 in three dimensional value growth and $n = 2$–3 for surface growth in thin layers [7], [40], see Table 2). In considering growth of more or less finely dispersed samples according to the already mentioned model considerations and experimental results in [10, 27] also fractional values of n in the range 1 to 1/3 have to be expected in both Eqns. (8) and (9). It becomes thus evident, that with fractional values $n < 1$ of the power index in Avrami Eqn. (8) not only first, second and third order reaction dependences, but also Kohlrausch-type stretched exponent relaxation relations can be described. In fact, the Kohlrausch formula (Eqn. (18)) is a typical case of a second order reaction kinetics dependence. Its integral form (Eqn. (19)) corresponds to the mentioned particular cases of the Avrami dependence with $n < 1$ (usually in glass-forming melts $(1–b) \approx (0.30–0.35)$, i.e. $b = (0.70–0.65) \approx 2/3$, see [7, 22].

Table 2. Avrami power indeces, n in Eqn. (8), see [6, 7] in dependence of mechanism and morphology.

Mechanism of nucleation	Growth morphology	Formula for k_n	n	Author
sporadic	spherical	$\frac{\omega_n}{n} v^3 J$	4	Avrami [6]
athermal	spherical	$\frac{\omega_n}{n} v^3 N^*$	3	Avrami [6]
sporadic	disk-like	$\frac{\omega_n}{n} v^2 h J$	3	Avrami [6]
athermal	disk-like	$\frac{\omega_n}{n} v^2 h N^*$	2	Avrami [6]
sporadic	needle-like	$\frac{\omega_n}{n} v h^2 J$	2	Avrami [6]
athermal	needle-like	$\frac{\omega_n}{n} v h^2 N^*$	1	Avrami [6]
surface sporadic	Surface growth	$\frac{\omega_n}{n} v^2 J_2$	3	Vetter [40]
surface athermal	surface radial growth	$\frac{\omega_n}{n} v^2 N_2^*$	2	Vetter [40]

In considering the discussion of Avrami Eqn. (8), let us further on observe, that in reduced coordinates $\theta = (t/\tau^{\#})$, where

$$\tau^{\#} = 1/[K_A(T)]^{1/n} \qquad (21)$$

the value $(t/\tau^{\#}) = 1$ determines an iso-conversion constant $\alpha_{iso} = \left(1 - \frac{1}{e}\right) = 0.63$ for any n-value (Fig. 3). Moreover, because of $-\ln(1–\alpha) \approx 1$ for the same value of α, the product $(1–\alpha)[-\ln(1–\alpha)]^{(n-1)/n} = F_n(\alpha)$ is also a constant as also evident from Fig. 3. Both properties of the Avrami dependence (Eqn. (8) apply for $n \geq 1$ as well as for $n < 1$ and are essential in analyzing non-isothermal reaction kinetics and

change. They define in a natural way the iso-conversional methods of non-isothermal determination of the parameters of Avrami type dependences, discussed here in details in Section 5.

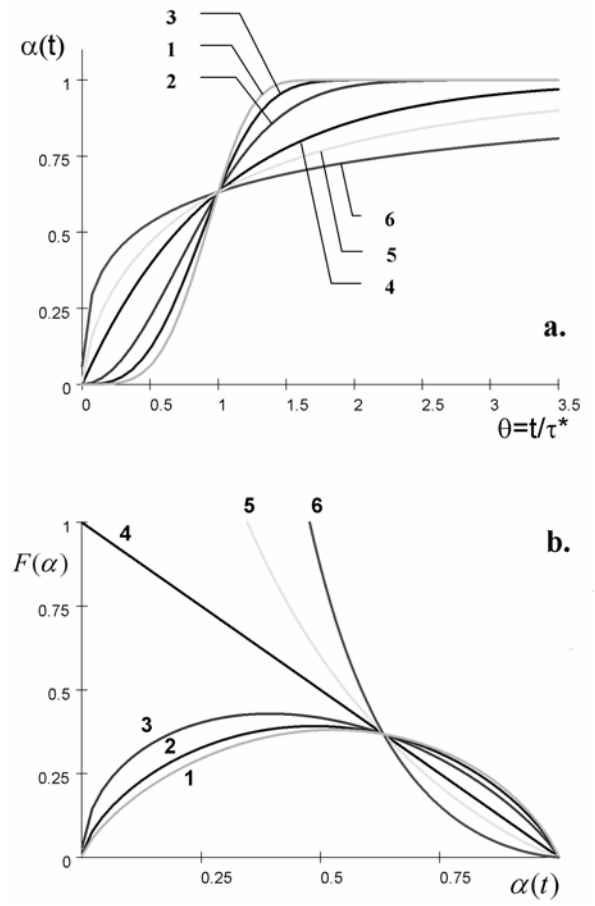

Fig. 3. Properties of the Avrami equation.
a. Avrami curves according to Eqn. (8) in coordinates $\alpha(t)$ *vs*. $\theta = t/\tau^*$, where the time τ^* is given with Eqn. (21). Note that at $\theta = 1$ all curves (for both $n \geq 1$ and for $n < 1$) have the same ordinate, $\alpha = \left(1 - \frac{1}{e}\right) = 0.63$. With 2, 3, 4 are denoted the Avrami power index values of $n > 1$ and with 4, 5, 6, $n = 1$, $n = 2/3$ and $n = 2/5$, respectively;
b. The course of the function $[1 - \alpha(t)]F(\alpha)$ with $F(\alpha)$ given according to Eqn. (10). With numbers are again indicated the n-values in Eqn. (8) as given above. Note that all $F(\alpha)$-curves have at $\alpha = 0.63$ approximately the same value, $\alpha = 1/e$.

An essential parameter to be also used in this connection is the time $\tau_{0.5}$ of half transition (or half conversion) in any process of change investigated: it is the time for α (or any other change coordinate defined with Eqs. (3) or (4)) to become equal to 0.5. Using either Eqn. (8) or Eqn. (13), (14), (15) this time is given by

$$\tau_{0.5} = \ln 2/K(T)^{1/n} \tag{22}$$

according to Eqn. (8) (i.e. also with $\tau_{0.5} = [\ln 2/K(T)]$ for first order reaction kinetics according to Eqn. (13) and with

$$\tau_{0.5} = 1/K(T) \tag{23}$$

and

$$\tau_{0.5} = 3/2.K(T) \tag{24}$$

for second and third order reaction kinetics (see Eqns. (14), (15) respectively).

Further on it is of essence to be mentioned, that the maximal value of the rate of conversion $\left(\frac{d\alpha}{dt}\right)_{\max}$ determined by the Avrami-type equations are given with

$$\frac{d\alpha}{dt}\Big|_{\max} = \left[(n-1)^{n-1}\,\omega K(T)\right]^{1/n} \exp\left(-\frac{n-1}{n}\right) \tag{25}$$

The time, at which this maximum is reached, is given with

$$\tau_{\max} = \left[\frac{n-1}{K(T)}\right]^{1/n} \tag{26}$$

It is evident, that at $n > 1$ both values correspond at to the inflexion point of the respective $\alpha(t)$-curve, determined by Eqn. (21).

From the $\alpha(t)$ *vs*. $\tau_{0.5}$-representation given on Fig. 4 it is evident that first, second and third order reaction kinetics, originally described by Eqns. (13), (14) and (15) with three seemingly quite differing dependences can be represented with sufficient accuracy by the Avrami Eqn. (8) respectively with n = 1, 2/3, 2/5. As seen the coincidence of the corresponding curves goes from $t/\tau_{0.5} = 0$ (i.e. at $\alpha(t) = 0$) through $t/\tau_{0.5} = 1$ to $t \to \infty$. On Fig. 5 the $(d\alpha/dt)$-curves, following with both Eqns. (9) and (25) are also illustrated for both $n \geq 1$ and for $n < 1$.

From Fig. 1 it was also seen that the Roginskii-type dependences Eqns. (6), (7) (for both $F(\alpha) = \alpha^{2/3}$ and $F(\alpha) = \alpha^{1/2}$) are sufficiently well represented with $\alpha(t)$-curves according to Eqn. (8) with n = 3 and 2, respectively (c.f. also Fig. 3).

Equations (18) and (19) show moreover, that the mentioned formal resemblance in the $\alpha(t)$-dependence is illustrated by the relative closeness of the respective differential relations – by the course of the $d\alpha/dt$-function in both cases.

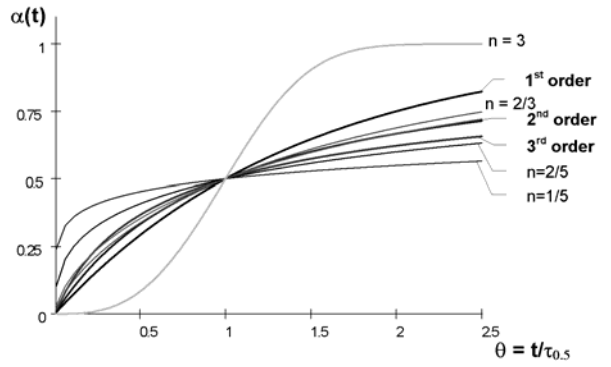

Fig. 4. The specification of first, second and third order reaction kinetics in terms of the Avrami equation, Eqn. (8), as an intermediate algorithm. With bold lines and text are indicated, beginning from below third, second and first order homogeneous reaction kinetics, respectively (c.f. Eqns. (13), (14) and (15)). With thinner lines are indicated the respective Avrami-curves, Eqn. (8) with $n = 1, 2/3, 2/5, 1/5$; on top is drawn the Avrami-curve with $n = 3$. In this way $n = 1$, 2/3 and 2/5 are chosen to represent the above indicated reaction kinetic curves.

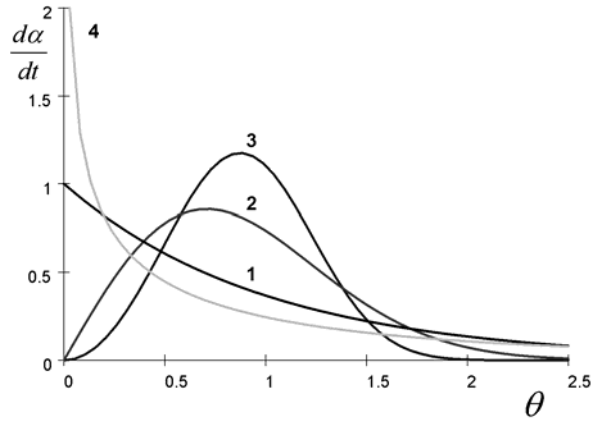

Fig. 5. Transition rate curves $d\alpha/dt$ *vs.* θ, Eqn. (21), according to first, second and third reaction kinetics, Eqns. (13), (14), (15) expressed as reaction rates, following from the Avrami equation, Eqn. (8), with $n = 1$, 2, 3 and $n = 2/3$. Note first that $n = 1$ is equal with first order kinetics and that for any $n > 1$ a maximum is displayed by the Avrami rate curves. Here are indicated the following rate dependences 1 – $d\alpha/dt = \exp(-\theta)$; 2 - $d\alpha/dt = 2\theta\exp(-\theta^2)$; 3 - $d\alpha/dt = 3x^2\exp(-\theta^3)$; 4 - $d\alpha/dt = 2/3.x^{-1/3}\exp(-x^{2/3})$.

The classical derivation of the Avrami equation in its isothermal formulation treated up to now can be simply made either in terms of the probabilistic models, stemming from Kolmogorov [5, 7], or more appropriate for our further developments via the remarkable notion of the extended volume $Y_n(t)$ and the so called Avrami theorem [6, 7]. According to this theorem, because of the interaction of growing crystallites, we have to write

$$d\alpha(t) = (1-\alpha)d[Y_n(t)] \qquad (27)$$

where $Y_n(t)$ is given in general as

$$Y_n(t) = \int_0^t I(t',T)dt'\left[\int_{t'}^t v(t'',T)dt''\right]^n$$

Thus $Y_n(t)$ is the virtual volume, formed by nucleation and growth, if no interaction should take place between growing crystallites.

Assuming time-constant values of both nucleation rate $I(t,T) \equiv I(T)$ and of growth rate $v(t,T) \equiv v(T)$ the extend volume becomes

$$Y_n(t) = \omega_n I(T)v^{n-1}\int_0^t (t-t')dt' \qquad (28)$$

Here and in Eqns. (25), (29) ω_n is a steric coefficient ($\omega = 4\pi/3$ at spherical drowth). Thus, in a known way of integration ([6, 7, 8], see Eqn. (28) follows directly the Avrami Eqn. (8) and $K_A(T)$ is thus defined *via* nucleation rate $I(T)$ and growth rate $v(T)$ as

$$K_A(T) = \omega I(T)[v(T)]^{n-1} \qquad (29)$$

This approach is used here in order to derive in the next Section 4 more easily the Avrami kinetics also in the non-isothermal case of the nucleation and growth models. We have also to mention, that the usual way to analyze isothermal results in terms of Eqn. (8) by putting the experimental isotherm in $\log[-\log(1-\alpha)]$ *vs.* $\log t$ coordinates and thus to determine both n and $K(T)$ will be also applied in a generalized Ozawa modification to analyze the non-isothermal case in the next Sections.

4. AVRAMI EQUATION AT NON-ISOTHERMAL CONDITIONS

To this point we summarized only results of the isothermal formulation of reaction phenomenology. Now we have to apply these results to the non-isothermal case. In doing so, we have first to specify additionally both the conversion function α, which is now dependent on both time, t, and temperature, T, as $\alpha(T,t)$ and to introduce temperature as a new argument into the formalism derived.

Anticipating in the following with Eqn. (17) only constant rates of temperature change, we have to write in heating run experimentation

$$T = qt + T_{in} \approx qt \qquad (30a)$$

and to employ the right hand side approximation, when the initial temperature, T_{in}, is sufficiently low, when compared with the temperature, T, where the reaction can be actually observed.

In cooling run experimentation, e.g. in melt crystallization at constantly increasing undercooling with Eqn. (17)

$$\Delta T = (T_m - T) \approx qt \tag{31}$$

Thus, we have to write for the time-dependent increase of the thermodynamic driving force (the supersaturation $\Delta\mu(T)$) of crystallization that

$$\Delta\mu(T) = \Delta S_m qt \tag{30b}$$

because of

$$\Delta\mu(T) = \Delta S_m \Delta T \tag{32}$$

The supersaturation is estimated here via the respective melting temperature, T_m, and the entropy of melting, ΔS_m, (see [7] for this approximation and for more precise solutions). In deriving the $\alpha(T,t)$ *vs*. $\alpha(t)_T$ connection (where $\alpha(t) \equiv \alpha$, employed up to now) we have to consider, that in fact the $\alpha(T,t)$ function, because of Eqn. (30), is in fact a composite function of t, i.e. we have to write $\alpha(T,t) = \varphi[f(t)]$. With the $f(t)$ function given by the right hand side of Eqn. (30) and employing the chain rule of differentiation of composite functions (see [31], p. 32) we obtain with Eqn. (17)

$$\frac{d\alpha(T,t)}{dT} = \frac{d\varphi[f(t)]}{df(t)}\frac{df(t)}{dt} = \frac{1}{q}\frac{d\alpha(t)}{dt}\Big|_T \tag{33}$$

Thus we have specified beside the dT *vs*. dt dependence also the $\alpha(T,t)$ *vs*. $\alpha(t)$ and the $d\alpha(T,t)$ *vs*. $d\alpha(t)$ connections. These connections should make no problem for $q = const.$ in Eqn. (17): in every differential equation such as Eqns. (9), (11), the argument can be directly replaced by another one, linearly connected with the initial argument. Nevertheless, as mentioned in [41] and elsewhere, this simple procedure still gives rise to questions in thermoanalytical literature, and made necessary the derivation indicated with Eqn. (33).

In order to analyze the kinetics of non-isothermal processes of phase transitions and chemical change we have, accounting for the properties of the Avrami equation, two ways open.

First we can use the circumstance, that (Figs. 3 and 4) both isoconversion points ($\alpha = 0.63$ or $\alpha = 0.5$) are reached at the reduced time $\theta = t/\sqrt[n]{K(T)} = 1$ or $\theta = t/\tau_{0.5} = 1$ for any value of the Avrami index n. For $n > 1$ (i.e. for phase change and solid state reaction) this isoconversion value corresponds to the inflexion point of the respective $\alpha(t)$ or $\alpha(T,t)$ dependences and thus also to the respective maximum in the $(d\alpha/dt)$ or $d[\alpha(T,t)/dT)]$-rate relations.

It is obvious, recollecting Eqns. (17), (30), (33), that because of the constant value of the cooling/heating rate, q, we can write for the maximal value of the rate of change or conversion

$$\frac{d}{dT}\left[\frac{d\alpha(T,t)}{dt}\right] = \frac{d}{dT}\frac{1}{q}\left(\frac{d\alpha(T,t)}{dT}\right) = 0 \tag{34}$$

For $n > 1$, this maximum in the $(d\alpha/dt)$ or $[d\alpha(T,t)/dT]$-dependence corresponds to the inflexion point, seen on Figs. 3 and 4. For $n < 1$ the same conversion value $\alpha(t)$ or $\alpha(T,t)$ is also observed when for $n > 1$ the inflection point is reached.

Returning to Eqns.(5) or (9) it thus turns out, than when always the same α-value is reached, the maximum in the $(d\alpha(T,t)/dT)$-dependences is determined for any q value by the maximum of the $K(T)$ *vs*. T dependence *via*

$$nq\frac{d}{dT}\left\{\left[K(T)\right]^{1/n}\right\} = 0 \tag{35}$$

In changing the argument from t to T and integrating the left-hand side of Eqn. (9a) in limits from 0 to α_{max} or from 0 to $\alpha_{0.5}$ according to

$$\int_0^{\alpha_{\max}} \frac{d\alpha}{(1-\alpha)} \cong \frac{n}{q^n}\int_0^{T_{\max}} K(T)T^{n-1}dT \tag{36a}$$

it turns out, that by using for $\alpha(t)$ an Avrami dependence for any n value the left hand integral in Eqn. (36) has the same constant value for both $\alpha_{\text{inflexion}}$ or $\alpha_{0.5}$.

In this way the maximal value of any theoretically constructed or experimentally obtained $d\alpha(T,t)/dT$ *vs*. T-rate curve is determined by the subintegral function in the right hand integral of Eqn. (36a), i.e. by the course of the $K(T)$ subintegral functions corresponding to the Eqns. (8), (13), (14), (15), (16).

Even more conveniently, using the Avrami-equation (8) is to employ Eqn. (9) in the form (9b); than we have to write

$$\int_0^{\alpha_x} \frac{d\alpha}{(1-\alpha)F(\alpha)} \cong \frac{1}{q}\int_0^{T_{\max}} K(T)^{1/n}\,dT \tag{36b}$$

where $F(\alpha)$ is given by Eqn. (10). As far as according to Fig. 3 both α_{in} and $F(\alpha)_{in}$ are constants for any n-value we have at this representation not only a constant value at the right hand side of Eqn. (36b), but the left hand integral is now considerably simplified and determined only by the temperature function of $K(T)$.

In this way the analysis of non-isothermal reaction and transition kinetics according to above so called isoconversional method of analysis is trans-

formed into a problem of the integration of the right hand integrals in Eqn. (36b). At the possible $K(T)$ dependences discussed in the next Section this problem is reduced to a transformation of the respective integrals to two higher transcendent function: to the Integral Exponent function $Ei(Z)$ or to the Gauss Error Function $erf(Z)$ with. The details of this transformation depend on the nature of $K(T)$, i.e. on the temperature function, of the expected kinetic coefficients, as given in Section 5 and in Appendixes 1 and 2.

5. TEMPERATURE DEPENDENCE OF THE KINETIC COEFFICIENTS

Thus we know, that the whole course of the $(d\alpha/dT)$-function at differing cooling or heating runs e.g. in DTA or DSC-arrangements is determined by the temperature function of $K(T)$ or of $K(T)T^{n-1}$ in Eqns. (5, 9) i.e. of the value $K_A(T)$ in the Avrami equation, using the present approach.

In the differing relations, underling above mentioned dependences, the $K^*(T)$ function ($K^*(T) = nK_A(A)^{1/n}$, *etc*.) can be written in general as

$$K^*(T) = K_0 \exp\left[-\frac{U(T)}{RT}\right] \tag{37}$$

where the particular form of the activation energy function $U(T)$ has to be determined in every case. In homogeneous reaction kinetics an Arrhenian type dependence with $U(T) = U_0 = \text{const}$ is usually assumed [11]. A similar approximation is also made sometimes in most cases of solid state reactions [8, 12]. However in general for topochemical reaction kinetics using appropriate models, based most conveniently on the Avrami theorem (see below Eqns. (41–43) leading to more complicated temperature relations are expected. Thus, $K_A(T)$ depends in such cases on the kinetic and thermodynamic barriers of crystal nucleation $I_0(T)$ and growth rates $v(T)$. In processes of relaxation and vitrification kinetics $U(T)$ in Eqn. (37) is dependent on the concrete mechanism of structural flow and on the change of the ξ-function in Eqn. (3) (see [7, 23, 24, 25] and literature cited there).

In cases of relaxation in glass-forming liquids the $U(T)$-function in Eqn. (37) is determined e.g. by the Vogel-Fulcher-Tammann equation [7] in terms of free volume concepts of liquids flow as

$$U(T) = RT/(T - T_0) \tag{38}$$

Here $T_0 \approx 0.5T_m$ is a constant, connected with the respective melting or liquidus temperature, T_m or T_{liq}. In the framework of configurational entropy considerations [7, 42, 43] similar or even more appropriate $U(T)$ – dependences can be derived and used in considering relaxation phenomena in glass-forming melts (see Section 8).

In processes of phase transition the particular structure of Eqn. (29) determines the temperature dependence of $K_A(T)$ according to existing models on nucleation rate and crystal growth kinetics as being defined by both a kinetic barrier of the type given with Eqns. (37), (38) and by second, thermodynamic barrier, determined by the work, $W_c(T)$, necessary to form a crystalline nucleus. According to the classical nucleation theory (see [7, 44, 45]),

$$\frac{W_c(T)}{RT} \approx \frac{W_c^0 \Phi}{RT} = \frac{B_0 \Phi}{RT\Delta\mu^2(T)} \tag{39}$$

Here B_0, W_c^0 are determined, according to Gibbs' capillary approximation (see [7, 45]) for a spherical nucleus as

$$B_0 \sim \frac{4}{3}\pi\sigma^3 V_m^2 \tag{40}$$

by the interphase energy, σ, at the nucleus/ambient phase interface by the molar volume V_m of the crystal and by the thermodynamic driving force, $\Delta\mu(T)$, of the crystallization process. The value of W_c^0 refers to non-catalyzed (homogeneous) nucleation and the factor Φ ($0 \le \Phi \le 1$) accounts in heterogeneously induced nucleation for the nucleating activity of foreign nucleation cores [7, 45]. In a good approximation (see [7]) for melt crystallization the value of $\Delta\mu$ is determined by Eqn. (32) *via* undercooling, ΔT, and the respective melting entropy, ΔS_m, of the crystallizing substance.

Thus, the temperature dependence of the dominant factor in Eqn. (29), the rate of nucleation, $I_0(T)$, can be written as

$$I_0(T) \approx const_1 \exp\left[-\frac{U(T)}{RT}\right]\exp\left[-\frac{B_0^{\#}\Phi}{RT\Delta T^2}\right] \tag{41}$$

where at temperatures $T \approx T_m$ the value of B_0 is to be replaced by $B_0^{\#} = \left(B_0 / \Delta S_m^2 RT_m\right)$.

In considering the Avrami-equation (8) as a particular dependence in describing models of crystal growth (by two-dimensional nucleation, via screw dislocations or by the continuous incorporation of ambient phase molecules on the roughened surface of the crystal (see [7], [44]), the rate of crystal growth in Eqn. (29) has to be written as

$$v(T) \cong const_2 \exp\left[-\frac{U(T)}{RT}\right]\Omega(T) \tag{42}$$

where Ω(T) depends on the concrete mechanism of growth. It is essential to note , that two-dimensional nucleation growth is of significance only in polymer melt crystallization (see [7,19, 44, 45]) and even there the work of two-dimensional nucleation rate, $W_2(T)$, is considerably lower than $W_c(T)$, $\left[W_2(T)/RT\right] \cong \left[B_2/RT\Delta\mu\right] << W_c^0(T)/RT$

Here W_c^0 indicates, as given with Eqn. (39) the value of the respective work for homogeneous formation of tri-dimensional nuclei (i.e. at $\Phi = 1$) and $W_2(T) \sim \sigma^2 V_m$ is the respective thermodynamic work to form a two-dimensional nuclei at the growing crystal face .

In both growth *via* screw dislocations ($\Omega(T) \sim const_3 \Delta\mu^2(T)$) and at continuous growth ($\Omega(T) \sim const_4 \Delta\mu(T)$) the temperature dependence of $\Omega(T)$) in Eqn. (42) can be neglected when compared with the exponents in Eqns. (41), (42). Thus, it follows that even in polymer melt nucleation (see [7], [44]) with

$$\exp\left(-\frac{W_c^0}{RT\Delta\mu^2(T)}\right)\exp\left(-\frac{W_2}{RT\Delta\mu(T)}\right)^{1/n} \approx$$

$$\approx \exp\left(-\frac{W_c^0}{RT\Delta\mu^2(T)}\left[1+\frac{W_2\Delta\mu(T)}{nW_c^0}\right]\right) \quad (43)$$

it can be taken, that at small undercoolings the temperature dependence of $K_A(T)$ in Eqn. (29) is determined (at medium Φ values) as

$$K_A(T) \approx \omega\ const_0 \exp\left(-\frac{U(T)}{RT}\right)\exp\left(-\frac{W_c\Phi}{RT\Delta\mu^2}\right) \quad (44)$$

i.e. by the thermodynamics and kinetics of the three dimentional nucleation process only.

On the other side, at preexisting populations of very active crystallization cores with $\Phi \approx 0$ (athermal nucleation in Avrami terminology [6]) also the possibility $I_0(T)$ = const has to be considered. This leads to dominant growth determined overall crystallization kinetics (see [7], [27]).

Taking moreover into account that in the vicinity of T_m the value of $W_c(T)$ dramatically increases (at $T \to Tm$, $W_c^0 \to \infty$, $U(T) \to U_0$ = const so that there $W_c(T) >> U(T)$) (see experimental evidence summarized in this respect in [46, 47] for the crystallization of $(NaPO_3)_x$-glasses and of pure H_2O). On the other side at temperatures, approaching on the contrary the glass transition temperature T_g (where usually $T_g \approx 2/3T_m$, see [7]) we have to expect there $W_c(T) << U(T)$. Thus, two possible approximations are to be considered in general as determining the temperature dependence of $K_A(T)$ in melt crystallization:

i.) in the vicinity of melting temperature, T_m:

$$K_A(T) \approx const \exp\left[-\frac{B_0^*\Phi}{\Delta T^2}\right] \quad (45)$$

with $B_0^* = B_0^{\#}/RT_m$ given with Eqn. (41) and

ii.) at great undercoolings (especially at temperatures in the vicinity of T_g)

$$K_A(T) \approx const \exp\left[-\frac{U_0}{RT}\right] \quad (46)$$

as this is discussed in more details in [46, 47]. It is to be also noted, that in writing Eqn. (46) in fact it is assumed, that the two barriers $[U(T) + W_c(T)]$ in above equations are replaced by a mean constant value, $\overline{U_0}$. The subintegral function in Eqn. (36b) determined by Eqn. (44) or by growth only in athermal nucleation are illustrated on Fig. 6.

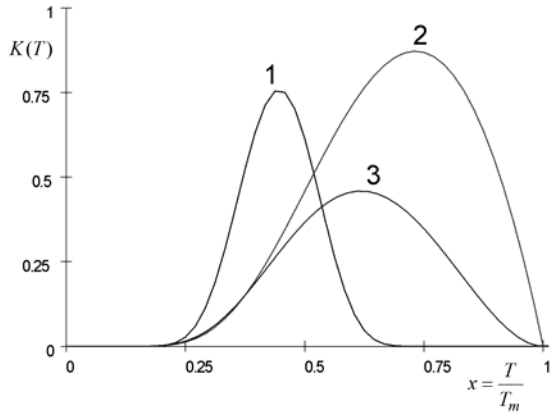

Fig. 6. The form of the subintegral functions in the right-hand integral of Eqn. (36b) at phase transition reactions for different mechanisms of nucleation and growth: 1 – 3D nucleation, according to Eqn. (44); 2 – crystal growth at continuous mechanism of incorporation; 3 – crystal growth at screw dislocations (both with Eqn. (42) and with $\Omega(T) = (1-x)$ and with $\Omega(T) = (1-x)^2$. The three K(T) curves are drawn with the same kinetic activation energies $U(T) = (2/x)$ and with $A_0 = 10^5$, 50 and 80, respectively. With x is indicated the reduced temperature, $x = T/T_m$.

These two approximations are used in the most often applied method of analysis of non-isothermal crystallization processes given in the next Section, and Eqn. (46) – also for the analysis of all cases of non-isothermal chemical reaction kinetics and especially in polymer crystallization (see [7, 19] and

in the crystallization of undercooled aqueous solutions [47]). An interesting case of nucleation, as pointed out in [17, 18], is the electrolytic crystallization of melts on the cathode under galvanostatic conditions. There a steadily increasing overvoltage $\Delta\varepsilon = q_0 t$, determines the supersaturation $\Delta\mu(t)$ and thus a formalism similar to Eqn. (45) has to be applied.

6. ISOCONVERSIONAL APPROXIMATIONS

According to these approximations the integration of the right-hand side of Eqn. (36b) is performed introducing for the subintegral function either Eqn. (45) (as first done in [17, 19, 20] for cooling run crystallization at relatively small under coolings, i.e. when in Eqn. (44) $T \cong T_m$) or – in most cases (beginning with [1, 14–16]) – by using Eqn. (46).

With the substitutions $\left(\frac{U_0}{RT}\right) = z$ and $\sqrt{\frac{B_0}{RT^2}} = z$ in both cases (Eqns. (45), (46)) the right hand integrals in Eqn. (36b) are brought (see Appendix 1) to two well known higher transcend-ental functions: the Exponential Integral Function *Ei*(*Z*) and the Gauss Error Function *erf*(*Z*) [48]. Introducing further on [49] the well known asymp-totic expansions of both transcendental functions two simple solutions

$$\log q = const - \frac{U}{nRT} \tag{47}$$

and

$$\log q = const - \frac{B\Phi}{n\Delta T^2} \tag{48}$$

are easily obtained (see [1, 14–16, 19, 49] and Appendix 1). Thus, in coordinates log*q* *vs*. 1/*T*, the value of (U_0/*n*) can be determined, as first shown by Henderson [16]. In a similar way, as initially demonstrated in [17, 19, 20] for cooling run experiments in nucleation controlled processes with *K*(*T*) according to Eqn. (29) leads to the Gaussian Error Function *erf*(*x*) and solutions (see [49]) of the type of Eqn. (48). This plot as demonstrated by Dobreva *et al*. in a series of publication is especially helpful in determining the nucleating activity Φ of substrates (crystallization cores) or other additives (eventually surfactants [50, 51, 52, 53]) in nucleation kinetics experiments (see Section 9), comparing plain (where $\Phi = 1$) and doped ($\Phi < 1$) melts [44, 53]. Thus especially significant technological problems can be solved [51–53] connected with synthesis of glass ceramics [51, 52] and of polymer materials [16, 53].

Strictly speaking, the right hand integral in Eqn. (36a) can be also brought to simple expressions, containing either the Gauss Error Function (with Eqn. (45), or to the Ei(*Z*)-function (at $n > 1$), and with Eqn. (37) (at $n < 1$) to the Incomplete Gamma Functions $\Gamma(n-1, Z)$, as also indicated in Appendix 1.

In Appendix 2 it is also shown, that even integrals, containing $K_A(T)$-subintegral functions of the type determined with Eqn. (44) can be also geometrically estimated with sufficient accuracy.

The main problems as they are discussed also by other well known authors [2, 41, 54] with the isoconversional methods is, however, not integration, but the unknown *n*-value. Only a full analysis of the $\alpha(T)$-curves, as first performed by Ozawa [3, 4] can determine both *n* and U_0 and thus also the type of the kinetic model equation in Eqn. (36) and in $F(\alpha)$ of Eqn. (9).

7. GENERALIZED OZAWA APPROACH

In 1971 Ozawa [3, 4] indicated a remarkable way out of the restrictions of the isoconversional approximations, which we employ here and enlarge to a more general procedure. This enlargement gives both an analytical and a graphical method to determine in one experiment both *n* (i.e. in our Avrami-function approach: the nature of the kinetic reaction model function $F(\alpha)$) and the respective $U(T)$ – function as real, experimentally accessible temperature dependences. To do this we begin our derivations again with Eqn. (9), using the form, indicated with Eqn. (9a). We have first, to redefine the extended volume $Y_n(t,T)$ employed in Eqn. (28) for constant temperatures in order to satisfy the requirements of Avrami theorem also in the non-isothermal case. For time independent nucleation and growth rates $I(T)$ and $v(T)$ we have now to write

$$Y_n(T) = \omega_n \int_0^T I(T)dt'' \left[\int v(T)dt''\right]^{n-1} = \omega_n \overline{Y_n}(T) \tag{49}$$

where ω_n, *I*, *v* have the same significance as in Eqns. (27–29).

The continuation possible, following Ozawa's idea, is to replace at constant heating/cooling rates in above integrals *via* Eqns. (17) and (30) d*t* and *t* by d*T* and *T*, and thus we obtain directly

$$Y_n(T) = \frac{\omega_n}{q^n} \quad \overline{Y_n}(T) = \frac{n\omega_n 1}{q^n} \int_0^T K(T) T^{n-1} dT \tag{50}$$

After integration according to Avrami theorem (c.f. Eqn. (27)) we have now in analogy to Eqn. (36)

and to Ozawa's procedure (see [3]) to write

$$-\log[1-\alpha(T)] = \frac{n}{q^n}\int_0^T K(T)T^{n-1}dT \qquad (51)$$

Here we have to integrate from $\alpha = 0$ to any $\alpha(T)$-value of the $\alpha(T,t)$-dependence, corresponding to the temperature T. In employing again Eqn. (17) we obtain in similarity to the isothermal Avrami process that

$$\lg\{-\lg[1-\alpha(T)]\} =$$

$$= -n\lg q + \lg\int_0^T K(T)T^{n-1}dT + \lg\lg e \qquad (52)$$

In this way (c.f. Eqn. (50)) only the value of

$$\overline{Y}_n(t) = \int_0^T I(T')dT'\left[\int_0^T v(T'')dT'\right]^{n-1} \qquad (53)$$

can be determined in coordinates $\lg\{-\lg[1-\alpha(T)]\}$ *vs*. $\lg q$ as $\lg Y_n(T)$. The slope of the respective straight line gives only the value of n and after integration of the sublogarithmic function could reveal also the value of $K(T)$.

The direct result of DTA or DSC-measurements is usually obtained in terms of $d\alpha(T,t)/dT$ *vs*. T plots. After a numerical integration we obtain the respective $\alpha(T)$ *vs*. T curves from which we can determine the values of $\alpha(T)$ corresponding to the respective q value, as prescribed by Ozawa in his $\lg\{-\lg[1-\alpha(T)]\}$ *vs*. $\lg q$ coordinates. This is an approach similar to the isothermal Avrami plot. According to the original derivation of Ozawa, it is assumed that a process of overall crystallization kinetics is investigated in terms of Avrami model. Here it becomes evident, that this procedure is applicable to any process, e.g. a chemical reaction, when we can assume that it is described by Avrami Eqn. (8), considered as a general dependence of change.

Now, following Ozawa, we have determined n; however, we have obtained following his method $K(T)$ and $U(T)$ only in the form of a logarithm of a relatively complicated integral, which can be brought approximately to well known transcendental functions (see Appendix 1, 2) in a similar way as done in the isoconversional case (Section 6).

In order to illustrate this task on Fig. 7 is shown the probable course of the subintegral functions and their change in dependence of cooling/heating rates q for various $K(T)$ dependences. On Fig. 8 the graphical way of integration of these dependences mentioned here and in Section 5 is illustrated.

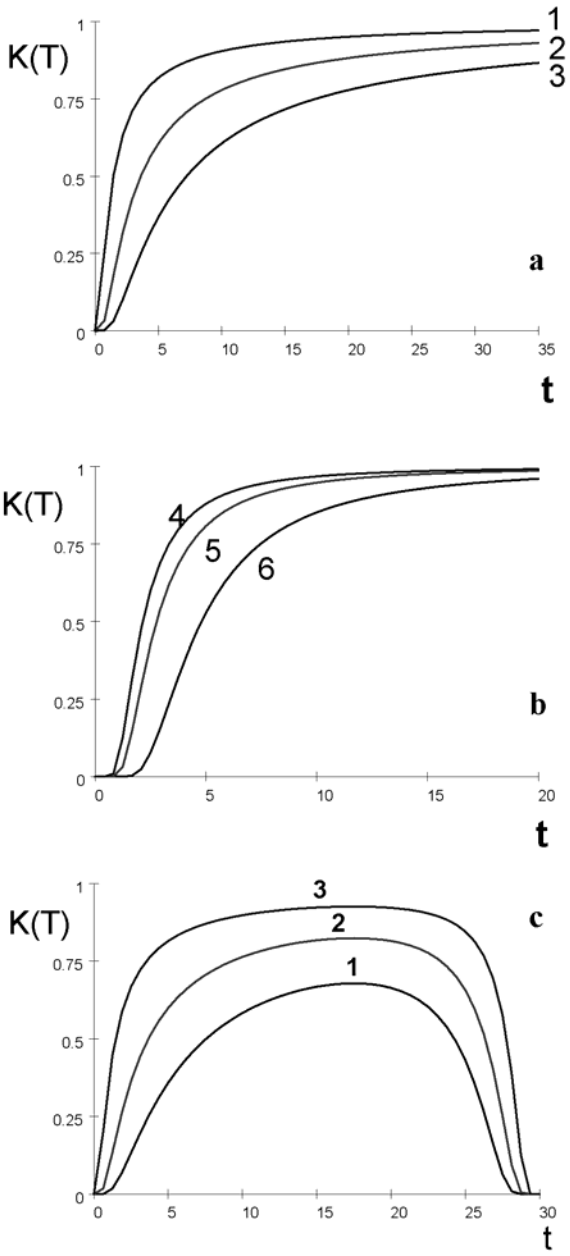

Fig. 7. Influence of cooling/heating rate, q, on the course of the subintegral functions in Eqn. (36b), when the temperature is expressed as $T = qt$, according to Eqn. (30a). a. At an Arrhenian kinetic barrier given with Eqn. (37); b. At a thermodynamic nucleation barrier approximately expressed via Eqn. (45); c. At a nucleation rate dependence, according to Eqn. (44). At picture **a**. the value of q is changed in relative units as $q_{1,2,3} = 1, 2, 5$; **b**. $q_{4,5,6} = 1, 3, 5$; and at **c**. $q_{1,2,3} = 1, 2, 5$. In calculating all three cases in the respective dependences, $U_0/R = 5$, $B/RT_m = 16$, $T_m = 30$, $A_0 = 1$.

A more general approach is, however, possible to determine directly both $U(T)$ and n in the framework of Ozawa's approach.

Suppose we have analyzed, using the already described Ozawa plot, the value of n in Avrami equation: thus we know the kinetic model, underlining the considered non-isothermal $\alpha(T)$-course.

Now we have to determine also the functional dependence and the value of $U(T)$, corresponding to the analyzed model.

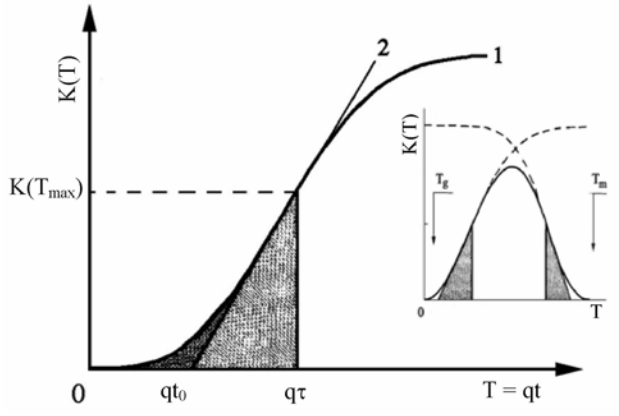

Fig. 8. Geometric interpretation of the determination of the integral, given with the right – hand side of Eqn. (36b). The curve 1, representing the subintegral function *K(T)* at Eqn. (45) with $T = qt$ is approximated by the shaded triangular area of the rectangle. The double shaded area left of the tangent straight line 1 is the part neglected by the approximation of the Gauss Error Function used (see Appendix 2).

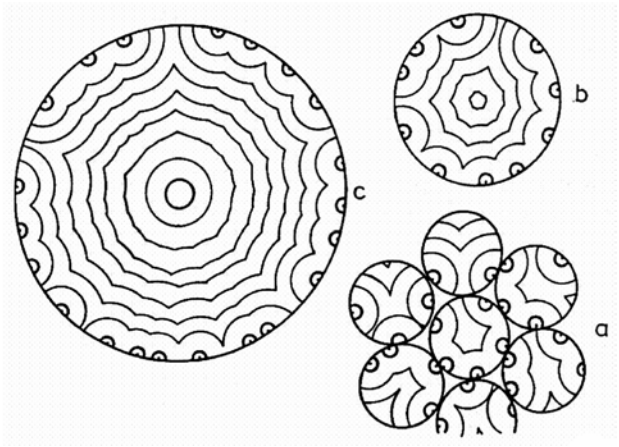

Fig. 9. Effect of mean radius, R_0 on the kinetics of crystallization of samples, constituted of an array of equal spheres (schematically): **a.** At a population of smallest spheres the nucleation event determines to a great extent the crystallization process: Thus, n = 3 in the Avrami equation is expected and found experimentally; **b.** An intermediate case: relatively great spheres allow both nucleation and growth and the formation of a crystallizing front at the end of the process; **c.** The change of the way of crystallization, induced by surface nucleation at relatively great spheres: a crystallization front is formed at the very beginning, proceeding (at a value $n = 1$ in the Avrami index in Eqn. (8)) into the volume of the sphere. For details and subsequent theoretical derivations, see [10].

From the Ozawa plots, we obtain in $\lg[-[1-\alpha(T)]]$ *vs*. $\lg q$ coordinates beside n also the value (for the temperatures and cooling rates q studied) of a function, which we call the Ozawa function, defined according to Eqns. (50–53) as

$$Oz(T) = \frac{1}{2.3}\,\boldsymbol{lg}\int_0^T (T')^{n-1} K(T')dT' =$$

$$= \boldsymbol{lg}\; n\,\frac{A_0}{2.3}\int_0^T (T')^{n-1}\,\boldsymbol{exp}\left[-\frac{U(T')}{RT'}\right] dT' \qquad (54)$$

Here $U(T)$ stands for any of the already discussed models of activation energies of $K(T)$, given with Eqns. (37–39). Taking the logarithmic derivative from above expression and accounting for the rules of differentiation of definite integrals we have to write

$$\frac{d[Oz(T)]}{dT} = \frac{T^{n-1}K(T)}{\int_0^T T^n K(T')dT} = \frac{T^{n-1}K(T)}{\exp[Oz(T)]} \qquad (55)$$

Thus, we obtain the subintegral function of $Oz(T)$ and $K(T)$ as

$$K(T) = \frac{1}{T^{n-1}}\exp[Oz(T)]\left[\frac{dOz(T)}{dT}\right] \qquad (56)$$

Thus, with Eqn. (37) it follows, that $K(T)$ can be obtained from the Ozawa plot as the product of the antilogarithm of the Ozawa function (Eqn. (54)) and the value of its temperature differential at temperature T (see Appendix 3 and Fig. 14 given there). After taking the logarithm from above expression we determine $U(T)/(RT)$ as

$$-\frac{U(T)}{2.3RT} = Oz(T) + \boldsymbol{lg}\left[\frac{dOz(T)}{dT}\right] + \boldsymbol{lg}\left[\frac{nK_0}{T^n}\right] \qquad (57)$$

Thus, we can analyze the nature of the $K(T)$-function according to anticipated temperature dependences, compatible with the kinetic model function $F(\alpha)$ expected. It is evident, that a standard computer programme connected with the DSC Ozawa plot results can thus directly reveal both the $K(T)$ and the $U(T)$ function. In doing so in a good approximation T^{n-1} in Eqns. (54), (55), (57) can be taken as a constant (e.g. $T^{n-1} = T_m^{n-1}$), when compared with the value of the corresponding exponential functions.

In analyzing cases of phase transition kinetics, e.g. in cooling run experimentation the $U(T)$ dependence as depicted with Eqn. (40) has to be anticipated, while in heating run experimentation Eqn. (37) should prevail as a rule. The above given derivation is graphically illustrated in Appendix 3.

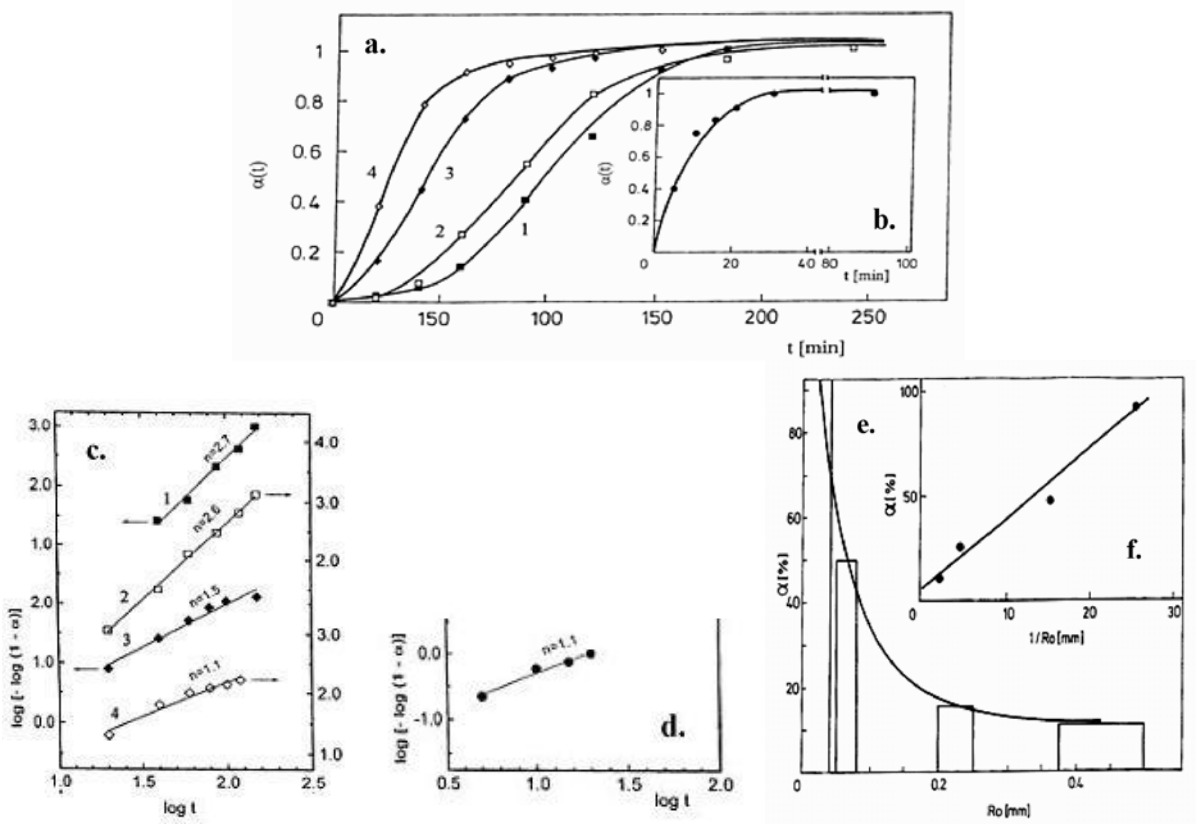

Fig. 10. Experimental verification of the influence of mean radius, R_0 of crystallizing glass semolina samples on the Avrami kinetics. a. Kinetics of overall growth of $NaPO_3$-glass: typical $\alpha(t)$-curves at constant temperature in the temperature range T = 575 to 605 K. Curve 1 - R_0 < 0.04 mm, T = 575 K; curve 2 - R_0 = 0.05–0.08 mm, T = 579 K; curve 3 - R_0 = 0.2–0.25 mm, T = 598 K; curve 4 - R_0 = 0.25–0.375 mm, T = 605 K. b. Kinetics of overall crystallization of diopside glass at 1333 K, R_0 = 1.25 mm with $R_0 \approx 1.0$ mm. c., d. The same results in Avrami coordinates lg[–lg(1–α)] *vs*. lg(t) coordinates, giving in dependence of R_0, a change of the Avrami coefficient n from 1 to 3. e. Proof of a reciprocal dependence $n \sim 1/R_0$ for $NaPO_3$ samples, crystallized at 575 K as a function of grain radius, R_0; f. – the same data in coordinates α vs. $1/R_0$. Experimental results from [10] where additionally experimental details are given.

8. KINETICS OF GLASS TRANSITIONS

Long years of investigations have revealed two essential points in the kinetics of glass transition (see [7, 21, 22, 23, 24]):

i) Both isothermal and non isothermal relaxation in glass-forming systems can not be described in terms of Maxwell's linear kinetics (Eqn. (20)), which corresponds to a first order dependence of structural change. This becomes evident in comparing Eqns. (20) and (13) in assuming, that $K(T)$ from Eqn. (13) is the reciprocal of a time independent Maxwellian time of relaxation (i.e. that $[1/K(T)] \equiv \tau^{\#}(T)$). On the contrary, it is well known (see [7, 39]) that only relaxational behaviour of the Kohlrausch-type (Eqns. (18), (19)) with a stretched exponent (ξ–ξ_0)-course satisfy experiment. As far as from such experiments as mentioned the stretched exponent index turns ut to be in the vicinity of (1–b) = 0.33 [7, 22] this gives in terms of Section 3 an indication that the relaxation in glass as a kinetic process is to be considered as of second order (i.e within Eqn. (6) (with p = 2) and by Eqn. (14) or with Eqn. (8) with n = 2/3). In fact, there were well founded proposals (see [39]) to treat relaxation in glasses according to the so called Adams-Williamson equation:

$$\frac{1}{\xi(T)} - \frac{1}{\xi_0} = \frac{t}{\tau^*(T)} \tag{58}$$

which is only another form of Eqn. (14) obtained from Eqn. (6) with the additional condition, that ξ–ξ_0 at t = 0.

ii) In both empirical approximations and kinetic models (see [7, 21, 22]) as well as in the framework of a generic thermodynamic approach (see [7, 23, 24, 25]) it has been shown that the general kinetic condition for glass transition to take place is that

$$\tau^*(T) q \Big|_{T=T_g} \approx const \tag{59}$$

Here $\tau^*(T)$ in the case of Maxwell's relaxation kinetics is given as $\tau^*(T) = [1/K(T)]$ and in more correct contemporary treatments this is according to Eqns. (18), (19) the value of the time dependent time of relaxation

$$\tau^*(T) \cong \frac{\tau_0(T)}{t^b} \tag{60}$$

With Eqns. (18), (19) the Frenkel-Kobeko-Rainer formula Eqn. (59) indicates, that at every cooling rate a distinct q-dependent part $\xi(T_g)$ of active structural entities ξ is frozen-in to form a glass.

In considering the expected temperature dependence of $\tau_0(T)$ as the reciprocal of the $K(T)$-function (e.g. Eqn. (37)) dependences, similar to the Bartenev-Ritland formula (see [7]) are obtained e.g.

$$\frac{1}{T_g} \cong const_1 - const_2 \log q \tag{61}$$

where the $const_{1,2}$ both are proportional to the respective activation energy.

A more detailed treatment of the consequences from the Bartenev's formula we have given elsewhere [7] (see also [54–57]. Here we would like only to show the analogy of Eqn. (61) with Eqn. (47), which could be directly written in the way as Eqn. (61). This analogy stems from the fact, that in vitrification it also turns out, that an isotransitional approach can be applied in order to derive Eqn. (61) and to treat vitrification as a non-isothermal relaxation process, in which second order type reactions bring about the freeze – i.e. the fixation of a distinct part of the systems building units into a vitreous state.

9. ILLUSTRATIVE COMPARISON WITH EXPERIMENTAL EVIDENCE

In current literature there is abundant experimental evidence confirming the main ideas and results, developed in the present contribution. Thermal analysis in its various possible forms is of great importance, and according to [58] only in a two years period 2002–2003 there have been well over 6000 citations of this method in articles covered by Web of Science.

Here we would like only to mention several results out of our own laboratory, which according to our feeling may illustrate in a significant way the significance of some of the approaches, developed here.

In a series of experiments, represented here by only two of our publications [10, 27] we investigated the applicability of Avrami-type equations (c.f. Eqn. (8)) to describe the isothermal kinetics of crystallization of simple inorganic glass-forming systems. We developed a model, similar to Mampel's one [28] to analyze in terms of Avrami theorem the dependence of the extended volume $Y_n(t)$ on the dispersity of the samples analyzed. Surface nucleation of every grain of the granulated glass constituting the DTA-samples was assumed and in fact microscopically confirmed. The theoretical analysis per-formed showed, that Avrami power coefficient n has in this case is a function of the mean radius d_0 of the glass semolina employed in every experiment. Thus in variance with the original Avrami model [6, 7], in which an infinitively large volume of the crystallizing sample is assumed, here a distinct dependence $n = f(1/R_0)$ was derived and confirmed experimentally (Fig. 10 and further results in [10]). Witness in this respect are crystallization experiments with both $NaPO_3$-glass semolina and with other inorganic glasses, as this is discussed in details in [10]. In this way, the Avrami power coefficient looses in most cases of DTA and DSC experiments its original significance, when semolina or powder-like samples are analyzed and discussed in terms of Eqn. (8). These experimental evidence summarized in [10, 27] gave one of the starting points of the present analysis.

On the other hand in polymer crystallization [44] in DTA or DSC arrangements, when to a great extent sufficiently large samples are employed so that Avrami model premises are fulfilled, the value of n has to depend in both isothermal and non-isothermal experiments on the interplay of $I(T)$ and $v(T)$ in accordance with Eqn. (29). Moreover, the values of n and $\overline{U}(T)$ determined isothermally and in cooling/heating run experimentation for the same case have to coincide.

Polyethilene terephtalate (PET) is a very convenient crystallization model [44, 50]. We determined in a series of preliminary experiments both the thermodynamic and the kinetic properties of our PET-melts (mainly temperature dependence of specific heats $Cp(T)$ and of viscosity $\eta(T)$ measurements were performed in this respect, see [44] and Fig. 11). In isothermal experiments we determined both n and $\overline{U}(T)$ of our PET-samples (see [19, 50]) and compared them with the $U(T)$ and $W_c(T)$ values, following for these melts from our $Cp(T)$ and $\eta(T)$ measurements. A good coincidence was found in this respect for both PET and several other polymers [19, 53]. Moreover, employing Eqns. (39), (41) we determined the nucleating activity, Φ, of various substrates in both PET [53] and in the already mentioned $NaPO_3$-glass (see [51, 52] and here Fig. 12

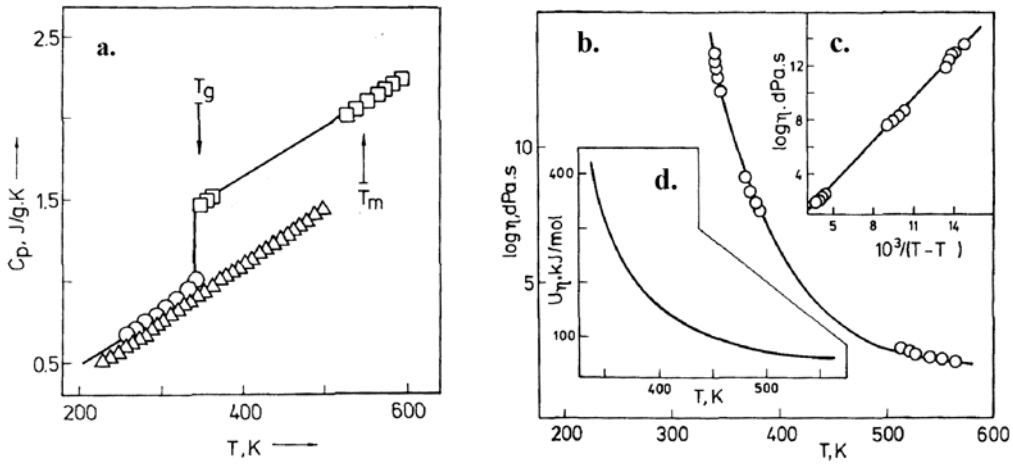

Fig. 11. Crystallization significant properties of polyethylene terephtalate (PET): necessary thermodynamic and kinetic data: specific heats, $C_p(T)$ and viscosity, $\eta(T)$. a. Results of *Cp(T) vs. T* measurements; from there ΔS_m and $\Delta\mu(T)$ were determined. Open squares: *Cp(T)* of undecooled PET melts; open circles: *Cp(T)* of crystallized PET samples; open triangles: *Cp(T)* of crystalline PET samples. b. $\eta(T)$ course of molten PET (open circles: experimental data) according to free volume model Vogel-Fulcher-Tammann formula, Eqn. (38). c. The same data in Vogel-Fulcher-Tammann coordinates, according to Eqn. (38). d. The influence of temperature on *U(T)* of PET, demonstrating the steep decrease of *U(T)* at approaching $T = T_m = 542$ K, where the thermodynamic barrier is more significant [46, 47]. From the η(T) data *U(T)* was determined. Experimental data from [50].

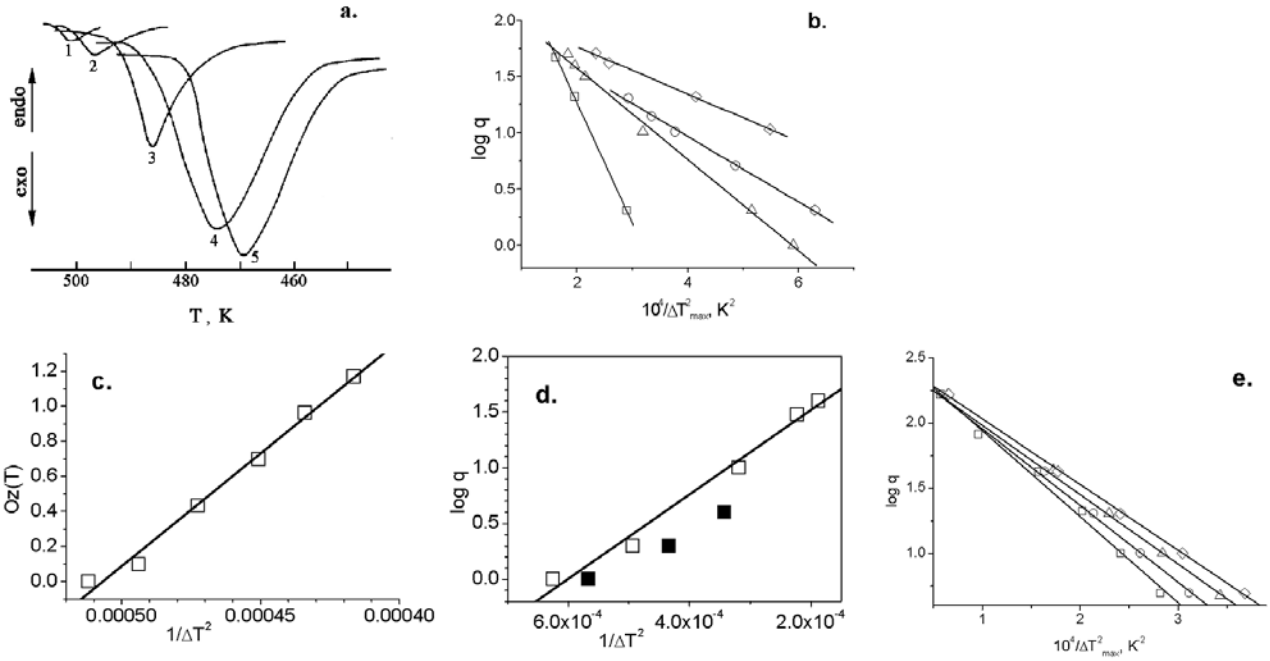

Fig. 12. Experimental evidence on the crystallization of polymer melts.
a. Non-isothermal cooling run curves with a typical crystallization peak of PET at different cooling rates: 1 - 1 K·min^{-1}; 2 - 2 K·min^{-1}; 3 - 10 K·min^{-1}; 4 - 30 K·min^{-1}; 5 - 40 K·min^{-1} (from [19]). b. Non-isothermal crystallization of several polymers in lg*q vs.* $1/\Delta T^2$ coordinates in accordance with Eqn. (48). From above: polyamide; polydecamethylene tereftalate; polyethylene tereftalate; isotactic polypropylene (from[19]). c. Results from the non-isothermal crystallization kinetics of PET thin films (Ozawa [3]) in coordinates – Ozawa function *Oz(T) vs.* $1/\Delta T^2$. Ozawa function expanded in terms of the Error Function series (see Appendix 1.). Comparison of the results on the crystallization of PET obtained by Dobreva and Gutzow [19], open squares – with the results of Ozawa [3] for the same polymer. d. The results from non-isothermal crystallization of PET by Dobreva *et al*. [53] and by Ozawa [3], according to the isoconversional approximation formula Eqn. (45). e. The results for the lg*(Oz(T))* – function in coordinates lg(*K*) *vs.* $1/\Delta T^2$ for plain PET. Results for PET doped with active insoluble substrates in coordinates, corresponding to Eqn. (48): top most line – plain PET; second from above – PET nucleated with Al_2O_3 particles; third line – PET nucleated with TiO_2 paricles; fourth line – PET nucleated with ZnO particles. Note the change of Φ from 1 to 0.6.

for the organic polymers). The results thus obtained we used in developing by induced crystallization both glass ceramics (see [7]) and organic polymer–inorganic composite materials [53]. Of more significance for the present analysis was, that in comparing our isothermal results with PET with those obtained by Ozawa [3] with the same object, similar values of both the Avrami coefficient n and of $U(T)$ were found (see Fig. 12).

The isothermal results with one of the crystallization models the $NaPO_3$-glass we employed in performing in 1999 on the "MIR" orbital station experiments on the effect of microgravity conditions on the induced crystallization of the same $NaPO_3$-model glass [46]. In doing so, we used at both cosmic conditions and in the reference experiments in the MUSC Laboratory in Cologne (Germany) non-isothermal simultaneous DTA-analysis of the induced crystallization experiments of the $(NaPO_3)_x$-glass. In both cases a good correspondence between isothermal and non-isothermal conditions was confirmed in the framework of the classical nucleation theory, summarized here in Section 4.

Lastly, we would like also to mention, that in [47] we developed an isoconversion experimental method to follow the non-isothermal crystallization of pure water and of various aqueous solutions in a LINKAM heating (cooling) stage microscope. The obtained results gave, using Eqns. (47), (48) quite similar results in both isothermal and in cooling run experiments. An electrochemical variant of Eqn. (48), in which $\Delta\mu$ was represented by overvoltage $\Delta\varepsilon(t)$ we used in [17, 18] in order to investigate the galvanostatic electrodeposition of Cd on Pt electrodes in $CdSO_4$ electrolytes.

10. CONCLUSIONS

It turns out, that it is possible using as a general algorithm Eqn. (8), corresponding to the Avrami model of overall crystallization kinetics, to describe quantitatively both phase transitions and topochemical reactions and structural changes corresponding to first, second or even third order non-isothermal reaction kinetics. Moreover, even glass transition and the Kohlrausch kinetics of isothermal and non-isothermal relaxation (i.e. kinetics of vitrification and glass stabilization) can be described, using the simple mathematics of the Avrami equation, as an intermediate mathematical algorithm.

It is shown, that the Avrami power index n indicates the nature of the $F(\alpha)$ function in Eqns. (5), (6), which indicates at $n \geq 1$ the kinetics of build up of interfaces in both topochemical reactions and Avrami-like phase transitions. With $n \leq 1$ structural changes, vitrification and homogeneous reactions can be described. This broad applicability of Avrami Eqn. (8) is by no means accidental or purely mathematical. On the contrary, in Section 3 it is shown, that Avrami-like dependences are in fact the particular case of very general relations, describing in a relatively simple way continuous change, taking place either at time – constant (at $n = 1$) values of the activation energy in Avrami-like coefficients

$$K(T) = K_0 \exp\left[\frac{U(T,t)}{RT}\right]$$

or (at $n > 1$, or $n < 1$) at time dependent, e.g. increasing $U(T, t)$-values.

The broad possibilities of Avrami equation have been already exploited in various applications, e.g. in the already cited ancient monography of Kazeev [33] in describing various metallurgical processes. In recent cosmological literature [59] efforts are summarized to use Avrami equation even as an algorithm, representing the history of the development of the Universe as a whole [59, 60]. In fact, such an analysis, if possible should require a non-isothermal formulation, may be in the form as it is discussed here, or as indicated in [60], accounting for the change of volume V of the Universe as a whole. Various models have been proposed in literature to use Avrami equation for different applications: both in its classical Kolmogorov-Avrami variant in melt crystallization, in Mampel's model for the crystallization of grained more or less finely dispersed solid samples [28], in chemical reaction models [7, 8, 32, 33] with special applications to DTA and DSC analysis [10, 27]. It is a really convenient model and this we hope is demonstrated also in the foregoing analysis. It is pointed out in Sections 3 and 8 that this broad applicability of Avrami-like dependences stems from the circumstance that it is based in fact on non-linear formulations of the phenomenological law of ireversible thermodynamics. Those who are interested in this problem are advised both to classical literature on this subject [61–63] and to the already cited publications [23, 24, 30].

In the present contribution on one side the classical isoconversional models, developed and employed many years ago for both heating [1, 16] and cooling runs [17, 19, 20] experimentation are described and unified and the possibilities and limitations of existing solutions are summarized. Particular attention, however, is given to Ozawa's method [3] of non-isothermal kinetic analysis. An attempt is made these methods to be enlarged and brought to more general applications in both chemical non

isothermal kinetics and in non isothermal phase transitions and new analytical and geometrical solutions are proposed in this respect.

Many attempts have been made, beginning with the already cited classical authors, like Kisinger [1] and Coats and Redfern [14] to develop methods of analysis of non-isothermally obtained kinetic results to determine both the nature of the process (in present terms we used here in this respect the $F(\alpha)$-function in the summaric $(1-\alpha)F(\alpha)$-dependence) and the value of the process significant activation energy $U(T)$. In doing so, most researchers prefer to use various variants of trial and error methods as optimization programs, in which out of 30 to 40 different kinetic possibilities to determine the $F(\alpha)$ in a more or less systematic manner as a best fit value [54, 64]. Out of number of recent analyses in this respect we would like to cite the efforts of Vlaev *et al*. [64, 65] and also [66]. In these investigations the most appropriate selection of optimum is attempted, based on possible maximal values of generalized R^2 factors. However, the critical reconsiderations of such efforts, made in [65] shows, that in reality it is very difficult, or even impossible to discern in between such a great variety of kinetic possibilities even in such standard cases as the thermal decomposition of $CaC_2O_2.2H_2O$.

Kissinger tried to resolve the same problem by introducing an analysis of the form $(d\alpha/dt)$ dependence. This form, as seen also by one of our mathematical models (Fig. 13), really changes, when the Avrami model with different n-values is used. However, in our opinion too much hope has been invested in such efforts of geometric form analysis of rate dependences. Moreover, beginning with Kissinger [1] and by most further authors, only Arrhenian type kinetic barriers have been considered at changing $F(\alpha)$-function. However, the analysis in Section 5 shows how differing the kinetic barrier can be even for the same $F(\alpha)$-function and that in phase transitions a complicated, non-Arrhenian thermodynamic barrier has to be expected.

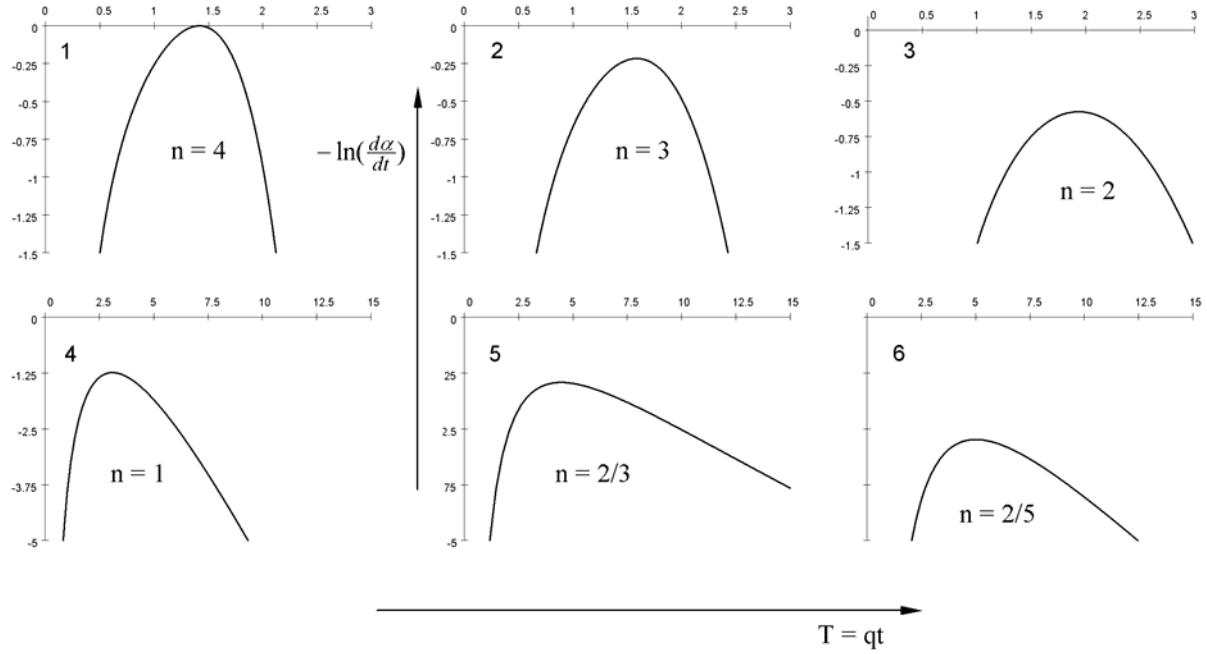

Fig. 13. Influence of the Avrami power index, n, on the form of the $d\alpha/dt$ *vs*. T-curves (in logarithmic scale on the ordinate). In all six cases $\ln\left[\frac{d\alpha}{dt}\right] = \ln nK(T)^{\frac{1}{n}} \exp\left[-K(T)t^n\right]$ is plotted against $T = qt$ for the same value of q, but for n, changing from $n = 4$ through $n = 1$ to $n = 2/5$. Curve 1 is constructed with $n = 4$; curve2 – with $n = 3$; curve 3 – with $n = 2$; curve 4 – with $n = 1$; curve 5 – with $n = 2/3$; curve 6 – with $n = 2/5$. In constructing the figures it was taken that in the expression $K(T) = A_0 \exp(-\frac{U_0}{T})$; $A_0 = 1$; $(\frac{U_0}{T}) = 5$; in all figures the temperature is defined as $T = qt$. Note the change in the appearance of the $\ln\left(\frac{d\alpha}{dt}\right)$ *vs*. $\left(\frac{T}{q}\right)$-curves. It is seen that an unambiguous distinction of the curve form from n (as anticipated by Kissinger) is very difficult; nevertheless a change from symmetric curves (at $n > 1$) to asymmetric curves for $n \leq 1$ is clearly observable.

This is why, in terms of present analysis it is assumed, that first a generalization, a standardization of all possible kinetics is necessary in the form of an intermediate Avrami-type equation. Than Ozawa's analysis determines the factor n and thus (out of not more than 10 possibilities n = 2/5, 2/3, 1, 2, 3, 4, or fractional values between 1 and 3) the general type of the kinetic process can be determined, independent of the value and nature of the activation energy $U(T)$. The method, described in Section 7 gives after that a method to determine at an already known n the real nature of $U(T)$ out of the analysis of the term we called here the Ozawa number Oz.

In doing this way, both new possibilities and also the necessary limitations are clearer visible.

In this way we hope, that with the present investigation we have indicated an alternative way of thermal analysis, which in its development an application could lead to more distinct results, which can be more straight word obtained.

***Acknowledgements**: We have to thank Prof. Dr. C. Schick and Prof. Dr. J. W. P. Schmelzer both from the University of Rostock, Germany, for a number of fruitful discussions. The financial support of NATO Securirty Through Science Programme, RIG 981956 is gratefully acknowledged.*

APPENDIX 1

With the mentioned substitutions $z = \sqrt{\frac{B_0}{RT^2}}$ for the subintegral functions in Eqn. (36b) we arrive with Eqn. (45) at

$$\frac{\sqrt{B_0}}{q}\int_0^Z \frac{\exp\left(-z^2\right)}{z^2}dz \qquad (a_1)$$

After successive integration in parts it follows

$$\int_0^Z \frac{\exp\left(-z^2\right)}{z^2}dz = \left[\frac{\exp Z^2}{Z^2} - \sqrt{\pi}\,erfc\left(Z\right)\right] \qquad (b_1)$$

where $erfc\left(Z\right) = 1 - erf\left(Z\right)$ and

$$erf\left(Z\right) = \frac{2}{\sqrt{\pi}}\int_0^Z \exp\left(-z^2\right)dz \qquad (c_1)$$

is the Gauss Integral form of the Probability function [48].

In a similar way and with the substitution $z = (U_0/RT)$ in the subintegral function (46), Eqn. (36) leads to an expressions of the type

$$\int_0^Z \frac{\exp\left(-z\right)}{z^2}dz = \left[\frac{\exp Z^2}{Z^2} - Ei\left(Z\right)\right] \qquad (d_1)$$

where

$$Ei\left(-Z\right) = \int_Z^\infty \frac{\exp\left(-z\right)}{z}dz \qquad (e_1)$$

is the Exponential Integral Function [48].

In employing the already mentioned well known asymptotic expansions of both the Exponential Integral Function

$$E_i\left(-Z\right) = \frac{\exp\left(-Z\right)}{Z}\left[1 - \frac{1!}{Z} + \frac{2!}{Z^2} - \frac{3!}{Z^3} + \ldots\right] \qquad (f_1)$$

and of Gauss' Error Function $erf\left(Z\right)$

$$erfc\left(Z\right) = 1 - erf\left(Z\right) =$$

$$= \frac{1}{\sqrt{\pi}}\frac{\exp\left(-Z^2\right)}{Z}\left[1 - \frac{1.3.1}{2Z^2} + \frac{1.3.3.1}{\left(2Z^2\right)^2} - \ldots\right] \qquad (g_1)$$

and using only the first members of both expansions Eqns. (47) and (48) are readily obtained. In deriving them *via* Eqn. (36a) $(1/T)$ or $(1/\Delta T_2)$ are neglected when compared with the same arguments in the exponent.

In a similar way also the integrals can be treated, in which (c.f. Eqn. (36a)) expressions of the type $K\left(T\right)T^{n-1}$ appear. With the same substitution made to obtain Eqn. (d_1) and integration by parts we arrive e.g. for n = 2/3 to the integral

$$\int -\frac{3}{2z^{2/3}}\exp\left(-z\right)dz = \frac{2}{3}\Gamma\left(\frac{1}{3}, Z\right) \qquad (h_1)$$

where $\Gamma\left(n, Z\right)$ is the so called Incomplete Gamma function [48]. With the asymptotic expansion

$$\Gamma\left(n, Z\right) \cong Z^{n-1}\exp\left(-Z\right)\left[1 + \frac{n-1}{Z} + \frac{(n-1)(n-2)}{Z^2} + \ldots\right]$$

similar to those indicated with Eqns. (f_1), (g_1) for the already mentioned transcendent functions results, similar to Eqns. (47), (48) can be obtained.

APPENDIX 2

In considering Figs. 7 it is evident, that for all the considered subintegral functions (cf. Eqns. (38), (41), (44–46) the value of the right hand integrals in Eqn. (36) can be approximated with the shade area determined by the rectangular triangle seen on Fig. 8.

$$J(\tau)=\int_0^{\tau} K(t)dt=\frac{1}{q}\int_0^{T_{\max}} K(T)dT=\frac{1}{2}(\tau-t_0)K(\tau) \quad (a_2)$$

Here with 2 is indicated the subintegral function $K(t)$, and with 1 – the tangent at $qt = q\tau$. It is obvious, that in approximating the unknown integral via Eq.(a2) we have neglected from a geometrical point of view the double shaded area on Fig. 8. For subintegral functions of the discussed exponential type this approximation is quite acceptable. Accounting for the linear T *vs*. t heating/cooling course (cf. Eqn. (17)) the slope of the mentioned tangent straight line is

$$\tan g\alpha=\frac{dK(t)}{dt}=\frac{K(\tau)}{(\tau-t_0)} \quad (b_2)$$

Thus, it follows that our integral is given simply as

$$J(\tau)=\frac{1}{2q}[K(\tau)]^2\left[\frac{dK(t)}{dt}\right]^{-1} \quad (c_2)$$

Discussing a cooling run in terms of Eqn. (41) we can write that

$$J(\tau)=\frac{\omega}{2q}constK(\tau)\left[\frac{dW(T)}{dt}\right]^{-1} \quad (d_2)$$

According to Eqns. (39, 41) $W(T)$ has the structure

$$W(T)=\frac{U(T)}{RT}+\frac{B_0^*}{RT\Delta T^2} \quad (e_2)$$

In all above expressions $T = qt$ and in the vicinity of melting point $RT \approx RT_m$ in the right hand member of Eqn. (e_2). In this way via Eqns.(c_2), (e_2) the integral $J(\tau)$, necessary for any isoconversional solution and also in the generalized Ozawa solution, discussed in Section 7 can be safely approximated geometrically in the indicated way, e.g. *via* Eqn. (2). With above approximations we have for the discussed case

$$\frac{dW}{dt}=-\left[\frac{U_0}{R}\frac{1}{q_0t^2}+\frac{B_0^*\Phi}{Rq_0^3}\frac{1}{t^4}\right] \quad (f_2)$$

In this way we may also write

$$J(\tau)=\frac{const}{2q_0}K(\tau)q_0\left[\frac{U_0}{R}\frac{1}{q_0t^2}+\frac{B_0^*\Phi}{Rq_0^3}\frac{1}{t^4}\right] \quad (g_2)$$

Thus the approximations, obtained analytically in Appendix 1 *via* the Gauss Error Function, follows directly from Eqn. (g_2) at $U(T)/RT = const$. Here, however, approximations are geometrically indicated, which may be used both at heating and cooling run experimentation from both "sides" of the $K(T)$-function, as this shown with both shaded areas of the small insert on Fig. 8.

APPENDIX 3

From the Ozawa plot, constructed out of several cooling rates (when a cooling run experiment is considered) we obtain directly the already discussed Ozawa function (Eq. (54)) in which desired $U(T)$-function is part of the subintegral function and the integral itself is under the logarithmus sign.

We have two way open to determine $U(T)$: first we can follow the analytical procedure given in Appendix 1, i.e. being the subintegral to the Gauss Error Function, expand this transcendent function as discussed there and thus obtain expressions, in which

$$Oz(T)=\frac{U(T)}{RT}+\lg[corrections] \quad (a_3)$$

where the expression in square brackets depends on the desired accuracy (i.e. on the members used of the asymptotic expansion). The second, geometric approach is more easily performed.

On the construction of Fig. 14 with 1 is indicated the possible temperature course of the Ozawa function Oz(T), given with Eqn. (54). This course is the result of experimental finding, obtained as described from the respective ($d\alpha/dT$) *vs*. T experimental curves after integration.

As far as

$$\frac{d}{dT}\left[\ln\int_0^T K(T)dT\right]=\frac{K(T)}{\int_0^T K(T)dT} \quad (b_3)$$

we obtain the subintegral function as

$$F(\tau)=\left[\int_0^T K(T)dT\right]\left\{\frac{d}{dT}\ln\left[\int_0^T K(T)dT\right]\right\}$$

as already indicated. Accounting for the experimental course of the possible subintegral functions, we have another already discussed dependence

$$\int_0^T K(T)dT=\exp\left[\ln\int_0^T K(T)dT\right]$$

From Fig. 14 it is evident, that thus the slope

$$\tan g\alpha=\frac{dOz(T)}{dT}=\frac{T_0-T}{Oz(T)}$$

or

$$(T_0 - T) = \frac{d[Oz(T)]}{dT} Oz(T)$$

Thus, it follows that:

$$F(T) \cong \frac{(T_0 - T)}{Oz(T)}$$

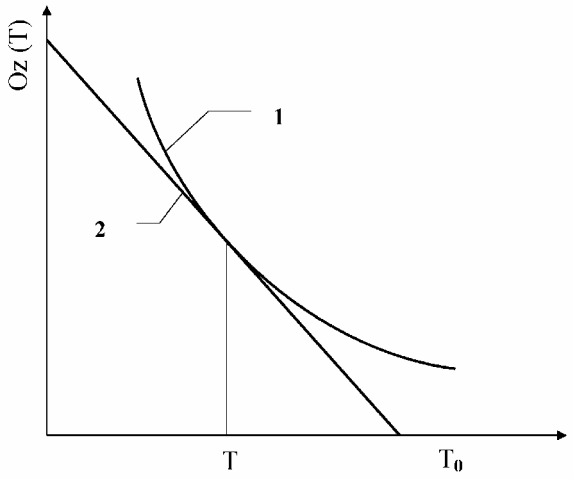

Fig. 14. The graphical determination of the subintegral *K(T)* function from a plot of Ozawa function *Ω(T) vs.* temperature, *T*. Note that according to Eqn. (56), *K(T)* is given directly by the value of $\Omega(T) = (lg\,\alpha)\int_0^T T^{n-1} K(T)dt$ - function (curve 1), multiplied by the slope $\left.\frac{d\Omega(T)}{dT}\right|_T$ of the tangent 2 to the *Ω(T)* curve – 1 at temperature *T*, when $T^{n-1} \approx T_m^{n-1}$.

REFERENCES

1. H. E. Kissinger, *Anal. Chem*., **29**, 1702 (1957).
2. S. Vyazovkin, N. Sbirrazzuoli, *J. Phys. Chem. B*, **107**, 882 (2003).
3. T. Ozawa, *Polymer*, **12**, 150 (1971).
4. T. Ozawa, *Thermochim. Acta*, **386**, 99 (2002).
5. A. N. Kolmogorov, *Izv. Akad. Nauk SSSR, Ser. Mathem*., **1**, 355 (1937).
6. M. J. Avrami, *Chem. Phys*., **7**, 1103 (1939); *ibid*., **8**, 212 (1940); *ibid*., **9**, 177 (1941).
7. I. Gutzow, J. Schmelzer, The Vitreous State: Thermodynamics, Structure, Rheology and Crystallization, Springer Verl., Berlin, New York, 1995.
8. D. Young, Decomposition of Solids, Pergamon Press, Oxford, London, 1966, Ch. 2.
9. P. P. Budnikov, A. M. Ginstling, Reactions in Mixtures of Solid Substances, Gosstroyizdat, Moscow, 1961 (in Russian).
10. I. Gutzow, R. Pascova, A. Karamanov, J. Schmelzer, *J. Materials Sci*. 33, 5265 (1998).
11. S. W. Benson, Foundations of Chemical Kinetics, McGraw Hill Book Co., New York, London, 1960.
12. W. E. Garner (Ed.), Chemistry of the Solid State, Butterworths, London, 1955.
13. S. Z. Roginskii, E. I. Schulz, *Z. Phys. Chem*., **A 138**, 21 (1928).
14. A. W. Coats, J. P. Redfern, *Nature* (*L*.), **201**, 68 (1964).
15. A. W. Coats, J. P. Redfern, *J. Polymer Sci*. **133**, 917 (1965).
16. D. Henderson, *J. Non-Cryst. Solids*, **30**, 301 (1977).
17. I. Gutzow, *Commun. Inst. Phys. Chem., Bulg. Acad. Sci*., **4**, 69 (1969) (in Bulgarian).
18. A. Dobreva, I. Gutzow, *Cryst. Res. Technol*., **25**, 927 (1990).
19. A. Dobreva, I. Gutzow, *Cryst. Res. Technol*., **26**, 473 (1991).
20. J. M. Barandiaran, J. Colmenero, *J. Non-Cryst. Solids*, **46**, 277 (1981).
21. M. V. Volkenstein, O. B. Ptizyn, *Zh. Eksp. Teor. Fiz*., **26**, 2204 (1956).
22. O. V. Mazurin, Glass Transition, Nauka, Leningrad, 1986 (in Russian).
23. I. Gutzow, D. Ilieva, F. Babalievski, V. Yamakov, *J. Chem. Phys*., **112**, 10941 (2000).
24. I. Gutzow, J. W. P. Schmelzer, B. Petroff, *J. Non-Cryst. Solids,* **354**, 311 (2008).
25. J. Möller, I. Gutzow, J. W. P. Schmelzer, *J. Chem. Phys.*, **125**, 094505 (2006).
26. B. V. Erofeev, N. I. Mitskevich, *Coll. Sci. Papers Inst. Chem. Acad. Sci. Belorussian SSR*, **5**, 3 (1956) (in Russian).
27. I. Gutzow, *J. Cryst. Growth*, **48**, 589 (1979).
28. K. Mampel, *Z. Phys. Chem*., **A 187**, 225 (1940).
29. W. Ebeling, Strukturbildung bei irreversiblen Prozessen, Teubner Verl., Leipzig, 1976.
30. I. Gutzow, Ts. Grigorova, J. W. P. Schmelzer, in: Nucleation Theory and Applications, J. W. P. Schmelzer, G. Roepke, V. B. Priezzhev, (Eds.) Dubna JINR, 2002, p. 428.
31. I. N. Bronshtein, K. A. Semendyayev, Handbook of Mathematics, Springer, Berlin, New York, 1998.
32. B. V. Erofeev, *Coll. Sci. Papers Inst. Chem. Acad. Sci. Belorussian SSR*, **5**, 13 (1956) (in Russian).
33. S. A. Kazeev, Kinetics in Application to Metal Science, GIOP Publ., Moscow, 1956 (in Russian).
34. I. Gutzow, Ts. Grigorova, I. Avramov, J. W. P Schmelzer, *Phys. Chem. Glasses*, **43 C**, 477 (2002).
35. I. Gutzow, Ts. Grigorova, S. Todorova, *J. Non-Cryst. Solids*, **304**, 4 (2002).
36. R. Kohlrausch, *Pogg. Ann. Phys. Chem*. (*L*.), **72**, 353 (1847).
37. F. Kohlrausch, *Pogg. Ann. Phys. Chem*. (*L*.), **160**, 225 (1877).
38. L. Boltzmann, *Wiener Akad. Wiss. Sitzungsberichte*, **70,** 275 (1874).
39. J. Morey, Properties of Glass, Reinhold Publ. Co., New York, 1954, pp. 138–140, 169–172.
40. K. J. Vetter, Electrochemical Kinetics, Springer Verl., Berlin, 1961.
41. J. Šesták, Heat, Thermal Analysis and Society,

Nucleus HK, Hradec Kralove, 2004, p. 155, 215.
42. L. H. Adams, J. H. Gibbs, *J. Chem. Phys*., **43**, 139 (1965).
43. I. Avramov, A. Milchev, *J. Non-Cryst. Solids*, **104**, 253 (1988).
44. L. Mandelkern, Crystallization of Polymers, McGraw-Hill, New York, 1964.
45. B. Mutaftschiev, The Atomic Nature of Crystal Growth, Springer Verl., Berlin, New York, 2001.
46. H. Reiss, R. Pascova, I. Gutzow, M. Müller, *J. Cryst. Growth*, **222**, 328 (2001).
47. N. Jordanov, C. Schick, I. Gutzow, *Compt. Rend. Acad. Bulg. Sci*., **61**, 11 (2008).
48. M. Abramowitz, I. A. Stegun, (Eds.), Pocketbook of Mathematical Functions, H. Deutsch Verl., Frankfurt/M, 1984, pp. 56, 81, 84.
49. S. Todorova, I. Gutzow, J. W. P. Schmelzer, in: Nucleation Theory and Applications, J. W. P. Schmelzer, G. Roepke, V. B. Priezzhev, (Eds.), Dubna JINR, 2002, p. 215.
50. A. Dobreva, A. Stoyanov, S. Tzuparska, I. Gutzow, *Thermochim. Acta*, **280/281**, 127 (1996).
51. V. Guencheva, E. Stoyanov, I. Gutzow, *Glass Sci. Technol*., **77**, 217 (2004).
52. V. Guencheva, E. Stoyanov, V. M. Fokin, I. Gutzow, *Phys. Chem. Glasses: Eur. J. Glass Sci. Technol. B*., **48**, 48 (2007).
53. A. Dobreva, T. Stoyanov, I. Gutzow, *J. Appl. Polymer Sci*., **48**, 473 (1991).
54. J. Šesták in: Comprehensive Analytical Chemistry, C. L. Wilson, D. W. Wilson (Eds.), Elsevier, Amsterdam, Oxford, 1984.
55. I. Gutzow, A. Dobreva, *J. Non-Cryst. Solids*, **129**, 266 (1991).
56. G. M. Bartenev, Structure and Mechanical Properties of Inorganic Glasses, Stroyizdat, Moscow, 1966 (in Russian).
57. M. A. DeBolt, A. J. Easteal, A. J. Macedo, C. T. Moynihan, *J. Amer. Ceram. Soc*., **59**, 16 (1976).
58. S. Vyazovkin, *Anal. Chem*., **76**, 3299 (2004).
59. B. Kaempfer, B. Lukacs, G. Paal, Cosmic Phase Transitions, Teubner Verl., Stuttgard, Leipzig, 1994, pp. 27, 33).
60. K. Avramova, *Cryst. Res. Technol*., **37**, 491 (2002).
61. H. B. Callen, Thermodynamics: Physical Theories of Equilibrium Thermodynamics and Irreversible Thermodynamics, Wiley, New York, 1963, p. 284–290.
62. I. P. Basarov, Thermodynamics, McMillan, New York, 1964.
63. R. Haase, Thermodynamik irreversibler Prozesse, Steinkopff Verl., Darmstadt, 1962.
64. L. T. Vlaev, I. G. Markovska, L. A. Lyubchev, *Thermochim. Acta*, **406**, 1 (2003).
65. L. T. Vlaev, N. Nedelchev, K. Gyurova, M. Zagorcheva, *J. Anal. Appl. Pyrolysis*, **81**, 253 (2008).
66. J-H. Yi, F.-Q. Zhao, H.-X. Gao, S.-Y. Xu, M.-C. Wang, R.-Z. Hu, *J. Hazardous Mater*. **153**, 261 (2008).

КИНЕТИКА НА ХИМИЧНИ РЕАКЦИИ И ФАЗОВИ ПРЕХОДИ ПРИ ИЗМЕНЯЩА СЕ ТЕМПЕРАТУРА: ОСНОВНО ПРЕРАЗГЛЕЖДАНЕ И НОВ ПОДХОД

Ив. Гуцов[1]*, С. Тодорова[2], Н. Йорданов[1]

[1] *Институт по физикохимия, Българска академия на науките, ул. „Акад. Г. Бончев“ бл. 11, 1113 София*
[2] *Институт по геофизика, Българска академия на науките, ул. „Акад. Г. Бончев“ бл. 3, 1113 София*

Постъпила на 1 октомври 2009 г.

(Резюме)

Даден е задълбочен анализ и е развит един нов подход на възможностите за описване на кинетиката на химичните реакции и на процесите на фозообразуване при изотермични условия, също така на процеси на структурна релаксация и на стъклообразуване, от гледна точка на неизотермичната кинетика. Основният проблем на изследване е установяването и на кинетичните модели и на активиращите енергии, определящи и ограничаващи процесите, които се изследват чрез едно единствено измерване при нагряване или охлаждане с ДТА или ДС калориметрия. Една възможност е да се използват съществуващите изоконверсионни методи на неизотермичен анализ и по-специално методът на анализ при охлаждане, който може да даде отлични резултати при процесите на кристализация на стопилки и при топохимичната реакционна кинетика. Въпреки това, в рамките на изоконверсионните методи не е възможно да се определят, както абсолютните стойности на активиращите енергии, така и механизмите на реакциите.

Основният метод се основава на подхода на Озава, където като алгоритъм на промяната се въвежда уравнението на Аврами, описващо, както хомогенна реакционна кинетика със степенни коефициенти $n \leq 1$, така и топохимични реакции и фазови преходи при $n = 1, 2, 3, 4$. Демонстрирано е как аналитични и геометрични подходи могат да се използват при определянето на кинетични модели и активационни енергии, чрез един нов и по-подходящ обобщен метод на Озава.

Получените теоретични резултати са онагледени с примери от кинетиката на зародишообразуване и растеж при кристализацията на полимерни стопилки, при преситени водни разтвори, при девитрификацията на стъкла и при стъклообразуването и електролитното отлагане на метали при галваностатични условия.

Bulgarian Chemical Communications, Volume 42, Number 2 (pp. 103–106) 2010

Antimicrobial activity of novel 3-substituted- 5-(pyridine-4-yl)-3H-1,3,4-oxadiazole-2-thione derivatives

K. K. Oza, H. S. Patel*

Department of Chemistry, Sardar Patel University, Vallabh Vidyanagar, Gujarat, India

Received May 7, 2009; Revised October 3, 2009

5-(Pyridine-4-yl)-3H-1,3,4-oxadiazole-2-thione was prepared from isonicotinic acid hydrazide (isoniazid). The Mannich reaction of 5-(pyridine-4-yl)-3H-1,3,4-oxadiazole-2-thione was carried out with formaldehyde and various 1-substituted piperazine derivatives. All the synthesized compounds were characterized by IRS and ^{1}H NMR spectral feature. Their thiol-thione tautomeric equilibrium is described. All the compounds were also screened for their antimicrobial activity.

Key words: Isonicotinic acid hydrazide, 1,3,4-oxadiazole-2-thione, Mannich base reaction, spectral studies, antimicrobial activity.

INTRODUCTION

Many drugs like antibiotics, antimycotics, circulatory system and antiparasitic ones contain piperazine ring [1–7]. Thus piperazine derivatives play the pivotal role in therapeutical application. 1,3,4,-oxadiazole-2-thione has been reported to exhibit antifungal, antibacterial, antileishmanial and insecticidal activities [8–13]. One of the anti-TB drugs i.e. isoniazide affords heterocyclic compounds, which have good biological properties [14]. Its Mannich bases were also reported recently for important biological properties [15]. In view of the important biological properties it was planned to synthesize Mannich bases with 5-(pyridin-4-yl)-3H-1,3,4-oxadiazole-2-thione with piperazine moiety. The route is given in Scheme 1.

EXPERIMENTAL

Melting points were determined by the open capillary method and were uncorrected. The IR spectra were recorded in KBr pellets on a Nicolet 760D spectrometer and ^{1}H NMR spectra were recorded in DMSO with TMS as internal standard on a Brucker spectrometer at 400 MHz.

Preparation of 5-(pyridine-4-yl)-3H-1,3,4-oxadiazole-2-thione (**2**). Compound (**2**) was prepared according to a reported method [16]. A mixture of 1 (0.01 mol), potassium hydroxide (0.015 mol), Carbon disulphide (0.015 mol) and ethanol (50 ml, 95%), was refluxed for 6 h. Excess of solvent was distilled off and the remaining residue was poured in ice cold water and acidified with acetic acid. The yellow coloured compound, thus obtained, was filtered and dried.

Preparation of 3-substituted-5-(pyridine-4-yl)-3H-1,3,4-oxadiazole-2-thione (**3a**–**i**). Compounds (**3a**–**i**) were prepared by a known method [15]. Amount of 5.6 mmol of substituted piperazine derivatives were added to mixture of 5.6 mmol of 2 in 30 ml of absolute ethanol. Portion of 5.6 mmol 37% formaldehyde were added dropwise to the above stirred suspension and the reaction mixture was heated under reflux for 24 h. After concentration under reduced pressure, the residue was recrystallized from absolute ethanol.

Preparation of S-methyl-5-(pyridine-4-yl)-3H-1,3,4-oxadiazole-2-thione (**4**). Compound (**4**) was prepared according to known method [17]. A mixture of **2** (0.005 mol), sodium hydroxide (0.005 mol) and methyl iodide (0.006 mol) was stirred in water for 14 h. The resulting solution was removed by vacuum evaporation, the products were collected by filtration and washed with water.

BIOLOGICAL SCREENING

Antibacterial activities

Antibacterial activities of all the compounds were studied against Gram-positive (*Staphylococcus aureus*, *Bacillus subtilis*) and Gram-negative (*E. coli*, *Salmonelly typhi*,) at a concentaration of 50 µg/ML by agar cup plate method. A DMSO system was used as a control in this method. Under similar conditions, using tetracycline as a standard for comparison, we carried out a control experiment. The area of inhibition of zone was measured in mm. Compounds **3d** and **3e** were found to be more active

* To whom all correspondence should be sent:
E-mail: drhspatel786@yahoo.com

against the above microbes. Other compounds were found to be less or moderately active than tetracycline. (Table 2).

Antifungal activities

The antifungal activities of all the compounds were studied at 1000 ppm concentration *in vitro*. Plant pathogenic organisms used were *Nigrospora Sp*., *Aspergillus niger*, *Rhizopus nigricum*, *Botrydepladia thiorbomine* and *Penicillium expansum*. The antifungal activity of all compounds was measured on each of these plant pathogenic strains on a potato dextrose agar (PDA) medium. Such a PDA medium contained potato 200 g, dextrose 20 g, and agar 20 g and 1 L of water. Five day old cultures were employed. The compounds to be tested were suspended (1000 ppm) in a PDA medium and autoclaved at 120ºC for 15 min at 15 atm pressure. These media were poured into sterile Petri plates and the organisms were inoculated after cooling down the Petri plates. The percentage inhibition for fungi was calculated after five days using the formula given below:

$$\text{Percentage of inhibition} = 100(X–Y)/X$$

where X = area of colony in control plate; and Y = area of colony in test plate.

The fungicidal activity displayed by various compounds is shown in Table 3.

RESULTS AND DISCUSSION

The Mannich base reaction of 5-(pyridine-4-yl)-3H-1,3,4-oxadiazole-2-thione has been performed successfully with 1-substituted piperazine derivatives. Both moieties have important applications in medicine. The structure of 3-substiuted- 5-(pyridine-4-yl)-3H-1,3,4-oxadiazol-2-thione was confirmed by elemental analysis and IR spectra showing absorption bands at 1625–1645 cm^{-1} (C=N), 1240–1260 cm^{-1} (C=S), 1040–1080 cm^{-1} (C–O), 3035–3085 cm^{-1} (C–H of Ar), 1480–1525 cm^{-1} (C=C of Ar), 1040–1080 cm^{-1} (N–N of 1,3,4-oxadiazole-2-thione). Additional bands appear due to substitution in the piperazine moiety, as follows: 1520 cm^{-1} ($–NO_2$), 2830 cm^{-1} (–CH of $–OCH_3$), 3550 cm^{-1} (–OH).

The examination of the data reveals that the elemental contents (Table 1) are consistent with the predicted structure shown in Scheme 1. The IRS and NMR data (Table 1) also allow a direct assignment of the predicted structure.

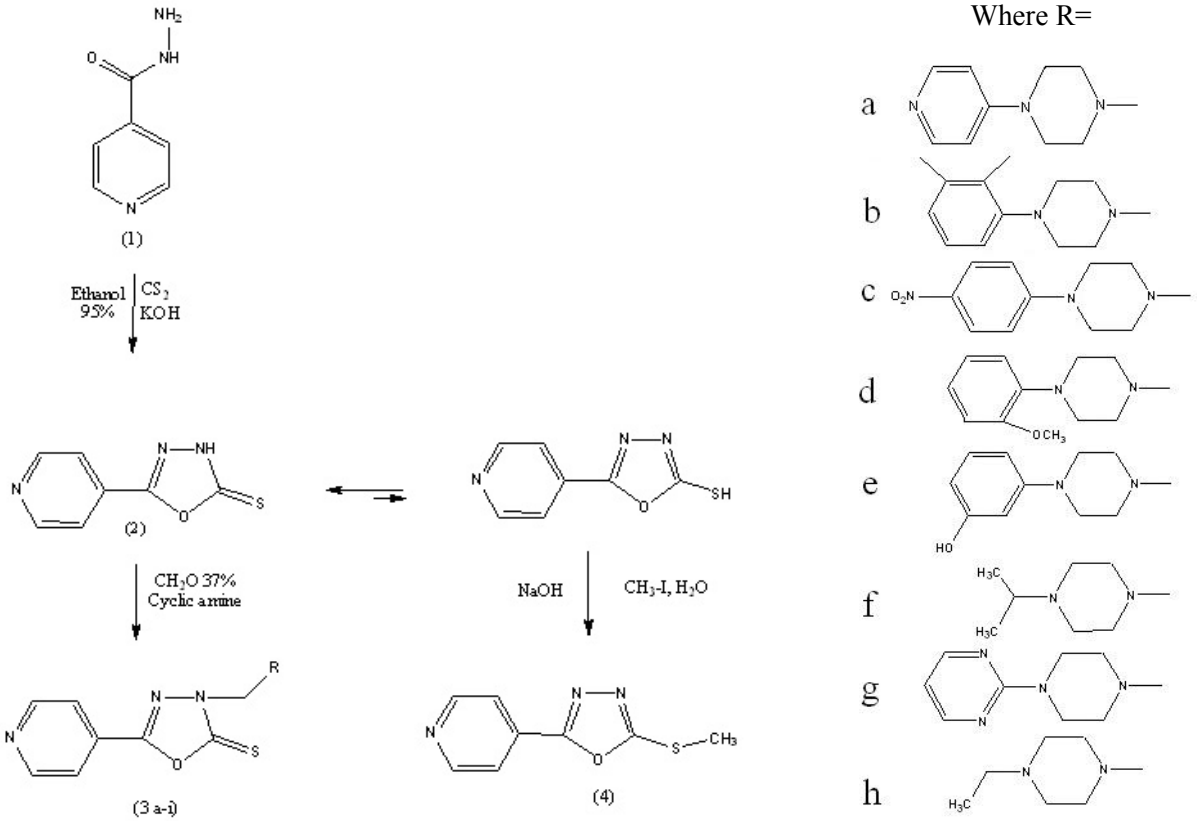

Scheme 1

Table 1. Analytical spectral data of compounds **2**, (**3a**–**i**) and **4**.

Comp.	Molecular formula (mol. mass)	Yield %	M.P., ºC	Elemental analysis, % Found (Calcd)				1H NMR δ, ppm
				C	H	N	S	
2	$C_7H_5N_3OS$ (179.20)	69	262	46.90 (46.92)	2.77 (2.81)	23.40 (23.45)	17.82 (17.89)	8.02 (d, 2H, Pyr.), 8.77 (d, 2H, pyr.), 14.14 (s, 1H, –NH), 1.9 (s, 1H, SH)
3a	$C_{17}H_{18}N_6OS$ (354.44)	58	102–103	54.00 (54.02)	4.28 (4.34)	23.60 (23.62)	12.00 (12.02)	8.02, 8.77 (four d, 8H, Ar–H.), 5.03 (s, 2H CH_2 exocyclic), 2.50, 3.19 (two t, 8H, pip.).
3b	$C_{20}H_{23}N_5OS$ (381.49)	60	103–105	62.90 (62.97)	6.00 (6.08)	18.30 (18.36)	8.35 (8.41)	8.00, 8.65 (two d, 4H, Ar–H.), 7.03–7.50 (m, 3H, Ar–H.), 4.95 (s, 2H CH_2 exocyclic), 2.48, 3.15 (two t, 8H, pip.).
3c	$C_{18}H_{18}N_6O_3S$ (398.44)	60	174–176	54.21 (54.26)	4.50 (4.55)	20.89 (21.09)	7.90 (8.05)	8.12, 8.87 (two d, 4H, Ar–H.), 7.03–7.50 (m, 4H, Ar–H.), 5.02 (s, 2H CH_2 exocyclic), 2.52, 3.17 (two t, 8H, pip.).
3d	$C_{19}H_{21}N_5O_2S$ (383.47)	63	116–118	59.50 (59.51)	5.4 (5.52)9	18.21 (18.26)	8.30 (8.36)	8.02, 8.77 (two d, 4H, Ar–H.), 7.02–8.00 (m, 4H, Ar–H), 5.11 (s, 2H CH_2 exocyclic), 2.52, 3.17 (two t, 8H, pip.), 3.10 (s, 3H –OCH3).
3e	$C_{18}H_{19}N_5O_2S$ (369.44)	55	111–115	58.50 (58.52)	5.10 (5.18)	18.90 (18.96)	8.60 (8.68)	8.05, 8.75 (two d, 4H, Ar–H.), 7.02–8.77 (m, 4H, Ar–H), 4.99 (s, 2H CH_2 exocyclic), 2.44, 3.11 (two t, 8H, pip.), 6.90 (s, H –OH)
3f	$C_{15}H_{21}N_5OS$ (319.43)	70	182–184	56.38 (56.40)	6.59 (6.63)	21.89 (21.92)	9.92 (10.04)	8.02, 8.77 (two d, 4H, Ar–H.), 5.11 (s, 2H CH_2 exocyclic), 2.52, 3.17 (two t, 8H, pip.), 2.69 (m, 1H –CH), 1.3 (m, 6H, $–CH_3$)
3g	$C_{16}H_{17}N_7OS$ (355.42)	65	139–141	53.99 (54.07)	4.79 (4.82)	27.59 (27.50)	9.00 (9.02)	8.02, 8.77 (two d, 4H, Ar–H.), 7.00–7.80 (m, 3H, Ar–H.), 5.10 (s, 2H CH_2 exocyclic), 2.59, 3.24 (two t, 8H, pip.),
3h	$C_{14}H_{19}N_5OS$ (305.40)	65	134–136	55.00 (55.06)	4.95 (4.88)	22.93 (22.90)	10.50 (10.48)	8.01, 8.71 (two d, 4H, Ar–H.), 5.05 (s, 2H CH_2 exocyclic), 2.52, 3.17 (two t, 8H, pip.), 2.38 (m, 2H $–CH_2$), 1.1 (t, 3H, $–CH_3$)
3i	$C_{15}H_{21}N_5OS$ (319.43)	63	93–98	56.35 (56.40)	6.59 (6.63)	21.90 (21.92)	10.04 (10.00)	8.02, 8.77 (two d, 4H, Ar–H.), 5.05 (s, 2H CH_2 exocyclic), 2.52, 3.17 (two t, 8H, pip.), 1.2 (t, 3H, CH_3), 1.5 (m, 2H, CH_2), 3.3 (t, 2H, CH_2)
4	$C_8H_7N_3OS$ (193.23)	50	130–132	49.70 (49.73)	3.59 (3.65)	21.70 (21.75)	16.50 (16.59)	8.00, 8.70 (two d, 4H, Ar–H.), 2.8 (s, 3H, CH_3)

Table 2. Antibacterial activity of compounds (**3a**–**i**) and **4**.

Comp.	Gram-positive		Gram-negative	
	Staphylococcus aureus	*Bacillus subtilis*	*E. coli*	*Salmonelly typhi*
3a	25	21	20	23
3b	22	23	22	19
3c	31	22	28	27
3d	45	46	44	41
3e	41	40	40	43
3f	29	27	26	28
3g	19	17	22	23
3h	21	22	25	30
3i	20	19	23	26
4	22	23	19	21
Tetracycline	40	41	42	39

Table 3. Antifungal activity of compounds (**3a**–**i**) and **4**.

Comp.	Zone of Inhibition at 1000 ppm, %				
	Nigrospora Sp.	*Aspergillus niger*	*Botrydepladia thiobromine*	*Rhizopus nigricum*	*Penicillium expansum*
3a	15	19	20	21	22
3b	21	23	15	14	20
3c	34	33	29	30	30
3d	46	46	41	40	40
3e	40	42	42	40	40
3f	22	26	22	29	30
3g	19	18	21	20	18
3h	18	17	20	23	25
3i	28	23	25	21	24
4	26	21	22	28	24

There are some studies on electronic structures and thiol-thione tautomeric equilibria of heterocyclic thione derivatives [18–20]. We observed that extensive thiol-thione tautomerism exists in compound **2**. In the 1H NMR signals of the SH protons were recorded although they were very weak and also the ready synthesis of the Mannich bases **3a**–**i** and compound **4** confirmed the tautomerism. It has been reported that the crystal structure of compounds like **2** corresponds to the thiol form too [21–23]. Finally, the crystal structure of **2** corresponded to the thione form, but there is thiol-thione tautomerism in solution.

The antibacterial activity of compounds was tested against some strains of bacteria. The results show that the prepared compounds are toxic or moderately toxic against the bacteria. The comparison of the antibacterial activity of some com-

pounds with tetracycline shows that these compounds have almost similar activity.

REFERENCES

1. W. Kostowski, Farmakologia. Podstawy Farmakoterapii, Wydawnictwo Lekaraskie, Warszawa, 1998.
2. A. Chmiel, S. Grudzinski, Biotechnologia i Chemia Antybiotykow, PWN, Warszawa, 1998.
3. M. Hepperle, J. Eckert, D. Gala, *Tetrahedron Lett*., **40**, 5655 (1999).
4. J. Eckert, Ch. Tze-Ming, R. M. Osterman, J. B. Lambert, D. Gala, *Tetrahedron Lett*., **40**, 566, (1999).
5. C. D. Eldred, B. Evans, S. Hindley, *J. Med. Chem*., **37**, 3882 (1994).
6. J. H. van Maarseveen, J. A. den Hartog, *Bioorg. Med. Chem. Lett*., **8**, 1531 (1998).
7. E. van Heyningen, C. N. Brown, *J. Med. Chem*., **8**, 174 (1965).
8. B. S. Holka, K. N. Poojary, B. Kalluraya, P. V. Gowda, *J. Heterocyclic Chem*., **5**, 276 (1995).
9. T. Ramalingam, A. A. Deshmukh, P. B. Sattur, *J. Indian Chem. Soc*., **58**, 269 (1981).
10. J. Hazarkia, J. C. S. Kataky, *Indian J. Heterocyclic Chem*., **7**, 197 (1998).
11. R. S. Varma, P. Varma, *Indian J. Heterocyclic Chem*., **6**, 171 (1997).
12. R. S. Varma, V. Bajpai, A. Kapil, *Indian J. Heterocyclic Chem*., **8**, 281 (1999).
13. R. Iqbal, N. H. Rama, N. Ahmed, K. Zamani, S. Ebrahim, N. Iqbal, *Indian J. Chem*., **37B**, 506 (1998).
14. Indian Pharmacopoeia, Government of India, Ministry of Health and Family Welfare, Delhi, 1996.
15. M. G. Mamolo, D. Zampieri, L. Vio, M. Fermeglia, M. Ferrone, S. Pricl, G. Scialino E. Banfi, *Bioorg. Med. Chem*., **13**, 3797 (2005).
16. F. Aydogan, Z. Turgut, N. Olcay, S. S. Erdem, *Turk. J. Chem*. **26,** 159 (2002).
17. D. A. Charistos, G. V. Vagenes, L. C. Tzavellas, C. A. Tsoleridis, N. A, Rodios, *J. Heterocycl. Chem*., **31**, 1593 (1994).
18. C. A. Tsoleridi, D. A. Charistos, G. V. Vagenes, *J. Heterocycl. Chem*. **34,** 1715 (1997).
19. S. Ozturk, M. Akkurt, A. Cansiz, A. Cetin, M. Sekerci, F. W. Heinemann, *Acta Cryst*., **E 60**, 0322, (2004).
20. S. Ozturk, M. Akkurt, A. Cansiz, M. Koparir, M. Sekerci, F. W. Heinemann, *Acta Cryst*., **E 60**, 0425 (2004).
21. S. Ozturk, M. Akkurt, A. Cansiz, M. Koparir, M. Sekerci, F. W. Heinemann, *Acta Cryst*., **E 60**, 0642 (2004).
22. M. S. Y. Khan, G. Chawla, M. A. Mueed, *Indian J. Chem*., **43B**, 1302 (2004).

M. Koparir, A. Cetin, A. Canasiz, *Molecules*, **10**, 475 (2005).

АНТИМИКРОБНА АКТИВНОСТ НА НОВИ 3-ЗАМЕСТЕНИ 5-(ПИРИДИН-4-ИЛ)-3Н-1,3,4-ОКСАДИАЗОЛ-2-ТИОНОВИ ПРОИЗВОДНИ

К. К. Оза, Х. С. Пател*

Химически департамент, Университет „Сардар Пател“, Валаб Видянагар, Гуджарат, Индия

Постъпила на 7 май 2009 г.; Преработена на 3 октомври 2009 г.

(Резюме)

Синтезиран е 5-(пиридин-4-ил)-3Н-1,3,4-оксадиазол-2-тион от хидразид на изоникотинова киселина (изониазид). Проведена е реакция на Маних на синтезираното съединение с формалдехид и различни 1-заместени пиперазинови производни. Всички синтезирани съединения са охарактеризирани с ИЧС и ^{1}Н ЯМР. Описано е тяхното тавтомерно равновесие тиол-тион. Всички съединения са изследвани за антимикробна активност.

Bulgarian Chemical Communications, Volume 42, Number 2 (pp. 107–112) 2010

Liquid-liquid extraction and recovery of bismuth(III) from hydrochloric acid media using *n*-octylaniline in chloroform

S. J. Kokate, Y. S. Shelar, H. R. Aher, S. R. Kuchekar*

P. G. Department of Analytical Chemistry, P. V. P. College, Pravaranagar, At/Po. Loni (Kd), Tal. Rahata, Dist. Ahmednagar, MS, India, 413713

Received August 28, 2009; Revised November 5, 2009

Liquid-liquid extraction of bismuth(III) with *n*-octylaniline in chloroform from hydrochloric and hydrobromic acid media was studied. Bismuth(III) was extracted quantitatively with 10 ml, 3.0% reagent in chloroform from 0.3 to 0.5 M hydrochloric acid and 0.04 to 0.1 M hydrobromic acid medium. It was stripped from organic phase with 0.01 M acetate buffer and estimated complexometrically. The optimum extraction conditions were evaluated by critical study of acidity, *n*-octylaniline concentration, equilibration time and effect of diluents. The method is free of interferences from large number of cations and anions. The method permits sequential separation of mercury(II), bismuth(III) and zinc(II) or cadmium(II). It was successfully applied for the separation of bismuth(III) from alloy samples. The log-log plot of distribution ratio versus n-octylaniline concentration at 0.1 and 0.2 M hydrochloric acid concentration gave a slope value 2.2 and 1.9 respectively. The probable extracted species is $(RNH_3^+)_2BiCl_5^{2-}$.

Key words: Liquid-liquid extraction, separation, bismuth(III).

INTRODUCTION

The natural abundance of bismuth is about 2×10^{-5}%. Most of the bismuth produced in the U.S is a byproduct of refining lead, copper, tin, silver and gold ores. The world production of bismuth is about 5000 tones per year [1]. Bi(III) compounds are used in semiconductors, cosmetic preparation, alloys and metallurgical additives [2]. Due to wide range of applications, separation of bismuth(III) is of analytical importance.

Liquid-liquid extraction is one of the most popular techniques employed for recovery of bismuth(III). High molecular weight anilines (HMWA), popularly known as liquid anion exchangers, uniquely combine some of the advantages of liquid-liquid extraction and ion exchange [3]. A novel reagent *n*-octylaniline has been used as an extractant for the extraction of some metal ions [4–7]. Literature survey revealed that N-*n*-hexylaniline was used for solvent extraction of bismuth(III) [8], but the method requires masking agent in study of diverse ions and lead is not separated though it is commonly associated with bismuth. Bis-(2,4,4-trimethylpentyl) monothiophosphinic acid (Cyanex 302) [9] is prominent organophosphorus extractant used for the extraction of bismuth(III). Bismuth(III) was extracted quantitatively with 0.05 M 18-crown-6 in methylene chloride from 1.0 M sulphuric acid in the presence of 0.75 M potassium iodide as a counter ion [10]. Cyanex-925 in xylene was used for extraction separation of bismuth(III) from aqueous solution [11], it was stripped with 2.0 M nitric acid. Spectrophtometric and atomic absorption spectrophotometric methods have been developed for the determination of flouroquinolone antibacterial agent by ion-pair complex formation with bismuth(III) tetraiodide [12]. The method is based on the formation of ion-pairs associated between drugs and the inorganic complex bismuth(III) tetraiodide.

Liquid-anion exchangers are based on primary, secondary and tertiary aliphatic amines owing to their generally greater solubility. Primary amines are used less frequently than secondary amines. The presence of an octyl group in the *para*- position in aniline renders this amine more basic and less soluble in water. The *n*-octylaniline, proposed as an extractant, combines both these characteristics because of substitution of long chain alkyl group in para position in aniline. In the present communication a selective, sensitive, less expensive and more precise method has been developed for liquid liquid extraction of bismuth(III). The proposed method is simple, fast and offers clearcut separation of bismuth(III) from mercury(II), zinc(II) or cadmium(II). The method is applied for separation of alloys and synthetic mixtures. The adventage of the method is that the reagent can be recovered for secondary use without loss of extraction efficiency.

* To whom all correspondence should be sent:
E-mail: shashi17@gmail.com

EXPERIMENTAL

Standard solution of bismuth(III) was prepared by dissolving 1.170 g of bismuth nitrate (BDH) in 4.0 ml concentrated nitric acid diluted to 100 ml with distilled water and standardized complexometrically [13, 14]. A 0.01 M solution of ethylenediamine tetraacetic acid was prepared by dissolving 3.722 g disodium salt of EDTA (Qualigen) in distilled water and diluting to 1000 ml and standardized complexometrically [13, 14]. A 0.01 M thorium nitrate solution was prepared by dissolving 5.88 g of thorium nitrate tetrahydrate (BDH) in water and diluting to 1000 ml with distilled water. Acetate buffer solution was prepared by dissolving 27.2 g of sodium acetate trihydrate in 400 ml water, adding 17.0 ml of glacial acetic acid (Qualigens) and diluting to 1000 ml.

n-Octylaniline solution 10% (v/v) was prepared by the method reported by Polhandt [15] diluting 10.0 ml of *n*-octylaniline with respective diluents to 100 ml. Working solutions were prepared by accurate dilution. Analytical grade of purity chemicals (BDH) were used wherever necessary.

Extraction procedure of the individual element (in absence of other element). To an aliquot of solution containing 2.0 mg of bismuth(III) in a 125 ml separatory funnel, enough hydrochloric and water were added to give final concentration of 0.4 M with respect to hydrochloric acid in a total volume of 25 ml. The aqueous phase was equilibrated once with 10 ml, 3% *n*-octylaniline solution in chloroform for 30 s. The phases were allowed to separate and the metal ion from the organic phases was back stripped with 25 ml portion of 0.01 M acetate buffer.

Determination procedure for bismuth(III). Transfer of the aqueous layer into 250 ml of conical flask. It was mixed with an excess of EDTA solution (10 ml 0.01 M) and titrated against 0.01 M thorium nitrate solution using 5 drops of 0.1% xylenol orange as an indicator. The end point was yellow to red violet transition [16].

Dissolution procedure for lead-bismuth alloy, sealing alloy and bismuth solder alloy [17]. A known weight (0.5 g) of each alloy was dissolved in concentrated nitric acid. The precipitated metastanic and antimonic acids were filtered off and weighed as their oxides. The filtrate was evaporated up to moist dryness to remove excess of acids. The residue was leached with diluted hydrobromic acid and made 100 ml with distilled water.

Dissolution procedure for tin-bismuth alloy [17]. A known weight (0.5 g) of the alloys sample was transferred into a 250 ml conical flask, a stem cut funnel was placed on it and heated gently with 20 ml of aqua regia to dissolve the alloys. The solution was treated with 10 ml successive addition of concentrated hydrochloric acid. The solution was evaporated almost to dryness on the stem bath after each addition. The residue was dissolved in diluted hydrochloric acid. The solution was filtered to remove silica or metastannic acid. The filtrate was diluted to 50.0 ml with distilled water. An aliquot of solution was analyzed for bismuth according to extraction procedure.

Mutual separation of bismuth(III), mercury(II) and zinc(II) or cadmium(II). The separation of bismuth(III) from mercury(II) and zinc(II) or cadmium(II) was achieved (separation Scheme 1). An aqueous solution was prepared containing a mixture of 0.5 to 2.0 mg bismuth(III), 0.5 to 1.0 mg mercury(II) and 0.66 to 1.32 mg zinc(II) or 0.5 mg cadmium(II) in 25.0 ml 0.5 M hydrochloric acid and transferred in separatory funnel. It was extracted with 8% (v/v) [7], 10.0 ml *n*-octylaniline in chloroform. It was found that aqueous phase containing zinc(II) or cadmium(II) determined complexometrically [18]. The organic phase contained bismuth(III) and mercury(II). The mercury(II) was stripped with 1.5 M ammonia and determined complexometrically [18]. Bismuth(III) was stripped with acetate buffer and determined complexometrically [16].

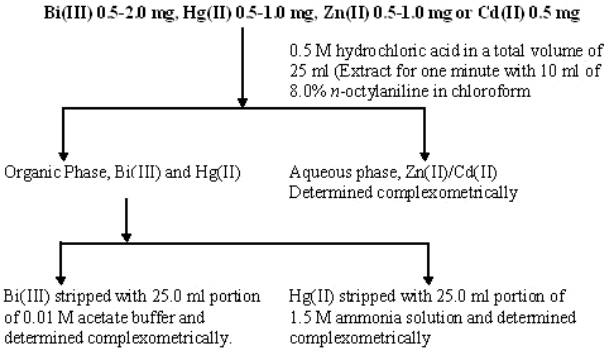

Scheme 1. Mutual separation of bismuth(III) mercury(II) and zinc(II) or cadmium(II).

RESULT AND DISCUSSION

Extraction as function of acidity. The extraction of 2.0 mg of bismuth(III) was studied from hydrochloric and hydrobromic acid media in the range 0.01 to 7.0 M with 3.0% *n*-octylaniline in chloroform keeping the aqueous to organic volume ratio 2.5:1. The extraction of bismuth(III) was found to be zero with 0.01 M hydrobromic acid and 3.8% at 0.01 M hydrochloric acid. The extraction of bismuth(III) increases with increase in acid concen-

tration and becomes quantitative in 0.3 to 0.5 M hydrochloric acid and 0.04 to 0.2 M hydrobromic acid. Upon further increase in hydrochloric and hydrobromic acid concentration the extraction of bismuth(III) decreases Fig. 1 and 2.

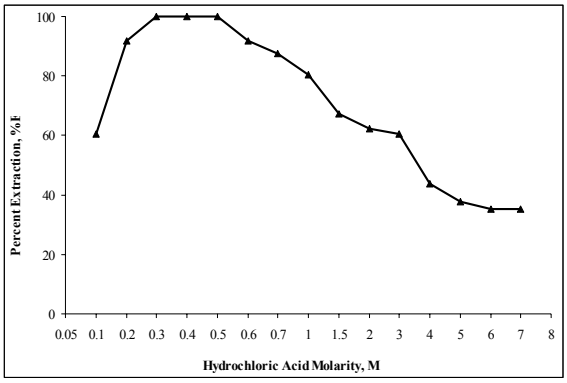

Fig. 1. Extraction behaviour of bismuth(III) as a function of hydrochloric acid concentration.

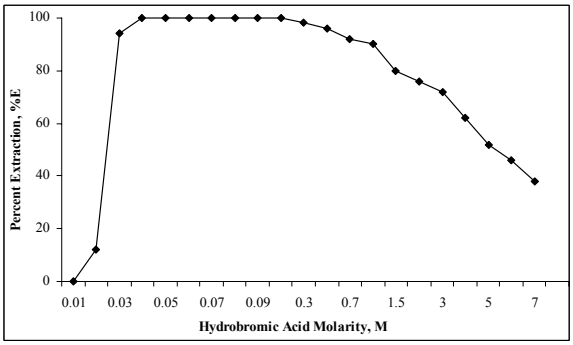

Fig. 2. Extraction behaviour of bismuth(III) as a function of hydrobromic acid concentration.

Extraction as a function of n-octylaniline concentration. Increase in *n*-octylaniline concentration was found to increase the extraction of bismuth(III). The excess of reagent concentration had no adverse effect on magnitude of extraction. It was found that, 10 ml of 3% *n*-octylaniline was sufficient for the quantitative extraction of 1 mg of bismuth(III) from 0.4 M hydrochloric acid. Therefore in the recommended procedure 3.0% *n*-octylaniline in chloroform has to be used to ensure complete extraction of bismuth(III).

Nature of the extracted species. The probable composition of the extracted species was ascertained by plotting a graph of $\log D_{[Bi(III)]}$ against $\log C_{[n\text{-octylaniline}]}$ at fixed hydrochloric acid concentration at 0.1 and 0.2 M (Fig. 3). The plots were linear with slope values 2.2 and 1.9, respectively, indicating the metal to amine ratio in the extracted species 1:2. The probable composition of the extracted species is $(RNH_3^+)_2BiCl_5^{2-}$ [19–20]. The $BiCl_5^{2-}$ ion in the aqueous solution replaces Cl^- ions from amine chloride in the organic phase. The mechanism of extracted species can be explained as follows:

$$(RNH_2)_{org} + HCl_{aq} \leftrightarrow (RNH_3^+Cl^-)_{org} \quad [1]$$

$$(2RNH_3^+Cl^-)_{org} + BiCl_5^{2-}{}_{aq} \leftrightarrow$$

$$\leftrightarrow (RNH_3^+)_2BiCl_5^{2-}{}_{org} + 2Cl^-_{aq} \quad [2]$$

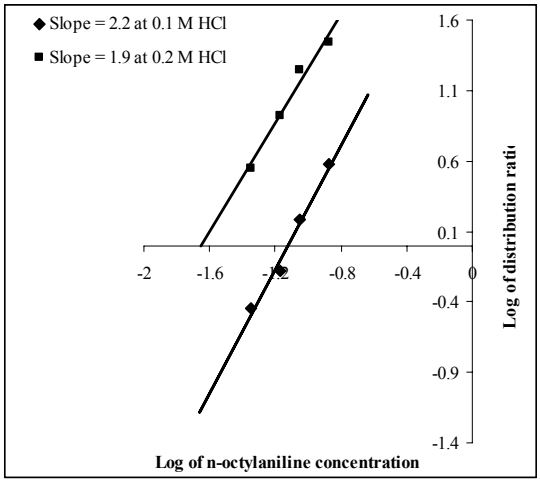

Fig. 3. Log-log plot of distribution ratio *versus* *n*-octylaniline concentration at 0.1 M and 0.2 M hydrochloric acid.

Extraction with various diluents. *iso*-Butylmethylketone, chloroform, toluene, xylene, benzene and carbon tetrachloride were examined for use as diluents in the extraction of bismuth(III) with *n*-octylaniline Table 1. The most efficient diluents were found to be chloroform and benzene. The chloroform was selected as diluent as it gives clear cut separation of the phases. However, a definite correlation between diluent and its dielectric constant could not be established.

Table 1. Effect of diluents on the extraction of bismuth(III) Bi(III) 2.0 mg, aqueous phase 0.4 M hydrochloric acid.

Diluents	Dielectric constant	Extraction (E), %	Distribution ratio (D)
Carbon tetrachloride	2.24	91.66	27.47
Benzene	2.28	100.0	∞
Xylene	2.30	Emulsion	-
Toluene	2.38	91.7	27.47
Chloroform	4.40	100.0	∞
iso-Butyl methyl ketone	13.10	97.9	117.69

Effect of diverse ions. The effect of various diverse ions was tested when bismuth(III) was extracted with 3.0% *n*-octylaniline in chloroform. The tolerance limit of individual diverse ions was determined with an error less than ± 2%. It was observed that the method is free of interference from a large number of cations and anions Table 2. Only the cations thallium(III) and lead(II) are co-extracted. The co-extraction was removed by separating bismuth (III) in hydrobromic acid medium.

*Effect of time of equilibration***.** When two immiscible phases were equilibrated for a period 1 s to 15 min the extraction was quantitative over a period of 30 s to 15 min. Therefore for the proposed method 5 s equilibration time was recommended in order to insure the complete extraction of bismuth(III). However, the prolonged shaking period (> 15 min) was found to have an adverse effect on the extraction and should be avoided.

APPLICATIONS

Analysis of synthetic mixtures. The proposed method was applied for extraction and separation of bismuth(III) from various synthetic mixtures. The results are reported in Table 3.

Table 2. Effect of diverse ions. Bi(III) 2.0 mg, aqueous phase 0.4 M hydrochloric acid, extractant 3.0% *n*-octylaniline in chloroform, strippant 0.01 M acetate buffer.

Foreign ion	Added as	Tolerance limit, mg
Ga(III)	$GaCl_3$	15
In(III)	$InCl_3$	15
Tl(I)	$TlNO_3$	20
Al(III)	$AlCl_3.6H_2O$	5
Fe(II)	$FeSO_4$	5
Fe(III)	$FeCl_3$	5
Sn(II)	$SnCl_2$	20
Sb(III)	$SbCl_3$	20
Mn(II)	$MnCl_2.6H_2O$	20
Mg(II)	$MgCl_2$	20
Zn(II)	$ZnSO_4.7H_2O$	5
Cd(II)	$Cd(NO_3)_2.2H_2O$	5
Hg(II)	$HgCl_2$	5
U(VI)	$UO_2(NO_3)_2.6H_2O$	20
Mo(VI)	$(NH_4)_6Mo_7O_{24}.12H_2O$	5
Co(II)	$CoCl_2.6H_2O$	5
Cu(II)	$CuSO_4.5H_2O$	10
Ni(II)	$NiCl_2.6H_2O$	20
V(V)	$NH_4VO_3H_2O$	5
Cr(VI)	$K_2Cr_2O_7$	5
Pd(II)	$PdCl_2$	2
Pt(IV)	$H_2PtCl_6.H_2O$	2
Os(VIII)	OsO_4	2
Ru(III)	$RuCl_3$	2
Rh(III)	$RhCl_3$	2
Au(III)	$HAuCl_4.xH_2O$	5
Ag(I)	$AgNO_3$	5
Re(VII)	$KReO_4$	20
As(III)	$AsCl_3$	20
W(VI)	$Na_2WO_4.2H_2O$	5
H_2O_2	H_2O_2, 30%	1.0 ml
Fluoride	Sodium fluoride	25
Phosphate	Na_2HPO_4	100
Oxalate	Oxalic acid	100
Malonate	Malonic acid	80
Citrate	Citric acid	40
Acetate	Sodium acetate	100
Salicylate	Sodium salicylate	100

Analysis of bismuth(III) from alloys. The bismuth(III) containing alloys *viz* lead-bismuth alloy, sealing alloy, bismuth solder alloy and tin-bismuth alloy were analyzed by proposed method and results of analysis were reported in Table 4.

Mutual separation of bismuth(III), mercury(II) and zinc(II) or cadmium(II). The proposed method gives separation of bismuth(III) from the mercury(II) and zinc(II) or cadmium(II), the results of analysis were reported in Table 5.

Statistical treatment of the analytical data. The evaluation and interpretation of an analytical data is verified statistically. It is measure of performance for analytical procedure. Various criteria were used to evaluate the analytical data. The obtained important values are reported in Table 6.

Table 3. Analysis of synthetic mixtures.

Composition, mg	Recovery of Bi(III), mg	Recovery, %	RSD (*n*=3), %
Bi(III) 2.0; Fe(III) 5.0	1.998	99.9	0.1
Bi(III) 2.0; Sn(II) 5.0; Fe(III) 2.0	1.988	99.4	0.6
Bi(III) 2.0; V(V) 2.0; Sn(II) 2.0	1.994	99.7	0.3
Bi(III) 2.0; U(VI) 5.0; Cr(VI) 2.0	1.994	99.7	0.3
Bi(III) 2.0; Cd(II) 2.0; Zn(II) 2.0	1.988	99.4	0.6
Bi(III) 2.0; Hg(II) 2.0; In(III) 5.0	1.998	99.9	0.1
Bi(III) 2.0; Fe(III) 5.0; Cr(VI) 2.0	1.984	99.2	0.8
Bi(III) 2.0; Cd(II) 2.0; Zn(II) 2.0; Hg(II) 2.0	1.984	99.2	0.8

Table 4. Analysis of alloys.

Sample alloy composition, %	Bi(III) present, mg	Bi(III) found, mg	Mean, mg	Average recovery, %	Relative error, %
Lead-bismuth alloy (Bi 15.4, Pb 84. 6)	2.0	2.00 1.99 1.98	1.99	99.5	0.5
Sealing alloy (Bi 58, Pb 36, Sb 6)	1.5	1.50 1.50 1.47	1.49	99.3	0.7
Bismuth solder alloy (Bi 27.5, Pb 27.5, Sn 45)	0.5	0.49 0.50 0.48	0.49	99.6	0.4
Tin-bismuth alloy (Bi 25, Sn 75)	2.0	1.99 1.98 1.99	1.99	99.5	0.5

Table 6. Statistical treatment of the analytical data*.

Mean (M)	1.99
Median (m)	1.98
Average deviation (d)	0.0043
Mean of average deviation (D)	0.0016
Standard deviation (s)	0.011
Mean of standard deviation (S)	0.004
Coefficient variation (C.V.)	0.57%

* Average of six determinations (n = 6).

Table 5. Mutual separation of mercury(II), bismuth(III) and zinc(II) or cadmium(II)

Mercury(II)			Bismuth(III)			Zinc(II)			Cadmium(II)		
Taken, mg	Found, mg	R, %	Taken, mg	Found, mg	R, %	Taken, mg	Found, mg	R, %	Taken, mg	Found, mg	R, %
1.0	0.99	99.35	2.17	2.15	99.1	-	-	-	0.5	0.499	99.9
0.5	0.49	98.5	1.08	1.07	99.8	-	-	-	0.5	0.499	99.9
1.0	0.99	99.9	1.62	1.60	99.3	-	-	-	0.5	0.493	98.6
0.5	0.49	98.5	0.54	0.52	98.0	-	-	-	0.5	0.495	99.1
0.5	050	100.0	2.17	2.15	99.1	-	-	-	0.5	0.499	99.9
1.0	0.98	98.0	2.17	2.17	100.0	0.66	0.646	98.0	-	-	-
0.5	0.49	98.0	1.08	1.07	98.8	1.32	1.307	99.0	-	-	-
1.0	0.99	99.1	0.54	0.53	99.4	0.66	0.659	99.8	-	-	-
0.5	0.49	98.9	2.17	2.14	98.9	1.32	1.300	98.5	-	-	-
0.5	0.50	100.0	0.54	0.53	99.4	0.66	0.659	99.9	-	-	-

CONCLUSION

The proposed method is very simple, selective, reproducible and rapid. It permits selective separation of bismuth(III) from other associated and toxic metal ions such as Fe(III), Sn(II), V(V), Cr(VI), U(VI), Cd(II), Zn(II), Hg(II) and In(III). It requires low reagent concentration. It is free of a large number of foreign ions, which are commonly associated with bismuth(III) in its natural occurrence. It is applicable for the separation of bismuth(III) in synthetic mixtures and alloys.

Acknowledgements: *We are thankful to Prof. M. B. Chavan, for his valuable guidance. The authors are also thankful to the Management, Pravara Rural Education Society and Principal of P. V. P. College Pravaranagar for providing necessary facilities.*

REFERENCES

1. J. S. Hwary, *Bull. Bi. Inst*., **78**, 1 (2001).
2. A. Afkhami, T. Madrakian, H. Siampour, *J. Braz. Chem. Soc*., **17**, 797 (2006).
3. A. K. De, S. M. Khopkar, R. A. Chatmper, Solvent Extraction of Metals, Van Nostrand Reinhold, London, 1970.
4. S. R. Kuchekar, M. B. Chavan, *Talanta*, **35**, 357 (1988).
5. G. N. Mullik, S. R. Kuchekar, M. B. Chavan, *Ind. J. Chem*., **25A**, 1073 (1986).
6. H. R. Aher, P. S. Gunjal, S. R. Kuchekar, M. B. Chavan, *Asian J. Chem*., **10**, 43 (1998).
7. S. R. Kuchekar, H. R. Aher, M. B. Chavan, *Ind. J. Chem.*, **42 A**, 1674 (2003).
8. R. B. Thorat, A. S. Burangale, N. B. Kadam Patil, Rasayan, *J. Chem*., **2**, 1 (2009).
9. S. G. Sarkar, P. M. Dhadke, *Sep. Purif. Tech*., **15**, 131 (1999).
10. R. G. Vibhute, S. M. Khopkar, *Bull. Bi. Inst*., **55**, 5 (1988).
11. J. N. Iyer, P. M. Dhadke, *Indian. J. Chem. Tech*., **10**, 665 (2003).
12. A. M. El-Brashy, M. E. S. Metwally, F. A. J. El-Sepai, *J. Chin. Chem. Soc*., **52**, 253 (2005).
13. A. I. Vogel, A Text Book of Quantitative Inorganic Analysis, Including Elementary Instrumental Analysis, 3rd edn., ELBS and Longman, London, 1975.
14. F. J. Welcher, The Analytical Uses of Ethylenediaminetetraacetic Acid, D. Van Nostrand Company Inc., New York, 1958.
15. C. Pohlandt, *Talanta*, **26**, 199 (1979).
16. J. Mendham, R. C. Denney, J. D. Barnes, M. J. K. Thomas, Vogel's Textbook of Quantitative Chemical Analysis, 6th Edition, Pearson Edition, Ltd, India, 2008 409.
17. G. B. Kolekar, T. N. Lokhnde, P. N. Bhosale, M. A. Anuse, *Anal. Lett*., **31**, 2241 (1998).
18. A. I. Vogel, Text book of Quantitative Analysis, Longmans Green, London, 1964, p. 433.
19. N. A. Borshch, O. M. Petrukhin, *Zh. Anal. Khim*., **33**, 1805 (1978).
20. C. P. Mane, M. A. Anuse, *J. Chin. Chem. Soc*., **55**, 807 (2008).

ТЕЧНО-ТЕЧНА ЕКСТРАКЦИЯ И ИЗВЛИЧАНЕ НА БИСМУТ(III) ОТ СОЛНОКИСЕЛА СРЕДА С ИЗПОЛЗВАНЕ НА *н*-ОКТИЛАНИЛИН В ХЛОРОФОРМ

С. Дж. Кокате, Я. С. Шелар, Х. Р. Ахер, С. Р. Кучекар*

Департамент „Аналитична химия“, Видя Патиштан Колеж, Праваранагар, Лони, Рахата, окр. Ахмеднагар, Махаращра 413713, Индия

Постъпила на 28 август 2009 г.; Преработена на 5 ноември 2009 г.

(Резюме)

Изследвана е течно-течната екстракция на бисмут(III) с *н*-октиланилин в хлороформ от хлороводородна и бромоводородна киселинна среда. Бисмут(III) е екстрахиран количествено с 10 ml 3% реагент в хлороформ от 0.3 до 0.5 M хлороводородна и от 0.04 до 0.1 M бромоводородна киселинна среда, отделен от органичната фаза с 0.01 M ацетатен буфер и определен комплексонометрично. Оптималните условия на екстракцията са оценени чрез изследване на влиянието на киселинността, концентрацията на *н*-октиланилин, времето за установяване на равновесие и ефекта на разредителите. Методът не се влияе от присъствие на голям брой катйони и анйони. Методът позволява последващо разделяне на живак(II), бисмут(III) и цинк(II) или кадмий(II) и е успешно приложен за разделяне на бисмут(III) от образци от сплави. Зависимостта в логаритмични координати на степента на разпределение от концентрацията на *н*-октиланилина при 0.1 и 0.2 M концентрации на солна киселина има стойности за наклона съответно 2.2 и 1.9. Вероятната екстрахирана форма е $(RNH_3^+)_2BiCl_5^{2-}$.

Bulgarian Chemical Communications, Volume 42, Number 2 (pp. 113–118) 2010

Electrocatalytic oxidation-reduction reactions of metal-hydride alloys with teflon-carbon additives

D. Uzun, P. Iliev, D. Vladikova, P. Andreev, S. Balova, V. Nikolova, S. Vassilev, K. Petrov*

Institute of Electrochemistry and Energy Systems, Bulgarian Academy of Sciences, Acad. G. Bonchev St., Block 10, 1113 Sofia, Bulgaria

Received May 27, 2009; Revised November 11, 2009

Model metal hydride (MH) electrodes for fast screening of MH alloys electrochemical performance have been developed in a former work of ours. The effect of additives (teflonized blacks or carbons) on the electrodes characteristics has been demonstrated. An attempt to explain this effect and to create a physical model of the reactions taking place in the MH electrodes has been done in the present study. Our working hypothesis is that simultaneous reactions of carbon oxidation and reduction of MH oxides are taking place thus creating spread out micro-galvanic elements.

The additivity principle has been applied in order to explain and to prove the electrochemical mechanism of the process. Partial polarization curves have been measured in order to demonstrate the possibility of working hypothesis. An original approach for quantitative estimation of the rate of the general reaction has been developed and applied by measuring: (i) X-ray diffraction and Impedance Spectroscopy for explanation of additives effect; and (ii) Real galvanic element between carbon free MH electrode and electrode with teflonized carbon blacks only is constructed and tested to prove the working hypothesis.

Key words: Metal hydride electrode, fast screening method.

INTRODUCTION

The fast electrochemical screening of different MH alloys is an effective tool in the development of Ni-MH batteries. Straightforward model electrodes for preparation and testing have been developed in a former work of ours [1]. The electrodes consist of MH alloys particles and teflonized blacks or carbons used as additives (binding agents) [2]. The effect of additives on the electrochemical perform-ance of the electrodes has been mentioned. The electrodes with teflonized Vulcan XC-72 have demonstrated a much better performance compared to the electrodes with teflonized blacks (Acethylene black) or teflonized carbons (Norit NK). The MH electrodes with teflonized Vulcan XC-72 are reaching their theoretical capacity after two cycles and remain stable with time. One possible explanation of such an effect is the reaction between the MH alloy and the carbon blacks leading to reduction of the alloy surface oxides. It is known that the $LaNi_5$ particles are partially oxidized during electrode preparation. The purpose of the first several cycles is the reduction of these oxides. Then the reaction of hydriding-dehydriding progresses rapidly, i.e. following a number of cycles the electrode capacity reaches a plateau [3, 4].

Our hypothesis is that oxidation-reduction reactions on spread micro galvanic elements are taking place. Such reactions are well known in the literature [5–9]. Due to the thermodynamical redox potentials differences of $LaNi_5$ oxides (mainly NiOx), E_0 = 1.59 V, and carbon, E_0 = 0.50 V, galvanic elements are created within the electrode pores. The nickel oxides on the MH particles surface are reduced and the carbon in the teflonized carbon blacks is oxidized. The partial reactions are possibly the following:

$$\text{anodic reaction : } RC_n - xe^- + yO \rightarrow RC_nO_y \qquad (1)$$

$$\text{cathodic reaction: } LaNi_5O_x + ye^- \rightarrow LaNi_5O_{x-y} + yO \qquad (2)$$

Most probably these are mainly nickel oxides reduction reactions, for example: $NiO_2 \leftrightarrow Ni(OH)_2$.

Possible physical model of such scattered micro-galvanic elements is schematically illustrated in Figure 1. It shows the structure of an electrode comprising the teflonized blacks fibres and bonded to them particles of metal-hydride alloy. Metal alloy particles and carbon in teflonized blacks have direct electronic contact. Within the electrode pores the metal and carbon particles realize an ionic (electrolytic) bond through the electrolyte, thus providing the necessary conditions for creation of galvanic element ($LaNi_5O_x$-C). The mixed electrode potential is established. The surface oxides reduction reaction (left side) proceeds on metal alloy particles, while

* To whom all correspondence should be sent:
E-mail: kpetrov@bas.bg

the oxidation reaction proceeds on carbon particles (right side).

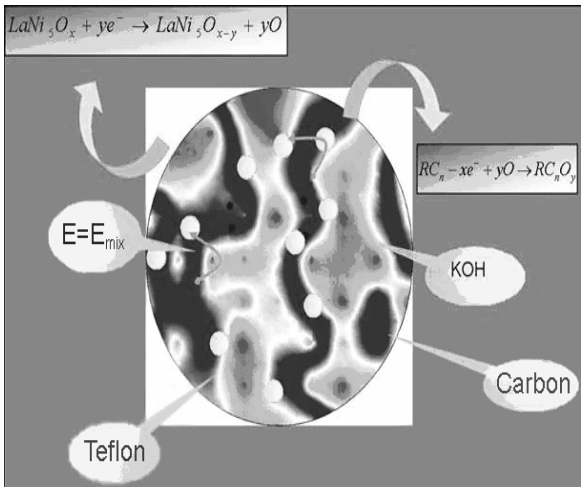

Fig. 1. Physical model of carbon-teflon electrode with spread micro-galvanic elements for electrocatalytic reactions of mMe:Ni:Co reduction and carbon oxidation in KOH electrolyte.

In the classical case of application of additivity principle [5, 6] there is an independent method to measure the rate of the overall reaction. In our case we cannot measure analytically the rate of carbon oxidation or metal oxides reduction. Following methods have been applied for independent estimation of the rate of the overall reaction: (i) X-ray analysis; (ii) Electrochemical Impedance Spectroscopy; and (iii) measurement of the current of real galvanic element between carbon free MH electrode and electrode with teflonized carbon blacks only.

EXPERIMENTAL

Standard metal hydride alloy produced by "Traibacher" with composition La:mMe:Ni:Co = 33:57:10% has been used for the MH electrodes preparation. The grain sizes of the supplied alloy are near 2 mm, grownd down to 0.063 mm. Three teflonized carbons (blacks) are tested: Vulcan XC-72, Acetylene black and Norit NK.

The Vulcan XC-72 carbon blacks are manufactured by "Cabot Corp.", USA. They have an active surface area of near 200 m^2/g. Their structure and composition are not disclosed by the company, however it has been confirmed that they have high electrochemical activity and are utilized for batteries and fuel cells electrode preparation worldwide. The Acetylene black are virtually pure carbon. They are produced by acetylene burning in oxygen free environment and virtually have no functional groups. Their surface area is close to 60–70 m^2/g. The Norit NK is an active carbon manufactured by "Norit Co." and utilized primarily for medical purposes. Its surface area is approximately 600 m^2/g, while its structure and composition are proprietary for the company.

The electrodes are prepared from a mixture of metal alloy and teflonized carbons (TC) in weight proportion of 60:40. The mixture is pressed onto a current collector formed from a nickel mesh at room temperature and pressure of 200 atm. The optimization of the ratio between the MH alloy and the teflonized carbons in parallel with the preparation procedure is described in our former work [3]. The geometrical area of the electrodes is either 1 cm^2 or 5 cm^2.

The electrochemical measurements are conducted in a three-electrode cell at room temperature. The counter electrode is a nickel plate, the reference electrode being Hg/HgO. The electrolyte is 8 M KOH. The Impedance Spectroscopy is carried out on an Autolab PGSTAT30/2 with an auxiliary FRA 2 (Frequency Response Analyzer). The measurements are performed under potentiostatic control with sine signal amplitude of 10 mV at an operating temperature of 20°C. The measured frequency span is from 0.1 kHz to 1 MHz. The X-ray measurements are carried out on a Philips APD-15 apparatus with copper luminous Cu Kα, λ = 1.54178 Å and graphite monochromator. A "Tacussel Electronique" BI-PAD Galvanostat/Potentiostat type is used for the electrochemical tests. All presented results reflect the average value of a minimum of three measured electrodes.

EXPERIMENTAL RESULTS

Oxidation-reduction reactions partial curves

The partial curves are plotted under galvanostatic control conditions. For the carbon oxidation anodic partial curves 1 cm^2 electrodes have been used prepared only with teflonized Vulcan XC-72, Acetylene black or Norik NK. MH alloy plus teflon powder electrodes have been utilized for the surface oxides reduction cathodic partial curves.

The partial curves are presented in Fig. 2. It is evident that the two partial curves intersect and the cross point's co-ordinates give the mixed current (i_m) and the mixed potential (E_m) values. It is apparent that the partial curves for the three additives bear similarity. All intersects with the reduction partial curve lay within its negative domain $(E_P)_к < (E_P)_{Me}$, hence there are grounds for a $LaNi_5O_x$-C micro-galvanic element emergence.

Figure 3 presents the details on large scale. The partial curves for oxidation of Vulcan XC-72 and reduction of MH alloy plus teflon powder are not shown. The cross point corresponds to a mixed

current i_m = 0.12 mA·cm^{-2} and a mixed potential of E_m= 205 mV. The Figure 3 illustrates the potential deviation as well, which is close to ±10 mV. Such potential deviation is quite normal for porous electrodes with highly developed surface. Consequently the calculated value for the current is approximate and close to $i_m \sim 0.1$ mA·cm^{-2}. Additionally, Figure 3 presents the open circuit potential for an electrode containing $LaNi_5$ and teflonized Vulcan XC-72. This potential varies within the range of 160–220 mV and we have concluded that there is a good agreement for the calculated from the partial curves and the measured on the real electrode open circuit potentials. This has supported our belief that the proposed mechanism for oxidation-reduction reactions on micro-galvanic elements is really taking place.

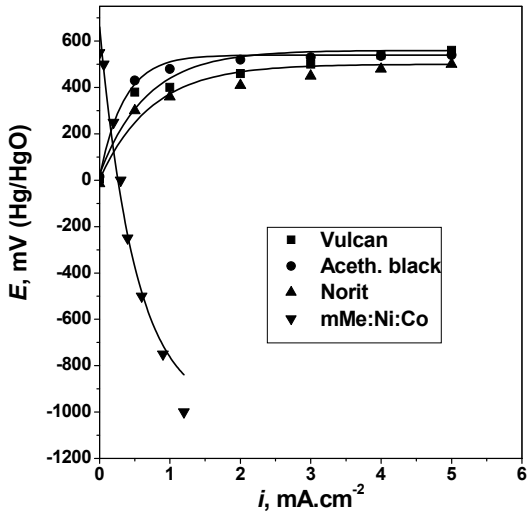

Fig. 2. Partial curves for reduction of mMe:Ni:Co -▼ and oxidation of teflonized Vulcan XC-72, acetylene black and Norit NK.

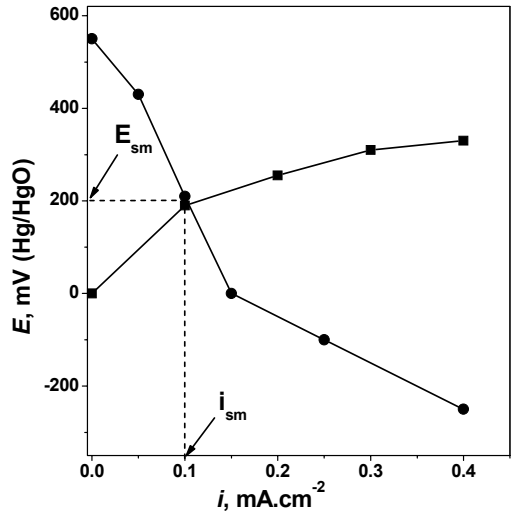

Fig. 3. Partial curves for reduction of mMe:Ni:Co +PTFE (●) and oxidation of teflonized Vulcan XC-72 (■).

X-ray analysis

Two types of electrodes have been analyzed – the first one prepared from teflonized Vulcan XC-72 and $LaNi_5$, and the second one produced from teflonized Acetylene black and $LaNi_5$. The analysis has been conducted on dry prepared electrodes and after they have been submerged in 8 M KOH for 15 hours. Our concept for this kind of experiment is that during the time of electrodes soaking wet in the electrolyte, a micro-galvanic element of the $LaNi_5O_x$-C type will be created. This will, probably, result in $LaNi_5$ surface oxides reduction.

Figure 4 depicts the X-ray analysis of dry and soaked in 8M KOH for 15 hours electrodes prepared with a Vulcan XC-72 additive: the curve 1 - dry electrode corresponds to the non-soaked electrode, while curve 2 is for the soaked electrode. The peaks belonging to the NiO_x are denoted by "(2)", indicating that on the surface there are predominantly NiO_x. The peaks at 2θ = 44^o correspond to the $LaNi_5O_x$ (Figure 4, 5). The intensity of the dry electrode is higher. This change however is not substantial to support our belief for visible reduction of the surface oxides that would back up our working hypothesis. The same is true for the peaks at 2θ = 52^o and 77^o belonging to the NiO_x.

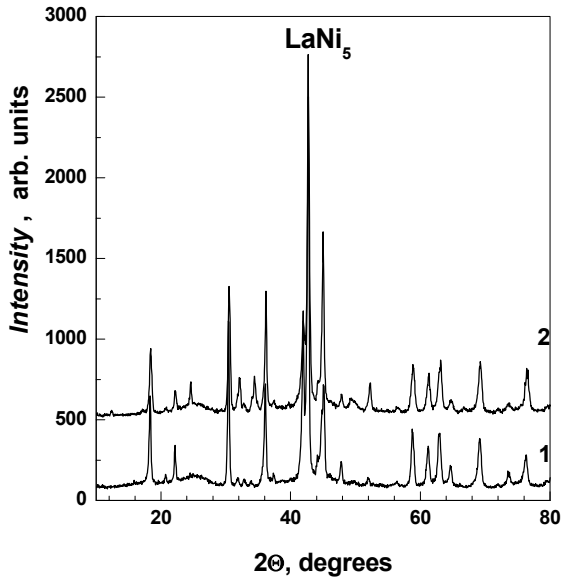

Fig. 4. X-ray diffraction pattern measured for dry and soaked mMe:Ni:Co electrodes; T = 25ºC; 8 M KOH; additive: teflonized Vulcan XC-72; 1 - dry electrode; 2- soaked electrode; time of wetting 15 hours.

X-ray diffraction pattern (pictures the X-ray analysis) of electrodes prepared with teflonized Acetylene black and $LaNi_5$ (Figure 5) bearing similarity to X-ray diffraction pattern in Figure 4, though the difference between the soaked and non-soaked electrode is practically absent.

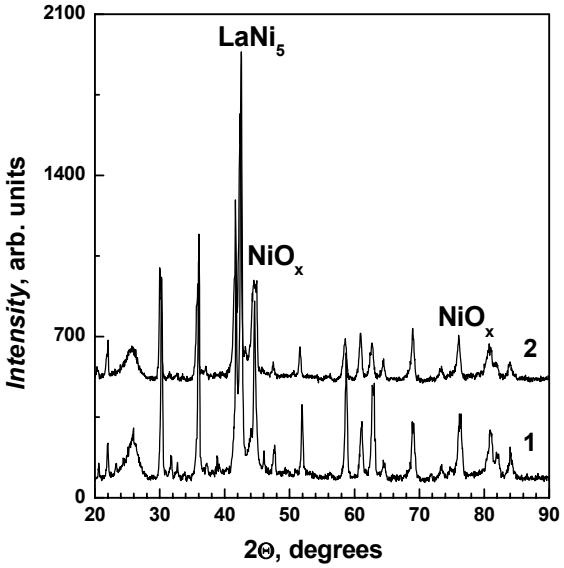

Fig. 5. X-ray diffraction pattern measured for dry and soaked mMe:Ni:Co electrodes; T = 25ºC; 8 M KOH; additive: teflonized Acetylene black; 1- dry electrode; 2 - soaked electrode; time of wetting -15 hours.

Electrochemical impedance measurements

According to our working hypothesis, the micro-galvanic elements ($LaNi_5O_x$-C) are created as soon as the electrodes are wetted and the oxidation-reduction reactions proceed until the reagents depletion, i.e. up to their chemical potential equalization. For these reasons the impedance measurements have been initiated immediately after the electrodes submergence. Figures 6, 7 and 8 depict the impedance spectra for 1 cm^2 electrodes prepared correspondingly with additives of Vulcan XC-72, Acetylene black and Norit NK. The electrolyte resistance of the three diagrams is uniform and close to R_L–0.5 Ω, which serves to demonstrate the good reproducibility of the results [10]. The electrochemical impedance spectra of the electrodes containing teflonized blacks, Figures 6 and 7 correspondingly for Vulcan XC-72 and Acetylene black follow an analogous pattern, which validates the fundamental similarity of the reactions [11]. Two processes are distinguished which occur at high and low frequency zones. The steep slope indicates the reactions capacitive nature with emphasized transport hindrances. The CPE (Constant Phase Element) existence suggests the presence of reduction products and particles that are not prone to dissolution. The low frequency zone represents a well-shaped semicircle, which is indicative of a reaction. Quantitatively, the reaction resistance for the Vulcan XC-72, Figure 6, is much lower compared to that for the Acetylene black electrodes, Figure 7. The ideal circle distortion makes us believe that more than a single process occurs, possibly a number of mixed (corrosion) reactions with closely spaced time constants. The curves traces, supported by basic corrosion considerations, lead us to the conclusion that the carbon oxidation is the hindered reaction.

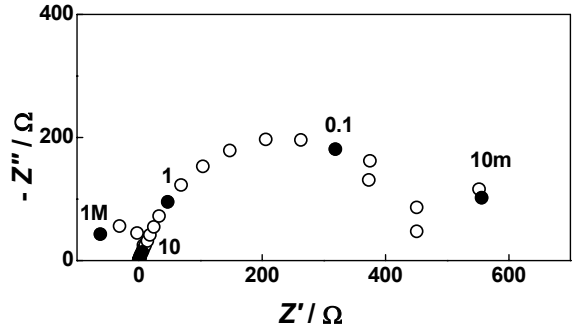

Fig. 6. Electrochemical impedance spectroscopy of mMe:Ni:Co electrode with additive teflonized Vulcan XC-72.

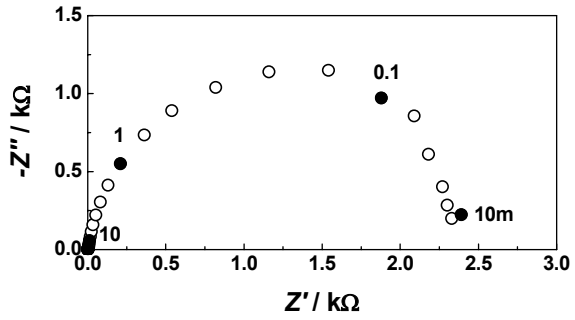

Fig. 7. Electrochemical impedance spectroscopy of mMe:Ni:Co electrode with additive teflonized Acetylene black.

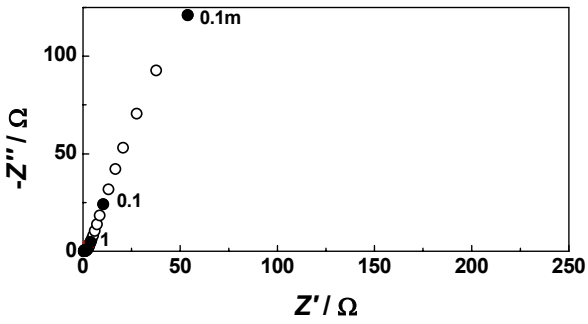

Fig. 8. Electrochemical impedance spectroscopy of mMe:Ni:Co electrode with additive teflonized Norit NK.

The electrodes prepared with the Norit NK have electrochemical impedance diagram again displayed within two zones, low- and high-frequency ones. It is worth mentioning that the low frequency zone is characterized by a very high resistance and it is rate determining for the process. This is most probably due to the carbon (Norit NK) presence whose crystal structure oxidation is considerably hindered.

The electrochemical impedance measurements lead us to the following conclusions: the reaction

resistance is lower than that for the electrodes with teflonized blacks (being lowest for Vulcan XC-72), where in all probability more than a single mixed (corrosion) reaction occurs and the rate determining step is the carbon oxidation reaction.

Practical $LaNi_5O_x$-C galvanic element preparation and corresponding measurements

Aiming to prove our working hypothesis we have prepared a real $LaNi_5O_x$-C galvanic element. The electrodes have geometrical surface area of S = 5 cm^2. The anode consists of teflonized Vulcan (50 $mg \cdot cm^{-2}$) only. The cathode is made of 100 $mg \cdot cm^{-2}$ MH alloy + 12 $mg \cdot cm^{-2}$ teflon powder. The cathode teflon powder content has been optimized in advance within the range of 10 to 15 $mg \cdot cm^{-2}$. The electrodes were mounted in a cell filled with 8 M KOH electrolyte. The current of the real galvanic element was measured by short-circuiting it *via* an ampermeter, while the cell voltage was measured with a voltmeter. The galvanic element block diagram is shown in Figure 9. The current and voltage measurements have been started immediately after the electrodes were submersion into the electrolyte.

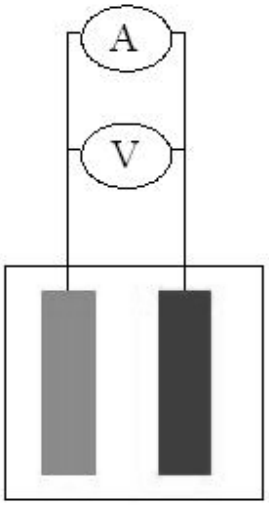

Fig. 9. Scheme of galvanic element; A- anode; B- cathode; ampermeter; voltmeter.

Figure 10 illustrates the relationships of short-circuit current *vs* time for galvanic elements comprising a MH alloy cathode and anodes made of teflonized Vulcan XC-72 (■) and teflonized Acetylene black (●). The galvanic element voltage is not shown in the figure, but it varied within the range from U = 24 mV to U = 0 mV for the time of the experiments. The plots reveal that the galvanic element comprising the Vulcan XC-72 anode supplies much higher currents compared to the Acetylene black anode. It seems that Vulcan XC-72 holds functional groups that are easier to oxidize [12]. For clarity the current-time relationship for the Acetilene black galvanic element is shown in the inset. It is apparent that the teflonized Vulcan XC-72 element demonstrates higher initial current densities approximating i = 0.03 $mA \cdot cm^{-2}$. This value of the current density is in a good agreement (within the same order of magnitude) with that calculated from the partial curves i_m value of i = 0.1 $mA \cdot cm^{-2}$ (see Figure 3). The calculated and measured potential and current values agreement, finding its proof in Figures 2, 3 and 10, serve to verify the progress of oxidation-reduction reactions on micro-galvanic elements, which makes us believe that our working hypothesis has been substantiated.

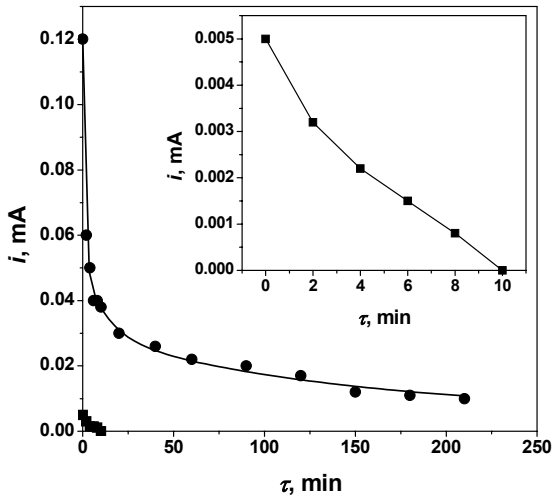

Fig.10. Dependence of galvanic element's short circueted-current from time; cathode mMe:Ni:Co + PTFE; anodes: teflonized Vulcan XC-72 (■) and teflonized Acetylene black (●).

CONCLUSIONS

An explanation of teflonized Vulcan XC-72 additive effect on the electrochemical behaviour of MH electrodes has been given. The working hypothesis for creation of scattered micro-galvanic elements, where reduction of $LaNi_5$ surface oxides and oxidation of carbon takes place, has been proven. It has been illustrated that the oxidation of Vulcan XC-72 is much faster than oxidation of Norit NK and acetylene blacks. The anodic reaction facilitation is most probably due to the fact that the Vulcan XC-72 possesses more RC_n functional groups.

The use of teflonized carbons/blacks in MH electrodes results in enhancement of the hydriding-dehydriding reaction rate and maintains the mMe(Co, Ni, Al) alloys in reduced state. One possible effect that may find its commercial application would be to lower the operation temperature and the pressure of the hydriding-dehydriding reactions on high capacity hydrogen containing MH alloys.

REFERENCES

1. K. Petrov, A. Rostami, A. Visintin, S. Srinivasan, *J. Electrochem. Soc*., **141**, 1747 (1994).
2. I. Iliev, S. Gamburtzev, A. Kaisheva, E. Budevski, *Bulg. Chem. Comm*., **7**, 223 (1974).
3. S. Srinivasan, K. Petrov, A. Anani, A. Visintin, *J. Power Sources* , **47**, 261 (1994).
4. A. K. Shukla, S. Venugoplan, B. Haripkarakash, *J. Power Sources*, **100**, 125 (2001).
5. C. Wagner, W. Traud, *Z. Elektrochem*., **44**, 391 (1938).
6. M. Spiro, P. L. Freund, *J. Electroanal. Chem*., **144**, 293 (1983).
7. I. Nikolov, K. Petrov, T. Vitanov, *J. Appl. Electrochem*., **26**, 703 (1996).
8. K.-M. Yin, *J. Power Sources*, **167**, 420 (2007).
9. C.-H. Chen, T.-K. Yeh, *J. Electroanal. Chem.*, **601**, 251 (2007).
10. Z. Stoynov, D. Vladikova, Differential Impedance Analysis, Marin Drinov Publ. House, Sofia, 2005.
11. Z. Stoynov, B. Grafov, B. Savova-Stoynova, V. Elkin, Electrochemical Impedance, Nauka, Moscow, 1991 (in Russian).
12. M. R. Tarasevich, Electrochemitry of Carbon Materials, Nauka, Moscow, 1984 (in Russian).

ВЛИЯНИЕ НА ВЪГЛЕН-ТЕФЛОНОВАТА СТРУКТУРА ВЪРХУ ЕЛЕКТРОКАТАЛИТИЧНИ ОКИСЛИТЕЛНО-РЕДУКЦИОННИ РЕАКЦИИ НА МЕТАЛ-ХИДРИДНИ СПЛАВИ

Д. Узун, П. Илиев, Д. Владикова, П. Андреев, С. Балова, В. Николова, С. Василев, К. Петров*

Институт по електрохимия и енергийни системи, Българска академия на науките, ул. „Акад. Г. Бончев“, блок 10, 1113 София

Постъпила на 27 май 2009 г.; Преработена на 11 ноември 2009 г.

(Резюме)

В предишна наша работа са разработени моделни метал-хидридни (МХ) електроди за бързо електрохимично охарактеризиране на МХ сплави. Изследван е ефектът на добавките (тефлонизирани сажди или въглени) върху характеристиките на електродите. В настоящото изследване е направен опит да се обясни този ефект и да се създаде физичен модел на системата. Нашата работна хипотеза е, че в моделните МХ електроди с добавки от тефлонизирани сажди или въглени едновременно протичат реакциите на окисление на въглените и редукция на МХ сплави върху разпръснати микрогалванични елементи. Приложен е адитивния принцип, за да се обясни и докаже електрохимичния механизъм на процеса. Измерени са парциалните поляризационни криви за да се покаже възможността за протичане на указаните реакции. Разработен е оригинален подход за количествена оценка на скоростта на общата реакция чрез измерване на: (i) рентгенова дифракция и електрохимична импедансна спектроскопия; и (ii) създаден, конструиран и тестван е реален галваничен елемент между електроди само от тефлонизирани въглени (сажди) и електроди само с МХ сплав с което е доказана работната ни хипотеза.

Bulgarian Chemical Communications, Volume 42, Number 2 (pp. 119–125) 2010

Synergistic effect of ethylphosphonic acid–Zn^{2+} system in controlling corrosion of carbon steel in chloride medium

A. Nithya[1], S. Rajendran[1,2]*

[1] *Corrosion Research Centre, Department of Chemistry, G.T.N. Arts College, Dindigul-624005, Tamil Nadu, India*
[2] *Corrosion Research Centre, Department of Physical Sciences, Servite College of Education for Women, Thogaimalai-621313, Tamil Nadu, India*

Received June 3, 2009; Revised December 8, 2009

The inhibition efficiency of ethylphosphonic acid (EPA) in controlling corrosion of carbon steel, immersed in an aqueous solution containing 120 ppm of Cl^- and sulphate ion, has been evaluated by weight loss method in the absence and presence of Zn^{2+}. Weight loss study reveals that the formulation consisting of 250 ppm of EPA, 50 ppm of Zn^{2+} and 73.58 ppm of sulphate ion has 84% inhibition efficiency in controlling corrosion of carbon steel, immersed in an aqueous solution containing 120 ppm of Cl^-. Synergism parameters suggest that a synergistic effect exists between EPA and Zn^{2+}. Polarization study reveals that this system functions as an anodic inhibitor. AC impedance spectra reveal that a protective film is formed on the metal surface. FTIR spectra reveal that the protection film consists of Fe^{2+}–EPA complex. This is confirmed by UV-visible reflectance spectra.

Key words: Carbon steel, corrosion inhibition, phosphonic acid, UV spectra, synergistic effect, F-test

INTRODUCTION

Inhibition of corrosion and scaling can be done by the application of inhibitors. It is noted that the effect of corrosion inhibitors is always caused by change in the state of surface, being protected due to adsorption or formation of hardly soluble compounds with metal cations. Several phosphonic acids have been used as corrosion inhibitors along with metal cation such as Zn^{2+} [1–5]. Phosphonic acids are the inhibitors which have been widely used due to their stability, ability to form complexes with metal cations and scale inhibiting properties [6–8]. Electrochemical techniques have been used in corrosion inhibition studies of carbon steel by phosphonic acids [9, 10]. The electrochemical techniques have provided only macroscopic details of the redox reaction and no mechanistic information [11–13]. To understand the mechanism of the effect of inhibitors on the metal surface analytical techniques for surface must be used [14, 15]. The aim of the present study is to investigate synergistic corrosion inhibition for the EPA and Zn^{2+} combination to carbon steel immersed in aqueous solution containing 120 ppm of Cl^- and 29.43 ppm of sulphate ion. The corrosion inhibition efficiency has been evaluated using weight loss method. Electrochemical studies such as polarization and AC impedance spectra have been employed. The protective film formed on the metal surface was characterized with the help of surface analytical techniques such as UV-visible reflectance spectra and Fourier transform infrared (FTIR) spectroscopy.

METHODS AND MATERIALS

Carbon steel (0.026% S, 0.06% P, 0.4% Mn, 0.1% C and the rest Fe) specimens of dimensions 4×1×0.2 cm were used for weight loss study. Carbon steel encapsulated in teflon was polished to a mirror finish and degreased with trichloroethylene. The surface area of the exposed metal surface was 1 cm^2. This specimen was used in electrochemical studies.

The experiment was carried out at room temperature (37°C). Three carbon steel specimens were immersed in 100 ml of the solution containing 120 ppm of Cl^- and sulphate ion and various concentrations of the inhibitor in the absence and presence of Zn^{2+} ($ZnSO_4.7H_2O$) for a period of 5 days. The weight of the specimen before and after immersion was determined using Shimadzu balance AY62. Inhibition efficiency (IE) was calculated from the relationship $IE = (1 - W_2/W_1)\times 100$, where W_1 = corrosion rate in the absence of inhibitor, and W_2 = corrosion rate in the presence of the inhibitor.

The carbon steel specimens were immersed in various test solution for a period of 5 days. After 5 days, the specimens were taken out and dried. The film formed on the surface of the metal specimens, was analysed by surface analysis technique.

* To whom all correspondence should be sent:
E-mail: srmjoany@sify.com, susairajendran@gmail.com

IR spectra were recorded with a Perkin-Elmer-1600 spectrophotometer. The FTIR spectrum of the protective film was recorded by carefully removing the film, mixing it with KBr and making the pellet.

Polarization study was carried out in an H and CH electrochemical work station Impedance Analyzer Model CHI 660A, provided with *iR* compensation facility, using a three electrode cell assembly. Carbon steel was used as working electrode, platinum as counter electrode and saturated calomel electrode (SCE) as reference electrode. After having done *iR* compensation, polarization study was carried out. The corrosion parameters such as linear polarization resistance (LPR), corrosion potential E_{corr}, corrosion current I_{corr} and Tafel's slopes (b_a and b_c) were measured.

AC impedance spectra were recorded in the same instrument used for polarization study, using the same type of three electrode cell assembly. The real part (Z') and imaginary part (Z") of the cell impedance were measured in Ohms for various frequencies. The charge transfer resistance (R_t) and double layer capacitance (C_{dl}) values were calculated.

UV-visible absorption spectra of solutions were recorded using a Hitachi Model U-3400 spectrophotometer. The same instrument was used for recording UV-visible reflectance spectra of the film formed on the metal surface.

RESULTS AND DISCUSSION

Corrosion rates of carbon steel, immersed in an aqueous solution containing 120 ppm of Cl^-, in the absence and presence of EPA and Zn^{2+} and sulphate ion, obtained by weight loss method are given in Table 1. The inhibition efficiencies are also given in this table.

Table 1. Corrosion rates (CR) of carbon steel, immersed in an aqueous solution containing 120 ppm of Cl^- ion in the absence and presence of inhibitor and the inhibition efficiencies (IE) obtained by weight loss method (when Zn^{2+} = 25 ppm, sulphate ion = 36.79 ppm; when Zn^{2+} = 50 ppm, sulphatae ion = 73.58 ppm). Inhibitor EPA + Zn^{2+}; Immersion period 5 days.

Cl^- ppm	EPA, ppm	Zn^{2+}, ppm					
		0		25		50	
		CR, mdd	IE, %	CR, mdd	IE, %	CR, mdd	IE, %
120	0	18.36	-	21.66	18	19.09	4
120	50	17.44	5	13.22	28	8.44	54
120	100	16.16	12	12.48	32	6.43	65
120	150	15.05	18	10.10	45	5.14	72
120	200	14.69	20	9.55	48	3.67	80
120	250	13.95	24	8.81	52	2.94	84

It is observed that when carbon steel is immersed in 120 ppm of Cl^-, the corrosion rate is 18.36 mdd. Upon addition of various concentrations of EPA, the corrosion rate slowly decreases. The inhibition efficiency gradually increases from 5% to 24% (250 ppm of EPA has 24% IE). That is the formulation consisting of 250 ppm of EPA in 120 ppm of Cl^- ion environment, has 24% IE.

The influence of a divalent metal ion, Zn^{2+}, on the efficiency of ethyl phosphonic acid, in controlling corrosion of carbon steel, is given in Tables 2 and 3. It is observed that in the presence of 25 ppm of Zn^{2+}, (and 36.79 ppm of sulphate ion), the IE of EPA slightly improves. The divalent Zn^{2+} ion forms a complex with EPA, diffuses towards the carbon steel surface, forms Fe^{2+}–EPA complex on metal surface and Zn^{2+} is released. In the presence of 50 ppm of Zn^{2+}, (73.58 ppm of sulphate ion), the inhibition efficiency of EPA further increases.

A synergistic effect exists between Zn^{2+} and EPA. For example 50 ppm of Zn^{2+} (73.58 ppm of sulphate ion) has 4% IE. (The negative IE indicates the acceleration of corrosion rate in presence of Zn^{2+} alone). 250 ppm of EPA has 24% IE. However, their combination has 84% IE. This is due to the synergistic effect existing between EPA and Zn^{2+}.

Synergism parameters were calculated using the relation:

$$S_I = (1 - I_{1+2})/(1 - I'_{1+2})$$

where $I_{1+2} = (I_1 + I_2) - (I_1 \times I_2)$; I_1 = inhibition efficiency of substance 1; I_2 = inhibition efficiency of substance 2; I'_{1+2} = combined inhibition efficiency of substance 1 and 2.

Synergism parameters are indications of synergistic effect existing between two inhibitors [16, 17]. The values of synergism parameters (Table 2) are greater than one, indicating synergistic effect existing between Zn^{2+} and various concentrations of EPA.

Table 2. Synergism parameters derived from inhibition efficiencies of EPA – Zn^{2+} system (when Zn^{2+} = 25 ppm, sulphate ion = 36.79 ppm; when Zn^{2+} = 50 ppm, sulphate ion = 73.58 ppm).

EPA, ppm	Zn^{2+}, ppm		S_I	Zn^{2+}, ppm		S_I
	0	25		0	50	
0	-	18	-	-	4	-
50	5	28	2.81	5	54	0.38
100	12	32	6.74	12	65	0.86
150	18	45	7.34	18	72	1.20
200	20	48	7.68	20	80	1.20
250	24	52	8.57	24	84	1.38

To investigate whether the influence of Zn^{2+} on the inhibition efficiencies of EPA is statistically significant, F-test was carried out [18]. The results

are given in Tables 3 and 4. In Table 3, the influence of 25 ppm of Zn^{2+} on the inhibition efficiencies of 50, 100, 150, 200 and 250 ppm of EPA is investigated. The obtained F-value 154.1 is statistically significant, since it is greater than the critical F-value of 5.32 for 1, 8 degrees of freedom at 0.05 level of significance. Therefore, it is concluded that the influence of 25 ppm Zn^{2+} on the inhibition efficiencies of various concentrations of EPA is statistically significant.

Table 3. Distribution of F-value between the inhibition efficiencies of various concentrations of EPA (0 ppm Zn^{2+}) and the inhibition efficiencies of EPA in the presence of 25 ppm Zn^{2+} (when Zn^{2+} = 25 ppm, sulphate ion = 36.79 ppm).

Source of variance	Sum of squares	Degrees of freedom	Mean square	F	Level of significance of F
Between	1587.6	1	1587.6	154.1	P > 0.05
Within	82.1	8	10.3		

In Table 4, the influence of 50 ppm of Zn^{2+} on the inhibition efficiencies of 50, 100, 150, 200 and 250 ppm of EPA is represented. The obtained F-value is 609.4 statistically significant, since it is greater than the critical F-value of 5.32 for 1, 8 degrees of freedom at 0.05 level of significance. Therefore, it is concluded that the influence of 50 ppm Zn^{2+} on the inhibition efficiencies of various concentrations of EPA is statistically significant.

Table 4. Distribution of F-value between the inhibition efficiencies of various concentrations of EPA (0 ppm Zn^{2+}) and the inhibition efficiencies of EPA in the presence of 50 ppm Zn^{2+} (when Zn^{2+} = 50 ppm, sulphate ion = 73.58 ppm).

Source of variance	Sum of squares	Degrees of freedom	Mean square	F	Level of significance of F
Between	7617.6	1	7617.6	609.4	P > 0.05
Within	99.6	8	12.5		

The potentiodynamic polarization curves of carbon steel immersed in an aqueous solution containing 120 ppm of Cl^- are shown in Fig. 1. The corrosion parameters such as corrosion potential (E_{corr}), corrosion current (I_{corr}), Tafel's slopes (b_a, b_c) and linear polarization resistance (LPR) are given in Table 5. When carbon steel is immersed in an aqueous solution containing 120 ppm of Cl^- ion, the corrosion potential is –490 V *vs* SCE. When the inhibitors are added (250 ppm of EPA, 50 ppm of Zn^{2+} and 73.58 ppm of sulphate ion), the corrosion potential shifts to the anodic side (–431 V *vs* SCE). Further, the LPR value increases from 7.31×10^2 Ohm·cm^2 to 96×10^2 ohm·cm^2 and the corrosion current decreases from 8.21×10^{-5} A/cm^2 to 0.494×10^{-5} A/cm^2. These results suggest that a protective film (probably, Fe^{2+}–EPA complex) is formed on the metal surface. This protects the metal from corrosion.

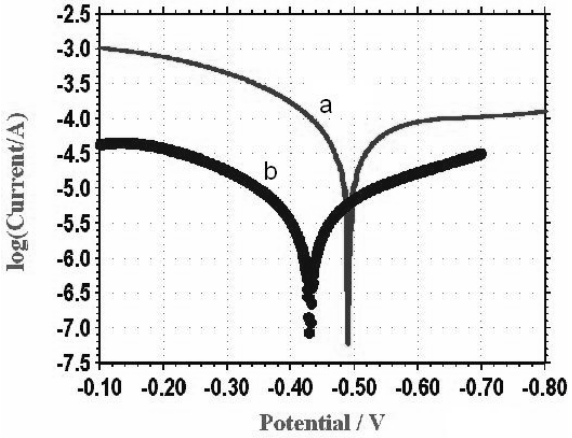

Fig. 1. Polarization curves of carbon steel, immersed in various test solutions 120 ppm Cl^- 120 ppm Cl^- + 250 ppm EPA + 50 ppm Zn^{2+} + 73.58 ppm of sulphate ion.

The AC impedance spectra of carbon steel, immersed in various test solutions are shown in Fig. 2. The AC impedance parameters such as charge transfer resistance (R_t) and double layer capacitance (C_{dl}) are given in Table 5. The equivalent circuit diagram in shown in Scheme 1. In the presence of inhibitors (250 ppm of EPA, 50 ppm of Zn^{2+} and 73.58 ppm of sulphate ion), the R_t value increases and C_{dl} value decreases. This indicates that a protective film is formed on the metal surface. The corresponding Bode's plots are shown in Fig. 3. It is observed that in the absence of inhibitors the real impedance value (log$Z$) is 2.28 Ohm. In the presence of inhibitors, this value increases to 2.62.

Table 5. Corrosion parameters of carbon steel, immersed in an aqueous solution containing 120 ppm of Cl^- ion obtained by polarization study and AC impedance spectra. Inhibitor EPA + Zn^{2+}.

System	E_{corr} mV *vs* SCE	b_c mV/dec	b_a mV/dec	LPR Ohm·cm^2	I_{corr} A/cm^2	R_t ohm·cm^2	C_{dl} F/cm^2	Impedance log$Z$, Ohm
120 ppm of Cl^- ion	490	506	189	7.31×10^2	8.21×10^{-5}	154	5.88×10^{-8}	2.28
120 ppm of Cl^- + 73.58 ppm of sulphate ion + 50 ppm of Zn^{2+} + 250 ppm of EPA	431	245	190	96×10^2	0.494×10^{-5}	455	1.98×10^{-8}	2.62

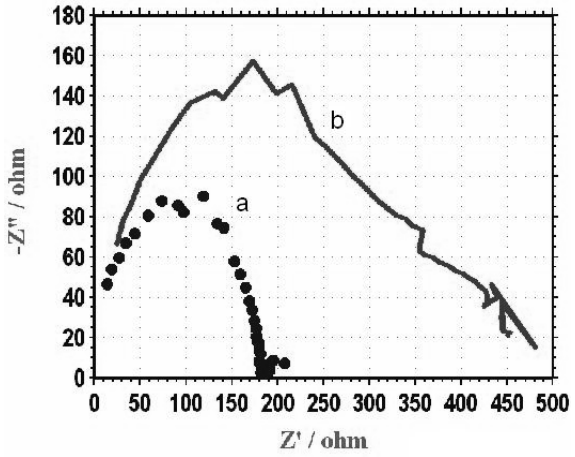

Fig. 2. AC impedance spectra of carbon steel, immersed in various test solutions (Nyquist's plots).

The FTIR spectrum of pure EPA (KBr) is shown in Fig. 4a. The various bands are assigned as follows [19]. The absorption bands due to the bending of O–P–O appear at 474.1, 502.9 and 598.1 cm^{-1}. The P–O stretching frequency occurs at 1071.7 cm^{-1}. The band at 1275.6 cm^{-1} represents P=O stretching. The band at 1415.8 cm^{-1} results from P–CH_2–CH_3 absorption. The P(O)OH group causes absorption at 2335, 2356.8 and 2955.6 cm^{-1}. Thus, based on the assignment of groups at various frequencies, ethyl phosphonic acid is characterized by the FTIR spectrum.

The FTIR spectrum of the film scratched from the surface of the metal, immersed in the environment consisting of 120 ppm Cl^-, 250 ppm EPA, 50 ppm Zn^{2+} and 73.58 ppm of sulphate ion is given in Fig. 4b. It is seen from the spectrum that the P–O stretching frequency decreases from 1071.7 cm^{-1} to 990 cm^{-1}. This also suggests that the O atom of the phosphonic acid is coordinated to Fe^{2+}. This confirms the formation of Fe^{2+}–EPA complex on the metal surface. Further, the band at 1340 cm^{-1} is due to $Zn(OH)_2$ [20–22].

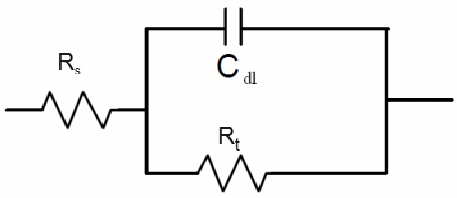

R_s = Solution resistance
R_t = Charge transfer resistance
C_{dl} = Double layer capacitance
Scheme 1. Equivalent circuit diagram.

The UV-visible absorption spectra of various test solutions are shown in Fig. 5. Fig. 5a is the absorption spectrum of a solution containing 250 ppm of EPA. Fig. 5b is the spectrum of the solution containing 100 ppm of Fe^{2+}. When 250 ppm of EPA and 100 ppm of Fe^{2+} are mixed the spectrum Fig. 5c is obtained. There is increase in intensity. A peak appears at 230 nm. This peak corresponds to Fe^{2+}–EPA complex formed in the solution.

The UV-visible reflectance spectrum of the film formed on the metal surface after immersion in the solution containing 120 ppm of Cl^-, 250 ppm of EPA, 50 ppm of Zn^{2+} and 73.58 ppm of sulphate ion is shown in Fig. 6. A peak appears at 230 nm. This peak corresponds to Fe^{2+}–EPA complex formed on the metal surface. This is in agreement with the UV-visible absorption spectrum, obtained in the case of aqueous solution.

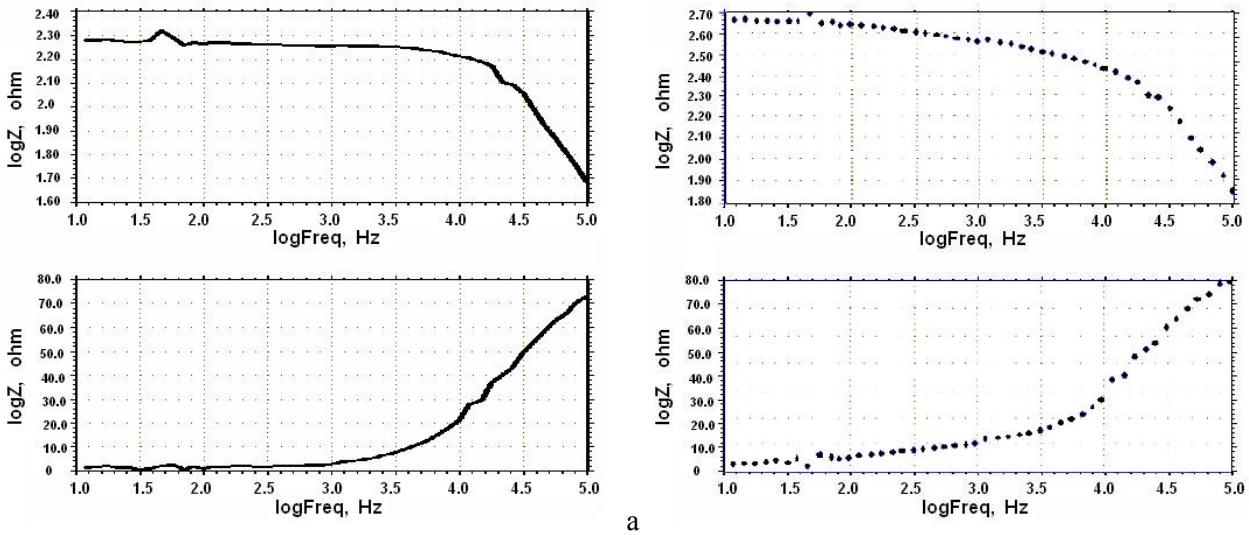

Fig. 3. AC impedance spectra of carbon steel, immersed in an aqueous solution (Bode plots); a. containing 120 ppm Cl^-; b. containing 120 ppm Cl^- + 250 ppm EPA + 73.58 ppm of sulaphate ion + 50 ppm Zn^{2+}.

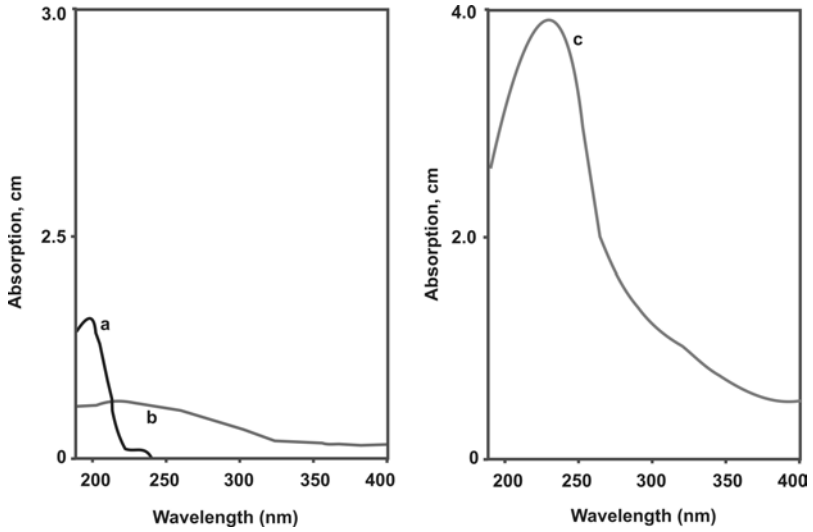

Fig. 5. UV-visible absorption spectra of solutions EPA 250 ppm, Fe^{2+} 100 ppm, EPA 250 ppm + Fe^{2+} 100 ppm.

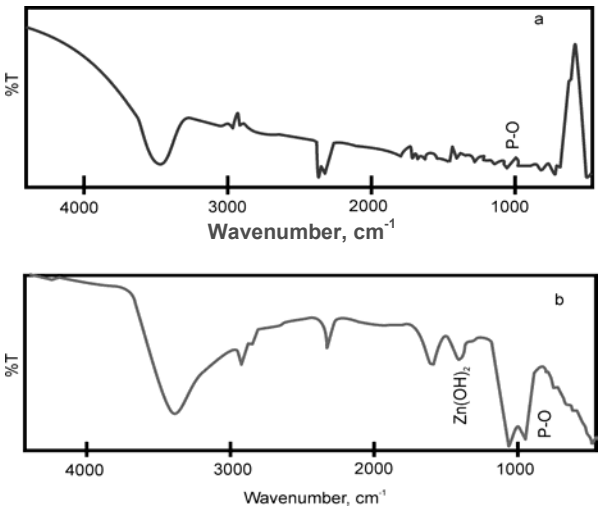

Fig. 4. FTIR spectra of pure EPA (KBr) film formed on carbon steel surface after immersion in the solution containing 120 ppm Cl^- + 250 ppm EPA + 73.58 ppm of sulphate ion + 50 ppm Zn^{2+}.

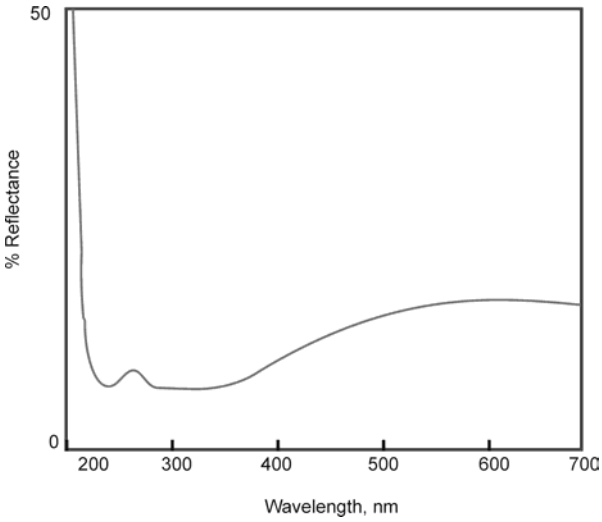

Fig. 6. UV-visible reflectance spectra of mild steel surface immersed in the environment 120 pm Cl^- + EPA 250 ppm + 73.58 ppm of sulphate ion + 50 ppm Zn^{2+}.

Mechanism of corrosion inhibition

Results of the weight-loss method reveal that the formulation consisting of 250 ppm ethyl phosphonic acid (EPA) and 50 ppm Zn^{2+} offers an inhibition efficiency of 84%. Results of the polarization study show that this formulation acts as an anodic inhibitor. The FTIR spectra show that Fe^{2+}–EPA complex and $Zn(OH)_2$ are present on the inhibited metal surface. The UV-visible reflectance spectrum shows the presence of Fe^{2+}–EPA complex on the metal surface.

In order to explain all the observations in a holistic way, a suitable mechanism of corrosion inhibition is proposed as follows:

When carbon steel specimen is immersed in the neutral aqueous environment, the anodic reaction is:

$$Fe \rightarrow Fe^{2+} + 2e^-$$

and the cathodic reaction is:

$$2H_2O + O_2 + 4e^- \rightarrow 4OH^-$$

When the environment, consisting of 120 ppm + 250 ppm EPA + 50 ppm Zn^{2+} + 73.58 ppm of sulphate ion is prepared, there is formation of Zn^{2+}–EPA complex in solution.

Now, when the metal (carbon steel) is immersed in this environment, the Zn^{2+}–EPA complex diffuses from the bulk of the solution to the surface of the metal.

On the surface of the metal, Zn^{2+}–EPA complex is converted into Fe^{2+}–EPA complex in the local anodic regions as the latter is more stable than the former [23].

$$Zn^{2+}\text{–EPA} + Fe^{2+} \rightarrow Fe^{2+}\text{–EPA} + Zn^{2+}$$

This reaction takes place on the surface of the metal in the local anodic regions. Also, formation of Fe^{3+}–

EPA complex to some extent cannot be ruled out.

Now, the released Zn^{2+} ions on the surface will form $Zn(OH)_2$ precipitate in the local cathodic regions.

$$Zn^{2+} + 2OH^- \rightarrow Zn(OH)_2 \downarrow$$

Thus, the protective film consists of Fe^{2+}–EPA complex and $Zn(OH)_2$.

CONCLUSION

The inhibition efficiency of EPA–Zn^{2+} system in controlling corrosion of carbon steel in an aqueous solution containing 120 ppm of Cl^-, has been evaluated by weight loss method. The present study leads to the following conclusion.

- Weight loss study reveals that the formulation consisting of 250 of ppm EPA, 50 ppm of Zn^{2+} and 73.58 ppm of sulphate ion had 84% inhibition efficiency in controlling corrosion of carbon steel immersed in an aqueous solution containing 120 ppm of Cl^- ion.
- Synergism parameters suggest that a synergistic effect exists between EPA and Zn^{2+}.
- Polarization study reveals that this system functions as anodic inhibitor.
- AC impedance spectra reveal that a protective film is formed on the metal surface.
- FTIR spectra reveal that the protective film consists of Fe^{2+}–EPA complex as well as of $Zn(OH)_2$, hydroxyl chloride and hydroxyl sulphate.
- The UV-visible absorption spectra reveal the formation of Fe^{2+}–EPA complex, in solution.
- The UV-visible reflectance spectra reveal the presence of Fe^{2+}–EPA complex on the metal surface.

Acknowledgement: *The authors are thankful to their management, St. Joseph's Research and Community Development Trust, Dindigul and to the University Grants Commission, India for their help and encouragement.*

REFERENCES

1. H. S. Awad, S. Turgoose, *Br. Corros. J.*, **37,** 147 (2002)
2. H. Amar, J. Benzakour, A. Derja, D. Villemin, B. Moreau, T. Braisaz, A. Tounsi, *Corros. Sci.*, **50**, 124 (2008)
3. D. Gopi, S. Manimozhi, K. M. Govindaraju, P. Manisankar, S. Rajeswari, *J. Appl. Electrochem.*, **37**, 439 (2007)
4. B. V. Apparao, K. Christina, *Indian J. Chem. Technol.*, **13**, 275 (2006)
5. S. Rajendran, A. J. Amalraj, J. W. Sahayaraj, R. J. Rathish, N. Anthony, N. Palaniswamy, *Trans. SAEST*, **40**, 35 (2005)
6. T. Du, J. Chen, D. Cao, *Bull. Electrochem.*, **13**, 13 (1997)
7. T. Harvoth, E. Kalman, G. Kutson, A. Rauscher, *Br. Corros. J.*, **29**, 215 (1994)
8. A. Shaban, E. Kalman, I. Biczol, *Corros. Sci.*, **35**, 1463 (1993)
9. B. Muller, I. Forster, *Corros. Sci.*, **38**, 1103 (1996)
10. Y. Gonzalez, M. C. Lafont, N. Pebere, F. Moran, *J. Appl. Electrochem.*, **26**, 1259 (1996)
11. J. R. Galvele, *Corros. Sci.*, **47**, 3053 (2005)
12. A. Alamr, D. F. Bahr, M. Jacroux, *Corros. Sci.*, **48**, 925 (2006)
13. N. P. Cosman, K. Faith, S. G. Roscoe, *J. Electroanal. Chem*., **574**, 261 (2005)
14. W. Yang, G. Zhao, M. Zhang, J. Congleton, *Corros. Sci.*, **33**, 89 (1992)
15. J. Cogleton, W. Zheng, H. Hua, *Corros. Sci.*, **30**, 555 (1990)
16. S. Rajendran, S. Shanmugapriya, T. Rajalakshmi, A. J. Amalraj, *Corrosion*, **61**, 685 (2005)
17. K. Anuradha, R. Vimala, B. Narayanasamy, J. A. Selvi, S. Rajendran, *Chem. Eng. Commun.*, **195**, 352 (2008)
18. S. Rajendran, A. Rosaly, S. Thangasamy, *J. Mater. Educ.*, **28**, 315 (2006)
19. R. M. Silverstein, G. C. Bassler, T. C. Morrill, Spectrometric Identification of Organic Com-pounds, John Willey & Sons, New York, 1986, p. 95.
20. I. Sekine, Y. Hirakawa, *Corrosion*, **42**, 272 (1986)
21. J. Sathiyabama, S. Rajendran, J. A. Selvi, J. Jeyasundari, *The Open Corrosion J.*, **2**, 76 (2009)
22. J. A. Selvi, S. Rajendran, V. G. Sri, A. J. Amalraj, B. Narayanasamy, *Portugaliae Electrochim. Acta*, **27**, 1 (2009).
23. S. Rajendran, B. R. Earnest, J. Peter, A. Peter, P. Regis, A. J. Amalraj, M. Sundaravadivelu, *Trans. SAEST,* **38**, 11 (2003).

СИНЕРГИЧЕН ЕФЕКТ В СИСТЕМАТА ЕТИЛФОСФОРНА КИСЕЛИНА-Zn^{2+} ЗА КОНТРОЛ НА КОРОЗИЯТА НА ВЪГЛЕРОДНА СТОМАНА В СРЕДА СЪДЪРЖАЩА ХЛОРИДИ

А. Нитя[1], С. Раджендран[1,2] *

[1] Център за изследване на корозията, Департамент по химия,
Колеж по изкуства Г.Т.Н., Диндигул 624005, Тамил Наду, Индия
[2] Център за изследване на корозията, Департамент по физични науки,
Колеж за образование на жените „Сервит“, Тогаймалай 621313, Тамил Наду, Индия

Постъпила на 3 юни 2009 г.; Преработена на 8 декември 2009 г.

(Резюме)

Чрез метода на тегловните загуби в отсъствие и присъствие на Zn^{2+} е определена инхибиторната ефективност на етилфосфорна киселина (ЕФК) за контролиране на корозията на въглеродна стомана потопена във водни разтвори съдържащи 120 ppm хлорни и сулфатни йони. Изследването на тегловните загуби показа, че разтвор съдържащ 250 ppm ЕФК, 50 ppm Zn^{2+} и 73.58 ppm сулфатен йон има 84% инхибиторна ефективност за контролиране на корозията на въглеродна стомана потопена във воден разтвор съдържащ 120 ppm хлорни йони. Параметрите сочат за присъствие на синергичен ефект между ЕФК и цинковите йони. Поляризационно изследване показа, че тази система работи като аноден инхибитор. АС импедансни спекти показаха образуване на защитен филм на повърхността на метала. ИЧ спектри показаха, че защитния филм се състои от комплекс на Fe^{2+} и ЕФК. Резултатът е потвърден и с отражателни спектри в УВ-видимата област.

Bulgarian Chemical Communications, Volume 42, Number 2 (pp. 126–129) 2010

Kinetics and mechanism of oxidation of curcumin by sulphate radical anion in aqueous acetonitrile solution

S. S. Midudhula[1], A. Mundra[2,]*

[1] *Department of Chemistry, Osmania University, Hyderabad – 500 007, India*
[2] *Department of Chemistry, Post Graduate College of Science, Saifabad, Osmania University, Hyderabad-500 004, India*

Received June 23, 2009

The photooxidation of curcumin in the presence of peroxydisulphate (PDS) in aqueous acetonitrile solution at pH 7.5 has been carried out in a quantum yield reactor using a high pressure mercury vapour lamp. The reactions were followed by measuring the absorbance at 420 nm. The initial rates were calculated from absorbance *versus* time plots using Microcal Origin computer program. The rates of photooxidation of curcumin by peroxydisulphate were found to increase with increase in [PDS], [curcumin] and light intensity. The quantum yields were found to depend on [curcumin] and independent of [PDS] and light intensity. The plots of log(rate) *versus* log[PDS] and log(rate) *versus* log[curcumin] are linear with a slope of less than one indicating fractional order dependence of rate on [PDS] as well on [curcumin]. On the basis of experimental results and product analysis a probable mechanism is supposed.

Key words: oxidation of curcumin, sulphate radical anion.

INTRODUCTION

Natural phenolic antioxidants from medicinal and edible plants have received much attention as promising reagents for reducing the risk of oxidation induced diseases. Curcumin is a famous biologically active phenolic compound, which is obtained from the plant *Curcuma longa* (turmeric), curcumin is used as a natural yellow pigment [1]. It has been known that increased dietary curcumin leads to improved chemoprevention of cancer [2–5], possibly through inhibition of the growth of blood capillaries in cancerous tissue. Curcumin also exhibits bactericidal action and may minimize oxidative damage through free radical scavenging [2]. The pharmacological activities of curcumin such as anti-inflammatory and anti-cancer effects have been linked to its antioxidant properties and its ability to inhibit lipid peroxidation [6].

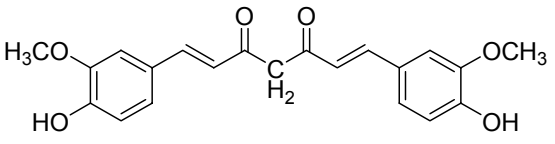

Curcumin

Bis (4-hydroxy-3-methoxyphenyl)-1,6-heptadiene-3,5-dione

Curcumin has also been found to inhibit strand break formation in DNA [7]. Structurally, curcumin consists of two ortho methoxylated phenols and β-diketone moiety (feruloyl moiety) and they are all in conjugation.

The free radical scavenging activity of curcumin involves radical trapping at the phenolic position as in the case of other phenolic antioxidants. However, the position that involves radical termination has not been defined so far because of the complexity of its highly conjugated structure.

It has been suggested by Jovanovic *et al.* [8] that keto-enol-enolate equilibrium of the heptadienone moiety of curcumin determines its physicochemical and antioxidant properties. In neutral and acidic aqueous solutions (from pH 3–7), the keto form dominates and curcumin acts as an extraordinarily potent H-atom donor. The H-atom donation occurs from the central $–CH_2–$ group in the heptadienone link because the C–H bonds in this group are very weak due to delocalization of the unpaired electron on the adjacent oxygens. The reaction mechanism of curcumin changes drastically above pH 8, where the enolate form of the heptadienone link predominates. As a consequence, the phenolic part of curcumin takes over as reaction site and electron transfer mechanism becomes operative. The methyl radical generated by pulse radiolysis and photochemically generated tert-butoxyl radical were found to react with curcumin by abstracting an H-atom from the central $–CH_2–$ group [8].

It is in this background, that the study of kinetics of oxidation of curcumin by sulphate radical anion, generated by the photolysis of peroxydisulphate has been undertaken.

* To whom all correspondence should be sent:
E-mail: adinarayana_mundra@live.com

EXPERIMENTAL

Curcumin was from Sigma Chemicals, USA. and was used as received. The solution of curcumin was prepared using a HPLC grade acetonitrile and that of peroxy-disulphate with doubly distilled water. The peroxy-disulphate solution was standardized cerimetrically using ferroin indicator. The concentration of curcumin was determined by measuring the absorbance at 420 nm and from known molar absorption coefficient value at this wavelength. Irradiations were carried out in a quantum yield reactor model QYR-20 using high pressure mercury vapour lamp. In general intensity measurements were carried out using ferrioxalate actinometry. In a typical reaction, curcumin and peroxydisulphate solutions were mixed in a specially designed 1-cm path length cuvette, which is suitable both for irradiations in the reactor as well as for absorbance measurements. The absorbance measurements were carried out on a Hitachi UV-visible spectrophotometer model 3410. The progress of the reaction was followed by measuring the absorbance at the λ_{max} of curcumin by interrupting irradiations at regular intervals of time (Fig. 1). The reaction rates have been calculated from the plots of absorbance versus time using a computer program. The quantum yields have been calculated from the initial rates of oxidation of curcumin and light intensity at 254 nm. This is the wavelength at which peroxydisulphate is activated to radical reac-tions. The light intensity at 254 nm was measured by peroxydisulphate actinometry.

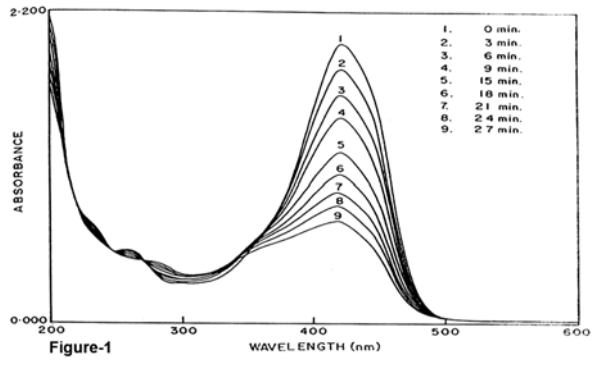

Fig. 1. Absorption spectra of photooxidation of curcumin in the presence of peroxydisulphate at different irradiation times. [curcumin] = 5.00×10^{-5} mol·dm^{-3}, [PDS] = 2.00×10^{-4} mol·dm^{-3}. Light intensity = 2.16×10^{15} photons·s^{-1}, water-acetonitrile = 1:3 (v/v)

RESULTS AND DISCUSSION

Photooxidation of curcumin in presence of peroxydisulphate in aqueous-acetonitrile solution has been carried out in a quantum yield reactor using a high pressure mercury vapour lamp. The initial rates of oxidation of curcumin were measured under different experimental conditions. The reaction rates of photooxidation of curcumin by peroxydisulphate were found to increase with increase in [PDS], [curcumin] and light intensity. The reaction order in [PDS] and [curcumin] was found to be fractional. The quantum yields were calculated from the initial rates of oxidation of curcumin and light intensity absorbed by peroxydisulphate at 254 nm. The quantum yields of the reaction have been found to depend on [curcumin] and to be independent of [PDS] and light intensity (Table 1).

Jovanovic *et al.* [8] have studied by laser flash photolysis and pulse radiolysis, the reactions of curcumin with methyl radical and tert-butoxyl radical in acidic, neutral as well as in alkaline media. Their results clearly indicate that the H-atom donation is the preferred reaction of curcumin at pH ≤ 7 and in nonprotic solvents. Curcumin undergoes proton-transfer equilibria with pK_{a1} = 8.55 and pK_{a2} = 10.41. The ionized curcumin is more water soluble and it is expected to be a better electron donor than the unionized form. On the other hand unionized curcumin may exist in the keto form and this form predominates in acidic and neutral aqueous solutions. In the keto form of curcumin, heptadienone linkage between the two methoxy phenol rings contains a highly activated carbon atom. It is obvious that the C–H bonds on this carbon should be very weak, due to delocalization of the unpaired electron on the adjacent oxygens, the radical formed by hydrogen atom donation may take the following resonance structures:

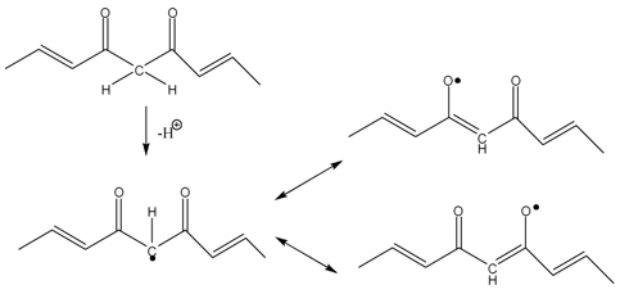

It is therefore suggested that the central –CH_2– group can serve as an H-atom donor in curcumin oxidations in acidic medium.

It is conceivable that in the present reaction system, sulphate radical anions generated in the initiation step, react with curcumin forming curcumin radicals. These radicals are formed by an H-atom donation by curcumin to sulphate radical anion. Spectral measurements have shown that curcumin absorbs substantially at 254 nm and the molar absorption coefficient has been found to be 10255 dm^3·mol^{-1}·cm^{-1} at this wavelength. It is therefore possible that in the present reaction system there

exists a competition between peroxydisulphate and curcumin for light absorption at 254 nm. As no photochemical change occurs in curcumin in the absence of peroxydisulphate, it is postulated that the photoexcited curcumin molecule transfers its energy to peroxydisulphate in a fast step and as a result peroxydisulphate becomes activated leading to the generation of sulphate radical anions.

Table 1. Effect of [PDS], [curcumin] and light intensity on the rates and quantum yields of oxidation of curcumin by sulphate radical anion $SO_4^{\bullet-}$ in aqueous-acetonitrile solution 1:3 (v/v). pH = 7.5, T = 300 K.

$[PDS]\times10^4$ mol·dm^{-3}	$[curcumin]\times10^5$ mol·dm^{-3}	intensity$\times10^{-15}$ photons s^{-1}	Rate$\times10^8$ mol·dm^{-3}s^{-1}	ϕ
2.00	5.00	2.16	2.90	2.62
4.00	5.00	2.16	5.58	2.58
8.00	5.00	2.16	9.00	2.08
10.00	5.00	2.16	10.1	2.00
4.00	2.00	2.16	4.00	0.752
4.00	1.00	2.16	2.36	0.230
4.00	0.500	2.16	1.53	0.080
4.00	0.100	2.16	0.34	0.005
5.00	5.00	2.16	6.74	2.45
5.00	5.00	2.55	8.13	2.55
5.00	5.00	3.14	10.8	2.70

The increase in quantum yield with increase in [curcumin] also supports this contention. It is likely that the excited state of curcumin is a triplet state as observed in the study of curcumin derived transients by Gorman *et al.* [9] who observed that laser excitation of curcumin led to the formation of triplet state with a life time of 1.5 μs. The quantum yield has been calculated using the intensity of light absorbed by peroxydisulphate at 254 nm.

In view of the above discussion, the mechanism of photooxidation of curcumin in the presence of peroxydisulphate may be described by the following scheme:

$$S_2O_8^{2-} \xrightarrow{h\nu} SO_4^{\bullet-}$$

$$\text{curcumin} \xrightarrow{h\nu} \text{curcumin*}$$

$$\text{curcumin*} + S_2O_8^{2-} \longrightarrow \text{curcumin} + 2SO_4^{\bullet-}$$

$$\text{curcumin} + SO_4^{\bullet-} \rightleftharpoons [\text{complex}]$$

$$[\text{complex}] \longrightarrow \text{curcumin}^{\bullet} + HSO_4^-$$

$$2\ \text{curcumin}^{\bullet} \longrightarrow \text{Dimer of curcumin}$$

The curcumin radical is formed as a transient by the hydrogen atom donation from the central -CH_2- group of curcumin to $SO_4^{\bullet-}$. The curcumin radicals further combines leading to the formation of dimer. The above proposed reaction scheme receives support from spectroscopic data. The formation of dimer as the product receives support from UV-visible spectrum of the product and also from mass spectral data of the product. The UV-visible spectrum of the product dimer is similar to the one reported by Masuda *et al.* [10]. Formation of cur-cumin dimer is further supported by mass spectral data evidencing the molecular ion with m/z value of 734 (Fig. 2).

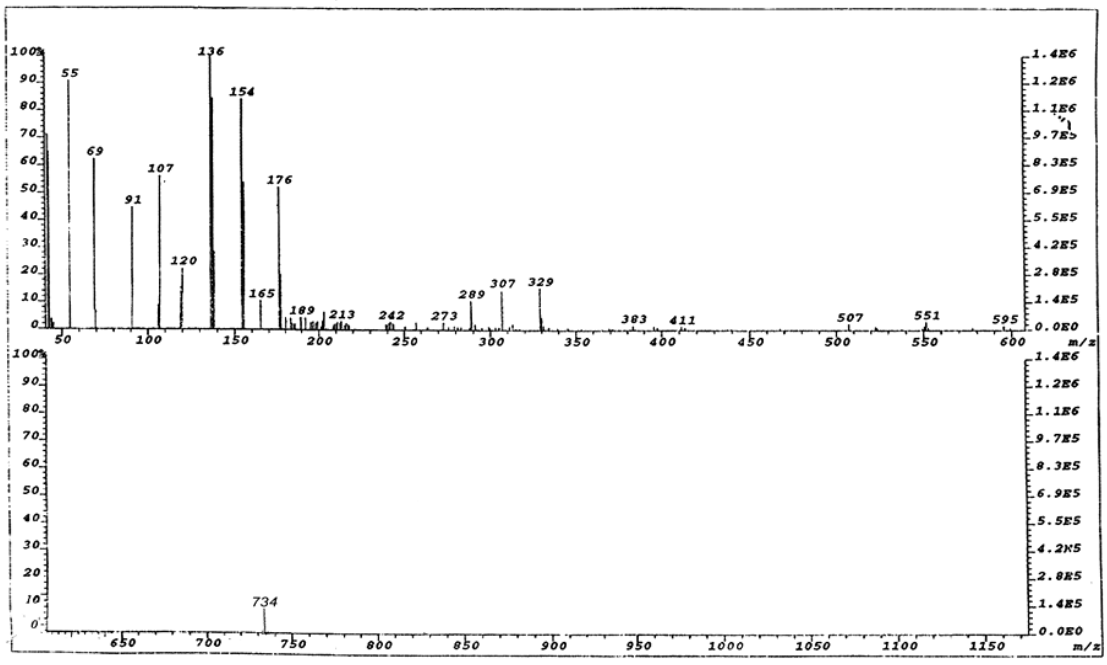

Fig. 2. Mass spectra of curcumin dimer.

REFERENCES

1. O. I. Auroma, *J. Am. Oil Chem. Soc.,* **75***,* 1999 (1988).
2. N. Venkatesan, *Br. J. Pharmacol.,* **124**, 425 (1998).
3. V. Rajakrishnan, P. Viswanathan, K. N. Rajsekaran, G. Gunashekaran, V. P. Menon, *Med. Sci. Res.,* **26**, 715 (1998).
4. A. Kahfif, S. P. Schantz, T. C. Chou, D. Edelstein, P.G. Sacks, *Carcinogenesis,* **19**, 419 (1995).
5. R. J. Anto, G. Kuttan, K. V. D. Babu, K. N. Rajsekaran, *Int. J. Pharm.,* **131**, 1 (1996).
6. E. Kuchandy, M. N. A. Rao, *Int. J. Pharm.,* **58**, 237 (1990).
7. M. Subramanian, M. N. A. Rao, P. A. T. Devasagayam, B. B. Singh, *Mutation. Research.,* **311**, 249 (1994).
8. S. V. Jovanovic, S. Steenken, W. C. Boone, M. Simic, *J. Am. Chem. Soc.,* **121**, 9677 (1999).
9. A. S. Gorman, I. Hamblett, V. S. Srinivasan, P. D. Wood, *Photochem. Photobiol.,* **59**, 389 (1994).
10. T. Masuda, K. Hidaka, A. Shinohara, T. Maeckawa, Y. Tekada, H. Yamaguch, *J. Agric. Food. Chem*., **47**, 71 (1990).

КИНЕТИКА И МЕХАНИЗЪМ НА ОКИСЛЕНИЕ НА КУРКУМИН СЪС СУЛФАТЕН АНЙОН-РАДИКАЛ ВЪВ ВОДЕН РАЗТВОР НА АЦЕТОНИТРИЛ

С. С. Мидудхула[1], А. Мундра[2]*

[1] Департамент по химия, Университет на Османия, Хайдерабад 500 007, Индия
[2] Департамент по химия, Колеж по науки за докторанти, Сайфабад, Университет на Османия, Хайдерабад 500 004, Индия

Постъпила на 23 юни 1009 г.

(Резюме)

Проведено е фотоокисление на куркумин в присъствие на пероксидисулфат (ПДС) във воден разтвор на ацетонитрил при pH 7.5 в реактор за изследване на квантовия добив с използване на лампа с високо налягане на живачни пари. Реакциите са изследвани чрез измерване на абсорбцията при 420 nm. Началните скорости са изчислени с помощта на компютърна програма Микрокал Ориджин от зависимостите абсорбция-време на реакция. Намерено е, че скоростите на фотоокисление на куркумин с пероксидисулфат се увеличават с увеличаване на концентрациите на ПДС, на куркумин и интензитета на светлината. Зависимостите log(скорост)-log[ПДС] и log(скорост)-log[куркумин] са линейни с наклон по-малък от единица и показват дробен порядък на зависимостта на скоростта от концентрацията на ПДС и от концентрацията на куркумин. На основа на експерименталните резултати и анализа на продуктите е предложен вероятен механизъм на реакцията.

Bulgarian Chemical Communications, Volume 42, Number 2 (pp. 130–137) 2010

Preparation of low-ash-content porous carbonaceous material from rice husks

S. A. Uzunova[1]*, I. M. Uzunov[2], S. V. Vassilev[3], A. K. Alexandrova[3], S. G. Staykov[1], D. B. Angelova[1]

[1] *University of Chemical Technology and Metallurgy, 8 Kliment Ohridski Blv., 1756 Sofia; Bulgaria*
[2] *Institute of General and Inorganic Chemistry, Bulgarian Academy of Sciences, Acad. G. Bonchev St., Block 11, 1113 Sofia, Bulgaria*
[3] *Institute of Electrochemistry and Energy Systems, Bulgarian Academy of Sciences, Acad. G. Bonchev St., Block 10, 1113 Sofia, Bulgaria*

Received May 22, 2009; Revised December 18, 2009

The effect of preliminary removal of silica from raw material was studied as well as that of the use of a new activating agent (carbamide) on the properties of porous carbonaceous material, obtained by chemical activation of rice husks. Two different approaches have been applied to prepare the porous carbonaceous material of low-ash content below 1% and specific surface area above 1000 $m^2 \cdot g^{-1}$. The first one consists in pyrolysis of rice husks at 450ºC with consecutive removal of silica with hydrofluoric acid and chemical activation at 700ºC (series of samples 1S). The second approach consists in removal of silica from the raw material – rice husks with a consecutive intermediate step of pyrolysis at 450ºC and chemical activation at 700ºC (series of samples 2S). Carbamide, NaOH and $ZnCl_2$ have been used as activating agents.

It was established that the sequence of treatment of the rice husks influences the value of the specific surface area of the two precursors: 495 $m^2 \cdot g^{-1}$ (for the series 1S) and 105 $m^2 \cdot g^{-1}$ (for the series 2S) and the specific surface area of the final product depends on the kind of the applied activating agent. The samples of carbonaceous material activated using carbamide possess specific surface areas of 1259 $m^2 \cdot g^{-1}$ and 1229 $m^2 \cdot g^{-1}$, respectively, ash contents – 0.88% and 1.5%, iodine adsorption capacity – 1133 $mgJ_2 \cdot g^{-1}$ and 983 $mgJ_2 \cdot g^{-1}$ and total pore volumes 0.81 $cm^3 \cdot g^{-1}$ and 0.70 $cm^3 \cdot g^{-1}$.

Due to their high specific surface areas and low ash contents the carbonaceous materials, prepared by us, can be investigated as adsorbents, catalyst supports, active materials for electrochemical power sources, including in super capacitors and etc.

Key words: porous carbon; rice husk; activation; carbamide; surface area

INTRODUCTION

Among the adsorption materials, porous carbons can be widely used as industrial adsorbents for separation, purification, and recovery processes due to their large surface area and porosity [1–3]. Recent applications using porous carbons as an electrode material for electric double layer capacitors or super-capacitors have inspired intensive research work worldwide focused on their porous structures and electrochemical behaviour [4–7]. Various carbon-containing raw materials have been used to prepare active carbons. Special attention is paid to the processing of agricultural wastes to active carbon materials [8–10].

Several series of hard carbons, used as anodes of lithium-ion batteries, have been prepared by pyrolysis of natural or agricultural precursors such as sugar [11–13], cotton [14] and coffee beans [15]. Among these, the rice husks occupy a special position, due to their high ash content. The composition of the rice husks depends on the kind of agrotechnical activities, the soil and the climatic conditions, in the region where the rice is grown. The chemical analyses indicate that rice husks consist of lignin, cellulose and hemi cellulose. The latter is a mixture of D-xylose, L-arabinose, methylglucoronic acid and D-galactose. What is characteristic of rice is the fact that its metabolism is connected with extraction from the soil and accumulation of amorphous SiO_2, mainly in the external epidermis layer of the rice husk. Its content varies from 15 up to 22% [16, 17].

Rice husk is a by-product of the rice milling industry and it accounts for about 20% of the whole rice grain. The amount of rice husk was estimated to be approximately 500 millions of tons in developing countries [18]. In Bulgaria, the annual production of rice exceeds 28000 tons. The processing of this renewable waste into products valuable for the practice will have a double sided effect – both for the economy and for the ecology.

The initial raw material for preparing carbonaceous material in the present work was rice husks from the Pazardzhik region (harvested in 2008). The

* To whom all correspondence should be sent:
E-mail: snejanka.uzunova@gmail.com

basic requirements to active carbon materials used in electrochemical power sources, including lithium-ion accumulators and super-capacitors, are the high specific surface area, low ash content and optimum porosity [19, 20]. It is known that the specific surface area, the porosity and the ash content in the active carbon material depend on the composition and properties of the precursor materials and on the method of activation. Two general methods are used for the preparation of activated carbon [21, 22]. The first one, the physical activation, consists in heating at a high temperature in the presence of a charcoal gasification reactant (H_2O or CO_2). The other method, chemical activation, consists of heating at a relatively lower temperature with the addition of a dehydration agent (e.g., H_3PO_4, $ZnCl_2$). Nowadays, there is a great interest in the alkali hydroxide activation process for the production of activated carbons [23]. The application of these activating agents to the preparation of carbon materials from rice husks leads to the obtaining of final products having high ash content, which is connected both with the chemistry of the process of activation and with the high ash content of the rice husks [24, 25]. Most of the authors, who have published results of their studies on the preparation of carbon materials of high specific surface area from rice husks, do not discuss the problem of the ash content in the raw material and in the final product [26]. Some of the authors have shown that micro quantities of silica in the carbon material influence favourably in case of using it into electrochemical power sources [27, 28].

With purpose to prepare a low ash content porous carbonaceous material, we removed in advance the main inorganic component of the rice husk composition. The removal of silica was carried out by treatment with hydrofluoric acid. The aim of the present work was to obtain porous carbon material with optimal characteristics (high specific surface area and low ash content) using two different approaches for processing of the rice husks and various activating agents. The first approach consists in the removal of silica from the rice husks pyrolysed in advance, followed by the consecutive step of chemical activation (series of samples 1S). The second approach is based on removal of silica from the raw rice husks and consecutive steps of intermediate pyrolysis and chemical activation (series of samples 2S). The effect of the activating action of carbamide was studied and compared to that of some of the most frequently applied substances for preparing porous carbon by chemical activation – NaOH and $ZnCl_2$ [19, 23].

EXPERIMENTAL

In order to eliminate mechanical admixtures the rice husks were washed several times with hot water and dried at 110ºC for 2 hours. The intermediate pyrolysis of the rice husks is carried out in a reactor at 450ºC. The temperature of the furnace was increased linearly from room temperature up to the value needed for pyrolysis at a heating rate of 4 deg·min^{-1} and temperature retention for 3 hours. The time interval, within which the temperature was maintained constant, is defined as "time of pyrolysis". The sample was taken out after cooling first the oven down to room temperature (samples 1S1 and 2S2).

The removal of SiO_2 was accomplished by treatment of the rice husks with 40% HF acid and washing with deionized water to reach pH 6.5 (samples 1S2 and 2S1). The process of activation was carried out by preliminary treatment of the precursors 1S2 and 2S2 with the activating agent at a ratio C:activator equal to 1:5 for $(NH_2)_2CO$ and $ZnCl_2$ and 1:4 for NaOH. The samples, prepared in this way, were carbonized in the absence of air at a temperature of 700ºC in the course of 1 hour.

The samples 1S3 and 2S3 were obtained using activator urea, the samples 1S4 and 2S4 – with activator NaOH and the samples 1S5 and 2S5 with activator $ZnCl_2$. After cooling the samples 1S4 and 2S4 were washed with hot deionized water to reach pH 6.5 and then dried at 110ºC. Aiming at removal of the ash residual the samples 1S5 and 2S5 were treated with hydrochloric acid (1:1) in hot state, upon refluxing for 1 hour. After removal of the acid, the samples were washed with hot deionized water to reach pH 6.5 and dried at 110ºC.

The phase composition was determined by a Philips ADP 15 diffractometer using CuK_α radiation. The infrared spectra were recorded on a Nicolet-320 FTIR spectrometer in a tablet of KBr. The measurement of the specific surface area by the BET method was carried out on an Area Meter, Strolein apparatus. The porous structure of the samples was measured by mercury intrusion porosimetry. The measurements were perfomed with an apparatus AutoPore 9200, MICROMERITICS. The thermal analysis was carried out on a SETARAM *Labsys Evo* apparatus in a corundum crucible at a heating rate of 10 deg·min^{-1} in air medium.

Carbon and hydrogen amounts in raw rise husks were determined by the so-called high-speed method of analysis. The method consists in burning of the sample into an oxygen flow. The semi-quantitative atomic emission spectral analysis with

excitation in direct current arch was accomplished on a spectrograph PGS, Germany. The admixtures of alkali elements and iron in the rice husks were determined by flame atomic absorption spectrometer SOLAR M5, Thermo. The ash content in the carbon materials was determined based on the Bulgarian standard method [29]. The iodine adsorption capacity was determined by titration of the residual solution of 10 ml with 0.1 N $Na_2S_2O_3$ in the presence of 1 ml of 1% starch solution as an indicator. The iodine adsorption capacity was determined based on the adsorbed iodine per mass unit of the adsorbent at the residual iodine concentration of 0.02 N [30].

RESULTS AND DISCUSSION

The complex thermal analysis (DTA, TG) Fig. 1 reveals the occurrence of an endothermal process up to 120ºC, connected with the liberation of moisture from the rice husks, amounting to 5%. The exothermal process, which takes place within the interval 260–493ºC, is characterized by a maximum at 348ºC, which is associated with thermal degradation of the organic components included in the the rice husks and transformation of the lignin cellulose material into carbon. There follows combustion of the carbon residue and this process is reflected in the curve by a maximum аш 454ºC.

The ash content in the carbon material depends on the quantity of inorganic admixtures in the initial raw material and on the way of activation of the material. The quantity of ash in the rice husks, used by us, amounts to 21% and as it can be seen from the data listed below, the ash contains also some other inorganic substances, in addition to the silica. The organic elemental analysis carried out reveals composition of the rice husks as shown on Table 1. According to these data, the organic component in the rice husks amounts to about 79%.

The semi-quantitative composition of the initial raw material was determined by emission spectral analysis (Table 2a). The quantity of the admixtures of sodium, potassium and iron in the rice husks was evaluated by atomic absorption analysis (Table 2b). The specific surface area of the raw rice husks, determined by the B.E.T. method is about 4 $m^2 \cdot g^{-1}$.

Figures 2a and 2b represent the data of the IR-spectroscopy analysis of the raw rice husks and the series of samples 1S (a) and 2S (b). The observed absorption bands in the spectrum of the 2S1 (Fig. 2b) reflect the changes, occurring in the phase composition of the rice husks as a consequence of their treatment with HF acid. Although it is a weak acid, the hydrofluoric acid causes partial hydrolysis of the lignin-cellulose material, building up the rice husks. In parallel to this process, the acid interacts actively with the silica, whose amount in the rice husks, used by us, amounts to 21%.

Table 1. Elemental organic analysis of raw rice husks.

Sample, mg	H_2O, mg	CO_2, mg	H, %	C, %	Residue, mg
5.980	2.350	8.600	4.305	38.400	1.270

Table 2a. Amount of some metallic ingredients as oxides in raw rice husk.

Ca, $\mu g \cdot g^{-1}$	Mn, $\mu g \cdot g^{-1}$	Mg, $\mu g \cdot g^{-1}$	Zn, $\mu g \cdot g^{-1}$	Cu, $\mu g \cdot g^{-1}$
$< 1 \times 10^2$	$n \times 10^1$	$n \times 10^1$	$< 1 \times 10^1$	$\sim 1 \times 10^1$

Table 2b. Amount of alkali and iron in raw rice husk.

Element	Quantity, $\mu g \cdot g^{-1}$
Na	370 ± 10
K	580 ± 10
Fe	330 ± 10

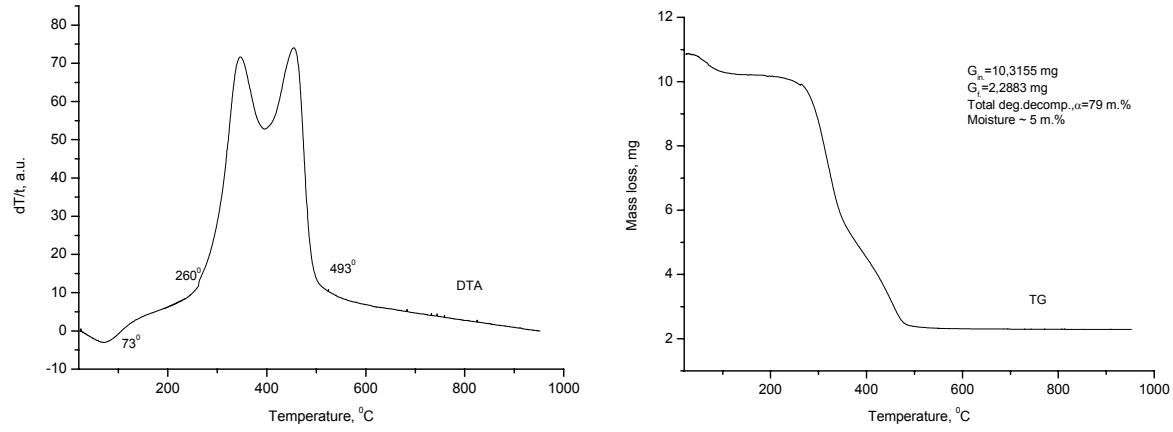

Fig. 1. Thermal analysis (DTA and TG) of raw rice husks.

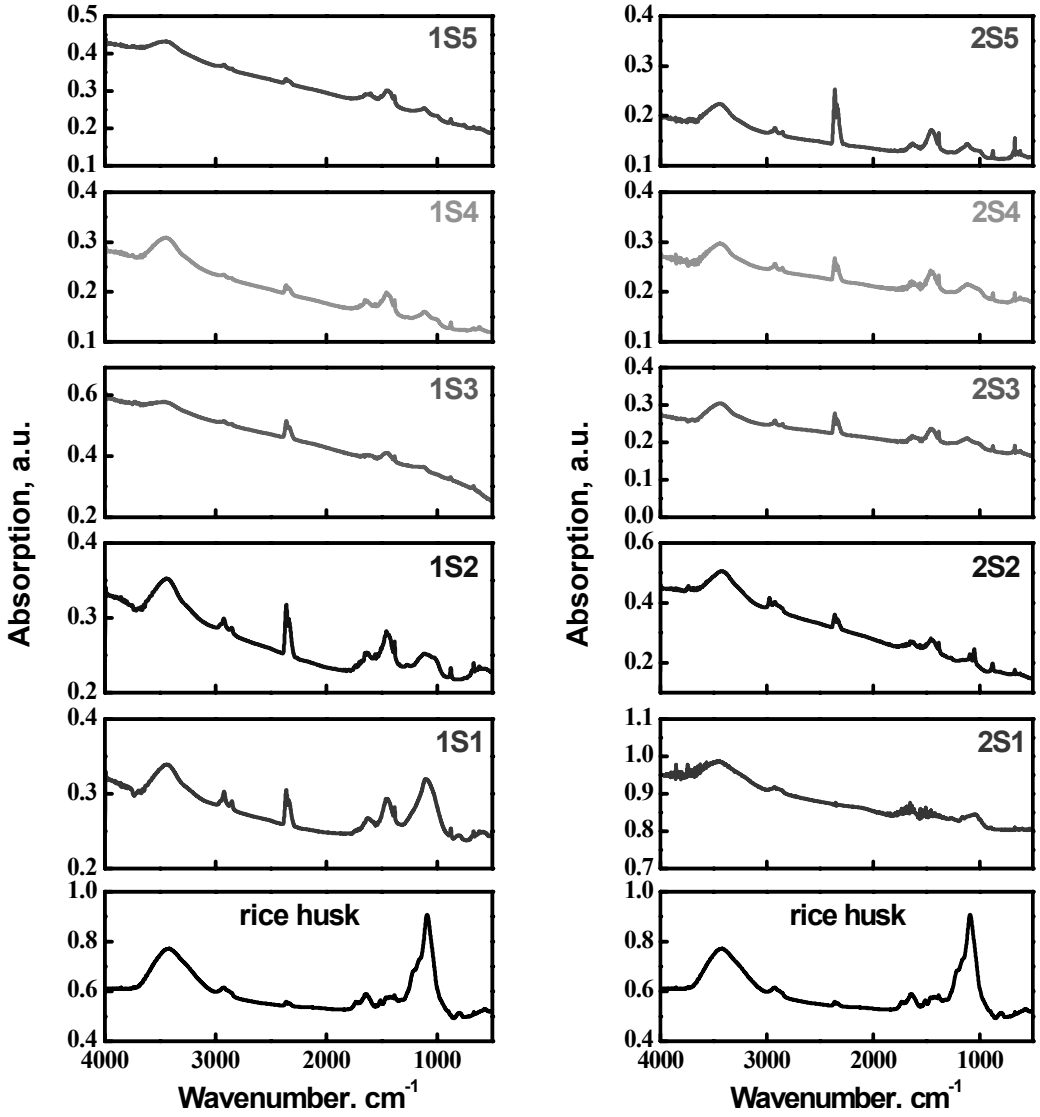

Fig. 2a, b. IR absorption spectra of raw rice husks (RH) and series of samples 1S (a) and 2S (b).

The bands in the interval 1350–1480 cm^{-1} can be attributed to be specific features, connected with the hydrocarbon structure of the rice husks. The absorption bands at 1733 and 1635 cm^{-1}, as well as the one at 1512 cm^{-1}, are due to stretching vibrations of the double bond C=O in the structure of the lignin-cellulose material. The absorption at 1425 and 1454 cm^{-1} is connected with bending vibrations of the bond C=O in the carboxylic groups, which depend on the presence of a metallic ion in the compound.

The presence of hydrated SiO_2 in the structure of the rice husks is proved by the bands in the low wavelength region of the spectrum (470–790 cm^{-1}), as well as by the intensive band at 1089 cm^{-1} with shoulders at 1159 and 1208 cm^{-1}. These are bands, typical of the two low-temperature forms of SiO_2 – tridymite and crystobalite [31].

The extraction of SiO_2 as a result of its interaction with HF acid leads to change in the IR-spectrum of the rice husks. This fact can be explained by partial hydrolysis of the lignin-cellulose material, as well as by processes of destruction, associated with the extraction of biogenic SiO_2. Its reaction with HF leads to disruption of its bonds with monosaccharides included in the composition of the rice husks. The basic bands of the two modifications of silica are missing in the spectrum of the acid treated material. The evidence for the SiO_2 still present in the structure of ash-purified material are the bands at 1038 cm^{-1}, attributed to elastic vibrations of the bond Si–O–C [32, 33], the one at 1456 cm^{-1}, due to vibrations of the bond C=O in the carboxyl groups, depending on the presence of Si, as well as the band at 1158 cm^{-1}, connected with the asymmetric vibrations of the siloxane bond Si–O–Si. In the spectrum of the rice husks, treated with hydrofluoric acid, there appears a new absorption band at 895 cm^{-1}, associated with, as well as the wide band at 1652 cm^{-1}, with stretching mode of the

bonds C–O–H and C=O of the acid-hydrolysed hydrocarbon composition of the material. The weak band at 1271 cm^{-1} is also connected with the C=O bond vibrations. The wide band with a maximum at 2924 cm^{-1} and a shoulder at 2867 cm^{-1}, which are present also in the spectrum of the raw rice husks, are connected with the methyl groups included in the composition of the husks. The hydroxyl groups of the structure of polysaccharides and lignin, as well as those of the chemisorbed water, are associated with the wide band at 3445 cm^{-1}.

The pyrolysis of the sample 2S1 implies thermal destruction of a large part of the lignin-cellulose material, which results in increase of the concentration of the SiO_2 remaining in the structure of the rice husks. As a consequence of this, there appear bands in the low wavelength region of the IR-spectrum, which are characteristic of crystobalite. The shape of the wide band in the region 1000–1200 cm^{-1} is changed. Among the group of bands, characteristic of the raw rice husks, again the one at 1383 cm^{-1} appears, connected with the presence of $–CH_3$ groups. The presence of $–CH_2$ and $–CH_3$ groups in the composition of pyrolysed material is associated with the band at 1449 cm^{-1}. Other absorption bands are also observed, characteristic of the acid-treated material.

The comparison of the spectra of the activated products with the spectrum of the precursor (2S2) shows that whatever the kind of the activating agent is and in spite of the increase of the temperature of calcination no changes occur in the phase composition of the material. This shows that the preliminary pyrolysis of the rice husks at 450ºC involves the building of a stable phase structure. The application of activating agents leads only to change in the value of the specific surface area and in the porous structure of the carbonaceous material.

The thermal destruction of rice husks at 450ºC (sample 1S1, Fig. 2a) leads to change in the phase composition of the material. The group of bands in the interval 1350–1730 cm^{-1} characteristic of the raw rice husks disappears. Other absorption bands appear having maxima at 1383, 1454 и 1626 cm^{-1}. The strongest band in the spectrum of raw rice husks with a maximum at 1089 cm^{-1} decreases its intensity in the spectrum of the pyrolysed husks as a consequence of the destruction of the hydrocarbon component. In principle this band is typical of tridymite, but it is also connected with vibrations of the C-OH bond and it is characteristic of the C–O–C type of structure of the material.

The treatment of the 1S1 sample with HF acid leads to removal of SiO_2 from the composition of the material, but it does not eliminate the other inorganic compounds. Some weak bands are still observed in the spectrum of the sample 1S2 in the low wavelength region, accounting for the presence of Me–O bonds. Fig. 3a, 3b represents the XRD patterns of raw rice husks and those of the sample series 1S (3a) and 2S (3b).

The XRD data are typical of lignin-cellulose material (RH). The double diffraction maximum reveals the presence of cellulose, while the broadening of the peak is connected with the lignin component and with the hydrated amorphous silica, contained in the rice husks [33, 34].

In the XRD patterns of the precursors 1S2, 1S2, as well as in those of the activated materials two widely stretching peaks are observed – at about 24º and at 42.8º. The broad peak at 2θ value of 24º is representing the (002) graphite basal plane. The weaker broad peak at 43º indicates that the (100) and (101) peaks have merged to yield a single reflection demonstrating a relatively higher degree of randomness in the materials. In the pattern of 2S2 precursor the second peak is not so well defined as in the activated materials 2S3, 2S4 and 2S5. Most probably this peak correlates with the greater activated surface of the carbon materials. In the cases of the samples 2S2 and 2S3 the presence of elemental silicon is observed. This can be explained by the nature of the starting material as well as by the conditions of preparation of the sample 2S3.

The change in the value of the specific surface area, the sorption capacity with respect to iodine, the ash content and the pore volume in the process of treatment and activation of the rice husks are represented in Table 3.

Depending on the sequence of the treatment steps of the rice husks precursors are obtained having different specific surface area: 495 $m^2 \cdot g^{-1}$ (1S2), in the cases when the pyrolysis is carried out before the treatment with HF acid and 105 $m^2 \cdot g^{-1}$ (2S2), when the HF acid treatment precedes the pyrolysis. After elimination of the silica the specific surface area of the rice husks grows up to seven times higher value and after the pyrolysis – up to twenty times higher. The activation with carbamide, NaOH and $ZnCl_2$ results in an increase of the specific surface area up to thirteen times. The highest specific surface area was displayed by the samples, obtained by activation with carbamide and NaOH. The materials activated with carbamide, 2S3 and 1S3, have low ash content. This is due to the fact that the carbamide is decomposed without leaving any residual at the temperature of activation. Moreover, the carbamide is often used in its quality of pyrogenic agent in the case of preparation of substances with a definite morphology [36].

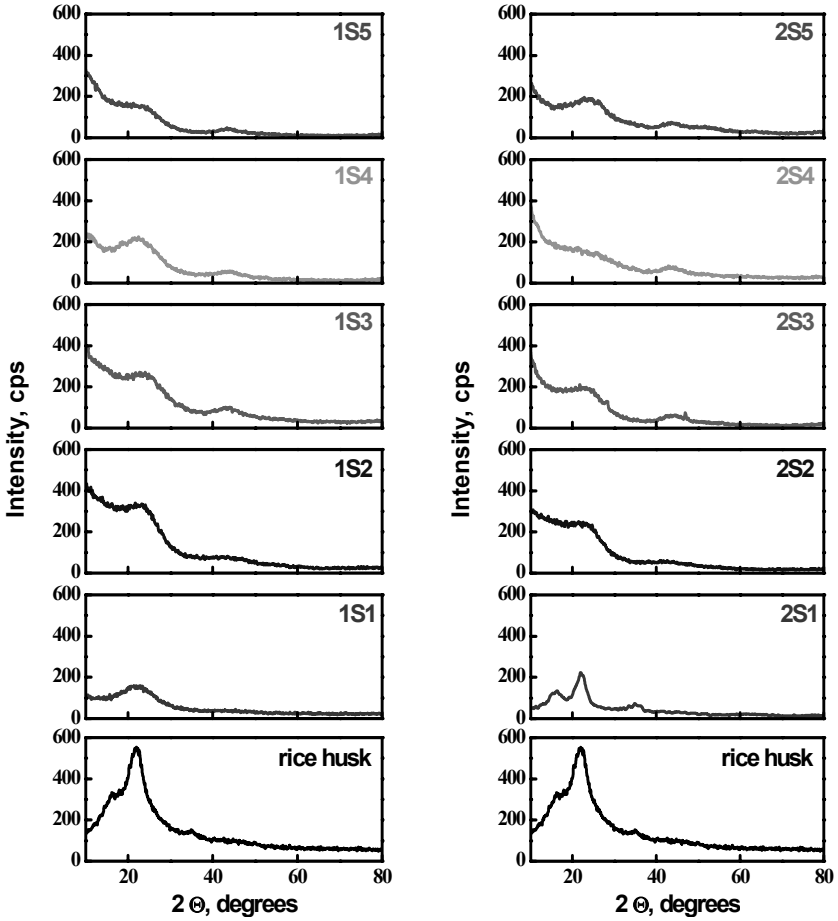

Fig. 3. XRD pattern of raw rice husk (RH) and of the samples 1S (a) and 2S (b).

Table 3. The pore volume, ash content, B.E.T. surface area and adsorption capacities of 2S and 1S series.

Sample code	Treatment conditions	Specific surface area, B.E.T., $m^2 \cdot g^{-1}$	Adsorption capacity, $mgJ_2 \cdot g^{-1}$	Ash content, %	Pore volume, $cm^3 \cdot g^{-1}$			
					Micro	Meso	Macro	Total
1S1	Pyrolysis	70	115	44	-	-	-	-
1S2	Desilicification	495	544	0.46	-	-	-	-
1S3	Activation with urea	1229	983	1.5	0.44	0.03	0.23	0.70
1S4	Activation with NaOH	1264	1028	18	0.62	0.08	0.04	0.74
1S5	Activation with $ZnCl_2$	1206	1085	2.0	0.34	0.27	0.12	0.73
2S1	Desilicification	5	-	0.34	-	-	-	-
2S2	Pyrolysis	105	120	0.84	-	-	-	-
2S3	Activation with urea	1259	1113	0.88	0.48	0.06	0.27	0.81
2S4	Activation with NaOH	1273	1018	20	0.60	0.11	0.08	0.79
2S5	Activation with $ZnCl_2$	888	844	4.8	0.24	0.31	0.13	0.68

It is known that the carbonization at higher temperature leads to formation of less stable and inactive carbon structure, which is connected with the presence of small quantities of oxygen-containing groups, due to which the materials have low porosity [26].

The probable mechanism of activation of the carbon material is associated with the interaction of carbamide with the OH and COOH groups, whereupon the $–NHCONH_2$ and the $–CONHCONH_2$ groups are being obtained. The latter groups at a temperature of 700ºC and in the absence of air decompose into NH_3 and CO_2. Thereupon part of the nitrogen of the carbamide can be included in the structure of the carbon, forming the so called diazo groups (–N=N–). A more detailed insight into the mechanism of activation of the pyrolysed carbon material with carbamide (with removal of the ash in advance) will be the subject of our future investigation.

The higher ash content of the samples, obtained using sodium hydroxide (S4), is connected with the specific mechanism of activation in this case. The carboxylic acids and methoxy phenols, obtained

during the preliminary pyrolysis of the rice husks, interact with NaOH whereupon the respective sodium salts are being obtained. It is also possible that a reaction is occurring between the alkaline base and the silica that still remains in the material.

The decrease in the ash content of the samples, obtained using $ZnCl_2$ after their treatment with hydrochloric acid (S5), shows that in the process of activation the zinc chloride in its quality of Lewis acid probably plays the role of a catalyst.

The experimental results prove that the sequence of the treatment steps of the rice husks does not affect the value of the specific surface area of the samples, prepared by activation with carbamide and NaOH, while the area of the samples, obtained by activation with $ZnCl_2$ depends on the treatments steps sequence. This effect is probably due to differences in the mechanism of activation when using different substances [37].

The sorption capacity of the carbon materials with respect to iodine grows up with the increase of the BET specific surface area in a way, which is not proportional. The obtained results can be explained based on a decrease in the pore radius with the increase of the specific surface area. Taking into account the fact that the area, occupied by the adsorbed nitrogen molecule (16.2 $Å^2$), is smaller than the area, occupied by the iodine molecule (27.0 ± 10 $Å^2$) and that the diameters of the pores of the carbon materials for adsorption of the two molecules are greater than 0.4 and 0.6 nm respectively, then we can state that with the increase of the specific surface area the number of micropores with dia-meter below 0.6 nm is increased too.

The total pore volume of the obtained carbon materials varies from 0.68 up to 0.81 $cm^3 \cdot g^{-1}$ and it grows up with the increase of the specific surface area. The greater volume of the macropores of the materials, activated with carbamide, is connected with the more intensive gas evolution in the case of using this activating agent.

The obtained results have practical importance in view of selecting the appropriate activating agent for synthesis of carbonaceous materials with variety of morphology, which can find a different usage in the practice.

CONCLUSION

The results of the investigation carried out show the effect of preliminary removal of silica and the use of urea as activating agent on the specific surface area and on the ash content of porous carbon materials, obtained from rice husks. The sequence of the treatment steps of rice husks influences considerably the value of the specific surface area of the precursors. In the cases of applying carbamide and NaOH as activating agents, the treatment sequence does not affect the surface area of the final product. Some influence on the value of this parameter is observed only in the case of using $ZnCl_2$ as activating agent.

The samples of carbon material, activated with carbamide, possess the highest specific surface area – 1259 $m^2 \cdot g^{-1}$ and 1229 $m^2 \cdot g^{-1}$, the lowest ash content – below 2%, iodine adsorption capacity 1133 $mgJ_2 \cdot g^{-1}$ and 983 $mgJ_2 \cdot g^{-1}$ and total pore volume is 0.81$cm^3 \cdot g^{-1}$ and 0.70 $cm^3 \cdot g^{-1}$.

The carbon materials, activated with carbamide, have larger volume of macropores in comparison to the rest of the carbon materials, due to intensive evolution of gas during the decomposition of carbamide in the course of activation treatment.

In view of the high specific surface area and the low ash content, the carbon materials, prepared by us, can find a practical application in all fields in which active carbons are used. It is clear that a practical application is a subject of thorough investigations for every specific case of usage of these materials.

Acknowledgements: *The authors gratefully acknowledge the financial support by the Bulgarian Science Foundation (Contract TKH-1705/07) and the National Centre for Advanced Materials UNION.*

REFERENCES

1. D. F. Quinn, J. A. Macdonald, *Carbon*, **30**, 1097 (1992).
2. O. N. Kononova, A. G. Kholmogorov, A. N. Lukianov, *Carbon*, **39,** 383 (2001).
3. S. A. Dastgheib, D. A. Rockstraw, *Carbon,* **39**, 1849 (2001).
4. H. Shi, *Electrochim. Acta*, **41**,1633 (1996).
5. G. Salitra, A. Soffer, L. Eliad, Y. Cohen, *J. Electrochem. Soc.*, **147**, 2486 (2000).
6. C. T. Hsieh, H. Teng, *Carbon*, **40**, 667 (2002).
7. H. Teng, Y. Chang, C. T. Hsieh, *Carbon*, **39**, 1981 (2001).
8. J. Dias, M. Alvim-Ferraz, M. Almeida, J. Rivera-Utrilla, M. Sanchez-Polo, *J. Environ. Management*, **85**, 833 (2007).
9. O. Ioannidou, A. Zabaniotou, Renew. Sustain. Energ. Rev., **11**, 1966 (2007).
10. V. Minkova, G. Angelova, M. Goranova, L. Ljutzkanov, V. Litchev, Bulg. Chem. Commun., **23**, 85 (1990).
11. W. Xing, J. S. Xue, J. R. Dahn, *J. Electrochem. Soc.*, **143**, 3046 (1996).
12. A. Gibaud, J. S. Xue, J. R. Dahn, *Carbon,* **34**, 499 (1996).
13. W. Xing, R. A. Dunlap, J. R. Dahn, *J. Electrochem. Soc.*, **145**, 62 (1998).

14. E. Peled, V. Eshkenazi, Y. Rosenberg, *J. Power Sources*, **76**, 153 (1998).
15. S. Yamada, H. Imoto, K. Sekai, M. Nagamine, in: Proc. 191st Meeting of the Electrochemical Society, May 1997, Montreal, Canada, p. 85..
16. J. A. Amick, *J. Electrochem. Soc.*, **129**, 864 (1982).
17. N. K. Sharma, S. Williams, Z. Zangwil, *J. Amer. Ceram. Soc.*, **67**, 715 (1984).
18. UN Food and Agriculture Organization (FAO); http://faostat.fao.org .
19. Y. Guo, J. Qi, Y. Jiang, S. Yang, Z. Wang, H. Xu, *Mater. Chem. Phys.*, **80**, 704 (2003).
20. G. T.-K. Fey, Ch.-L. Chen, *J. Power Sources*, **97-98**, 47 (2001).
21. J. Laine, S. Yunes, *Carbon*, **30**, 601 (1992).
22. Z. Hu, M. Srinivasan, Y. Ni, *Carbon*, **39**, 877 (2001).
23. D. Lozano-Castello, M. A. Lillo-Rodenas, D. Cazorla-Amoros, A. Linares-Solano,*Carbon*, **39**, 741 (2001).
24. Y. Guo, K. Yu, Z. Wang, H. Xu, *Carbon*, **41**, 1645 (2000).
25. D. Kalderis, S. Bethanis, P. Paraskeva, E. Diamadopoulos, *Bioresour. Technol.*, **99**, 6809 (2008).
26. C. Yun, Y. Park, C. Park, *Carbon*, **39**, 559 (2001).
27. A. Wilson, J. Dahn, *J. Electrochem. Soc.*, **142**, 326 (1995).
28. J. Xue, K. Myrtle, J. Dahn, *J. Electrochem. Soc.*, **142**, 2927 (1995).
29. BDS ISO 1171.
30. ASTM D 3860-89a.
31. A. Vlasov, V. Florinskaya, A. Venediktov, K. Dutova, V Morozov, E. Smirnova, Infrared Spectra of Inorganic Glasses and Crystals, Khimiya, Leningrad, 1972, Ch. 1.
32. A. A. M. Daifullah, B. S. Girgis, H. M. H. Gad, *Mater. Lett.*, **57**, 1723 (2003).
33. W. Nakbanpote, B. Goodman, P. Thiravetyan, *Colloids Surf. A*, **304**, 7 (2007).
34. S. Hanna, L. Farag, N. Mansour, *Thermochim. Acta*, **81**, 77 (1984).
35. L. Kennedy, J. Vijaya, G. Sekaran, *Mater. Chem. Phys.*, **91**, 471 (2005).
36. W. Yang, G. Zhang, J. Xie, L. Yang, Q. Liu, *J. Power Sources*, **81-82**, 412 (1999).
37. O. Gyu, P. Chong, *Fuel*, **81**, 327 (2002).

ПОЛУЧАВАНЕ НА НИСКОПЕПЕЛЕН ПОРЕСТ ВЪГЛЕРОДЕН МАТЕРИАЛ ОТ ОРИЗОВИ ЛЮСПИ

С. А.Узунова[1]*, И. М. Узунов[2], С. В. Василев[3], А. К. Александрова[3], С. Г. Стайков[1], Д. Б. Ангелова[1]

[1] Химикотехнологичен и металургичен университет, бул. „Климент Охридски“ № 8, 1756 София
[2] Институт по обща и неорганична химия, Българска академия на науките, ул. „Акад. Г. Бончев“, бл. 11, 1113 София
[3] Институт по електрохимия и енергийни системи, Българска академия на науките, ул. „Акад. Г. Бончев“, бл. 10, 1113 София

Постъпила на 22 май 2009 г.; Преработена на 18 декември 2009 г.

(Резюме)

Изследвано е влиянието на предварителното отстраняване на силициевия диоксид от изходната суровина и използването на нов активиращ агент (карбамид) върху свойствата на порест въглероден материал, получен чрез химично активиране на оризови люспи. Използвани са два различни подхода за получаване на порест въглероден материал с ниско пепелно съдържание, под 1% и специфична повърхност над 1000 $m^2 \cdot g^{-1}$. Първият се състои в пиролиз на оризови люспи при 450ºC с последващо отстраняване на силициевия диоксид с флуроводородна киселина и химическа активация при 700ºC (серия проби 1S). Вторият – в отстраняване на силициевия диоксид от суровите оризови люспи с последваща междинна пиролиза при 450ºC и химическа активация при 700ºC (серия проби 2S). Като активиращи агенти бяха използвани карбамид, NaOH и $ZnCl_2$.

Установено бе, че последователността на обработка на оризовите люспи влияе върху специфичната повърхност на двата прекурсора: 495 $m^2 \cdot g^{-1}$ (за серия 1S) и 105 $m^2 \cdot g^{-1}$ (за серия 2S) и специфичната повърхност на крайния продукт в зависимост от вида на използвания активиращ агент. Пробите от въглероден материал активирани с карбамид притежават съответно: специфична повърхност 1259 $m^2 \cdot g^{-1}$ и 1229 $m^2 \cdot g^{-1}$; пепелно съдържание 0.88% и 1.5%; сорбционен капацитет на J_2 1133 $mgJ_2 \cdot g^{-1}$ и 983 $mgJ_2 \cdot g^{-1}$; общ обем на порите 0.81 $cm^3 \cdot g^{-1}$ и 0.70 $cm^3 \cdot g^{-1}$.

Поради високата си специфична повърхност и ниско пепелно съдържание получените от нас въглеродни материали могат да се изследват като адсорбенти, носители на катализатори, активни материали за електрохимични източници на ток, включително и в суперкондензатори.

Bulgarian Chemical Communications, Volume 42, Number 2 (pp. 138–140) 2010

Areas of ionic, electronic and mixed conductivity in Nb/Nb_2O_5/electrolyte system

Chr. A. Girginov[1], A. S. Zahariev[2], A. A. Girginov[1]*

[1] *Department of Physical Chemistry, University of Chemical Technology and Metallurgy, 8 Kliment Ohridski Blv., 1756 Sofia, Bulgaria*

[2] *Department of Chemistry, Technical University of Sofia, 8 Kliment Ohridski Blv., 1000 Sofia, Bulgaria*

Received July 6, 2009

The ionic (J_i) and electronic (J_e) current components of the total current density through the (+)Nb/Nb_2O_5/electrolyte systems as well as the total current density are calculated using the respective expressions describing the dependence of current on field strength. The areas of electronic, mixed and ionic conductivity during the anodic film growth of (+)Nb/Nb_2O_5/electrolyte system are determined. The current efficiency during the anodic film growth is calculated and it is presented as a function of the total current density as well. A dependence of the areas of mixed conductivity and of current efficiency on the nature of the electrolyte solution is found out.

Key words: anodic Nb_2O_5 film, electric conductivity, current efficiency.

INTRODUCTION

The current (J) that flows in (+)metal/anodic oxide film/electrolyte systems consists of three components: $J = J_i + J_e + J_{dis}$. The ionic current (J_i) causes the growth of the anodic film by migration of ions (metal and oxygen containing ones) under the influence of the electric field applied. The electronic current (J_e) through the anodic oxide has no effect on the film growth. The dissolution current is negligible ($J_{dis} \approx 0$) upon anodization in electrolytes not dissolving the film. In all cases, the ionic conductivity is investigated at high current densities (at very high field strengths, respectively). Under these conditions, validation of the so called high field approximation takes place. Moreover, the electronic current density in this case is very low, hence the total current is equal to the ionic one ($J \approx J_i$).

The dependence of the ionic current on the electric field strength $J_i(E)_T$ is described by the Gunter-Schultze-Betz equation [1, 2]:

$$J_i = A_G.\exp(B_G E)_T \,, \qquad (1)$$

where A_G and B_G are constants depending on the metal (oxide) nature and on the temperature.

The electronic conductivity is studied usually during anodic polarization of already formed oxide films at potentials lower than the formation voltage, i.e. at comparatively low field strengths. Under such conditions the following empirical equation for the $J_e(E)_T$-dependence has been found [3]:

$$J_e = \alpha_e.\exp(\beta_e E^{1/2})_T, \qquad (2)$$

where α_e and β_e are constants depending on the nature of contact electrolyte and on the temperature. Different models [4] have been proposed to explain the mechanisms of the electronic conductivity (Schottky emission, Poole-Frenkel effect, Fowler-Nordheim tunneling). Only the Christov's model [5] explains a dependence of J_e on the nature and concentration of the contact electrolyte. In this model, the electrolyte was considered as a semiconductor and redox couples in it were assumed to play the role of electron donors.

In this work field strength areas of ionic, electronic and mixed conductivity and current efficiency are determined for the system (+)Nb/Nb_2O_5/electrolyte.

RESULTS AND DISSCUSION

Numerous data both for the ionic and for electronic conductivity in the (+)Nb/Nb_2O_5/electrolyte system have been reported in the literature [6–9]. The values of the constants in Eqn. (1) have been determined for ionic current during anodization of niobium [7]. The ionic current does not depend on the electrolyte nature. On the contrary, the electronic current depends on the nature of electrolyte and its concentration [6]. Same dependence has been found recently by Ono *et al.* [8] for the leakage current, which varies tenfold within pH 1.6–10 range during lower-voltage anodic polarization of anodized Nb in aqueous solutions with different concentration ratios of phosphoric acid and ammonia. The electronic current in the respective system has been measured [6] after anodic film formation using different contact electrolytes. Two contact electrolytes have been implemented, i.e. aqueous borate electrolyte (ABE)

* To whom all correspondence should be sent:
E-mail: assen@uctm.edu

having pH 6 and non-aqueous ammonium salycilate in dimethylformamide (AS/DMF). Two concentrations of AS/DMF have been used during measurements as well. The values of the constants in Eqns. (1) and (2) determined at 293 K are given in Table 1.

Table 1. Values of the constants in Eqns. (1) and (2).

System (+)Nb/Nb_2O_5/electrolyte				
Ionic current (Eqn. (1))		Electronic current (Eqn. (2))		
A_G, $A\cdot cm^{-2}$	B_G, $cm\cdot V^{-1}$	Electrolyte	α_e, $A\cdot cm^{-2}$	β_e, $cm^{1/2}\cdot V^{-1/2}$
1.00×10^{-12} [7]	3.40×10^{-6} [7]	ABE [6]	3.10×10^{-9}	3.07×10^{-3}
		0.1 M AS/DMF [6]	1.10×10^{-9}	2.74×10^{-3}
		0.6 M AS/DMF [6]	1.90×10^{-9}	2.83×10^{-3}

The ionic and electronic current densities are calculated using the values of the constants from Table 1 and they are presented in Fig. 1 as a function of field strength.

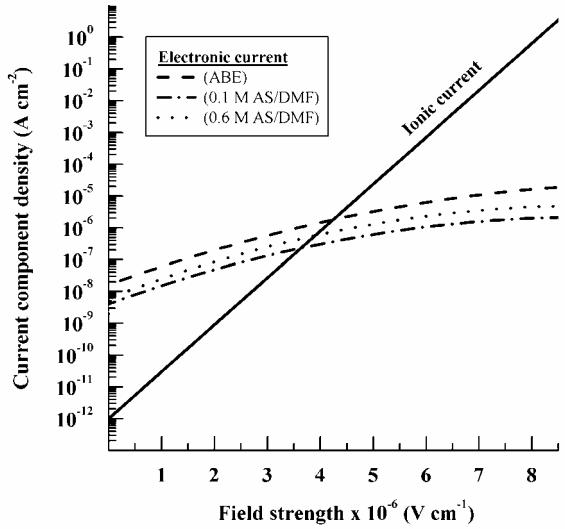

Fig. 1. Ionic and electronic current densities *vs*. field strength for the system (+)Nb/Nb_2O_5/electrolyte.

Ikonopisov and Machkova [10] have proposed that the relation of the ionic to the electronic current can be used for determining the areas of ionic, electronic and mixed conductivity. According to their conclusions, when a certain current component (ionic or electronic) is fifty times greater than the other, it could be assumed as a predominant one. In the range between $J_e = 50J_i$ and $J_i = 50J_e$ an area of mixed conductivity is observed. Since the electronic current depends on the nature and concentration of the electrolyte solution, the change of electrolyte is expected to influence the ranges of conductivity areas.

The areas of electronic, mixed and ionic conductivity are outlined for three different contact electrolytes. An example for ABE is presented in Fig. 2. The values of electric field strength limiting the mixed conductivity area are presented in Table 2. The table data reveal that the area of mixed conductivity for the system under consideration has the same value for the three electrolyte solutions. The electrolyte nature only affects the area's boundaries shift.

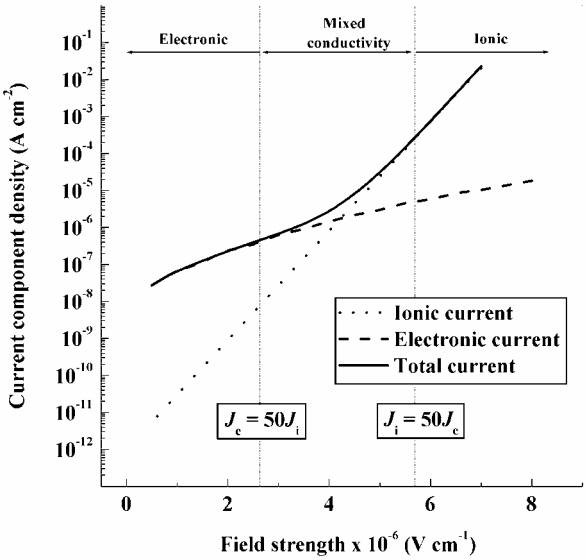

Fig. 2. Ionic, electronic and total current densities *vs*. field strength for the system (+)Nb/Nb_2O_5/ABE.

Table 2. Electric field boundaries of the conductivity areas in the system (+)Nb/Nb_2O_5/electrolyte.

Electrolyte	Field strength $E\times10^{-6}$, $V\cdot cm^{-1}$		
	Electronic conductivity ($J_e = 50J_i$)	Mixed conductivity	Ionic conductivity ($J_i = 50J_e$)
ABE	$E < 2.63$	2.63–5.71	$E > 5.71$
0.1 M AS/DMF	$E < 2.33$	2.33–5.35	$E > 5.35$
0.6 M AS/DMF	$E < 2.01$	2.01–5.08	$E > 5.08$

The determination of the current efficiency (λ) for three electrolytes can be performed by the following expression:

$$\lambda = \frac{J_i}{J_i + J_e}. \qquad (3)$$

The dependence of current efficiency (λ) on the total current density (J) for the three contact electrolytes is shown in Fig. 3. The results show that the current efficiency depends on the nature and concentration of the contact electrolyte as it is expected in advance. The results presented allow outlining the values where the total current (J) is mainly ionic ($\lambda > 98\%$) and the growth of anodic Nb_2O_5 is efficient. Moreover, when $\lambda < 2\%$ J is predominantly electronic then negligible changes in the oxide thickness should be expected. The lowest values of the efficiency are those obtained during anodic polarization

of Nb/Nb_2O_5 in ABE.

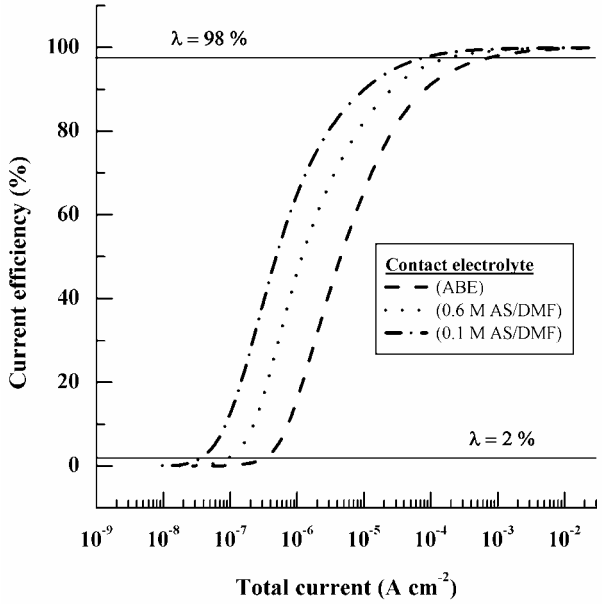

Fig. 3. Current efficiency as a function of total current density for three contact electrolytes.

CONCLUSION

The determination of ranges of ionic and electronic conductivity for the (+)Nb/Nb_2O_5/electrolyte systems makes possible to define the current ranges where the anodic film formation is carried out at high efficiency. Moreover, the ranges of the electric field (working voltage, respectively), wherein the electrolyte capacitors are expected to be reliable, can also be estimated by the method employed.

***Acknowledgements**: The authors are indebted to the National Science Fund, the Ministry of Education, for funding this work under contract BYX-307/2007.*

REFERENCES

1. A. Güntherschulze, H. Betz, *Z. Phys.,* **91,** 70 (1934).
2. A. Güntherschulze, H. Betz, *Z. Phys.,* **92,** 367 (1934).
3. S. Ikonopisov, *Electrochim. Acta,* **14,** 761 (1969).
4. V. Trifonova, A. Girginov, *J. Electroanal. Chem.* **107,** 105 (1980).
5. S. Christov, *J. Electroanal. Chem.* **105,** 275 (1979).
6. S. Ikonopisov, N. Elenkov, *J. Electroanal. Chem.,* **86,** 417 (1978).
7. M. Lohrengel, *Mater. Sci. Eng.*, **R11**, 243 (1993).
8. S. Ono, K. Kuramochi, H. Asoh, *Corros. Sci.*, **51**, 1513 (2009)
9. K. Nagahara, M. Sakairi, H. Takahashi, K. Matsumoto, K. Takayama, Y.Oda, *Electrochim. Acta,* **52,** 2134 (2007).
10. S. Ikonopisov, M. Machkova, *Compt. Rend. Acad. Bulg. Sci.*, **37,** 1661 (1984).

ЗОНИ НА ЙОННА, ЕЛЕКТРОННА И СМЕСЕНА ПРОВОДИМОСТ В СИСТЕМАТА Nb/Nb_2O_5/ЕЛЕКТРОЛИТ

Кр. А. Гиргинов[1], А. С. Захариев[2], А. А. Гиргинов[1]*

[1] Катедра „Физикохимия“, Химикотехнологичен и металургичен университет, бул. „Климент Охридски“ № 8, 1756 София
[2] Катедра „Химия“, Технически университет - София, бул. „Климент Охридски“ № 8, 1756 София

Постъпила на 6 юли 2009 г.

(Резюме)

Йонната (J_i) и електронна (J_e) компонента на тока, както и тоталната плътност на тока (J), протичащ в системата (+)Nb/Nb_2O_5/електролит, са пресметнати чрез уравненията, описващи тяхната зависимост от силата на електричното поле. Определени са зоните на електронна, смесена и йонна проводимост по време на формирането на анодни оксидни филм в системата (+)Nb/Nb_2O_5/електролит. Пресметнатата ефективност на тока по време на нарастването на анодните филми е представена като функция от тоталната плътност на тока. Намерено е, че зоната на смесена проводимост както и ефективността на тока зависят от природата и концентрацията на контактния електролит.

Bulgarian Chemical Communications, Volume 42, Number 2 (pp. 141–146) 2010

Phenol adsorption on activated carbons with different structure and surface properties

B. Petrova[1], T. Budinova[1,*], B. Tsyntsarski[1], N. Petrov[1], G. Bardarska[2], C. Ania[3], J. Parra[3]

[1] *Institute of Organic Chemistry, Bulgarian Academy of Sciences, Acad. G. Bonchev St., Block 9, 1113 Sofia, Bulgaria*
[2] *Institute of Economics, Bulgarian Academy of Sciences, 3 Aksakov St., 1040 Sofia, Bulgaria*
[3] *Instituto Nacional del Carbon, CSIC, Apartado 73, 33080, Oviedo, Spain*

Received July 15, 2009; Revised January 14, 2010

The adsorption of phenol from aqueous solution on activated carbons, produced from agricultural wastes, was studied. Production of carbon adsorbents from agricultural wastes (apricot stones, cob-corn and bean pods) for water treatment is investigated in the paper. Activated carbons (AC) are prepared by pyrolysis of biomass materials in a flow of steam. It is established that the activated carbon obtained by pyrolysis of apricot stones in the presence of water vapour shows the highest adsorption capacity – 172 mg/g. The results from the investigation show that the determining factors for the adsorption of phenol are the porosity parameters.

Key words: agricultural wastes, activated carbon, adsorption, phenol.

INTRODUCTION

Industrial activity is responsible for generating a large volume of organic compounds, which are often difficult or sometimes impossible to remove by conventional biological treatment processes [1]. Phenol is one of the most common organic water pollutants. Phenol and substituted phenols are toxic organic pollutants, usually present in industrial waste waters, especially these from oil refineries, coal conversion plants, pharmaceuticals, *etc*., and as a class of organics they are similar in structure to the more common herbicides and insecticides, which can explain the fact that they are resistant to biodegradation. In the presence of chlorine in drinking water, phenols form chlorophenols, that have a medicinal taste, which is quite objectionable. Phenol compounds are No 11 in the list of 126 chemicals, which have been acknowledged as priority pollutants by United Environmental Agency [2, 3]. The effective removal of these pollutants from wastewater is a problem of great importance and interest for the society worldwide. There are many methods such as catalytic and photocatalytic oxidation [4, 5], ozonation [6], nanofiltration [7], chlorination [8], adsorption [9, 10], but among them the most widely used method is adsorption onto the surface of activated carbon [10].

Porous carbons have been widely applied in liquid-phase adsorption, separation and purification processes. The high cost of commercial activated carbon has stimulated interest in the examination of the feasibility of using cheaper raw materials for its production. Substitute materials tested include different sources of biomass (wood material, agricultural by-products, residual polymer materials, residual materials from coal conversion, *etc*. [11–15].

The typical activated carbon particles, whether in a powdered or granular form have porous structure consisting of a network of interconnected macropores, mesopores, and micropores which provide good adsorption capacity towards organic molecules due to the high surface area of the activated carbon. The surface chemistry of the activated carbon and its chemical characteristics such as nature, polarity and solubility of surface ions and functional groups determine the nature of bonding between molecules of adsorbate and activated carbon.

In this paper we will focus on investigating and comparing of the adsorptive properties towards phenol of three different samples of activated carbons, obtained by pyrolysis in the presence of water vapour from some wide-spread agricultural by-products (apricot stones, cob-corn and bean pods), and their application for removal of phenol from aqueous solution.

MATERIALS AND METHODS

Preparation of activated carbons

Different agricultural by-products (apricot stones, cob-corn and bean pods) were used as raw materials for preparation of activated carbons. The samples were pyrolysed in a stream of water vapour in the equipment, shown in Figure 1.

* To whom all correspondence should be sent:
E-mail: goriva@orgchm.bas.bg

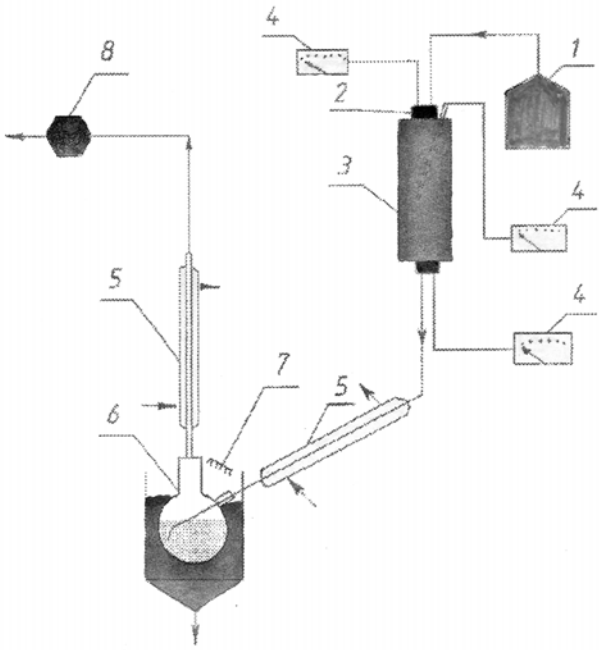

Fig. 1. Equipment for production of carbon adsorbents: 1 - generator of water vapour; 2 - reactor; 3 - furnace; 4 - thermocouple; 5 - cooler; 6 - collector for liquid products; 7 - water cooling.

According to the specific characteristics of the initial raw materials the preparation of the activated carbons from apricot stones, cob-corn and bean pods, is performed in different ways. The details of the procedures for producing activated carbons from these agricultural wastes are as follows:

The activated carbon from apricot stones has been prepared by one-step pyrolysis of crashed apricot stones in the presence of water vapour. In this method carbonization and activation were performed simultaneously in contrast with the two-stage process of carbonization and consecutive activation. Apricot stones (100 g) were heated in our laboratory installation (Fig. 1) in a flow of water vapour (120 ml/min) with a heating rate of 15°C/min up to a final carbonization temperature of 800°C. The duration of treatment at the final temperature is 1 h. After the treatment the sample is left to cool down in flow of water vapor. The obtained activated carbon is denoted as Carbon A.

Bean pods and cob corn were carbonized and after that activated with water vapor because otherwise the initial waste materials would hinder the passing of the activating agent (water vapor) through the sample. Bean pods and cob-corn wastes were carbonized as 50 g of the raw material (fraction 1–5 mm) by heating in the laboratory installation (Fig. 1) with heating rate of $60^{o}C \cdot min^{-1}$ up to a carbonization temperature of 600°C. The sample was maintained at the final temperature for 10 min, and then cooled down to ambient temperature in flow of water vapor. After that the solid product was activated with water vapor at 700°C for 1 hour. These activated carbons are denoted as Carbon B – from cob corn and Carbon C – from bean pods.

The volatile products were carried by water vapor into receiver where they were condensed.

Pore structure analysis

The textural characterization was carried out by measuring N_2 adsorption isotherm at –196°C and applying an ASAP 2010 M instrument (Micromeritics Corp., Norcross GA). Before the experiments the sample (ca. 0.3 g) was outgassed at 150°C under vacuum for ca. 24 h. Different model methods (i.e. BET and Dubinin-Radushkevich) were applied to the N_2 adsorption isotherm in order to calculate the specific surface area and micropore volume [16].

Oxygen-containing functional groups

The amount of oxygen-containing functional groups with increasing acidity was determined by Boehm's method of titration with basic solutions of different base strengths ($NaHCO_3$, Na_2CO_3, NaOH, C_2H_5ONa): carboxylic groups (analyzed with titration of $NaHCO_3$), carboxylic groups in lactone like binding structures (determined from the difference between the consumption of $NaHCO_3$ and Na_2CO_3), phenolic hydroxyl groups (determined from the difference between NaOH and Na_2CO_3 consumption) and carbonyl groups (determined from the difference between NaOEt and NaOH consumption) as well as the total amount of basic groups, determined by titration of HCl. For this purpose the samples were agitated for at least 16 hours with 0.05 N solutions of the four bases. The amount of Na^+ ions remaining in the solution was determined by adding an excess of standard HCl water solution and back-titration [17]. The basic groups content of the samples was determined with 0.05 N HCl [18].

pH Measurements

The pH values of the obtained carbons were measured according to the following procedure: exactly 4.0 g of carbon was weighted into a 250 ml beaker, and 100 ml of bi-distilled water (pH= 5.70) was added. The beaker was covered with a watch glass, and the mixture was boiled for 5 min. The suspension was set aside, and the supernatant liquid was poured off as hot as possible but not below 60°C. The decanted portion was cooled down to ambient temperature, and its pH value was measured to the nearest 0.1 pH unit.

Table 1. Proximate and elemental analysis of the raw precursors and the activated carbons, produced by steam pyrolysis.

No.	Raw material/ Activated carbon	Proximate analysis, %		Ultimate analysis, %				
		Ash	Volatiles	C	H	N	S	O
1	Apricot stones/	0.20/	80.60/	51.50/	6.30/	0.20/	0.10/	41.90/
	Activated carbon A	2.01	3.70	89.50	2.40	0.90	0.80	6.40
2	Cob-corn/	5.00/	84.49/	45.50/	6.34/	0.62/	0.06/	47.48/
	Activated carbon B	15.10	20.80	62.90	3.50	0.54	0.05	33.01
3	Bean pods/	6.09/	80.07/	43.25/	5.98/	0.92/	0.11/	49.74/
	Activated carbon C	22.80	30.26	60.25	3.90	0.73	0.16	34.96

Table 3. Porosity characteristics and adsorption capacities of the activated carbons, produced from apricot stones, cob-corn and bean pods.

No.	Activated carbon, produced from:	Iodine number, mg/g	Surface a area-BET m^2/g	Pore volume, cm^3/g			
				Micro	Meso	Macro	Total
1	A – apricot stones	900	960	0.760	0.100	0.040	0.91
2	B – cob-corn	650	500	0.270	0.080	0.050	0.40
3	C – bean pods	500	258	0.107	0.070	0.033	0.21

Adsorption Measurements

All adsorption experiments were carried out by using an adsorbent sieve fraction with particles 0.2 mm in size. The adsorption capacity of the adsorbents towards phenol was investigated by using aqueous solution of phenol. Phenol was obtained from Merck (99% purity). The phenol solutions were prepared in the concentration range of 100–300 mg/l. The principle of our experiments was as follows: 100 mg of activated carbons were mixed with 50 ml of phenol solution with desired concentration in 100 ml capacity stopped flasks. The stopped flasks containing the adsorbent and the adsorbate were agitated for predetermined time intervals at room temperature on a mechanical shaker. At the end of agitation, the suspension was filtered through microporous filter paper (hydrochloric acid filter and hydrofluoric extraction, FILTRAK 390). The suspensions were shaken to reach stable equilibrium (2 hours). The phenol concentrations were determined spectrophotometrically at maximum adsorbance wavelength λ = 269 nm using Pfaro 300 UV spectrophotometer.

RESULTS AND DISCUSSION

Chemical composition

The analysis of the structure and the composition of the agricultural wastes is very important because it allows to obtain preliminary results on their application as a source for yielding of liquid and solid products with definite properties, and to select the appropriate method of their treatment as well. Chemical composition data of the raw precursors and the produced activated carbons are shown in Table 1.

Activated carbon obtained by one step method of pyrolysis in the presence of water vapour of apricot stones possesses a higher content of carbon, lower content of oxygen and ash, which are desirable features for activated carbon production. Comparatively, carbons from bean pods and cob-corn have higher ash content, higher amount of oxygen and lower content of carbon.

Surface oxygen groups

The functional groups on the surface of activated carbons have strong effect on the adsorption properties. Table 2 compares the amounts of different oxygen groups on the surface of activated carbons.

Table 2. Quantification of oxygen groups on activated carbons surface (meq/g).

Activated carbon	pH	Acidic surface functional groups				Basic groups
		Carboxyl	Lactonic	Hydroxyl	Carbonyl	
A	10.7	0.13	0.19	0.09	0.98	1.24
B	9.2	BDL*	BDL	0.25	2.95	2.60
C	10.7	BDL	BDL	0.21	1.31	7.40

* BDL – below detection limit.

The data in Table 2 show the influence of the raw materials on the character of the oxygen-containing groups. It is determined that various oxygen-con-taining groups with different chemical properties are present on the activated carbon surface. The surface of all three samples of activated carbons has basic nature. Acidic groups (carboxylic and lactone-like binding structures) are detected only on the surface of activated carbon prepared from apricot stones, whereas phenolic hydroxyl and carbonyl groups are present in all three carbon samples. The amount of basic groups is nearly six times higher for carbon C in comparison with Carbon A, which is in a good agreement with the

measured pH values. Such basic activity could be due to the presence of oxygen containing groups of basic nature or related to the species in the inorganic matter of this carbon. The determined amount of carboxylic groups in lactonic structures in the activated carbon from apricot stones is probably due to the method of activation, namely simultaneous performing of the processes of carbonization and activation.

Textural characteristics

The porosity has a strong effect on the adsorption properties of the activated carbons. Table 3 compares the porosity characteristics of activated carbons obtained from apricot stones, cob-corn and bean-pods. The samples obtained from apricot stones have the largest total volume of the pores, with significant prevalence of the micropores. The samples from bean pods and cob-corn have considerably lower surface area and volume of micropores. We have reported that the composition of agricultural by-products has a strong influence on the final porosity and chemical features of solid product obtained from pyrolysis and activation. It was found that the low ratios of lignine:cellulose favor the development of predominantly microporous materials [19].

Activated carbon adsorption of phenol from water solution

Effect of contact time. The distribution of adsorbed substance between activated carbon and adsorbate solution for the system at equilibrium is of importance for determining the maximum adsorption capacity of activated carbon for phenol. Figure 2 shows the effect of the time interval of treatment on the removal of phenol by activated carbon obtained from apricot stones. Phenol adsorption increases sharply for a short period of time and then shows a gradual increase when the equilibrium is approached. This behaviour can be attributed to the relative decrease in the number of available sites on the carbon surface as the process advances.

The plots show that the amount of phenol adsorbed on the adsorbents (mg/g) varies in single smooth and continuous curve, leading to saturation and thus suggesting the possibility of the formation of monolayer coverage of phenol on the surface of the adsorbent.

The data indicate that the removal of phenol attains equilibrium in 60 minutes for all initial concentrations of the phenol solution. The kinetic curves of the removal of phenol versus time of treatment for carbon B and C show the same dependence.

Adsorption isotherm. Adsorption is a well known equilibrium separation process for treatment of water containing organics. The adsorption isotherm of phenol on carbon A is presented in Figure 3. The amount of phenol adsorbed at equilibrium per carbon mass unit for all concentrations (100–300 mg/l) is presented as a function of the equilibrium phenol concentration. The adsorption isotherm in Figure 3 could be assigned to the L(2) class according to the Giles classification [20]. L-type isotherms correspond to the completion of monolayers in experimental concentration ranges.

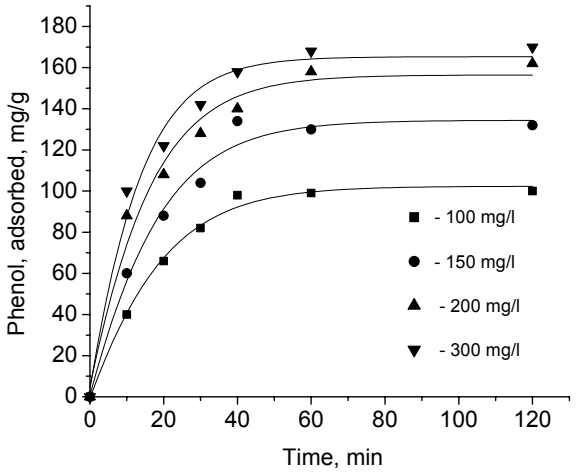

Fig. 2. Effect of treatment time and initial concentrations of phenol on the adsorption on Carbon A. Conditions: carbon concentration 100 mg/50 ml, Phenol concentrations:(■) 100 mg/l, (●)150 mg/l, (▲) 200 mg/l, and (▼) 300 mg/l.

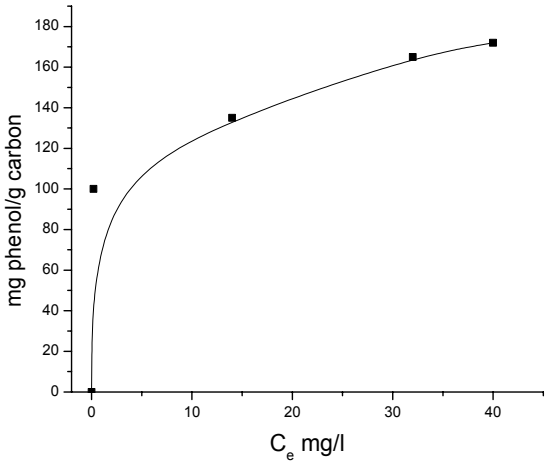

Fig. 3. Phenol isotherm on activated carbon A. Phenol concentrations 100–300 mg/l; treatment time, 120 min, carbon concentration 100 mg/50 ml.

The linear form of the Langmuir's equation [16] is applied to calculate the adsorption capacity of activated carbons:

$$q_{eq} = Q_o b C_{eq}/1 + bC_{eq} \quad (1)$$

where C_{eq} is residual (equilibrium) pollutant concentration (mg/l); q_{eq} – amount of pollutant bound to the adsorbent (mg/g); Q_o – maximum amount of the pollutant per unit weight of adsorbent, mg/g; b – constant related to the affinity of adsorption sites (l/mg); Q_o represents the practical limiting adsorption capacity when the surface is completely covered with pollutant molecules.

The Langmuir plots for adsorption of phenol on carbons A, B and C are presented in Figure 4.

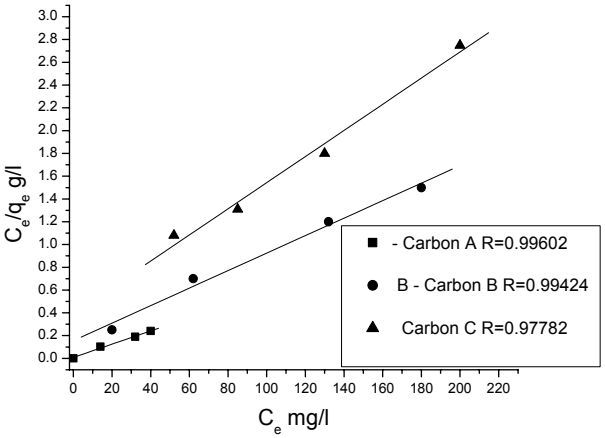

Fig. 4. Langmuir plots for adsorption of phenol on different types of activated carbons: ■ - A; ● - B; ▲ - C.

The linear plot of C_e/q_e *versus* C_e shows that adsorption obeys the Langmuir's isotherm model (Figure 4). The calculated values of Q_o and b are presented in Table 4.

Table 4. Data for phenol adsorption obtained from Langmuir's plots.

Type of activated carbon	Q_o, mg/g	b, l/mg	R*
A	172	0.07330	0.99602
B	130	0.00770	0.99424
C	89	0.40567	0.98724

R* -correlation coefficient.

All these isotherms are fitted to the experimental adsorption data. Correlation coefficients, calculated for these isotherms by using linear regression procedures, show that the Langmuir's isotherms fit excellent to the experimental data. This confirms too that the removal of phenol from solution on the prepared carbons can be described by the Langmuir's theory, which states that the adsorption proceeds *via* a monolayer formation, displaying the typical L-shape according to Giles classification too (Fig. 2).

The adsorption capacity of 172 mg/g for phenol on activated carbon, produced after pyrolysis of apricot stones in water vapour, is higher than those from bean pods and cob-corn. The activated carbon A, possesses considerable high specific surface area (BET), and significant total pore and micropore volumes. The activated carbon C, which possesses lower specific surface area, shows nearly 52% lower adsorption capacity than activated carbon A.

The studies on the mechanism of phenol retention on activated carbons have shown that it is a complex one and that adsorption may take place on different active sites and it strongly depends on the pore texture, surface chemistry and the mineral matter content. The adsorption capacity of carbon materials is not related in a simple form with their surface area and porosity. The adsorption capacity depends on the access of the organic molecules to the inner surface of the adsorbents, which depends on their size. Thus, under appropriate experimental conditions, small molecules such as phenol, can access micropores and for this reason the activated carbon from apricot stones with higher content of micropores has the highest value of adsorption capacity towards phenol. It has to be mentioned too that independently of the lower content of micropores, Carbon B and Carbon C show high adsorption capacity, which is obviously due to the surface chemistry (higher content of oxygen group-carbonyl and basic groups in comparison with Carbon A).

Mattson and co-workers suggested that aromatic compounds are adsorbed on carbons by a donor-acceptor complex mechanism, with the carbonyl oxygen of the carbon surface acting as an electron donor, and the aromatic ring of the adsorbate acting as acceptor [26]. This is valid especially for carbon B, which has 3 times higher content of carbonyl groups and 3 times lower content of micropores in comparison with Carbon A, whereas the adsorption capacity is slightly lower – 130 mg/g.

CONCLUSIONS

Activated carbons, produced from agricultural wastes as apricot stones, bean pods, cob-corn after steam pyrolysis, are suitable for treatment of phenol polluted water. The most active is activated carbon from apricot stones, followed by activated carbon from cob-corn and bean pods. The most substantial factors with big influence on phenol adsorption are the surface area and porosity characteristics. The obtained adsorption capacity of 172 mg phenol by 1 g activated carbon shows that the activated carbon from apricot stones is highly promising. Using the agriculture wastes for producing activated carbon, needed for water treatment, is an ecologically friendly approach with socio-economic effect.

Acknowledgements: *The authors acknowledge financial support for this work by MEYS-NFSI, Bulgaria (grant 02-222/17.12.2008).*

REFERENCES

1. F. Caturla, M. Martin-Martines, M. Molina-Sabio, F. Rodriguez-Reinoso, R. Torregrosa, *J. Coll. Interface Sci*. **124**, 528 (1998).
2. EU Water Framework Directive, Directive 2000/60/EC, Ogg. J., L 327, 22 December 2000.
3. Environmental quality standards for priority substances and certain other pollutants, Directive 2008/105/EC, 16 December 2008.
4. F. Larachi, I. Ihuta, K. Belkacemi, *Catal. Today*, **64**, 309 (2001)
5. Md. Ahmaruzzaman, *Adv. Coll. Interface Sci*., **14**, 48 (2008).
6. C. Cooper, R. Burch, *Water Res*., **33**, 3695 (1999).
7. J. M. Arzuada, M. J. Lopez-Munoz, J. Aguado, A. Sotto, *Desalination*, **221**, 253 (2008).
8. V. V. Goncharuk, Ecological Aspects of Modern Technologies of Protecting Water Medium, Kiev, Naukova Dumka, 2005, p. 400 (in Russian).
9. H. B. Crauford, G. Cline, Water Treatment Plant Design, Kh. A. Halhouli, N. A. Darwish, N. M. Ahlhoon (Eds.), American Society of Civil Engineers, American Water Works Association, Mc Graw Hill, New York, (1990) p. 457.
10. L. R. Radovic, C. Moreno-Castilla, J. Rivera-Utrilla, in: Chemistry and Physics of Carbon, v. 27, L. R. Radovic (Ed.), Marcel Dekker, New York, 2001, p. 227–405.
11. E. D. Larsen, Proc. 2nd Olle Lindström Symposium on Renewable Energy-Bioenergy, 9–11 June, 1999, Royal Institute of Technology, Stockholm, Sweden, 1999, p. 1–3.
12. T. Budinova , E. Ekinci, F. Yardim, A. Grimm, E. Bjornbom, V. Minkova, M. Goranova, *Fuel Proc. Technol*., **87**, 899 (2006).
13. N. Petrov, T. Budinova, M. Razvigorova, E. Ekinci, F. Yardim, V. Minkova, *Carbon*, **38**, 2069 (2002).
14. N. Petrov, T. Budinova, M. Razvigorova, J. Parra, P. Galiatsatou, *Biomass and Bioenergy*, **32**, 1303 (2008).
15. F. Rodriguez-Reinoso, M. Molina-Sabio, M. T. Gonzales, *Carbon*, **33**,15 (1995).
16. S. J. Gregg, K. S. W. Sing, in: Adsorption, Surface Area and Porosity; Academic Press, London, 1982, p. 1.
17. H. P. Boehm, in: *Adv. Catal. Rel. Subj*., vol. 16, D. D. Eley, H. Pines, P. B. Weisz (Eds.), Academic Press, New York, 1966, pp. 179–274.
18. E. Papier, S. Li, J. B. Donnet, *Carbon*, **25**, 243 (1987).
19. D. Savova, E. Apak, E. Ekinci, F. Yardim, N. Petrov, T. Budinova, M. Razvigorova, V. Minkova, *Biomass and Bioenergy*, **21** 1333 (2001).
20. C. H. Giles, T. H. MacEwan, S. N. Nakhwa, D. Smith, *J. Chem. Soc*., 3973 (1960).
21. K. Laszlo, E. Tombasz, C. Novak, *Colloids Surf. A: Physicochem. Eng. Aspects*, **306**, 95 (2007).
22. A. P. Terzyk, *J. Colloid Interface Sci*., **2689**, 310 (2003).
23. K. F. Loughin, M. M. Hassan, E. O. Ekhator, G. F. Nakhia, Proc. 5th Int. Conf. Fundamentals of Adsorption, Kluwer, Boston, 1996, pp. 537–544.
24. T. M. Grant, C. J. King, *Ind. Eng. Chem. Res*., **29**, 264 (1990).
25. I. I. Salame, T. J. Bandosz, *J. Coll. Interface Sci*., **264**, 307 (2003).
26. J. S. Mattson, Jr., H. B. Mark, M. D. Malbin, Jr., W. J. Weber, J. C. Crittenden, *J. Colloid Interface Sci*., **31**, 116 (1969).

АДСОРБЦИЯ НА ФЕНОЛ ВЪРХУ АКТИВНИ ВЪГЛЕНИ С РАЗЛИЧНИ СТРУКТУРНИ И ПОВЪРХНОСТНИ ХАРАКТЕРИСТИКИ

Б. Петрова[1], Т. Будинова[1,*], Б. Цинцарски[1], Н. Петров[1], Г. Бардарска[2], К. Аня[3], Х. Пара[3]

[1] Институт по органична химия с център по фитохимия, Българска академия на науките, ул. „Акад. Г. Бончев“, блок 9, 1113 София

[2] Икономически институт, Българска академия на науките, ул. „Аксаков“ № 3, 1040 София

[3] Институт по въглерод, Апартадо 73, 33080 Овиедо, Испания

Постъпила на 15 юли 2009 г.; Преработена на 14 януари 2010 г.

(Резюме)

Изследвана е адсорбцията на фенол върху активни въглени, получени от отпадни селскостопански продукти (кайсиеви костилки, бобени шушулки и кочани от царевица). Активните въглени са получени чрез пиролиз в присъствие на водна пара. Процесът пиролиз в присъствие на водна пара дава възможност да се получат течни и газообразни продукти и високоефективни активни въглени. Резултатите показаха, че най-висока адсорбционна способност спрямо фенол (172 mg/g) показва активния въглен, получен при процеса пиролиз на кайсиеви костилки.

Bulgarian Chemical Communications, Volume 42, Number 2 (pp. 147–152) 2010

Studies on acridone derivatives with and without inclusion complex formation with β-cyclodextrin

S. S. Nayak[1,*], S. Panda[2], P. M. Panda[3], S. Padhy[3]

[1] *S. B. R. Govt. Women's (Auto) College, Berhampur 760001, India*
[2] *PG Department of Chemistry, Berhampur University, Bhanja Vihar 760007, India*
[3] *Department of Microbiology, M. K. C. G. Medical College and Hospital, Berhampur 760004, India*

Received September 20, 2009; Revised January 14, 2010

Using keto group of acridone pharmacophore, three important acridone derivatives namely thiosemicarbazone, semicarbazone and oxime have been synthesised which have significant antimicrobial activity. In order to increase the bio-accessibility of these compounds, inclusion complexes have been prepared with a non-toxic oligosaccharide, β-cyclodextrin. The synthesis of derivatives and their inclusion complexes have been ascertained from the changes in spectral characteristics and melting point data. The aqueous phase solubility studies reveal 1:1 stoichiometry between the compound and β-cyclodextrin in the inclusion complex. The calculation of thermodynamic parameters ΔG (change in free energy), ΔH (change in enthalpy) and ΔS (change in entropy) of the complexes indicates the inclusion complex formation to be spontaneous and exothermic in nature. The determination of thermodynamic stability constants suggests existence of weak intermolecular forces in between host and guest in the inclusion complex. The study of antimicrobial activity indicates that the microbes like *E. coli* and *P. aeruginosa* are susceptible to acridone and its derivatives and the susceptibility increases further after the formation of inclusion complexes.

Key words: Acridone derivatives, inclusion complex, β-cyclodextrin, phase solubility, thermodynamic stability, antimicrobial study.

INTRODUCTION:

Acridone and its derivatives are important pharmacophores for the designing of several chemotherapeutic agents (anti cancer, anti bacterial, anti protozoal) because of their strong affinity towards DNA and intercalative properties [1–3]. These compounds are suggested to be highly efficacious in preventing and treating diseases such as asthma, allergic rhinitis, atopic dermatitis, gastrointestinal allergies, *etc*. [4].

Since bio-accessibility of a drug depends upon its solubility, one of the factors limiting the pharmacological activities of acridone and its derivatives is their poor solubility in aqueous solutions [5]. The solubility of these compounds can be enhanced by forming inclusion (host-guest) complexes with β-cyclodextrin (β-CD), an easily available and less expensive encapsulator, which in turn increases drug efficiency [6].

Although a series of 10-N-susbstituted acridones, bearing alkyl side chains with tertiary amino groups at the terminal position have been reported [7], there are few reports regarding the synthesis of acridone derivatives involving the keto group.

In this paper an attempt has been made to synthesize acridone and its thiosemicarbazone, semicarbazone and oxime derivatives in their purest forms. Respective inclusion complexes of these compounds with β-CD have been synthesized. The formation of acridone, its derivatives and their inclusion complexes has been ascertained from their spectral characteristics. The stability of the inclusion complexes has been studied from thermodynamic measurements. As these compounds contain quinolone group, they are expected as potential drugs against some bacteria and accordingly antimicrobial activity studies have been made against a Gram positive bacterium, *Escherichia coli* and Gram negative bacterium, *Pseudomonas aeruginosa.*

EXPERIMENTAL

Apparatus and materials

All chemicals are procured form the local market and are of suitable Anal R grade. Double distilled water is used as the solvent for dilution. Other solvents employed are redistilled before use. The elemental analysis has been performed in a CHN analyzer. Electronic spectra are recorded on Shimadzu UV-1700 spectrophotometer while IR spectra are recorded in KBr pellets in the 400–4000 cm^{-1} region in a Shimadzu 8400 S FTIR spectrophotometer. Melting points are recorded by open

* To whom all correspondence should be sent:
E-mail: swapna_nayak7@yahoo.com

capillary method. Antimicrobial screening by Kirby-Bauer method has been done by employing Muller Hinton agar plates in normal saline medium and sterilised cotton swabs.

Phase solubility measurements

The aqueous phase solubility of acridone and its derivatives at various concentration of β-CD has been studied by Higuchi-Connors method [8]. Accurately weighed sample of these compounds in quantities exceeding their aqueous solubility are shaken in a rotary flash shaker at room temperature with aqueous solution of β-CD in increasing concentration (0–10 mM/L) in a series of stoppered conical flask for a period of 48 hours till equilibrium is established. The solutions are filtered through Whatman No 1 paper and are analyzed in a UV-Vis spectrophotometer at 380–420 nm range. The various values of optical density (OD) at λ_{max} have been plotted against different concentration of β-CD.

Syntheses of acridone and its derivatives

Synthesis of acridone. Acridone has been synthesised as per Allen and Mckee [9]. 0.2 mole of N-phenylanthranilic acid (I) in 100 ml of conc. H_2SO_4 is refluxed in a 500 ml flask on a boiling water bath for four hours and then poured into a 1 L flask containing hot water slowly and carefully. The yellow precipitate formed is filtered after boiling for few minutes and then the moist solid is again boiled for five minutes with a solution of 0.28 mole Na_2CO_3 in 400 ml of distilled water. The precipitate is collected with suction and washed well with water. After drying, the crude acridone (II) obtained is then recrystalised form a mixture of aniline and acetic acid.

Synthesis of derivatives. 1 g of hydroxylamine hydrochloride and 1.5 g of crystallized sodium acetate are dissolved in 10 ml water to which 0.5 g of acridone is added and shaken. Alcohol is added till turbidity disappeared to give a clear solution. Then the solution is refluxed for 2 hours on a water bath with condenser. The resulting solution is poured carefully into ice-cold water where the crystals of acridoxime (III) are obtained. These are recrystallised from alcohol and water mixture and finally dried. Similarly the semicarbazone (IV) and the thiosemicarbazone (V) derivatives have been prepared using 1 g of semicarbazide hydrochloride and 1 g of thiosemicarbazide hydrochloride, respectively. The synthesis of acridone and its derivatives are shown in Scheme 1.

Synthesis of inclusion complexes

The inclusion complexes of acridone and its derivatives have been synthesised as per co-precipitation method [10, 11]. The solution of the synthesized compounds are prepared in required concentrations (0.03M) and were added drop wise to previously stirred β-CD solution. The mixtures are stirred at room temperature for 48 hours, filtered. Then the content is and cooled for another 48 hours in refrigerator. Finally, the precipitate obtained is filtered through G-4 crucible, washed with distilled water and dried in air for 24 hours.

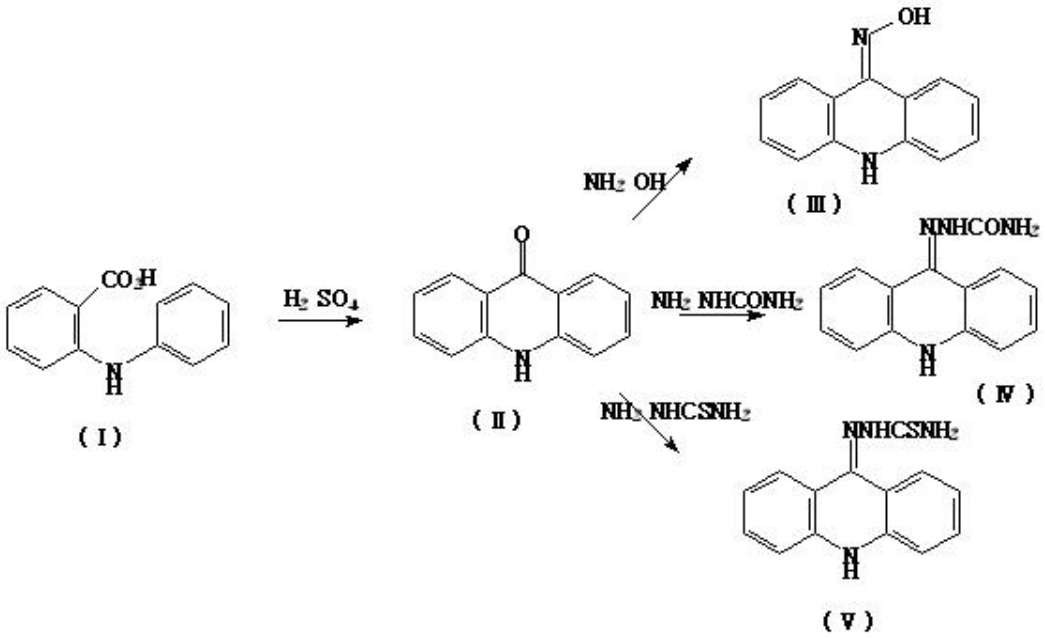

Scheme 1.

Study of thermodynamic properties

The thermodynamic stability constant (K_T) at room temperature of the complexes are calculated using Benesi-Hilderbrand relation [12].

$$1/\Delta A = 1/\Delta\epsilon + 1/K[\text{guest}]_0\,\Delta\epsilon.1/[\beta\text{–CD}]_0 \quad (1)$$

The stability constant K (during deencapsulation) of each complex has been calculated with increasing temperature. The slope of the linear plot of ln$K$ *versus* I/T gives rise to the calculation of ΔH (change in enthalpy) and then ΔS (change in entropy) was calculated using the integrated from of the van't Hoff equation.

$$\text{Ln}K = [-\Delta H/RT] + \Delta S/R \quad (2)$$

The value of ΔG was calculated from the value of K_T at 298 K using the equation:

$$\Delta G = -RT.\ln K_T \quad (3)$$

Study of antimicrobial activity

The disk diffusion method for antimicrobial susceptibility test is the Kirby-Bauer method [13, 14]. Muller-Hinton agar plates with normal saline medium have been used for this test. The bacterial inoculums are prepared by making a direct saline suspension of colonies of same morphological type that are selected from an 18–24 hour agar plate. The turbidity with sterile saline is adjusted. Within 15 minutes after adjusting the turbidity, a sterile non-toxic swab is dipped on an applicator into the adjusted suspension. A maximum of 5 disks on a100 mm plate are placed on the surface of the agar plate. The plates are inverted and are placed in an aerobic incubator at 35ºC. After 16–18 hours of incubation, the diameters of zones of complete inhibition (ZCI) are measured.

RESULTS AND DISCUSSION

Synthesis and characterisation of acridone and its derivatives

The synthesis of acridone and its derivatives are ascertained from elemental analysis, melting point (m.p.) measurement and changes in spectral (UV-Vis and IR) characteristics (Table 1). The elemental composition nearly matches with theoretical data. Infrared data of $C{=}O_{str}$ at 1674 cm^{-1}, $N{-}H_{str}$ at 3274 cm^{-1}, $C{-}N_{str}$ at 1161 cm^{-1} *etc*. and m.p. at 350ºC indicate the formation of acridone. Similarly, $C{=}N_{str}$ at 1560 cm^{-1}, $C{=}S_{str}$ at 1141cm^{-1}, $C{-}N_{str}$ at 1160 cm^{-1} etc and m.p. at 302ºC; $C{=}N_{str}$ at 1560 cm^{-1}, $C{=}O_{str}$ at 1635 cm^{-1}, $C{-}N_{str}$ at 1159 cm^{-1} $N{-}H_{def}$ at 1533 cm^{-1} *etc*. and m.p. at 292ºC; $C{=}N_{str}$ at 1641 cm^{-1}, $N{-}H_{str}$ at 3321 cm^{-1}, $O{-}H_{str}$ (oxime) at 3240 cm^{-1} *etc*. and m.p. at 322ºC suggest the formation of acridone thiosemicarbazone, acridone semicarbazone and acridoxime respectively.

Synthesis and characterisation of inclusion complexes

The syntheses of inclusion complexes of acridone and its derivatives are confirmed from change in melting point data, colour and spectral characteristics (Table 1). The m.p. of acridone, its thiosemicarbazone, semicarbazone and oxime derivatives are 350ºC, 302ºC, 292ºC and 322ºC respectively where as their corresponding inclusion complexes have m.p. 359ºC, 315ºC, 306ºC and 334ºC respectively. Higher m.p. values of inclusion complexes than the compounds may be due to the fact that an extra amount of thermal energy is required to bring the molecules out of β-CD cavities. Secondly, the UV-Visible absorption maxima of these compounds undergo blue shift and the peaks become broader, weaker and smoother after the formation of their inclusion complexes. Thirdly, IR frequencies due to different bonds present in the above compounds undergo a distinct downward shift towards lower energy when they form inclusion complexes. All these observations clearly demonstrate transference of the compounds from a more protic environment (aqueous media) to a less protic environment (cavity of β-CD) i.e. encapsulation of the compounds in the cavity of β-cyclodextrin. The changes in the spectral characteristics of the compounds after inclusion complex formation are attributed to development of some weak intermolecular forces like hydrogen bonding, van der Waal forces, hydrophobic interactions etc in between the host and guest molecules [15].

Phase solubility studies

The phase solubility plots of acridone and its derivatives are shown in Fig. 1. In each case, it is seen that there is a linear increase in solubility of these compounds with increasing concentration of β-CD. At a higher concentration of β-CD, a small negative deviation is observed. Since the slopes of all plots are less than unity, the stoichiometry of the inclusion complexes is 1:1 as reported by Z. Szetli [16].

The thermodynamic stability constants (K_T) of inclusion complexes are determined by the above Benesi-Hilderbrand relation (Eqn. (1)).

Good linear correlations (Fig. 2) are obtained for a plot of $1/\Delta A$ *versus* $1/[\beta\text{–CD}]_0$ for acridone and its derivatives. The values of K_T for both the complexes are calculated using the relation:

Table 1. Analytical data of acridone and its derivatives withwithout inclusion complex formation with β-cyclodextrin.

Sl No	Compound	m.p., ºC	Yield, %	Colour	Elemental analysis Found (Calculated), %				λmax nm	IR (KBr), cm^{-1}
					C	H	N	O/S		
1	Acridone	350	78	Greenish yellow	80 (80.2)	4.8 (4.6)	8.4 (8.2)	7.0 (7.18)	403, 385	1674 (C=O), 3274(N–H), 1161 (C–N), 1633 (C=C), 1572 (ring)
2	Acridone/ β-CD complex	359	81	Yellow	-	-	-	-	401, 383	1662 (C=O), 3270 (N–H), 1155 (C–N)
3	Acridonethio-semicarbazone	302	76	Bright yellow	62.66 (62.68)	4.5 (4.47)	20.81 (20.89)	11.97 (11.94)	405, 376	1560 (C=N), 1141 (C=S), 1160 (C–N), 3275 (N–H)
4	Acridonethio-semicarbazone/ β-CD complex	315	80	Yellow	-	-	-	-	403, 374	1553 (C=N), 1140 (C=S), 1156 (C–N)
5	Acridone-semicarbazone	292	78	Bright yellow	66.62 (66.66)	4.8 (4.76)	22.25 (22.22)	6.32 (6.35)	409, 381	1560 (C=N), 1635 (C=O), 1159 (C–N), 1535 (N–H)
6	Acridone-semicarbazone/ β-CD complex	306	80	Yellow	-	-	-	-	406, 379	1556 (C=N), 1633 (C=O), 1156 (C–N), 1532 (N–H)
7	Acridoxime	322	80	Bright yellow	74.31 (74.29)	4.8 (4.76)	13.3 (13.3)	7.59 (7.62)	406, 383	1641 (C=N), 3240 (O–H), 3321 (N–H)
8	Acridoxime/ β-CD complex	334	81	Yellow	-	-	-	-	403, 381	1640 (C=N), 3234 (O–H), 3315 (N–H)

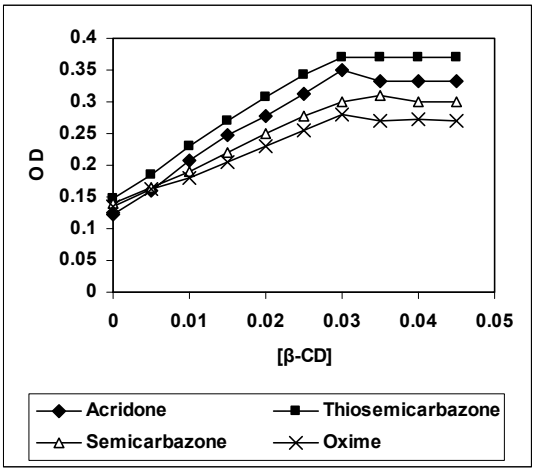

Fig. 1. Phase solubility plot (OD *vs*. [β–CD]) of acridone and its derivatives.

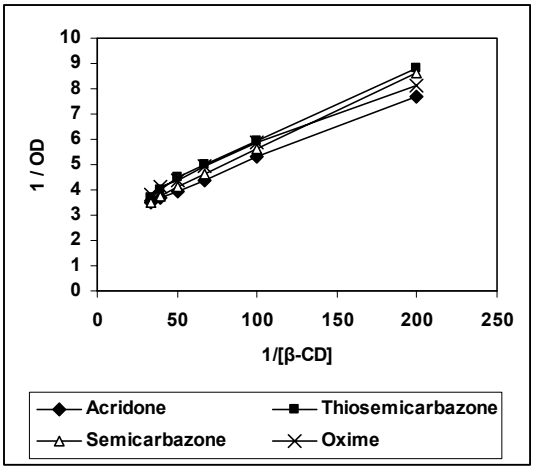

Fig. 2. Plot (1/OD *vs*. 1/[β–CD]) of acridone and its derivatives.

$$K_T = \frac{Intercept}{Slope} \quad (4)$$

The K_T values are found to be 104, 95.5, 108.3 and 155.5 M^{-1} corresponding to inclusion complexes of acridone and its thiosemicarbazone, semicarbazone and oxime. The data obtained are within 100 to 1000 M^{-1} (ideal values) indicating appreciable stabilities of the inclusion complexes [16].

Thermodynamic properties

The thermodynamic parameters associated with binding of acridone and its derivatives with β-CD for 1:1 stoichiometry have also been calculated by determining the *K* values (during deencapsulation) at different temperatures. The *K* values are found to decrease with increasing temperature (deencapsulation) as expected for an exothermic process [17]. The plot of ln*K* as a function of inverse absolute temperature produced linear plots (Fig. 3). In each case, the slope corresponds to ($-\Delta H/R$) [18]. From this value and value of K_T at 298 K, ΔG, ΔS and ΔH have been calculated (Table 2). As can be seen from the table, ΔG values are negative for all complexes. These data suggest the spontaneous formation of inclusion complexes. Secondly, the values of ΔH are negative at 298 K which suggests that the complex formation is an exothermic and enthalpy controlled process. Also, the negative enthalpy change is due to stabilization of the compound within the cavity of β-CD by weak intermolecular forces as suggested earlier. The small negative entropy change (ΔS) is

due to steric barrier caused by less free movement of guest molecules within the cavities of host. The study further suggests that change in entropy (ΔS) in destabilizing inclusion complexes is compensated by change in enthalpy (ΔH) which is in agreement with the observation of Stalin *et al*. (2006) [19].

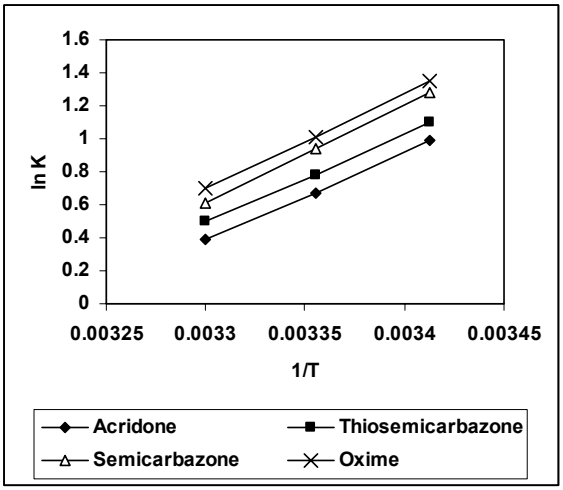

Fig. 3. Plot (1/ln$K$ *vs*. 1/T) of acridone and its derivatives.

Table 2. Thermodynamic parameters of inclusion complex of acridone and its derivatives at 298 K.

Sl No	Compound	K M^{-1}	ΔG kJ/mol	ΔH kJ/mol	ΔS kJ/mol
1	Acridone/β-CD complex	104	–11.5	–43.7	–0.11
2	Acridone-thio-semicarbazone/β-CD complex	95.5	–11.3	–31.6	–0.07
3	Acridone-semicarbazone/β-CD complex	108.3	–11.6	–46.8	–0.12
4	Acridoxime/β-CD complex	155.5	–12.5	–48.25	–0.12

Antimicrobial screening

The results obtained in the Kirby-Bauer plate method (Fig. 4) for the antimicrobial susceptibility test show that acridone and its derivatives are susceptible to both *Pseudomonas aeruginosa* and *Escherichia coli* (Figs. 5, 6).

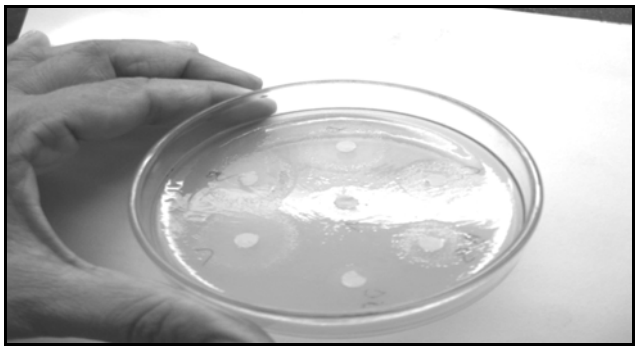

Fig. 4. Kirby-Bauer plate method of antimicrobial screening.

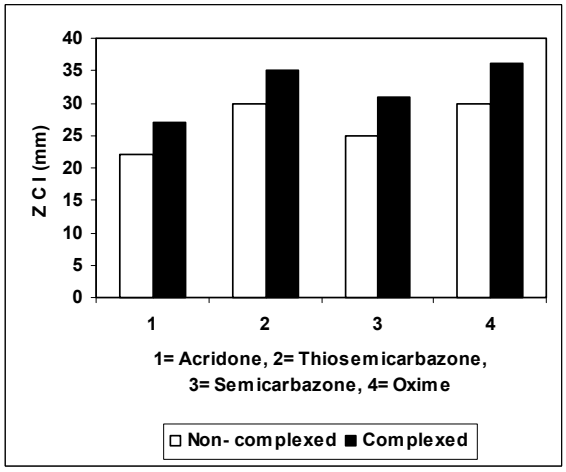

Fig. 5. Antimicrobial susceptibility test acridone and its derivatives against *P. aeruginosa*.

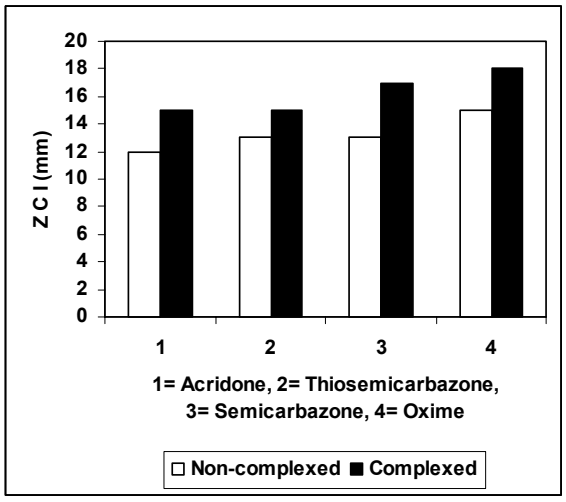

Fig. 6. Antimicrobial susceptibility test acridone and its derivatives against *E. coli*.

When inclusion complexes of these compounds are tested against the above microbes, the antimicrobial activity increases significantly. This is due to enhanced solubility of the drug which becomes more available to specific tissues leading to increased antimicrobial activity. It may be noted that the opportunistic pathogen *Pseudomonas aeruginosa* is resistant to a number of antibiotics by developing a protective biofilm around itself. But acridone and its derivatives are found to be effective against this pathogen. The drug efficiency increases further after the formation of inclusion complexes with β-cyclodextrin.

CONCLUSION

From the above results and discussions it is clear that the solubility of acridone and its derivatives can be improved by inclusion complex formation with β-CD which is a very good analytical tool for enhancing the bio-availability of drugs. The negative ΔG, ΔH, ΔS values support the formation of the

inclusion complexes. Cyclodextrins are now widely used for the stabilization of many drugs [20]. Acridone and its derivatives show antibacterial activity, which can further be enhanced by forming their inclusion complexes.

REFERENCES

1. P. Belmont, I. Dorange, *Expert Opinion on Therapeutic Patents*, **18**, 1211 (2008).
2. P. Belmont, J. Bosson, T. Godet, M. Tiano, *Anti-Cancer Agents Med. Chem.*,**7,** 139 (2007).
3. A. Verloop, W. Hoogentraten, J. Tipker, *Drug Design*, **7,** 165 (1976).
4. http://en.wikipedia.org/wiki/acridone/
5. B. Pose-Vilarnovo, I. Perdomo-Lopez, M. Echezarreta-Lopez, *Eur. J. Pharm. Sci*., **13,** 325 (2001)
6. V. G. Belikov, E. V. Kompantseva, *Khim.-Farm. Zh*., **24**, 19 (1990).
7. J. X. Kelly, M. J. Smilkstein, R. A. Cooper, K. D. Lane, R. A. Johnson, A. Janowsky, R. A. Dodean, D. J. Hinrichs, R. Winter, M. Riscoe, *Antimicrob. Agents Chemother.*, **51**, 4133 (2007).
8. T. Higuchi, K. A. Connors, *Adv. Anal. Chem. Instrum*., **4** ,117(1965)
9. C. F. H. Allen, G. H. W. Mckee, *Org. Synth.*, **2**, 15(1943)
10. N. Shufang, F. Xiawen, P. Ying, Y. Xingang, W. Chow, P. Weisan, *Arch. Pharm. Res*., **30,** 991 (2007).
11. S. Panda, J. K. Tripathy, *J. Env. Res. Dev*., **3,** 45 (2008).
12. M. S. Syamala, B. N. Rao, V. Ramamurthy, *Tetrahedron*, **44**, 7234(1988)
13. M. J. Pelzar, E. C. S. Chan, N. R. Kreig, Microbiology, Wiley Interscience, New York, 1983.
14. K. J. Ryan, C. G. Ray, Sherris Medical Microbiology**,** McGraw Hill, London, 2004.
15. Q. Chen, D. Guowang, *Chem. J. I*, **6**, 37 (2004).
16. Z. Szetli, Controlled Drug Bioavailability, Wiley Interscience, 1985.
17. R. A. Rajewski, V. J. Stella, *J. Pharm. Sci*., **85**, 1142 (1996).
18. Y. L. Loukas, V. Vraka, G. Gregoridias, *J. Pharm. Biomed. Anal*., **16,** 263 (1997).
19. T. Stalin, P. V. Rani, B. Shanthi, A. Sekar, N. Rajendiran, *Indian J. Chem., Sec. A*, **45,** 1113 (2006).
20. A. V. Astakhova, N. B. Demina, *Pharm. Chem. J*., **38,** 105 (2004).

ИЗСЛЕДВАНЕ НА ПРОИЗВОДНИ НА АКРИДОН И НА КОМПЛЕКСИ ЧРЕЗ ВКЛЮЧВАНЕ НА β-ЦИКЛОДЕКСТРИН

С. С. Наяк[1,]*, С. Панда[2], П. М. Панда[3], С. Падхи[3]

[1] *Държавен девически колеж, Берхампур 760001, Индия*
[2] *Департамент по химия, Университет Берхампур, Бханджа Вихар 760007, Индия*
[3] *Департамент по микробиология, Медицински колеж и болница, Брхампур 760004, Индия*

Постъпила на 20 септември 2009 г.; Преработена на 14 януари 2010 г.

(Резюме)

Синтезиране са три важни производни на акридона – тиосемикарбазон, семикарбазон и оксим – използвайки кето групата, които имат значителна антимикробна активност. За увеличаване на биологичното възприемане на тези съединения са синтезирани комплекси чрез включване на един нетоксичен олигозахарид β-циклодекстрин. Синтезът на производните и техните комплекси са потвърдени чрез промените в спектралните характеристики и данни за точка на топене. Изследванията на разтворимостта във вода показа стехиометрия 1:1 между съединението и β-циклодекстрина в комплекса. Изчисленията на термодинамичните параметри ΔG (промяна на свободната енергия) ΔH (промяна на енталпията) и ΔS (промяна на ентропията) на комплексите показва спонтанно образуване и екзотермичност на процеса. Определянето на термодинамичните стабилитетни константи предполага съществуване на слаби междумолекулни сили между гост и приемник в комплекса. Изследването на антимикробната активност показва, че микробите като *E. Coli* и *P. Aeruginosa* са чувствителни към акридон и неговите производни и чувствителността се увеличава допълнително след образуването на комплексите чрез включване.

Bulgarian Chemical Communications, Volume 42, Number 2 (pp. 153–160) 2010

Consumption of quercetin and rutin in reactions with free radicals

O. T. Kasaikina[1]*, Z. S. Kartasheva[1], V. D. Kancheva[2], N. V. Yanishlieva[2], I. R.Totseva[2]

[1] *N. N. Semenov Institute of Chemical Physics, Russian Academy of Sciences, 4 Kosygin St., Moscow 119991, Russia*
[2] *Institute of Organic Chemistry with Centre of Phytochemistry, Bulgarian Academy of Sciences, Acad. G. Bonchev St., Block 9, 1113 Sofia,*

Received October 14, 2009

The consumption of flavonols quercetin and rutin in reactions with various free radicals has been studied in homogeneous solutions and in micellar systems of cetyl trimethylammonium chloride by UV spectrophotometry. Free radicals were produced by azoinitiators AAPH and AIBN decomposition in water and in organic medium, respectively. Both quercetin and rutin were used as free radical acceptors to determine the rates of free radical formation in the decomposition of cumene hydroperoxide (ROOH) and hydroperoxides derived from sunflower oil oxidation (LOOH) catalyzed by cetyl trimethylammonium chloride in organic and water media. It was found that apparent rutin consumption rates are 4 -10 times lower than quercetin consumption rates under the same conditions. The ratio of free radical initiation rate to that of flavonol consumption and the stoichiometric factors for quercetin and rutin are discussed.

Key words: quercetin, rutin, free radicals, lipid hydroperoxides, micelles of cetyl trimethylammonium chloride.

INTRODUCTION

Quercetin (Qu) and rutin (Ru) are naturally occurring polyphenolic compounds and they possess a wide range of biological activities [1–4], of which antioxidant and free radical scavenging activities have been extensively explored [5–13]. Quercetin was used as a free radical acceptor to measure the rates of free radical formation during initiator decay in micelle solution by inhibitor method [14].

Lipid hydroperoxides (LOOH) are important factors for oxidation stability of food, cosmetics and other products, containing lipids, due to their ability to decompose into free radicals [1, 2]. Surfactants are commonly used in food, perfume and pharmaceutical industries to stabilize products from stratification. Lipid hydroperoxides are found to be surface-active [15, 16], so hydroperoxides can form mixed aggregates with micelle-forming surfactants. It was shown that oxidation rate of fish oil emulsion (O/W) decreased when oil droplets in water were stabilized by cationic surfactants [15]. Contrary to that, cationic surfactants (S^+) were found to accelerate the oxidation of hydrocarbons and plant oils in organic medium [17–21]. The key stage of lipid oxidation, which is affected by cationic surfactant, is hydroperoxide decomposition, resulting in free radical generation. The rate of free radical generation in mixed micelles LOOH-S^+ was found to depend on a counterion of cationic surfactant, and the most pronounced effect was established in the case of chloride of cetyl trimethylammonium [16, 21]. In the study [16] quercetin was used as a free radical acceptor to measure the initiation rate by the inhibitor method.

It is known that surfactant micelles can alter the partitioning and reactivity of phenolic antioxidants in reverse and direct micelles and emulsions [2–7]. Rutin, considered to be quercetin glycoside (Fig. 1), is more hydrophilic than its aglycon, so rutin localization and partitioning in micelle solution can differ from that of quercetin. Here we report a quantitative kinetic study of the consumption of both quercetin (Qu) and rutin (Ru) in reactions with free radicals formed by micellar systems cetyltrimethylammonium chloride (CTAC) – lipid hydroperoxide or CTAC-cumene hydroperoxide and by azoinitiators AAPH in water and AIBN in organic medium, respectively. It is of interest to compare the consumption kinetics of Qu and Ru, which differ only by the hydrophilic 3-O-sugar substituent.

MATERIALS AND METHODS

Quercetin (Qu), rutin (Ru) and 2,2'-azodiisobutyramidine dihydrochloride (AAPH) (from Fluka, Switzerland) were purchased with highest purity available and used as it was received. Azobis(isobutyronitrile) (AIBN) was purified by recrystallization from ethanol. Cetyl trimethylammonium chloride (CTAC) (Fluka) was used as received. Chlorobenzene and water were purified by double distillation.

* To whom all correspondence should be sent:
E-mail: kasaikina@chph.ras.ru

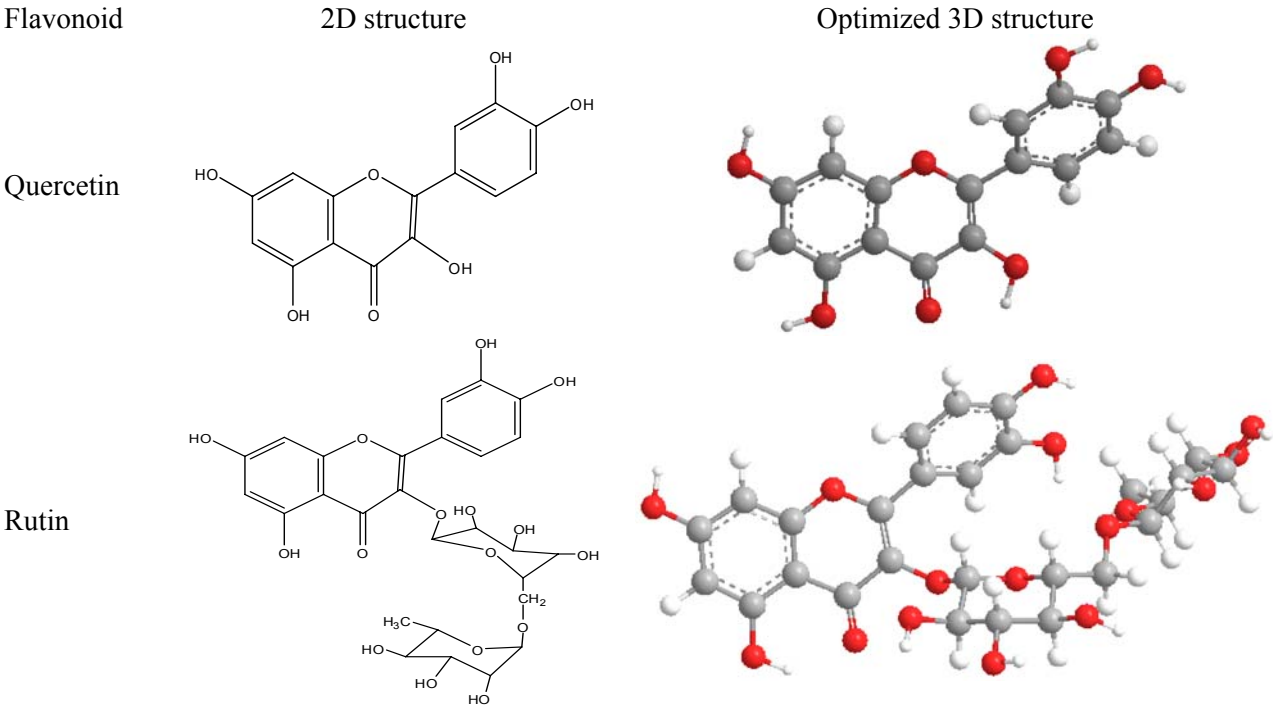

Fig. 1.

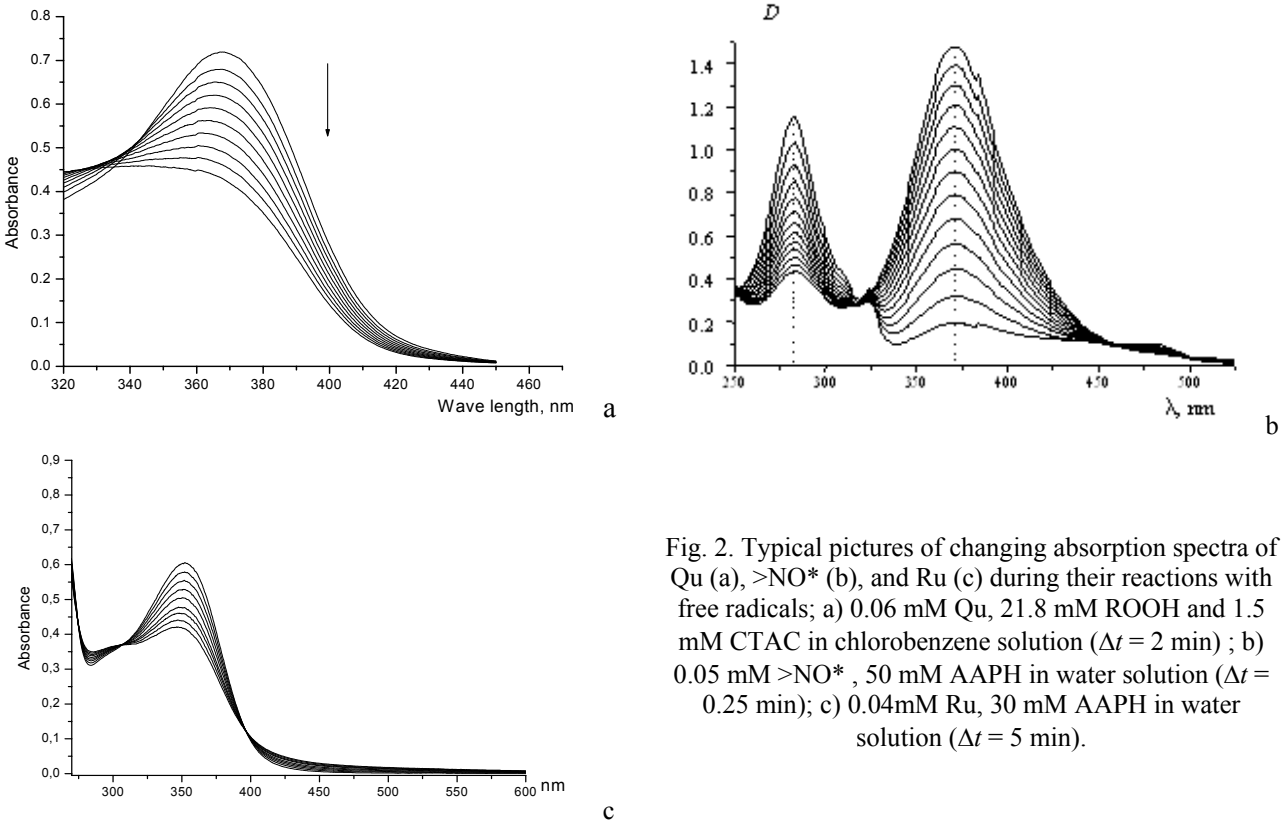

Fig. 2. Typical pictures of changing absorption spectra of Qu (a), >NO* (b), and Ru (c) during their reactions with free radicals; a) 0.06 mM Qu, 21.8 mM ROOH and 1.5 mM CTAC in chlorobenzene solution (Δt = 2 min) ; b) 0.05 mM >NO* , 50 mM AAPH in water solution (Δt = 0.25 min); c) 0.04mM Ru, 30 mM AAPH in water solution (Δt = 5 min).

As lipid hydroperoxides we used the hydroperoxides (LOOH) derived from the autooxidation of sunflower oil. Besides, kinetically pure triacylglycerols of sunflower oil (TGSO) were obtained by cleaning sunflower oil from pro- and antioxidants and trace metals by adsorption chromatography [22]. The lipid oxidation was carried out in a glass vessel by blowing air through the samples at a rate of 1.6 l/h at 80ºC. Cumene hydroperoxide (ROOH, Aldrich) was purified according the method described in [19]. Hydroperoxide concentration was determined by the iodometric method.

The rates of quercetin and rutin consumption were determined by UV spectrophotometry and compared with the consumption rate of the stable nitroxyl radical 4-(spirotetrahydrofuran-2′-yl)-2-spirocyclohexyl-1,2,3,4-tetrahydroquinolin-1-oxyl (>NO*), synthesized according to a known procedure [23]. This nitroxyl radical is a specific trap for peroxyl radicals since their spin adduct (quinone-nitrone) shows a characteristic absorption band in the visible spectrum [24]. The reactions producing free radicals were carried out in quartz cuvette of an Ultrospec 1100 pro spectrophotometer at 37ºC as follows: 2.5 ml of an initiator (AAPH or AIBN or mixture of hydroperoxide with CTAC) solution was placed in a cuvette and held at 37°C for 15 min; thereafter 5–25 μl of stock solution of acceptor (Qu, Ru or >NO*) were added and electronic absorption spectra of reaction mixture were recorded at intervals. Typical pictures of changing absorption spectra of Qu, >NO*, and Ru during their reactions with free radicals are represented in Fig. 2. All kinetic data are the mean arithmetic result of three independent experiments and were processed using the computer program Origin 7.

RESULTS

Both quercetin (Qu) and rutin (Ru) have rather intensive characteristic absorption bands that decrease during their consumption in reactions with free radicals (Fig. 2). Optical characteristics of Qu and Ru are represented in Table 1.

There is a hypsochromic shift of λ_{max} and a slight decrease of ε in water media, compared with those for Qu and Ru in chlorobenzene solution. Noteworthy, CTAC doesn't affect optical characteristics of flavonols in organic media, whereas in water solutions marked bathochromic shifts are observed in the presence of CTAC, which point to an interaction of Qu and Ru with CTAC micelles.

Figs. 3 and 4 show the consumption of Qu and Ru in the system of reverse mixed micelles of CTAC and lipid hydroperoxides in chlorobenzene solution. It must be noted that no flavonol consumption was observed when the same amounts of CTAC or hydroperoxides were taken separately (lines 1 and 2 in Figs. 3 and 4). The rates of Qu and Ru consumption under the experimental conditions do not depend on the initial concentration of flavonols. This is known to be typical for inhibitor consumption in reactions with free radicals when an inhibitor traps all the radicals produced with a constant initiation rate (R_i) [1–3, 9, 25].

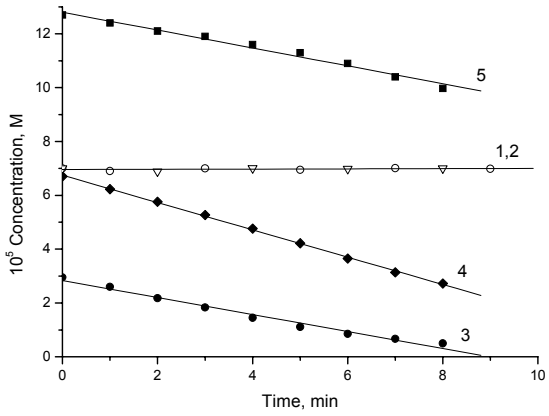

Fig. 3. Kinetic curves of Qu consumption in the presence of 1.65 mM CTAC (1), 20 mM LOOH (2), and in mixture 1.65 mM CTAC and 20 mM LOOH (3–5) in chlorobenzene solution at 37°C; $-d[Qu]/dt = 6.4\times10^{-8}$ M/s (3–5).

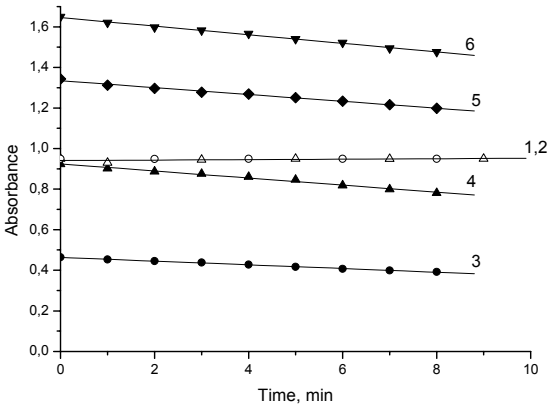

Fig. 4. Kinetic curves of Ru absorption decay in the resence of 1.65 mM CTAC (1), 20 mM LOOH (2), and in the mixture 1.65 mM CTAC and 20 mM LOOH (3–6) in chlorobenzene solution at 37ºC; apparent $-d[Ru]/dt = 1.8\times10^{-8}$ M/s (3–6).

Table 1. Optical characteristics Qu and Ru in organic and water media.

Media	Quercetin		Rutin	
	λ_{max}, nm	ε, $M^{-1}\cdot s^{-1}$	λ_{max}, nm	ε, $M^{-1}\cdot s^{-1}$
Chlorobenzene	373 ± 1	$(2.00 \pm 0.05)\times10^4$	360 ± 1	$(1.50 \pm 0.05)\times10^4$
Chlorobenzene + 1.65 mM CTAC	373 ± 1	$(2.00 \pm 0.05)\times10^4$	360 ± 1	$(1.50 \pm 0.05)\times10^4$
Water	367 ± 1	$(1.80 \pm 0.05)\times10^4$	351 ± 1	$(1.40 \pm 0.05)\times10^4$
Water + 1.65 mM CTAC	382 ± 1	$(1.70 \pm 0.05)\times10^4$	382 ± 1	$(1.20 \pm 0.05)\times10^4$
Water + ABAP	368 ± 1	$(1.80 \pm 0.05)\times10^4$	355 ± 1	$(1.45 \pm 0.05)\times10^4$
Buffer + ABAP	368 ± 1	$(1.70 \pm 0.05)\times10^4$		

ε – the molar extinction coefficient determined from the dependence of absorbance at λ_{max} on molar concentration of Qu or Ru accordingly.

$$-d[Qu]/dt = R_i/n_{Qu}; \quad (1)$$

$$-d[Ru]/dt = R_i/n_{Ru}; \quad (2)$$

Here, n_{Qu} and n_{Ru} are the stoichiometric factors for Qu and Ru, which denote the number of free radicals trapped by each flavonol molecule. It follows from Eqns. (1) and (2) that the ratio of Qu and Ru consumption rates is equal to the reverse ratio of their stoichiometric factors:

$$\{d[Qu]/dt\}/\{d[Ru]/dt\} = n_{Ru}/n_{Qu} \quad (3)$$

According to the data in Fig. 3 and 4, this ratio is equal $n_{Ru}/n_{Qu} = 3.6$. In other words, Qu traps smaller amounts of radicals than Ru. This result is unexpected because Qu is known to be a more efficient antioxidant than Ru [6–13]. Fig. 5 shows the antioxidant effects of Qu and Ru in TGSO autooxidation at 80ºC. It is seen that the induction periods (τ) in the presence of Qu are longer and the rates during the induction period are lower than those for oxidation in the presence of Ru. As a rule, the longer the induction period, the higher the stoichiometric factor is. When R_i remains constant, the induction period is proportional to n:

$$\tau = n\,[\text{Inhibitor}]/R_i \quad (4)$$

Under autooxidation conditions R_i increases in the course of reaction and antioxidants can undergo side reactions, which affect the duration of the induction period. The data of Table 2 show that the higher the initial concentration of flavonols is, the lower is the ratio τ_{Ru}/τ_{Qu}. So, Ru undergoes side reactions in a greater extent than Qu.

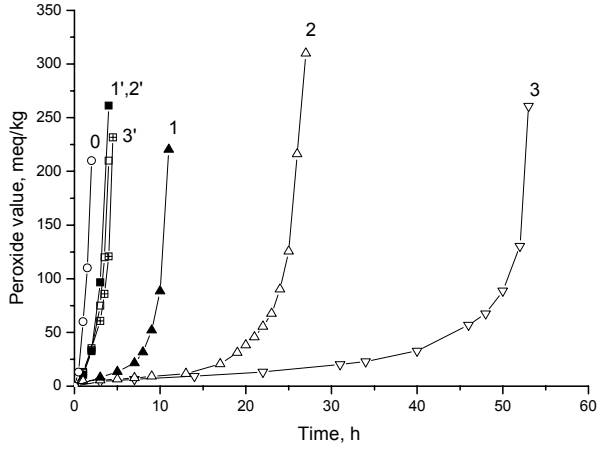

Fig. 5. Kinetic curves of TGSO autooxidation at 80ºC in the absence (0) and in the presence of 0.1 mM Qu (1) and Ru (1'), 0.5 mM Qu (2) and Ru (2'), and 1.0 mM Qu (3) and Ru (3').

To compare stoichiometric factors for Qu and Ru and their ratio in organic and water media we have studied the rates of Qu and Ru consumption in reactions with radicals produced in micellar system CTAC – cumene hydroperoxide (ROOH) in both organic and water media, and with radicals produced by azoinitiators AAPH and AIBN decomposition in water and organic media as well.

Table 2. The ratio of induction periods in the sunflower oil autoxidation in the presence of Qu and Ru at 80ºC.

Initial concentration of flavonols, mM	0.1	0.5	1.0
The ratio of induction periods, τ_{Ru}/τ_{Qu}	0.27	0.11	0.07

Fig. 6 shows that Qu is consumed faster than Ru (Table 3) in the system of reverse mixed micelles of CTAC and ROOH in chlorobenzene solution. The ratio of their consumption rates is equal to: $\{d[Qu]/dt\}/\{d[Ru]/dt\} = n_{Ru}/n_{Qu} = 10.4$. At the same initial concentration of all the components however in the system of normal mixed micelles CTAC-ROOH in water, the ratio of Qu and Ru consumption rates was found to be equal to: $\{d[Qu]/dt\}/\{d[Ru]/dt\} = n_{Ru}/n_{Qu} = 4.0$. Thus, the rate of Ru consumption is evidently lower than that of Qu both in organic and water media.

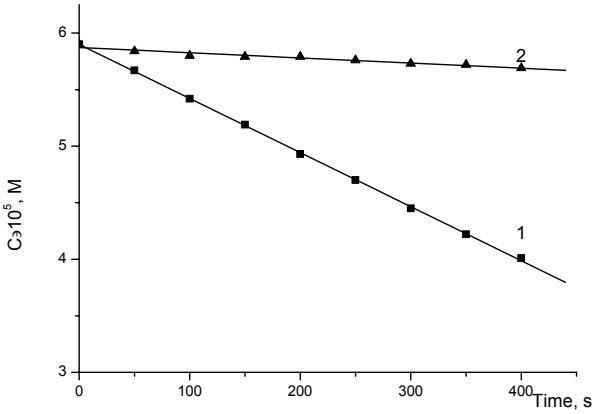

Fig. 6. Kinetic curves of Qu (1) and Ru (2) consumption in the system: 1.65 mM CTAC, 20 mM ROOH in chlorobenzene media at 37°C; $[Qu]_0 = [Ru]_0 = 5.9\times10^{-5}$ M

Table 3. The Qu and Ru consumption in reaction with free radicals produced by ROOH decomposition in micellar system ROOH-CTAC at 37ºC.

System under study	–d[Qu]/dt, $\times10^8$, M/s	–d[Ru]/dt, $\times10^8$, M/s
1.65 mM CTAC, 20 mM ROOH in chlorobenzene	4.78	0.457
1.65 mM CTAC, 20 mM ROOH in water	0.475	0.117

Fig. 7 shows that the rates of consumption of Qu (curve 1) and Ru (curve 2) in water solution of AAPH are proportional to the AAPH concentration.

The initiation rate, when azoinitiators are used, is equal to $R_i = k_i$ [AAPH] [1, 2, 25]. So, the slopes of the lines in Fig. 7 are equal to k_i/n, as follows from Eq. (1) and (2). There are some discrepancies in published values of k_i for AAPH at 37ºC (in s^{-1}): 0.4×10^{-6} [28]; 1.6×10^{-6} [7, 29]; 0.8×10^{-6} [6]. We have measured the free radical formation rate during AAPH decomposition by inhibitor method using stable nitroxyl radical 4-(spirotetrahydrofuran-2′-yl)-2-spirocyclohexyl-1,2,3,4-tetrahydroquinolin-1-oxyl (>NO*) as an acceptor. The chemical reaction of >NO* with peroxyl radicals is known [24] to result in quinone-nitron formation, i.e. the stoichiometric factor for >NO* is equal to 1:

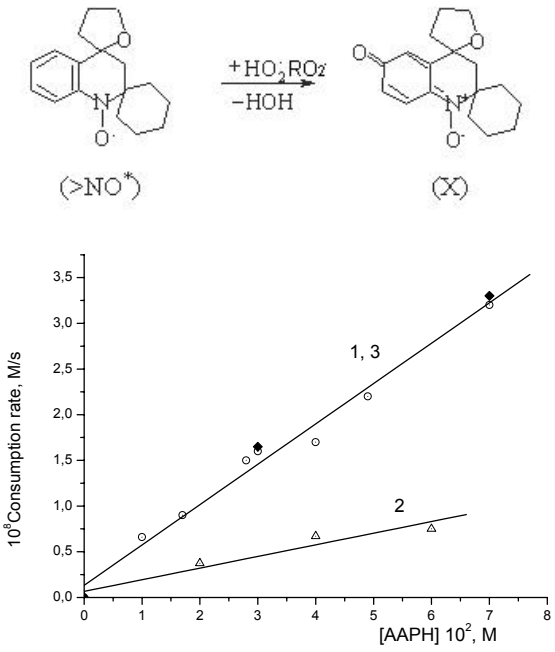

Fig.7. Dependencies of Qu (1) and Ru (2) consumption rates on AAPH concentration in water (o) and buffer (Δ) (pH = 7.2) solutions at 37°C; (3) - the rates of >NO* consumption (♦).

Fig. 7 shows that the values of the rates of quinone-nitron accumulation and Qu consumption practically coincide. It follows that the stoichiometric factor for Qu in the reaction with peroxyl radicals resulted from AAPH decomposition in water solution is equal to 1 and the apparent value for the rate constant of AAPH decomposition into free radicals in water (pH = 6.8) and in phosphate buffer (pH = 7.2) solutions is equal to $k_i = 0.44\times10^{-6}$ s^{-1}. On the basis of these results, the stoichiometric factor for Ru in the reaction with peroxyl radicals resulted from AAPH decomposition in water solution is equal to 4.

The rates of Qu and Ru consumption in chlorobenzene solution in reaction with peroxyl radicals produced by organic soluble azoinitiator AIBN are presented in Table 4. In this case the Qu consumption rate is nearly twice lower than that of >NO*, and the stoichiometric factor for Qu is equal to 2, which coincides with the value reported earlier [6, 14, 30]. The stoichiometric factor for Ru in the reaction with peroxyl radicals resulted from AIBN decomposition in chlorobenzene is equal to 10.

Table 4. Qu, Ru, and >NO* consumption rates in reaction with free radicals produced by 50 mM AIBN decomposition in chlorobenzene solution at 37ºC.

Free radical acceptor	Consumption rate $\times10^8$, M/s	n
Qu	0.8 ± 0.1	1.9 ± 0.2
Ru	0.15 ± 0.02	10 ± 1
>NO*	1.5 ± 0.1	1 ± 0.1

DISCUSSION

It must be noted that in all cases the rates of Qu and Ru consumption are concentration independent when [Qu], [Ru] ≥ 2×10^{-5} M (see, for example, Fig. 3 and 4). According to the theory [2, 6, 13, 25, 30] it means that the chain termination by flavonols (FlOH)

$$LO_2^{\bullet} + FlOH \rightarrow \text{products} \qquad R = k_F [LO_2^{\bullet}][FlOH]$$

is faster than the recombination/dispropotionation of peroxyl radicals:

$$LO_2^{\bullet} + LO_2^{\bullet} \rightarrow \text{products} \qquad R = 2k_t[LO_2^{\bullet}]^2$$

When the relationship (5) is valid:

$$k_F[FlOH][LO_2^{\bullet}] > 2k_t[LO_2^{\bullet}]^2, \qquad (5)$$

the rate of the inhibitor consumption is determined by the free radical initiation rate, R_i, as it is described by Eqns. (1) and (2): $-d[FlOH]/dt = R_i/n$.

To discuss the strange differences between the stoichiometric factors for Qu and Ru, we consider their consumption in reactions with free radicals initiated by the decomposition of known initiators (I). When all the radicals produced are scavenged by the antioxidant (FlOH), i.e. the relationship (5) is valid, the main reactions describing free radical initiation and termination may be represented as follows [6–13, 25]:

$$I \rightarrow rO_2^{\bullet} \qquad R_i = k_i [I] \qquad (i)$$

$$rO_2^{\bullet} + FlOH \rightarrow rO_2H + FlO^{\bullet} \qquad (i1)$$

$$rO_2^{\bullet} + FlO^{\bullet} \rightarrow \text{product-1} \qquad (i2)$$

$$FlO^{\bullet} + FlO^{\bullet} \rightarrow \text{product-2} \qquad (i3)$$

$$FlO^{\bullet} + FlO^{\bullet} \rightarrow FlOH + \text{product (quinone)} \qquad (i4)$$

The stoichiometric factor, determined as $n = R_i/(-d[FlOH]/dt)$, is equal to 1, when the radical termination occurs via the reactions i1 and i3. When the $rO_2^{\bullet}$ and $FlO^{\bullet}$ terminations occur *via* (i1), (i2) and/or (i4), the stoichiometric factor is equal to $n = 2$. This simplest consideration shows that the participation of antioxidant intermediate radicals ($FlO^{\bullet}$) in $rO_2^{\bullet}$ termination and the regeneration of FlOH in some reactions (here it is i4) lead to increase in n.

The data obtained (Fig. 6 and Table 4) show that quercetin is characterized by $n_{Qu} = 1$ in water solution and $n_{Qu} = 2$ in organic medium. The latter value coincides with that obtained for Qu in organic solutions by other authors [6, 25, 29]. A lower value n_{Qu}, obtained in water solutions, points to a change of quercetin intermediate radical ($Qu^{\bullet}$) reactivity in reactions i2 and i4, which are responsible for $n > 1$. In some studies stoichiometric factors are determined by the inhibition period (τ) according to the dependence (6):

$$n = R_i \cdot \tau / [FlOH]_0 \qquad (6)$$

This approach can result in higher values of n, because induction periods sum up antioxidant effects over all intermediate products. In the case of Qu (pentahydoxyflavon), the molecules of product-1 and product-2, containing phenolic hydroxyl groups, can interact with free radicals and elongate the induction period. So, stoichiometric factors deter-mined as the ratio between R_i and the initial consumption rates can be lower than n estimated on the basis of the induction periods.

In the case of Ru, the apparent stoichiometric factors are $n_{Ru} = 4$ in water and $n_{Ru} = 10$ in chlorobenzene solution (Fig. 6 and Table 4). Fig.5 and all the data available [6–13, 26] indicate that Ru is a less effective antioxidant than Qu. A lower consumption rate of Ru compared with Qu decay points to a regeneration of Ru-chromophore system in some reactions: In water solution, the assumed regeneration occurs to a lower extent than in chlorobenzene solution. To explain the low Ru consumption rates, we hypothesize about an intramolecular H-abstraction in rutin phenoxyl radical, which resulted in regeneration of all the hydroxyl groups and transfers the radical center to glycoside tail (Scheme 1).

The new transformed radical ($Rut^{\bullet}$) interacts with other radicals and/or substrates to form the products, which possess the same chromophore group as Ru. This makes the Ru transformation reactions invisible by spectrophotometry and decreases the apparent Ru consumption rate.

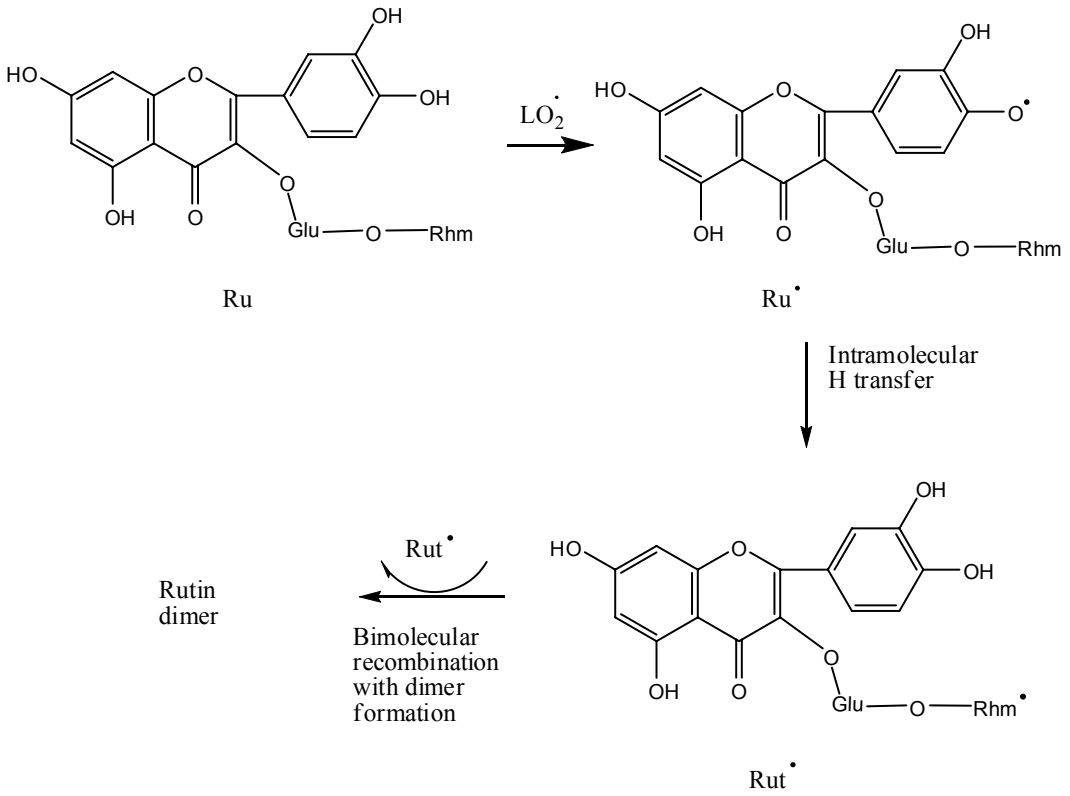

Scheme 1.

The intramolecular radical transformation changes the relatively stable initial phenoxyl radical inactive in oxidation chain propagation ($FlO^{\bullet}$) into alkoxyl radical $Rut^{\bullet}$, which is more active in H- abstraction than phenoxyl radical is. So, this reaction can be considered as an intramolecular chain transfer of an inhibitor radical, which causes a decrease in the antioxidant efficiency of Ru. Naturally, in water solution due to hydration of glycoside tail, the rate of intra-molecular transformation would be lower than that in organic medium. So, the difference between antioxidant effects of Ru and Qu would be greater in organic nonpolar medium than in water solutions. For example, the ratio between the induction periods τ_{Ru}/τ_{Qu} in oil medium, which are presented in Table 2, is less than 0.27. This ratio in AAPH-initiated oxidation of linoleic acid in SDS micelles at 37ºC inhibited by Qu and Ru in water solution is equal to 0.53 [7] and in CTAB solution $\tau_{Ru}/\tau_{Qu} = 0.6$ [7].

CONCLUSION

The results of the present kinetic study demonstrate that stoichiometric factors for flavonols depend greatly on the medium. Using quercetin and rutin as free radical acceptors it has also been shown that cetyltrimethylammonium chloride (CTAC) catalyzes the decomposition of hydroperoxides derived from sunflower oil oxidation (LOOH) into free radicals at physiological temperature. Noteworthy, the rate of free radical initiation by the mixture of CTAC and LOOH is ~1.5 times higher than that caused by the mixture of CTAC with cumene hydroperoxide at the same concentrations.

Acknowledgements: *This work is partly supported by the Russian Foundion for Basic Research, grant No 07–03–00379, Scientific School, grant No 5236.2006.3, and the National Science Fund at the Ministry of Education, Bulgaria, grant BIn4/04.*

REFERENCES

1. F. Shahidi, in: Natural Antioxidants. Chemistry, Health Effects and Applications. F. Shahidi (Ed.), AOCS Press, Champaign, IL, 1997, pp. 1–11.
2. E. N. Frankel, Lipid Oxidation, 2nd Edition, The Oily Press, PJ Barnes & Associates, England, 2005.
3. W. Bors, W. Heller, C. Michel, K. Stettmaier, in: Handbook of Antioxidants. E. Cadenas, L. Packer, (Eds.), Marcel Dekker, New York, 1996, pp. 409–466.
4. N. Yanishlieva, M. Heinonen, in: Antioxidants in Food, Practical Applications, J. Pokorny, N. Yanishlieva, M. Gordon (Eds.), CRC Press, Woodhead Publ Ltd., Cambridge, 2001, pp. 210–263.
5. A. Roedig, M. H. Gordon, *J. Am. Oil Chem. Soc*., **75**, 169 (1998).
6. V. Roginsky, *Arch. Biochem. Biophys.* **414**, 261 (2003).
7. B. Zhou, Q. Miao, L. Yang, Z.-L. Liu, *Chemistry – A European Journal*., **11**, 680 (2005).
8. S. V. Jovanovich, S. Steenken, M. Tosic, B. Marijanovich, M. G. Simic, *J. Am. Chem. Soc.,* **116**, 4846 (1994).
9. A. Hopia, M. Heinonen, *J. Am. Oil Chem. Soc.,* **76**, 139 (1999).
10. V. Kancheva, R. Taskova, I. Totseva, N. Handjieva, *Riv. Ital. Sost. Grasse*, **84**, 9 (2007).
11. V. Butkovic, L. Klasinc, W. Bors, *J. Agric. Food Chem*., **52,** 2816 (2004).
12. W. Bors, W. Heller, C. Michel, M. Saran, *Methods Enzymol.,* **186**, 343 (1990).
13. V. A. Belyakov., V. A. Roginsky, W. Bors, *J. Chem. Soc., Perkin Trans.,* **12,** 2319 (1995).
14. Z. S. Kartasheva, O. T. Kasaikina, *Russ. Chem. Bull.* **43**, 1657 (1994).
15. S. S. Kellerby, D. J. McClements, E. A. Decker, *J. Agric. Food Chem.,* **54**, 7879 (2006).
16. N. A. Trunova, Z. S. Kartasheva, T. V. Maksimova, Yu. G. Bogdanova, O. T. Kasaikina, *Colloid. J.,* **69**, 655 (2007).
17. O. T. Kasaikina, V. D. Kortenska, Z. S. Kartasheva, G. M. Kuznetsova, T. V. Maximova, T. V. Sirota, N. V. Yanishlieva, *Colloids Surf., A - Physicochem. Eng. Aspects*, **149**, 29 (1999).
18. L. M. Pisarenko, O. T. Kasaikina, *Russ. Chem. Bull*., *Int. Ed.,* **51**, 449 (2002).
19. L. M. Pisarenko, T. V. Maksimova, O. T. Kasaikina, *Russ. Chem. Bull. Int. Ed.,* **54**, 1855 (2005).
20. V. G. Kondratovich, V. D. Kortenska, Z. S. Kartasheva, N. V. Yanishlieva, I. R. Totzeva, M. I. Boneva, O. T. Kasaikina, in: Peroxides at the Beginning of the Third Millennium. Synthesis, Properties, Application, V. L. Antonovsky, O. T. Kasaikina, G. E. Zaikov (Eds.), Nova Science Publ., New York, 2004, pp. 261–269.
21. O. T. Kasaikina, V. D. Kancheva, T. V. Maximova, Z. S. Kartasheva, N. V. Yanishlieva, V. G. Kondratovich, I. R. Totseva, *Oxid. Commun.,* **29,** 574 (2006).
22. A. Popov, N. Yanishlieva, J. Slavcheva, *Compt. Rend. Acad. Bulg. Sci*., **21**, 443 (1968).
23. A. B. Shapiro, E. G. Rozantsev, L. S. Povarov, V. I. Grigos, *Bull. Acad. Sci. USSR, Div. Chem. Sci.,* **14**, 1069 (1965).
24. T. V. Lobanova, O. T. Kasaikina, L. S. Povarov, A. B. Shapiro, A. B. Gagarina, *Dokl. Akad. Nauk SSSR,* **245**, 1154 (1979).
25. E. T. Denisov, I. B. Afanas'ev, in: Organic Chemistry and Biology, CRC Press, Boca Raton, FL, 2005.
26. V. Kancheva, D. Dinchev, M. Tsimidou, N. Nenadis, *Riv. Ital. Sost. Grasse*, **84**, 77 (2007).
27. S. Burda, W. Oleshek, *J. Agric. Food Chem*., **49**, 2774 (2001).
28. W. A. Pryor, Th. Strickland, D. F. Church, *J. Am. Chem. Soc*., **110**, 2224 (1988).

29. E. Niki, N. Noguchi, M. Iwatsuki, Y. Kato, in: Proc. Int. Symp. Natural Antioxidants. Molecular Mechanisms and Health Effects, L. Packer, M. G. Traber, W. Xin, (Eds.), AOCS Press, Champain, Illinois, 1995.p. 1–8.
30. V. Roginsky, E. A. Lissi, *Food Chem*., **92,** 235 (2005).
31. A. Popov, N. Yanishlieva, Autoxidation and Stability of Lipids, Publ. House Bulg. Acad. Sci., Sofia, 1976, pp. 71–72 (in Bulgarian).

ИЗРАЗХОДВАНЕ НА КВЕРЦЕТИН И РУТИН В РЕАКЦИИ СЪС СВОБОДНИ РАДИКАЛИ

О. Т. Касаикина[1]*, З. С. Карташева[1], В. Д. Кънчева[2], Н. В. Янишлиева[2], И. Р. Тоцева[2]

Институт по химическа физика „Н. Н. Семьонов“, Руска академия на науките, ул. „Косигин“, № 4, Москва 119991, Русия
Институт по органична химия с център по фитохимия, Българска академия на науките, ул. „Акад. Г. Бончев“, бл. 9, София 1113

Постъпила на 14 октомври 2009 г.

(Резюме)

Изучено е изразходването на флавонолите кверцетин и рутин по реакция със свободни радикали в хомогенни разтвори и мицеларни системи, съдържащи цетилтриметиламониев хлорид чрез прилагане на УВ-спектроскопия. Свободните радикали се зараждат при разпадането на азоинициаторите 2,2`-азобисизобутил-амидиндихидро-хлорид, ААРН и азобис(изобутилонитрил), АИБН съответно във водна и органична среда. И двата антиоксиданта кверцетин и рутин са използвани като акцептори на свободни радикали за определяне скоростите на образуване на свободни радикали при разпадането на кумиловите хидропероксиди (ROOH) и на хидропероксидите, получени при липидното автоокисление (LOOH), катализирано от цетилтриметиламониевия хлорид в органична и водна среда. Установено е, че скоростта на изразходване на рутина е 4–10 пъти по-бавна от скоростта на изразходване на кверцетина при същите експериментални условия. Дискутирано е съотношението на скоростта на зараждане на свободните радикали и на изразходването на флавонолите и стехиометричния фактор на кверцетина и рутина.

Bulgarian Chemical Communications, Volume 42, Number 2 (pp. 161–166) 2010

Oxidation of lindane in contaminated water under solar irradiation in the presence of photocatalyst and oxidizing agents

G. Krishnamurthy[1,*], M. Sona Bai[2]

[1] *Department of Chemistry, Bangalore University, Central College Campus, Bangalore-560 001, India,*
[2] *Department of Chemistry, Goutham College, Bangalore, India*

Received June 5, 2009; Revised January 25, 2010

The oxidation of lindane is investigated by photooxidation and photocatalytic procedures using solar light irradiation. The photocatalyst used in photocatalysis is Degussa P25 TiO_2. The degree of oxidation is followed by chemical oxygen demand (COD) measurements. The oxidation process is carried out at different initial concentrations of lindane varying from 0.05×10^{-2} M to 1.0×10^{-2} M. The photooxidation and photocatalytic oxidation are studied in the presence of $H_2O_2/K_2Cr_2O_7$ to check the effect of oxidizing agents on the rate of oxidation. The higher rate of oxidation is observed in the presence of H_2O_2 when compared to $K_2Cr_2O_7$ in photocatalysis. The decrease in the concentration of lindane during oxidation is also followed by UV-visible absorption studies. The oxidation of lindane follows the first order kinetics and the value of the rate constant k, as calculated, is 0.43×10^{-4} s^{-1}.

Key words: photooxidation, solar irradiation, photocatalyst, COD measurement, lindane.

INTRODUCTION

Wastewater treatment is one of the challenging areas of the environmental pollution control as our hydrosphere is getting contaminated with significantly high concentrations of various chemicals. These chemicals include the pesticides used mainly in agriculture; dyes used in the textiles, laboratory reagents, *etc*. Pesticides constitute one of the major classes among pollutants. In recent years pesticide compounds (insecticides, herbicides, fungicides, nematodes, rodenticides, *etc*.) are being increasingly used in the control of pests. Many of these chemicals persist for long periods causing contamination of water, soil and air environment. Many of these pesticides and organochlorine compounds are toxic, carcinogenic and mutagenic. The contamination of water by these chemicals has become a major and serious problem globally and removal of these contaminants has become very challenging.

There are several techniques of removal of contaminants from the water [1–4] and some of them are found to be inefficient procedures. Biological oxygen demand (BOD) and the chemical oxygen demand (COD) [5–7] are among the waste water quality indicators, which are essentially laboratory tests to determine the pollutant content. Any oxidizable material present in a natural waterway or in an industrial or wastewater will be oxidized both by biochemical (bacterial) or chemical processes. Recent developments in the domain of chemical water treatment have led to improved oxidative degradation procedures, which are generally referred to as advanced oxidation processes (AOP). Among AOP the photooxidation has attracted much attention for the degradation of pesticides and organic pollutants in contaminated water [8–11]. Photooxidation uses the energy in light to destroy environmental contaminants, applicable both as a waste clean-up and a pollution control technique.

In photocatalysis TiO_2 is a widely used photocatalyst [8–11]. A wide range of photonic efficiencies are observed among various TiO_2 phases and formulations. Studies have shown that mixtures of anatase and rutile TiO_2 perform better than either individual rutile or anatase phases of TiO_2 [12] and the high photocatalytic activity is reported in some mixed-phase TiO_2 preparations such as Degussa P25. The commercial Degussa P25 TiO_2 contains 80 to 90% of anatase and 10 to 20% of rutile [12]. The inactivity of pure-phase rutile is due in part to rapid rates of recombination. In mixed-phase TiO_2, charges produced on rutile by visible light are stabilized through electron transfer to lower energy anatase lattice trapping sites. These results suggest that within mixed-phase titania (P25) there is morphology of nanoclusters containing typically small rutile crystallites interwoven with anatase crystallites. The transition points between these two phases allow for rapid electron transfer from rutile to anatase. Thus, rutile acts as an antenna to extend the photoactivity into visible wavelengths [13] and the structural

* To whom all correspondence should be sent:
E-mail: gkmurthy_2005@yahoo.com

arrangement of the similarly sized TiO_2 crystallites creates catalytic "hot spots" at the rutile-anatase interface. Hence, the commercial Degussa P25 TiO_2 photocatalyst has been chosen for the photocatalytic oxidation study in order to compare with direct photooxidation and chemical oxidation.

In the present work the oxidation of lindane by direct photolysis and photocatalytic oxidation by chemical oxygen demand (COD) measurement method is discussed. Lindane is an organochlorine insecticide. Consumption or acute exposure to lindane can cause health hazards in humans, aquatic animals and birds [14]. Hence, the suitable procedure for the decontamination of lindane from the aquatic environment is needed. In this regard, in the present study the oxidation of lindane by solar light irradiation and by an oxidizing agent in the presence/absence of catalyst has been explored. The analyses are made by oxygen demand measurements (COD tests) and also by UV-visible absorption studies.

EXPERIMENTAL

Materials

Lindane is obtained from Rallis India Ltd., an Agrochemical Research Station, Bangalore, India. The purity of the compound was about 98.5% and it was used as obtained from the industry without further purification. Benzene hexachloride (BHC) is the 100% pure form of the product while lindane is slightly less pure (> 99% pure). There are eight separate three dimensional forms (isomers) of BHC; the gamma configuration being one of those forms. Lindane refers only to the γ-isomer of BHC [14].

The other materials such as potassium dichromate, ferrous ammonium sulphate (FAS), silver sulphate, mercuric sulphate, hydrogen peroxide, H_2SO_4 and Ferroin indicator of Merck chemicals are used for the study. Degussa P25 TiO_2 as supplied by the company has surface area of about 50 m^2/g and anatase and rutile ratio is 4:1 (80%:20%).

Analytical Methods

Photooxidation and photocatalytic oxidation procedures are employed to study the oxidation of lindane in which COD measurement and absorption studies are used as analytical methods to follow the degradation of lindane. The value of COD indicates the concentration of the lindane in the solution. The COD values give the extent of degradation of lindane under solar illumination.

The UV-visible spectra of the samples were obtained using Shimadzu UV-VIS-160 model instrument. The decrease in the absorption intensity of the bands corresponds to the wavelengths, 198 nm and 190 nm indicating the degradation of lindane.

Reactors

Photoreactor. The photoreactor unit consists of the optical convergence lens of circumference of 39 cm which was fixed at the appropriate height in such a way that the entire area of the reaction vessel would focused by the sun light and it was maintained carefully throughout the experiment. It consists of a glass reaction vessel of circumference 34 cm, 1 litre capacity, which was mounted on a magnetic stirrer. The entire set up is encased in a cabinet.

COD (chemical oxidation) reactor. The experimental setup used for COD test is a round bottom flask fitted with reflux condenser (water cooled). The heating was done using heating mantle.

Experimental procedure

Photooxidation of lindane at 0.1×10^{-2} M concentration has been studied under solar light irradiation. The solution of about 500 ml was kept under constant stirring during irradiation. The solar irradiation was performed between 11 a.m. to 2 p.m. during June and September months in 2008. The experimental setup was made on the roof of the research laboratory in Bangalore, India. The latitude and longitude are 12.58 N and 77.38 E, respectively. The average intensity of sunlight was around 1.16×10^{3} $W\cdot cm^{-2}$. The solar light was concentrated by using convex lens and the reaction mixture was exposed to this concentrated solar light. The samples were withdrawn before the start of irradiation and at 30, 60, 90 and 120 min during irradiation in about 30 ml quantities each time. The similar procedure was involved in photocatalysis, but in the presence of Degussa P25 TiO_2 photocatalyst. The samples from the photocatalysis were centrifuged to remove suspended photocatalyst. Then COD measurements were made for these samples using strong oxidizing agent potassium dichromate. The process is largely followed by measuring chemical oxygen demand (COD) of the solution and also studied by UV-visible absorption measurements. The COD determination involves the use of oxidizing agent, such as potassium dichromate, to oxidize the chemical in acidic aqueous medium. The other reagents such as silver sulfate were added as catalyst and mercury sulfate in order to avoid the formation of silver halide [5–7, 15, 16].

RESULTS AND DISCUSSION

Chemical Oxygen Demand (COD) measurement

The degree of oxidation is followed by chemical oxygen demand (COD) measurements. The samples of photooxidation and photocatalytic oxidation experiments are used for COD measurements. In general the COD value indicates the extent of contamination of water by the pollutants. In this study, it also implies the concentration (amount) of lindane oxidized. The general reaction of potassium dichromate with lindane is given by the equation:

$$C_6H_6Cl_6 + 2Cr_2O_7^{2-} + 2H_2SO_4 \rightarrow$$
$$\rightarrow 6CO_2 + 2H_2O + 6HCl + 2Cr_2SO_4 \qquad (1)$$

The COD calculations are made using the following relationship:

$$COD = 8000\,(V_2 - V_1)N/V \qquad (2)$$

Where V_2 is the volume of FAS used in the blank sample, V_1 is the volume of FAS in the original sample, and N is the normality of FAS. If millilitres are used consistently for volume measurements, the result of the COD calculation is given in mg/L.

Higher COD value indicates higher concentration of contaminants in the water. On treating any particular waste water (of particular concentration) the COD should decrease. Here, COD test itself is considered as the chemical oxidation. However, this method itself introduces lots of toxicants such as chromium ions, acid, *etc*., along with the degradation of lindane. Hence, a suitable environmental friendly method is essential for removal of water contaminants. In this regard, photooxidation by natural or artificial light irradiation is prominent.

Optimal concentration of lindane

The optimal concentration of lindane was determined by conducting COD experiments at various concentrations such as 0.05×10^{-2} M, 0.1×10^{-2} M, 0.5×10^{-2} M and 1.0×10^{-2} M in the presence of fixed amount of oxidizing agent and catalyst. The COD value is doubled for 0.1×10^{-2} M concentration of lindane and further there is a slight decrease in the proportional COD values. This may be due to decrease in the catalytic activity of the silver ions and competitive reactions with the degradation metabolites. Therefore, 0.1×10^{-2} M solution of lindane is used as optimum concentration for this study. The corresponding COD values are given in Table 1. Similarly, optimal refluxing time was determined and it was found to be 1.5 h for the above optimal concentration.

Table 1. The COD (chemical oxidation) values corresponding to various concentrations of lindane.

Concentration, $\times10^{-2}$ M	COD value, $\times10$ mg/L
0.05	15.34
0.1	33.21
0.5	131.30
1.0	228.57

Photooxidation and photocatalytic oxidation

The photooxidation is carried out under solar light at various concentrations of lindane as mentioned above. The COD values of the samples are determined in these experiments after 120 minutes of irradiation. The decrease in the COD values implies the increase in the oxidation of lindane. The COD values at the various initial concentrations of lindane used in the photooxidation experiments are plotted as shown in Fig. 1. The higher COD values in chemical oxidation indicate the greater amount of oxygen required for the oxidation of lindane. The lower COD values in the photooxidation and photocatalytic oxidation imply the oxidation of lindane by these processes as shown in Fig. 1. The COD values in photocatalytic oxidation are significantly less than 50% (curve a) of that of photooxidation (curve b) as depicted in the figure. This implies the effect of catalyst on the oxidation of lindane. The concentration of lindane has become zero after 90 min. of solar irradiation. It can also be seen from the figure that the maximum in oxidation has occurred for 0.1×10^{-2} M lindane, which is the optimal concentration. The COD values for the photooxidation and photocatalytic oxidation of lindane for 0.1×10^{-2} M concentration, at different time intervals are given in Table 2. The decrease in COD values with increase in solar irradiation time implies an increase in the oxidation of lindane.

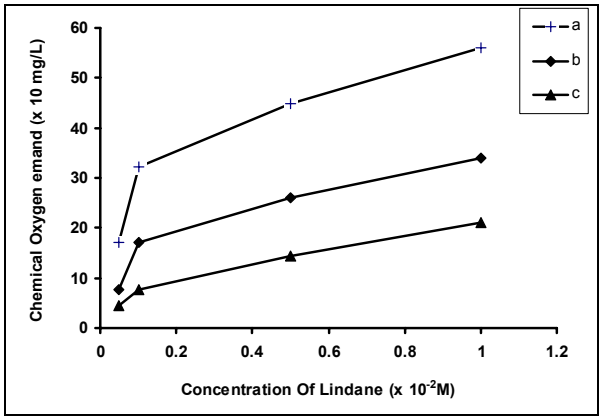

Fig. 1. Plots of COD values as a function of concentration of lindane in which the curves, a, b and c correspond to chemical oxidation, photooxidation and photocatalytic oxidation, respectively.

Table 2. COD values for the photooxidation and photocatalytic oxidation of lindane **(**0.1×10^{-2} M**)** at different time intervals.

Irradiation time, min	COD value, ×10 mg/L	
	Photooxidation	Photocatalytic oxidation
0	33.44	33.21
30	25.24	10.56
60	21.80	7.88
90	18.16	0.0
120	17.68	0.0

The UV-visible spectral studies have also been employed. The spectra for the initial sample (before irradiation) and for the samples after 30, 60, 90 and 120 minutes of solar irradiation are shown in Fig. 2. The λ_{max} for lindane is found to be at 198 nm. The intensity of absorption decreases with increase in irradiation. The absorption intensity is decreased considerably after 120 min. of irradiation. This indicates nearly 70% oxidation of lindane, whereas in photocatalysis in the presence of Degussa P25 TiO_2, the complete oxidation of lindane takes 0 min. of irradiation. The bands at 198 nm and at 190 nm are characteristic of aromatic $\pi\rightarrow\ \pi^*$ transition. The decrease in intensity of absorption bands shows the degree of oxidation of the compound in other words the degradation of lindane.

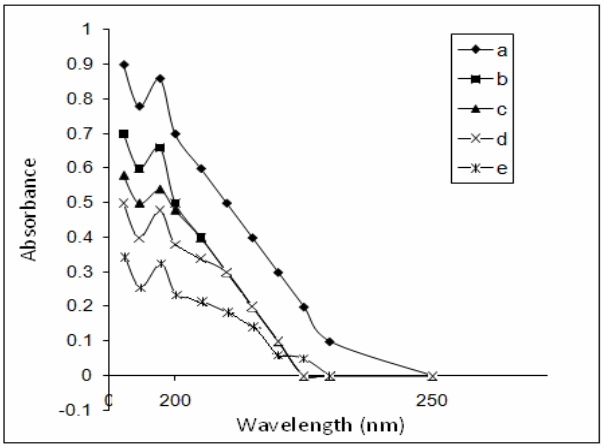

Fig. 2**.** Superimposed UV-visible absorption spectra: a. sample before solar irradiation; b. sample after 30 min. of irradiation; c. sample after 60 min; d. sample after 90 min.; e. after 120 min..

However, in photo/photocatalytic oxidation experiments for efficient oxidation, the intensity of the solar light focused on to the reaction solution is very important. The amount of radiation intercepted by a planetary body varies inversely proportional to the square of the distance between the star and the planet. The Earth's orbit and obliquity change with time (over thousands of years), sometimes forming a nearly perfect circle, and at other times stretching out to an orbital eccentricity of 5% (currently 1.67%). The total solar illumination remains almost constant but the seasonal and latitudinal distribution and intensity of solar radiation received on the Earth's surface also varies [17]. Fig. 3 is the solar spectrum, which shows the absorption of sun light at different wavelength regions. However in the present research work photo/photocatalytic oxidation using solar light was performed as described previously.

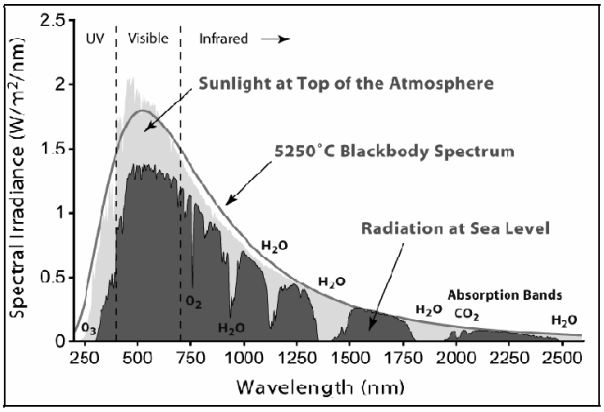

Fig. 3. Solar radiation spectrum which shows the radiation of sunlight at the top of the atmosphere, at sea level and black body radiation.

Effect of oxidizing agent on the rate of photo/photocatalytic oxidation

The degree of conversion is depending on several factors and one of them is the formation of photo-generated reactive radical species. Therefore, the photo/photocatalytic oxidation experiments were conducted in the presence of oxidizing agents such as H_2O_2 and $K_2Cr_2O_7$. The presence of oxidizing agents causes the formation of OH radicals under light illumination more efficiently in the presence of photocatalysts. The OH radicals are highly potent oxidants, which enhance the rate of oxidation. The oxidation of lindane in these processes is analyzed by COD determination at different time intervals during illumination. The COD values from the photo-oxidation and photocatalytic oxidation experiments in the presence of H_2O_2/$K_2Cr_2O_7$ are plotted against the illumination time as shown in Fig. 4. The curves a, b and c correspond to photooxidation of lindane carried out in the absence of oxidizing agent, in the presence of H_2O_2 (5 ml of 0.01 M) and in the presence of $K_2Cr_2O_7$ (5 ml of 0.01 M), respectively. The higher rate of oxidation is observed in the presence of H_2O_2 than that in the presence of $K_2Cr_2O_7$ (Table 3). The reason may be the ease of formation of greater number of OH radicals in the presence of H_2O_2 when compared to $K_2Cr_2O_7$. The dichromate may directly oxidize lindane to some extent since it is a strong oxidant provided the media is acidic, but the formation of the essential

OH radicals is considerably less. Hence, the higher rate can be expected in the presence of H_2O_2. However, the rate of oxidation of lindane is much higher in the presence of both catalyst and oxidizing agents, i.e. in the photocatalysis. There is a rapid decrease in the COD values in these experiments (curves d, e and f). The curves d, e and f correspond to photocatalytic oxidation of lindane carried out in the absence of oxidizing agent, in the presence of H_2O_2, and in the presence of $K_2Cr_2O_7$ at 5 ml of 0.01 M concentration, respectively. The highest rate of oxidation is observed with H_2O_2, when compared to dichromate.

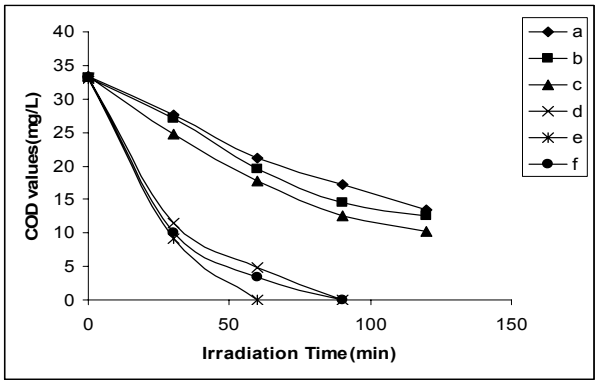

Fig. 4. Plot of COD values as a function of solar irradiation time for the oxidation of lindane in which the curves a, b and c correspond to the photooxidation experiments and the curves d, e and f correspond to photocatalytic oxidation experiments. The curves a and d, b and e, and c and f correspond to the experiments carried out in the absence of oxidizing agent, in the presence of H_2O_2 and in the presence of $K_2Cr_2O_7$, respectively.

Table 3. COD values for the photooxidation and photocatalytic oxidation of lindane (0.1×10^{-2} M) in the presence of H_2O_2 and $K_2Cr_2O_7$ as additional oxidizing agents.

Irradiation time, min	COD values in photooxidation experiments			COD values in photocatalytic oxidation experiments		
	Without Oxidant	With H_2O_2	With $K_2Cr_2O_7$	Without Oxidant	With H_2O_2	With $K_2Cr_2O_7$
0	33.34	33.25	33.3	33.22	33.0	33.12
30	27.6	27.0	24.8	10.56	8.72	9.12
60	21.2	19.5	17.8	7.88	0.0	1.35
90	17.3	14.6	12.5	0.0	0.0	0.0
120	13.5	12.5	10.2	-	-	-

Efficiency and kinetics of photooxidation and photocatalytic oxidation

The efficiency 'η' of photo/photocatalytic oxidation is defined by conversion degree as follows:

$$\eta = [(COD_0 - COD)/COD_0]\times100 \quad (\%) \quad (3)$$

Where, COD_0 and COD denote the concentrations at the initial moment and given time t, respectively. Fig. 5 is a plot of η(%) *versus* irradiation time, which implies the percentage of conversion of lindane to product to be high at the beginning and later it became almost constant. About 70% efficiency of total oxidation is achieved within 90 min of irradiation in photooxidation. However, 100% efficiency is achieved in photocatalysis in 90 min of irradiation.

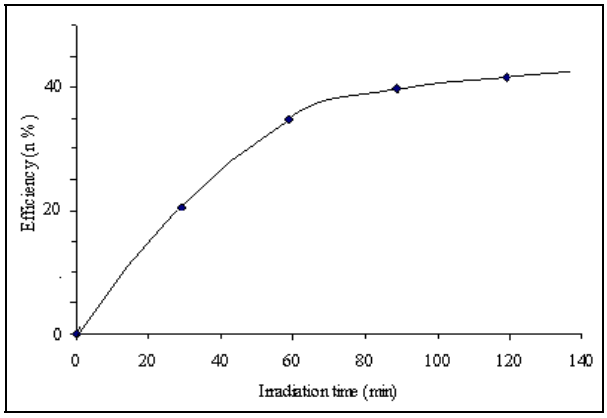

Fig. 5. Plot of oxidation efficiency 'η(%)' *versus* irradiation time.

COD concentration can be fitted well by the following apparent first-order kinetics:

$$\ln(COD_0/COD) = kt \quad (4)$$

Where, k is the apparent first-order reaction rate constant, which is found to be 0.43×10^{-4} s^{-1} for the oxidation of lindane. Fig. 6 represents the plot of $\log(COD_0/COD)$ *versus* irradiation time, in which the initial rate of oxidation is high. About 70% of degradation (of total oxidation) has taken place in the course of 1.5 h of irradiation, whereas the rate constant for photocatalytic oxidation is 1.27×10^{-4} s^{-1}, in which 100% oxidation has taken place.

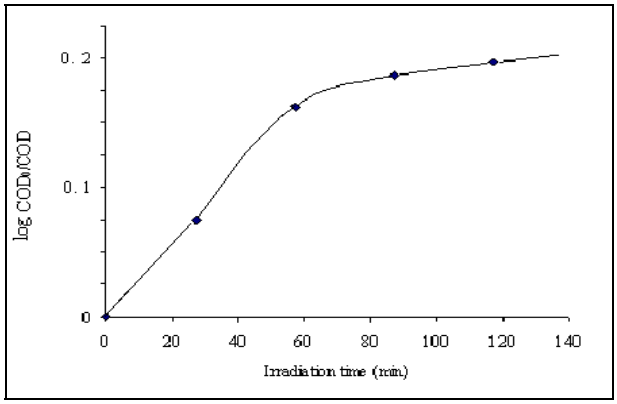

Fig. 6. Plot of $\log(COD_0/COD)$ *versus* irradiation time.

CONCLUSION

In this research work a comparative study of photooxidation and photocatalytic oxidation of lindane has been explored by using oxygen demand

measurement procedure. The photocatalytic oxidation is found to be doubly efficient than direct photooxidation at 0.1×10^{-2} M concentration of lindane in the presence of commercially available Degussa P25 TiO_2. The method is more simple and cost effective as it uses the more abundant solar light for the oxidation of lindane. This procedure can be extended to study the detoxification of other water contaminants. The efficiency of the solar photo/photocatalytic oxidation is enhanced considerably in the presence of oxidizing agents. Decrease in the COD values in the presence of oxidizing agents implies an increase in the oxidation of lindane. Comparatively higher rate of degradation is observed with H_2O_2 than that with potassium dichromate.

REFERENCES

1. D. G. Frodin, Guide to Standard Floras of the World, Cambridge University Press, Cambridge, 2001.
2. R. J. Goodland, Oikos, **26**, 240 (1975).
3. R. Ulanowicz, Ecology: The Ascendant Perspective, Columbia, 1997.
4. C. Molles Jr., Ecology: Concepts & Applications, Fourth Edition Manuel, University of New Mexico, McGraw Hill Publishing, 2008.
5. J. C. Philip, Survey of Industrial Chemistry, John Wiley & Sons, New York, 1987.
6. C. N. Sawyer, P. L. McCarty, G. F. Parkin, Chemistry for Environmental Engineering and Science, 5th Edn., McGraw-Hill, New York, 2003.
7. L. S. Clescerl, A. E. Greenberg, A. D. Eaton., Standard Methods for Examination of Water and Wastewater, 20th Edn., American Public Health Association, Washington, 1999.
8. C. S. Turchi, D. F. Ollis., *J. Catal*., **122**, 178 (1990).
9. L. G. Devi, G. Krishnamurthy, *Oxid. Commun*., **27**, 577 (2004).
10. L. G. Devi, G. Krishnamurthy**,** *J. Environ. Sci. Health, Part B*, **43**, 553 (2008).
11. L. Gomathi Devi, G. Krishnamurthy**,** *J. Hazard. Mater*., **162**, 899 (2009);
12. A. G. Agrios, K. A. Gray, E. Weitz, *Langmuir*, **19,** 1402 (2003).
13. S. Bakardjieva, J. Šubrt, V. Štengl, M. J. Dianez, M. J. Sayagues, *Appl. Catal. B: Environ*., **58**, 193 (2005).
14. A. G. Smith, in: Handbook of Pesticide Toxicology, Vol. 3, Classes of Pesticides, W. J. Hayes Jr., E. R. Laws, Jr. (eds.), Academic Press Inc., New York, 1991.
15. T. M. Orlando, T. B. McCord, G. A Grieves, *Icarus*, **177**, 528 (2005).
16. N. N. Greenwood, A. Earnshaw, Chemistry of the Elements, 2nd Edn., Butterworth-Heinemann, Oxford, 1997.
17. A. Berger, M. F. Loutre, *Quaternary Sci. Rev*., **10**, 297 (1991).

ОКИСЛЕНИЕ НА ЛИНДАН В ЗАМЪРСЕНИ ВОДИ ПОД ДЕЙСТВИЕ НА СЛЪНЧЕВА СВЕТЛИНА В ПРИСЪСТВИЕ НА ФОТОКАТАЛИЗАТОР И ОКИСЛИТЕЛЕН АГЕНТ

Г. Кришнамурти[1,]*, М. Сона Бай[2]

[1] *Департамент по химия, Университет на Бангалор, Бангалор 560001, Индия*
[2] *Департамент по химия, Колеж Гутам, Бангалор, Индия*

Постъпила на 5 юни 2009 г.; Преработена на 25 януари 2010 г.

(Резюме)

Изследвано е окислението на линдан чрез фотоокисление и във фотокаталитични процеси с използване на слънчева светлина. Използван е фотокатализатор TiO_2 Degussa P25. Степента на окисление е определена чрез измерване на химически потребния кислород (ХПК). Окислителният процес е провеждан при различни начални концентрации на линдан - от 0.05×10^{-2} M до 1.0×10^{-2} M. Фотоокислението и фотокаталитичното окисление са изследвани в присъствие на H_2O_2 и $K_2Cr_2O_7$ за да се проследи ефекта на окислителни агенти върху скоростта на окисление. При фотокатализа по-висока скорост на окисление е наблюдавана в присъствие на H_2O_2 в сравнение с $K_2Cr_2O_7$. Намалението на концентрацията на линдан по време на окислението е следено чрез абсорбцията в УВ-видима област. Окислението на линдан следва кинетиката на реакция от първи порядък и изчислената стойност на скоростната константа k е 0.43×10^{-4} s^{-1}.

Bulgarian Chemical Communications, Volume 42, Number 1 (pp. 167–173) 2010

Water splitting in PEM electrolysis with Ebonex supported catalysts

A. E. Stoyanova*, E. D. Lefterova, V. I. Nikolova, P. T. Iliev, I. D. Dragieva, E. P. Slavcheva

Institute of Electrochemistry and Energy Systems, Bulgarian Academy of Sciences, Acad. G. Bonchev St., Block 10, 1113 Sofia, Bulgaria

Received January 12, 2010; Revised February 19, 2010

A series of mono- and bi-metallic compositions, containing Pt, Co and Pt-Co in various ratios, supported on Ebonex were prepared using the borohydride wet chemical reduction method. It was found that PtCo/Ebonex shows enhanced efficiency toward oxygen evolution in PEM water electrolysis compared to pure metallic Pt. The activity changes in the order: Pt3Co2/Ebonex > Pt3Co2> Pt3Co/Ebonex > Pt/Ebonex > Co/Ebonex. The effect was explained by the formation of solid solution between the metallic components combined with hyper-hypo-d-electron metal-support interactions. These effects, together with the high stability of the supporting material against oxidation, give reason to consider Ebonex as alternative support for the anodic catalytic materials used in PEM water electrolysis.

Key words: PEM water electrolysis, Pt, Co, Ebonex.

INTRODUCTION

Polymer Electrolyte Membrane Water Electrolysers (PEMWE) are the newest development in the electrolyser technology with high potential for further improvements and with main advantages, compared to conventional alkaline water electrolysis such as no use of fluid electrolyte, lower energy parasitic losses and very high purity of the produced hydrogen [1]. However, this technology is still expensive since the used catalysts are predominantly Pt and Pt alloys. The main source of energy dissipation during the electrochemical splitting of water is the oxygen evolution reaction (OER). Therefore, the synthesis of highly active and cost efficient OER catalysts is of great importance for the effective functioning of PEMWEs.

One way to reduce the cost of the catalysts is to alloy Pt with other less expensive transition metals (Fe, Co, Ni, Cu, Mo, Sn, Pd, Ir) [2–14]. Alloying with base metals can reduce the amount of Pt and at the same time increase the stability of the catalyst impeding the Pt surface mobility and thus, preventing the particles growth and formation of clusters [9, 15]. Another way is the development of composite catalysts with increased activity through realization of synergetic effects with the catalytic substrate [9, 16, 17]. The main advantage of the most used carbon support is its very high surface area combined with excellent electroconductivity. Its big disadvantage is the lack of stability at high anodic potentials.

Recently, Magneli phase titanium oxides with general formula Ti_nO_{2n-1} known under the trade name Ebonex (Atraverda Inc., UK) have been investigated as a substitute support material of carbon [18–20]. Ebonex has a unique combination of electrical conductivity approaching that of a metal and high corrosion resistance approaching that of ceramics. The primary role of Ebonex is to suppress the agglomeration of catalyst particles during the synthesis. In addition, interelectronic and/or interionic interactions with the metallic components, affecting the catalytic efficiency of the composite material are expected since its hypo-d-electron character suggest an ability to interact with metals such as Pt, Ni, Co.

The method of wet chemical reduction with $NaBH_4$ is a well known technique for synthesis of nanoscale metal particles, metal nanowires and similar materials with various chemical compositions. The most important prerequisite for nanoparticles synthesised by the borohydride reduction process is the knowledge of and the control over the kinetic parameters determining their nucleation and growth. The nucleation rate and growth are tools for control of those nanoparticles in size, shape, structure and properties, that provides a large choice for their most successful applications [21].

Our previous investigations showed that Pt-Co/Ebonex catalyst prepared by the borohydride reduction method facilitates essentially the oxygen evolution reaction in alkaline aqueous solutions compared to both the supported Pt/Ebonex and unsupported Pt-Co catalysts [7].

The aim of this research is to investigate the catalytic efficiency of mixed Pt-Co catalyst dis-

* To whom all correspondence should be sent:
E-mail: antonia.stoyanova@gmail.com

persed on the interactive support of Ebonex in regard to oxygen evolution in PEM water electrolysis.

EXPERIMENTAL

Synthesis of the catalysts. A series of mono- and bi-metallic compositions, containing Pt, Co and Pt-Co in various ratios, was prepared using the borohydride wet chemical reduction (BH) method. The synthesis of the catalyst nanoparticles and their deposition upon Ebonex required first synthesizing of platinum and cobalt ethylenediamine complexes serving as metal precursors according to a previously developed preparation procedure [7, 22, 23]. In a second stage, the prepared aqueous solutions of the precursors (single- and mixed-metal complexes) were impregnated on the surface of the support and then reduced by addition of sodium borohydride solution under continuous stirring at 40°C for several minutes. The procedure was carried out with different ratios of precursors in order to obtain the desired composition (Table 1).

Table 1. Pt:Co ratio, Pt cell parameter and crystal size of the synthesized mono and bimetallic materials

Sample	Initial composition, Pt:Co ratio, at.%	Pt cell parameter, Å	Crystal size, nm
Pt/Ebonex	1:0	3.9191 ± 0.0018	4.2 ± 0.7
Pt3Co/Ebonex	3:1	3.9050 ± 0.0037	3.9 ± 0.6
Pt3Co2/Ebonex	3:2	3.8783 ± 0.0149	2.1 ± 0.4
Pt3Co2	3:2	3.8539 ± 0.0002	2.3 ± 0.2
Co/Ebonex	0:1	amorphous	

Characterization of the synthesized electrocatalysts. The phase composition, morphology and surface structure of the catalysts under study were investigated by X-Ray diffraction (XRD) and X-ray photoelectron spectroscopy (XPS). XRD spectra were recorded by X-ray diffractometer Philips APD-15. The diffraction data were collected at a constant rate of 0.02 $^{o}.s^{-1}$ over an angle range of $2\theta = 10–90^{o}$. The average particle size (in our case it coincides with crystallite size) was calculated from the broadening of the XRD peaks using the Scherrer's equation [24]. The XPS of the samples were recorded with an ESCALAB MK II (VG Scenific, England) electron spectrometer. The photoelectrons were excited with a twin anode X-ray source using Mg Kα (hv = 1253.6 eV) radiation. C1s photoelectron line at 285.0 eV was used as a reference for calibration.

Laboratory PEM cell and test procedure. The electrochemical tests were performed on membrane electrode assemblies (MEAs), using a Nafion 117 membrane (Alfa Aesar) as an electrolyte. The catalysts under study were investigated as electrodes for the oxygen evolution reaction, while a commercial E-TEK catalyst containing 20% Pt on carbon support was used to prepare both the hydrogen (HE) and the reference electrodes (RE). The electrodes have a complex multilayer structure, consisting of gas diffusion, backing, and catalytic layers. The backing layer was made of a mixture of carbon particles (Shawinigan Acetylene Black) and 30% of PTFE suspension, deposited on thin carbon cloth, serving as a gas diffusion layer. The catalytic layer was spread upon the backing one as an ink (catalyst particles mixed with diluted Nafion ionomer) by several steps. After each step the electrode was dried for 30 min at 80ºC and weighted, using an analytical microbalance Boeco, Germany. The procedure was repeated until a metal loading of 5 mg·cm^{-2} was reached. Then the electrodes were hot pressed onto the PEM electrolyte forming the test MEA. The hot pressing was performed stepwise in the regime of gradual temperature and pressure increase starting from 50ºC and 6 kg·cm^{-2} and ending with 120ºC and 12 kg·cm^{-2}, respectively.

The PEM electrochemical cell used for testing of the prepared catalysts is presented in Fig. 1. It consists of two gas compartments, where the hydrogen and oxygen evolution take place, separated by the MEA.

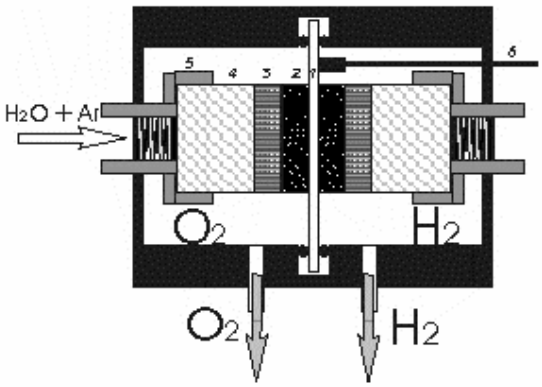

Fig. 1. Scheme of the test PEM electrolytic cell: 1) Nafion membrane; 2) catalytic layer; 3) carbon cloth; 4) foamed Ni plate; 5) PTFE rings; 6) reference electrode.

The HE and RE are located in one compartment so that during the operation, the former ensures the atmosphere required for the stable potential of the latter. The complete design of the model test PEM electrolyser includes also graphite cloths, which ensure a good electronic contact and foamed nickel plates, serving as current collectors. The whole stack is fastened on both sides by metal springs and is insulated form the stainless steel housing of the cell by PTFE rings.

The CV curves were recorded at room (20°C) temperature, using a potential scanning rate of 20 $mV \cdot s^{-1}$. The steady state polarisation tests were run in galvanostatic mode at operating temperature of 80°C. All electrochemical measurements were carried out with a commercial Galvanostat/Potentiosat POS 2 Bank Elektronik, Germany.

RESULTS AND DISCUSSION

Fig. 2 represents the XRD spectra of the synthesized mono and bimetallic materials and in Table 1 the results obtained by X-ray diffraction analysis are summarized.

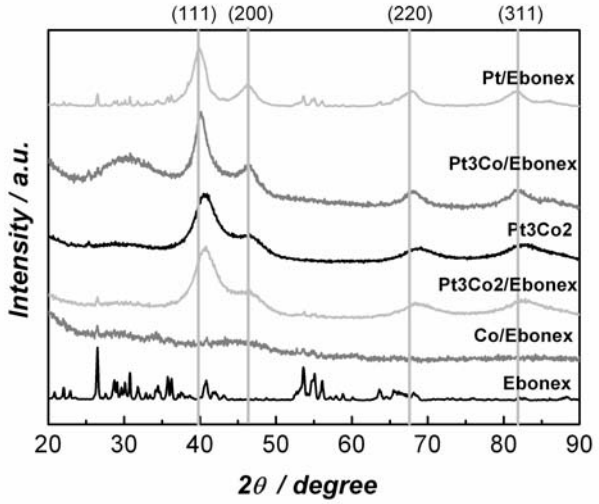

Fig. 2. XRD spectra of the studied Pt and Pt-Co catalysts.

The patterns show that the monometallic Co sample is amorphous, while the rest of the samples have Pt peaks with varying half-width and 2Θ position, reflecting the differences in the size of the metal crystallites and the crystal lattice parameters. The calculated parameters of the crystal unit cell for the Pt/Ebonex sample correspond to pure Pt. For all other samples in the series the parameters of the lattice are lower. This is an indication of inclusion of Co inside the Pt unit cell and formation of solid metal solution. In addition, there is a trend to decrease the crystal size, respectively increase in the catalyst specific surface area with the increase in the Co content. The particle diameters calculated from full width of the half-peak maximum are in the range 4.2 to 2.1 nm.

The smallest crystal size has the catalyst Pt3Co2 deposited on Ebonex, suggesting an increased surface area and enhanced activity in accordance with other authors who reported higher catalytic activity of Pt-based binary electrocatalysts (Pt-Co, Pt-Cr, Pt-Ni) [3, 8, 25, 26]. The data of unsupported sample (Pt3Co2) are not significantly different from those deposited on Ebonex.

The electrochemical investigation of the catalytic activity was performed by the method of cyclovoltammetry (CV) and steady state polarization. The CV gives some qualitative information about the electrochemical activity and the nature of the processes occurring on the catalyst surface. CV curves of MEAs containing Pt3Co2/Ebonex catalyst or unsupported nanoparticles at the same ratio, Pt3Co2 at the anode are presented in Fig. 3. The latter curve was included in order to follow the influence of the substrate on the catalyst performance.

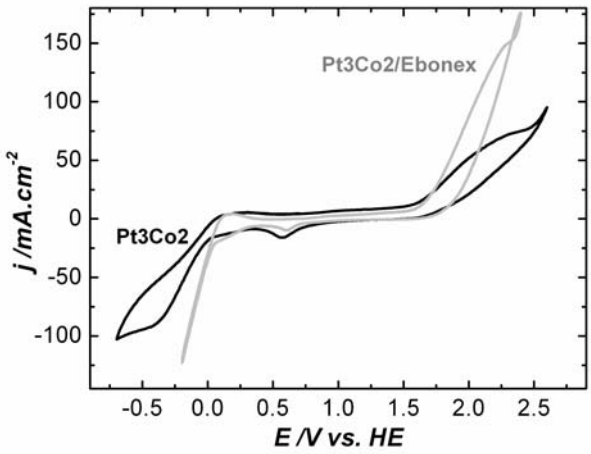

Fig. 3. Cyclovoltammetric curves of Pt3Co2/Ebonex and unsupported Pt3Co2 nanoparticles at 20ºC and scanning rate of 20 $mV \cdot s^{-1}$.

The observed current peaks corresponding to the formation of oxygen coverage on the surface (Pt–O, Pt–OH) are not very well depicted on both CV curves shown. They are spread in a broad potential range. Both hydrogen and oxygen evolution reactions start at lower overpotentials, when the Pt3Co2 nanoparticles are deposited on Ebonex. The effect is more pronounced for the OER, which commences at potential of about 1.5 V.

The main results from the steady state electrochemical characterisation of the prepared catalysts, incorporated in MEAs are summarised in Fig. 4. The galvanostatic polarization curves of the partial electrode reaction (OER) involved in the electrolytic water splitting are recorded at typical PEMWE operation temperature of 80°C. For comparison in Fig. 4 data are included from polarisation experiments performed on MEAs with different Pt:Co ratios deposited of Ebonex as well as unsupported Pt3Co2 nanoparticles at the anode and a constant total metal loading of 5 $mg \cdot cm^{-2}$.

It can be seen that the monometallic Co/Ebonex sample shows an insignificant catalytic action, while all Pt-Co catalysts, supported on Ebonex have higher catalytic effect compared to the Pt/Ebonex monometallic sample and unsupported catalyst. This

demonstrates the positive influence of the cobalt inclusions on the activity of Pt, observed also by other authors [4, 7, 8] and secondly the Ebonex support [7, 9, 16, 20, 27].

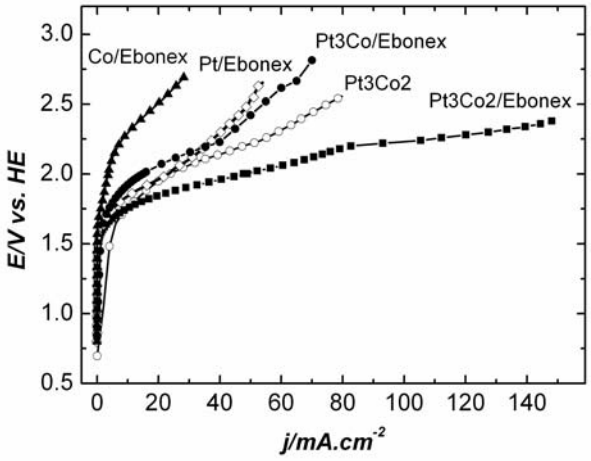

Fig. 4. Galvanostatic polarisation curve of Pt-Co catalysts with varying metal ratios at 80ºC.

The best catalytic activity for oxygen evolution reaction is exhibited by the sample 3Pt2Co/Ebonex (sample with the lowest crystal size). It has higher efficiency relative to all other compositions, including Pt/Ebonex. Despite the similarity in the cells parameters the activity on Ebonex supported catalyst is higher. The activity changes in the order: Pt3Co2/Ebonex > Pt3Co2 > Pt3Co/Ebonex > Pt/Ebonex > Co/Ebonex. The combination of elements from the left side of the transition series in the Periodic Table, having empty or half-filled vacant semi-d-orbitals (hypo-d-electronic metal) with metals of the right half of the transitions series, having internally paired d-electrons (hyper-d-electronic metals) is already a proven approach to obtain efficient catalyst with decreased noble metal loadings. Such composite catalysts exhibit a well pronounced synergism toward OER and HER [7, 16, 27]. By dispersion (grafting) of transition metal intermetallic phases on the active centres of selected catalytic supports, it is possible to achieve a strong synergetic effect known as strong metal-support interaction (SMSI). In this way, it is possible to decrease the amount of the catalysts for a unit of electrode surface and to increase essentially the catalytic activity of the composite catalyst [19, 26–28].

Having these facts in mind, the positive effect of Ebonex support could be explained by formation of solid solution between the metallic components (registered in XRD spectra) combined with hyper-hypo-d-electron metal-support interaction between the metal components and the substrate.

In order to verify this assumption the surface state of the as-prepared Pt/Ebonex, Pt3Co2/Ebonex and Pt3Co2 catalysts has been studied further by photoelectron spectroscopy. The results obtained are represented in Fig. 5 and summarised in Table 2.

The results shown in Fig. 5 and Table 2 indicate that the Pt 4f spectrum (Fig. 5a) can be deconvoluted with three doublet components corresponding to 3-valence states of the platinum [29]. The metallic state Pt^0 is dominant for all samples. Small amount of $Pt(OH)_2$ and PtO_2 are present too.

The Co 2p core level spectrum is characterized by two components due to Co $2p_{3/2}$ and Co $2p_{1/2}$, and shake-up satellites. The Co $2p_{3/2}$ binding energies of Co^{2+} and Co^{3+} are very close and this makes determination of the oxidation states uncertain. But BE separation of the satellite signals from the Co $2p_{3/2}$-Co $2p_{1/2}$ photo lines, as well as spin orbital splitting are dependent on the chemical state of cobalt. The high spin Co^{2+} compounds such as CoO (780 eV), $Co(OH)_2$ (780–781 eV) exhibit strong satellite lines, which are located at about 5–6 eV above the main line, in contrast to Co^{3+} that exhibits a weak satellite shifted to higher binding energies (Co_3O_4, CoOOH) [29–31]. The separation of the Co $2p_{3/2}$-$2p_{1/2}$ spin-orbit components is larger by about 1 eV for the high spin Co^{2+} compared to the low spin Co^{3+} valence states. The splitting is usually 16.0 eV for Co^{2+} and 15.0 eV for Co^{3+} and Co^0. The spectrum of metallic cobalt does not contain shake-up satellite and gives rise at 778 eV Co $2p_{3/2}$.

Fig. 5b shows deconvoluted Co2p spectra for catalysts Pt-Co 3:2. Three components can be distinguished. In accordance with the above data the component with lowest BE corresponds to metallic cobalt (Table 2). The appearance of both components at ~781 and ~785.6 eV and the value 15.7–15.8 eV for spin-orbital splitting means that cobalt is present in the second valence state. The intensity proportion between Co^0 and Co^{2+} indicates that only 34–35% are in the metallic state. Namely, this part of cobalt incorporates into platinum cell. Taking into account the XRD patterns, the remaining larger part of the cobalt is in the amorphous state.

Additionally, from the fact, that the O1s spectra are situated around 532 eV (Fig. 5c), which corresponds to metal–OH bonds, one can conclude that the Co^{2+} and Pt^{2+} states are in the hydroxide form i.e. $Co(OH)_2$ and $Pt(OH)_2$ respectively. The low energy O1s component at about 530 eV due to the oxygen in the metal–O–metal bond and high energy component (533.5-534 eV) can be assigned to adsorbed H_2O and/or C=O bonds [29, 32].

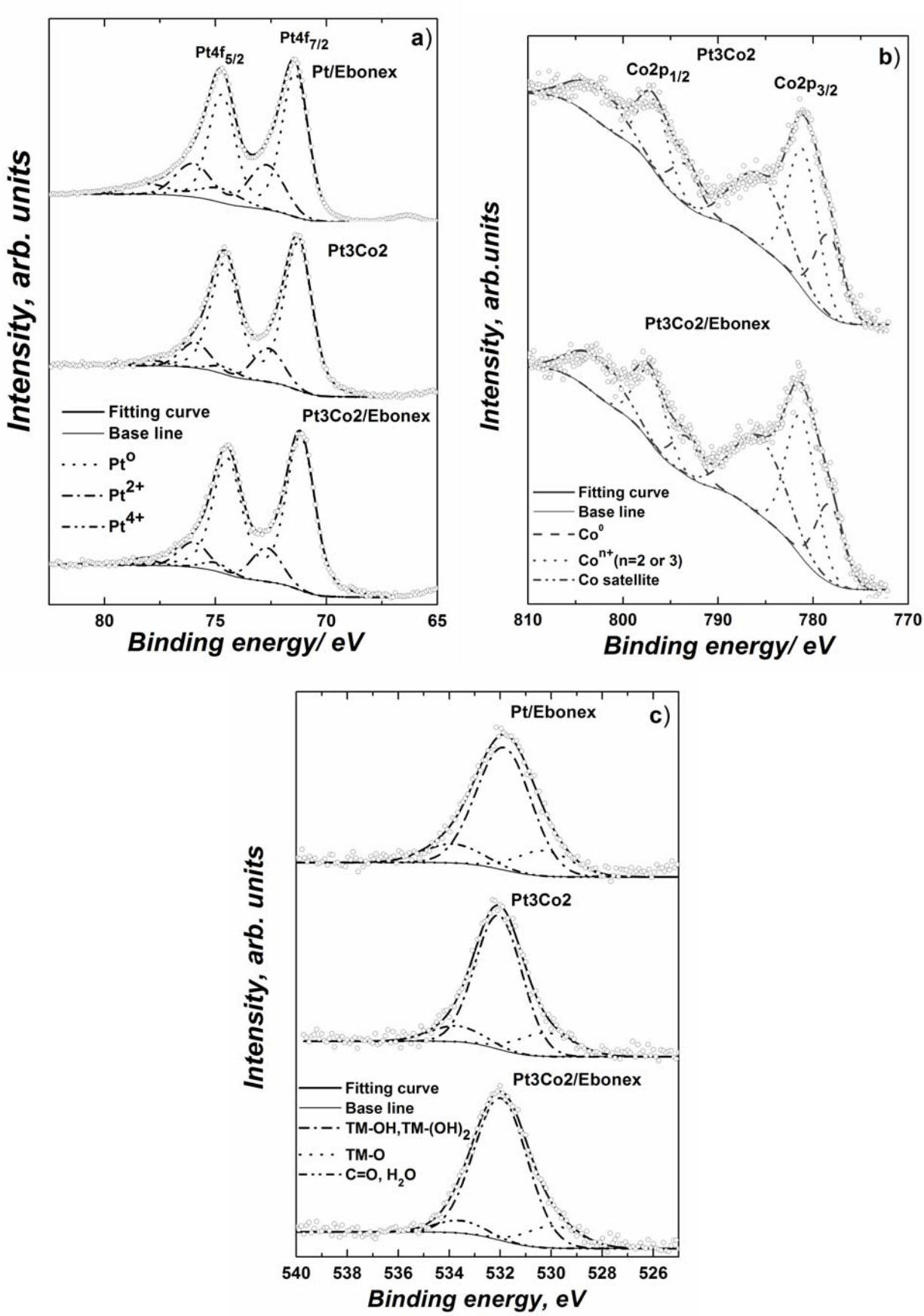

Fig. 5. XPS spectra of Pt-containing catalysts: a) Pt 4f, b) Co2p, c) O1s.

Table 2. Summarized data from XPS spectra.

XPS lines		Pt4f$_{7/2}$			Co2p$_{3/2}$					O1s		
Sample	Chemical species	Pt^0	Pt^{2+} PtO $Pt(OH)_2$	Pt^{4+} PtO_2 $Pt(OH)_4$	Co^0		Co^{2+} $Co(OH)_2$, CoO		Satellite	TM–O	$TM(OH)_x$	H_2O, C=O
						spin orbital splitting		spin orbital splitting		(TM = Pt, Ti, Co)		
Pt/Ebonex	BE eV	71.42	72.70	74.76						530.27	531.86	533.85
	%	65.47	25.37	9.16						15.33	72.57	12.11
Pt3Co2	BE eV	71.28	72.61	74.61	778.36	14.99	781.08	15.68	785.61	530.19	532.06	533.71
	%	78.93	17.45	3.62	35.30		64.70			15.65	74.26	10.09
Pt3Co2/	BE eV	71.17	72.68	74.96	778.28	15.03	781.15	15.84	785.60	529.90	531.97	533.58
Ebonex	%	79.73	16.43	3.84	34.30		65.70			12.68	80.72	6.60

The results imply the formation of solid solution of both metals and verify to a great extent the expected formation of surface bonds between the metallic components of the catalyst and the supporting material.

In order to check the stability of the synthesized catalysts the development of the electrode potential with time was followed under galvanostatic conditions at current density of 100 mA·cm^{-2} for period of 24 h. These results show a stable catalytic property of the Pt-Co/Ebonex catalyst. The measured initial electrode potential was 1.72–1.75 V. It varied slightly during the first 8 hours of the test and after reaching a value of about 1.6 V, no further changes were observed (Fig. 6).

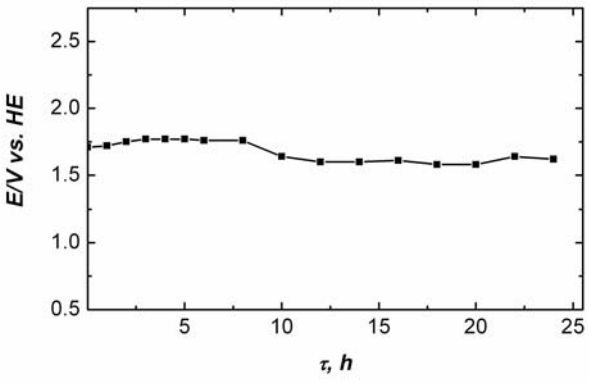

Fig. 6. Long-term performance of Pt3Co2/Ebonex recorded in a galvanostatic mode at 80ºC and current density 100 mA·cm^{-2}.

CONCLUSIONS

The results demonstrate that Pt-Co/Ebonex catalysts, obtained by the borohydride method of wet chemical reduction possess enhanced efficiency toward oxygen evolution compared to pure Pt. The effect is explained by the formation of solid solution between the metallic components combined with hyper-hypo-d-electron metal-support interactions. These effects together with the high stability of the supportive material against oxidation, give reason to consider Ebonex as alternative support for the anodic catalytic materials for PEM water electrolysis.

Acknowledgments: *This research work has been financially supported by the National Science Found at Bulgarian Ministry of Education and Science, contract DTK 02/68.*

REFERENCES

1. E. Rasten, G. Hagen, R. Tunold, *Electrochim. Acta,* **48**, 3945 (2003).
2. P. Paunović, O. Popovski, A. Dimitrov, D. Slavkov, E. Lefterova, S. Hadži Jordanov, *Electrochim. Acta*, **52**, 4640 (2007).
3. L. Xiong, A. Manthiram, *Electrochim. Acta*, **50**, 2323 (2005).
4. L. Xiong, A. M. Kannan, A. Manthiram, *Electrochem. Commun.*, **4**, 898 (2002).
5. L. Profeti, E. Ticianelli, E. Assaf, *Fuel,* **87**, 2076 (2008).
6. N. R. Elezovic, B. M. Babic, V. R. Radmilovic, Lj. M. Vracar, N. V. Krstyajic, *Electrochim. Acta*, **54**, 2404 (2009).
7. E. Slavcheva, V. Nikolova, T. Petkova, E. Lefterova, I. Dragieva, T. Vitanov, E. Budevski, *Elecrochim. Acta*, **50**, 5444 (2005).
8. M. Min, J. Cho, K. Cho, H. Kim, *Electrochim. Acta*, **45**, 4211 (2000).
9. G. Dieckmann, St. Langer, *Electrochim. Acta,* **44**, 437 (1998).
10. B. Grgur, N. Markovic, P. Ross, *J. Phys. Chem. B*, **102**, 2494 (1998).
11. K. Wang, H. A. Gasteiger, N. M. Markovic, P. N. Ross, *Electrochim. Acta*, **41**, 2587 (1996).
12. P. Millet, N. Dragoe, S. Grigoriev, V. Fateev, C. Etievant*, Int. J. Hydrogen Energy,* **34**, 4974 (2009).
13. E. Slavcheva, I. Radev, S. Bliznakov, G. Topalov, P. Andreev, E. Budevski, *Electrochim. Acta*, **52**, 3889 (2007).
14. E. Slavcheva, I. Radev, G. Topalov, E. Budevski,

Electrochim. Acta, **53**, 362 (2007).
15. E. E. Farndon, D. Pletcher, *Electrochim. Acta*, **42**, 1281 (1997).
16. G. Topalov, E. Lefterova, E. Slavcheva, in: Proc. Int. Hydrogen Energy Congress and Exhibition, IHEC 2007*,* 13–15 July 2007, Istanbul*,* Turkey, p. 1.
17. T. Teda, H. Igarashi, H. Uccida, M. Watanabe, *J. Electrochem. Soc*., **146**, 3750 (1999).
18. E. Slavcheva, V. Nikolova, E. Lefterova, P. Iliev, G. Ivanova, I. Dragieva, in: Nanoscience & Nanotechnology, Vol. 4, I. Dragieva, E. Balabanova (Eds.), Heron Press, Sofia, 2004, p. 258.
19. E. Antolini, E.R. Gonzalez, *Solid State Ionics*, **180**, 746 (2009).
20. Lj. M. Vracar, S. Lj. Goikovic, N. R. Elezovic, V.R. Radmilovic, M. Jaksis, N. V. Krstavic, *J. New Mater. Electrochem. Systems*, **9**, 99 (2006).
21. I. Dragieva, Z. Stoynov, K. Klabunde, *Scr. Mater.*, **44**, 2187 (2001).
22. I. Dragieva, S. Stoeva, P. Stoimenov, E. Pavlikianov, K. Klabune, *Nanostruct. Mater*., **12**, 267 (1999).
23. I. Dragieva, S. Stoeva, P. Stoimenov, Z. Stoynov, BG Patent No 103629 (03.08.1999).
24. E. Antolini, *Mat. Chem. Phys*., **78**, 563 (2003).
25. Y. Takasu, N. Ohashi, X.-G. Zhang, Y. Murakami, H. Minagawa, S. Sato, K. Yahikozawa, *Electrochim. Acta*, **41**, 2595 (1996).
26. J. Hwang, J. Shik Chung, *Electrochim. Acta,* **38**, 2715 (1993).
27. G. Topalov, E. Slavcheva, D. Labou, I. Radev, E. Lefterova, S. Neophytides, in: Nanoscience & Nanotechnology, Vol. 7, I. Dragieva, E. Balabanova (Eds.), Heron Press, Sofia, 2007, p. 200.
28. M. B. Vukmirovic, J. Zhang, K. Sasaki, A. U. Nilekar, F. Urib, M. Mavrikakis, R. R. Adzic, *Electrochim. Acta*, **52**, 2257 (2007).
29. A. S. Aricò, A. K. Shukla, H. Kim, S. Park, M. Min, V. Antonucci, *Appl. Surf. Sci.,* **172**, 33 (2001).
30. A. Shukla, M. Neergat, P. Bera, V. Jayaram, M.S. Hegde, *J. Electroanal. Chem*., **504**, 111 (2001).
31. D. Briggs, M. Seah, Practical Surface Analysis, Vol. 1: Auger and X-Ray Photoelectron Spectroscopy, 2nd edn. Wiley, Chichester, 1996.
32. B. Wessling, PhD Thesis, RWTH Aachen University, Aachen, 2007.

РАЗЛАГАНЕ НА ВОДА ЧРЕЗ ПЕМ ЕЛЕКТРОЛИЗА С КАТАЛИЗАТОРИ ВЪРХУ НОСИТЕЛ ЕБОНЕКС

А. Е. Стоянова*, Е. Д. Лефтерова, В. И. Николова, П. Т. Илиев, Й. Д. Драгиева, Е. П. Славчева

Индтитут по електрохимия и енергийни системи, Българска академия на науките, ул. „Акад. Г. Бончев“, бл. 10, 1113 София

Постъпила на 12 януари 2010 г.; Преработена на 19 февруари 2010 г.

Серия от моно- и биметални състави, съдържащи Pt, Co и Pt-Co в различни съотношения, отложени върху Ебонекс, са получени по метода на мократа борхидридна редукция. Установено е, че PtCo/Ebonex показва по-висока ефективност по отношение на отделянето на кислород в ПЕМ водната електролиза в сравнение с чистата метална Pt. Активността се променя в реда: Pt3Co2/Ebonex > Pt3Co2 > Pt3Co/Ebonex > Pt/Ebonex > Co/Ebonex. Резултатът е обяснен с образуването на твърд разтвор между металните компоненти, комбиниран с хипер-хипо-d-електронни взаимодействия между метала и носителя. Тези ефекти, заедно с високата стабилност на носителя срещу окисляване, дават основание Ебонекс да се разглежда като алтернативен носител за анодни каталитични материали, използвани в ПЕМ водната електролиза.

Bulgarian Chemical Communications, Volume 42, Number 2 (pp. 174–179) 2010

Mathematical modelling of biodegradation of monochloroacetic acid by *Xanthobacter autotrophicus* GJ10 immobilized in polyacrilamide gel

E. K. Vasileva*, K. K. Petrov, V. N. Beschkov

Institute of Chemical Engineering, Bulgarian Academy of Sciences, Acad. G. Bonchev St., Block 103, 1113 Sofia, Bulgaria

Received February 2, 2009; Revised October 1, 2009

The biological method of waste water remediation includes the participation of peculiar bacterial strains, capable of utilizing the halogenated aliphates as a carbon source.

In the present paper a kinetic model of the process of monochloroacetic acid biodegradation via glycolic acid production was developed. This model allowed the evaluation of the effects of microbial growth and diffusion limitations inside the gel particles on the process rate and the separate contributions of the free and immobilized cells for the overall fermentation process upon multiple uses.

The model results were tested on the process carried out by the strain *Xanthobacter autotrophicus* GJ10 used in the process of degradation of the highly toxic 1,2-dichloroethane and suitable for remediation of monochloroacetate contaminated media.

Key words: biodegradation, monochloroacetic acid, immobilization, *Xanthobacter autotrophicus* GJ10, polyacrylamide, mathematical modeling.

INTRODUCTION

The short-chain halogenated aliphatic compounds, such as 1,2-dichloroethane, are frequent constituents of industrial waste waters [1]. They are produced in millions of tons annually and because of the toxic effects of these compounds on humans as well as on the natural environment, there is growing interest in technologies for their removal. The monochloroacetic acid (MCA) is an intermediate product of degradation of the strongly toxic 1,2-dichloroethane. Biotechnologies, involving the use of microorganisms, able to degrade both pollutants to nontoxic final products, were developed in the last years. For this purpose, specialized bacterial strains that are able to use halogenated aliphatics as sole carbon and energy sources were used [2, 3]. As one of the most successful MCA degrading strains was evaluated the strain *Xanthobacter autotrophicus* GJ10.

The multiple use of bacteria requires their immobilization, either by entrapment in gels or fixed on solid supports. It both cases problems associated with mass transfer resistance may arise as well as with the cell detachment from the support. The correct performance of the process requires the knowledge of the contribution of the immobilized cells and of the free ones growing independently after detachment from the matrix. Another important feature is the estimation of the inhibition effects enhanced due to the mass transfer resistance in the gel particles and in the biofilms.

In the present paper a mathematical model is proposed to evaluate all these effects accompanying the microbial biodegradation of monochloroacetic acid.

This model enables to evaluate quantitatively these effects and to estimate their importance on the net process.

MATHEMATICAL MODELLING

The purpose of the mathematical modelling in the present paper was to estimate quantitatively the contribution of the cells entrapped in the gel particles, and in the free culture, after leaking from the gel. Leakage of cells from external layers of the particles may lead to cell growth in the bulk phase, which would compete and could even suppress the contribution of immobilized cells to the studied biodegradation [4–6]. Another effect of the cell detachment is the particle exhaustion and the failure of further use. Therefore, the mathematical modelling helps to estimate quantitatively the sustainability of the immobilized biocatalyst.

Our mathematical model is based on the following assumptions:

i) The monochloroacetic acid (MCA, *S*) is considered as a carbon source for microbial growth

* To whom all correspondence should be sent:
E-mail: vasileva@ice.bas.bg

but as an inhibitor at higher concentrations as well. It is converted into glycolic acid (GA, *P*) according to the net scheme:

$$\mathrm{CH_2Cl–COOH} \rightarrow \mathrm{CH_2(OH)–COOH} \rightarrow \text{mineralization}$$

$$\frac{dc_S}{dt} = -k_1 \frac{dX}{dt}$$
$$\frac{dc_P}{dt} = k_1 \frac{dX}{dt} - k_2 X c_P \qquad (1)$$

As a simplification, we considered the second step of further glycolic acid mineralization as a single consecutive first-order reaction.

ii) The process for immobilized cells follows kinetic equations with a structure identical to that for a free culture (1) but possibly with different rate constants because of different conditions the cells are living under. The yield coefficients are considered the same as those for a free culture.

iii) There is no migration of bacterial cells within the particles although they are not uniformly distributed because of different supply of substrate [4, 7, 8]. Leakage of cells growing at the periphery of the particles into the broth may take place.

iv) No partitioning effects for the solutes exist, i.e. the solubility of the species is considered to be the same in the bulk and in the gel particles.

v) It is established that the first step of the monochloroacetic acid biodegradation is associated with considerable substrate inhibition, particularly for the microbial growth [9, 10]. We shall consider that the substrate inhibition follows the equation proposed by Andrews [11]. Hence, the equation of microbial growth takes the form:

$$\mu = \mu_{\max} \frac{c_S}{K_s + c_S + K_i c_S^2} . \qquad (2)$$

No product inhibition was considered, neither for the first step, nor for the final mineralization. Based on these assumptions, the mathematical model for spherical particles represents the following set of partial differential equations written in dimensionless form, cf. the List of symbols:

$$\frac{\partial \bar{c}_S}{\partial T} = \frac{\partial^2 \bar{c}_S}{\partial \rho^2} + \frac{2}{\rho}\frac{\partial c_S}{\partial \rho} - \Phi_S^2 . \bar{X} c_S$$
$$\frac{\partial \bar{c}_P}{\partial T} = R_D \left(\frac{\partial^2 \bar{c}_P}{\partial \rho^2} + \frac{2}{\rho}\frac{\partial \bar{c}_P}{\partial \rho} \right) + \Phi_S^2 . \bar{X} - \Phi_P^2 X \bar{c}_P \qquad (3)$$

with the following initial and boundary conditions:

$$T = 0, \ \bar{c}_i = 1 \qquad (4a)$$

$$\rho = 0, \ \partial \bar{c}_i / \partial \rho = 0, \qquad (4b)$$

$$\rho = 1, \ \partial \bar{c}_i / \partial \rho = Bi_i (\bar{c}_{is} - \bar{c}_{i\infty}), \qquad (4c)$$

The notations in Eqn. (6) are as follows:

$$T = D_S t / R^2, \ \rho = r/R, \ \bar{c}_i = c_i / c_S^0,$$
$$\Phi_S^2 = k_1 \mu_{\max,im} R^2 X_{im}^0 / (D_S c_S^0),$$
$$\Phi_P^2 = k_2 R^2 X^0 / (D_S c_S^0), \qquad (5)$$
$$\bar{\mu}_{im} = \mu_{im} R^2 / D_S, \ \bar{\mu}_{\max,im} = \mu_{\max,im} R^2 / D_S$$

For a batch culture, the variation of product concentration in the broth with time is given by the following equations, with the associated initial conditions:

$$V \frac{dc_{P\infty}}{dt} = -AD_P \left(\frac{\partial c_P}{\partial r} \right)_{r=R} + V(Y_{P/X} \frac{dX_\infty}{dt} - k_2 X c_{P,\infty}) \qquad (6)$$

$$V \frac{dX}{dt} = V\mu_\infty X_\infty + \beta A \left[\mu_{im} X_{im} \right]_{r=R}$$
$$t = 0, X_\infty = X_\infty^0, c_P = c_{P,\infty}^0 \qquad (7)$$

The cells leakage is taken into account by the multiplier β, being the apparent thickness of the peripheral layer of the gel particles where cells leakage takes place, cf. the List of symbols.

Eqns (6, 7) can be rewritten in the following dimensionless form:

$$\bar{c}_P = -R_{DA} L \int_0^t \left(\frac{\partial \bar{c}_P}{\partial \rho} \right)_{\rho=1} dT + Y_{P/X} \bar{\mu} . \bar{X}_\infty - (k_2 R^2 / D_S c_S^0) \bar{X}_\infty \bar{c}_P \qquad (8)$$

$$\frac{d\bar{X}}{dT} = \bar{\mu}_\infty \bar{X}_\infty + \bar{\beta} L \left[\bar{\mu}_{im} \bar{X}_{im} \right]_{\rho=1},$$
$$T = 0, \bar{X}_\infty = 0, \eta = 0, \bar{\mu} = \mu R^2 / D_S \qquad (9)$$

The term $\bar{\mu}_\infty \overline{X_\infty}$ in Eqn. (9) accounts for the growth of the cells leaked to the broth. The second term on the right hand side of Eqns. (5, 9) takes into account the share of the cells leaked to the broth from the periphery of the gel particles.

The meaning of the dimensionless parameters in Eqns. (6–9) is as follows:

Φ_S^2 is the Thiele modulus being proportional to the ratio of the characteristic reaction time (the growth-associated biotransformation) and the time for diffusion $R2/D$.

Φ_P^2 is the Thiele modulus for the second step of the consecutive reactions, i.e. the mineralization of glycolic acid to water and carbon dioxide.

$R_D = D_S/D_P$ *is* the ratio of diffusivities of MCA to GA. This ratio was taken as $R_D = 1$, accounting for the similar structures and masses of the MCA and GA molecules.

The Biot numbers *Bi*i for the different species (*i*th) are considered high enough to neglect the external mass transfer resistance.

K_S is the MCA saturation constant for free culture and μ is the specific cell growth rate taking into account the consumption of MCA as well as the substrate inhibition effects according to the Eqs. (2–4).

The multiplier β takes into account the rate of cell leakage from a layer at the periphery of the spherical gel particles. If no gel destruction takes place, it is reasonable to assume that the maximum possible value of the dimensionless factor $\overline{\beta}$ may reach a unity if the cells from the whole particle volume leak into the surrounding medium. It means that in the latter case $\overline{\beta}$ =1, $\mu_{im}X_{im} \approx \mu_{\infty}X_{\infty}$. In case of no cell leakage, $\beta = 0$.

$L = A.R/V$ is a dimensionless parameter taking into account the particles interfacial area and their concentration. In case when the particles concentration is low and provided the spherical solid particles are of a uniform radius, this parameter is related to the bed porosity, ε, by the equation:

$$L = \frac{N_p \pi d_p^2}{V}\frac{d_P}{2} = \frac{3N_pV_p}{V} = 3(1-\varepsilon), \qquad (10)$$

Where N_p and V_p are the number of particles and the volume of a single particle, respectively. Hence, the parameter L can be calculated knowing the particles volume and the volume of the fluid.

There are eleven parameters in the model (2–9). Some of them can be evaluated from independent sources or experiments and thus facilitating the parameter estimation from experimental data for lactic acid fermentation by entrapped cells. These parameters are given in Table 1 with explanation of the way they are estimated or used further.

Many of the parameters could be taken from experimental data for free culture of the same strain, namely K_s, K_P, $Y_{P/X}$ and μ_{max} [9, 10]. The diffusivity D_S is taken from the literature for aqueous media [12].

The effect of immobilized cells on the solute's diffusion coefficients is considered quantitatively by Lefebvre and Vincent [7] and Gutenwik *et al*. [8]. One may expect that the solutes diffusivities may vary during one run within the gel pores because of microbial growth. In our case we shall consider constant diffusivities during one run, taking into account only their change from run to run.

The Biot number is considered to be high enough to provide well-stirred state conditions in the broth. The specific particle area parameter L was determined from the void volume of the mixture particles/broth.

The left four parameters (Φ_L^2, $\mu_{max,\,im}$, Φ_P^2, and β) have to be estimated from the model, cf. Eqns. (6–9) and based on the experimental data.

The set of differential equations (6) with the initial and boundary conditions (Eqns. (6a–c), (7), (8)) could be solved numerically. We used an implicit finite difference scheme coupled with the Thomas algorithm for solving the resulting linear algebraic equations.

For the purpose of parameter estimation the experimental results on the studied microbial biodegradation, published recently [13] were used. The parameter estimation was accomplished by minimization of sum of the squares of the differences between the experimental and the calculated values of monochloroacetic (*S*) and glycolic acid (*P*) concentrations at each moment of sampling.

$$Sum = \sum_j \left[(S_j^{calc} - S_j^{exp})^2 + (P_j^{calc} - P_j^{exp})^2 \right] \qquad (11)$$

The sums of the square differences of the normalized concentrations were very low, i.e. ~10^{-4}–10^{-6} orders of magnitude and always less than 0.001 for the estimated parameters.

RESULTS AND DISCUSSION

The values of the estimated model coefficients are given in Tables 1, 2, 3. It was interesting to note, that the maximum growth rate for the immobilized cells was determined with very high accuracy, namely:

$$\mu_{max,im} = 0.023\ h^{-1} \qquad (13)$$

Slight differences in the initial approximations during the estimation procedure gave very large discrepancies in the sum of least squares. This strong sensitivity is an indication of the model reliability. This value for $\mu_{max,im}$ is much lower, i.e. one order of magnitude than the specific growth rate for free cells. Probably it is due to the spatial limitations for the cell growth inside the particles.

Table 1. List of the model parameters and their values

Parameter	Values	Reference
Bi, Biot number, dimensionless	> 1000	Own assumption
D_S, diffusivity of monochloroacetic acid, (m^2/s)	1.37×10^{-9}	[15]
D_P, diffusivity of glycolic acid, (m^2/s)	1.37×10^{-9}	Own assumption
k_1, rate constant for monochloroacetic to glycolic acid fermentation, included in Φ_L^2, dimensionless		Included in the Thiele modulus, Φ_S^2,
k_2, rate constant of the second step of microbial degradation, included in Φ_P^2, $((kg/m^3)^{-1}\cdot h^{-1})$	-	Included in the Thiele modulus Φ_P^2
K_i, substrate inhibition constant, $(kg/m^3)^{-1}$	0.0406	From the free cells experiments [14]
K_s, saturation constant for monochloroacetic acid in Monod's equation, (kg/m^3)	0.0123	Own data from the free cells experiments
L, particle specific surface area parameter, dimensionless, Eqn. (10)	Different values	Own data
$Y_{P/X}$, product yield factor for free cells, dimensionless	1.0	Own data from the free cells experiments
$\overline{\beta}$ cells leakage factor, ($0 < \overline{\beta} < 1$), dimensionless	Different values	To be determined in the present paper
μ_{max}, specific maximum microbial growth rate for free cells, (h^{-1})	0.155	Own data from the free cells experiments
$\mu_{max,\,im}$, specific maximum microbial growth rates for immobilized cells, (h^{-1})	Different values	To be determined in the present paper
Φ_S^2, Thiele modulus on monochloroacetic acid conversion, dimensionless, Eqn. (5)	Different values	To be determined in the present paper
Φ_P^2, Thiele modulus on glycolic acid conversion, dimensionless, Eqn. (5)	Different values	To be determined in the present paper

Table 2. Parameter values estimated at MCA initial concentration of 5 mM.

Run No.	Φ_S^2, [-]	Φ_P^2, [-]	$\mu_{max,\,im}$ [h^{-1}]	$\overline{\beta}$, [-]
R1	11.15	1×10^{-4}	0.023	2.4×10^{-2}
R2	3.5	1×10^{-4}	0.023	1.7×10^{-2}
R3	6.32	1×10^{-4}	0.023	1.86×10^{-2}
R4	8.97	1×10^{-4}	0.023	1.87×10^{-2}
R5	8.6	1×10^{-4}	0.023	1.93×10^{-2}

Table 3. Parameter values estimated at MCA initial concentration of 10 mM.

Run No.	Φ_S^2, [-]	Φ_P^2, [-]	$\mu_{max,\,im}$, [h^{-1}]	$\overline{\beta}$, [-]
R1	2.14	0.1×10^{-4}	0.023	4.2×10^{-4}
R2	10.9	1×10^{-4}	0.023	1.52×10^{-2}
R3	17.36	0.51×10^{-4}	0.023	1.53×10^{-2}
R4	8.84	0.51×10^{-4}	0.023	1.54×10^{-2}
R5	8.647	0.1×10^{-4}	0.023	1.55×10^{-2}
R6	1×10^{-6}	0.1×10^{-4}	$\sim10^{-7}$	3.2×10^{-5}

The comparison of the values for the Thiele modulus Φ_S^2 for the first process shows that it stays stable at the lower initial concentration, i.e. there is slight cell leakage into the broth, which is compensated by the microbial growth inside the particles. This statement corresponds to the stable and very low values of the leakage factor $\overline{\beta}$. In the case of higher MCA initial concentration (i.e. 10 mM) the Thiele modulus passes through a maximum tending to zero for the last run. Obviously, in this case, the particles are already exhausted due to the leakage and the growth cannot compensate these losses, probably due to substrate inhibition. The initial values at the immobilized cell concentration X_{im}^0 prior to each run estimated from Φ_S^2 vary between 90 and 880 kg/m^3. For a reference, the free cell concentrations in the stationary phase are about 5 kg/m^3.

It is important to mention, that the leakage factor remains stable during the runs at both initial concentrations. Its values are very close to each other except for the first and last runs at 10 mM. The last fact could be explained by the extremely low initial cell concentrations in the first and the last experiments.

A review of the obtained parameter values shows that the Thiele modulus Φ_P^2 for the second process is practically constant at both initial MCA concentrations, no matter of the runs. This fact shows that the mineralization of glycolic acid is not inhibited by MCA or GA and that the immobilized cells are sufficiently active for all experiments.

A comparison of the modelling and experimental results from [13] is shown in Fig. 1. It illustrates the transient processes for a single run and the process stability for multiple repeated runs.

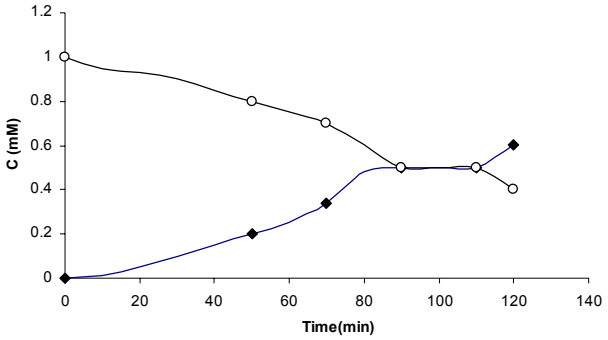

Fig. 1. Comparison of experimental data for monochloroacetic and glycolic acid with the model ones. (–o–) - monochloroacetic acid; (–♦–) - glycolic acid. The lines present results of mathematical modelling.

CONCLUSIONS

On the basis of the analysis of experimental results applying mathematical modeling we have come to the following conclusions:

The mathematical modelling of the process showed that for the present experiments loss of activity due to cell leakage was compensated by microbial growth inside the particles for 5 consecutive runs. Moreover, microbial growth was strongly retarded inside the particles and the second step of microbial mineralization was slightly dependent on the initial substrate concentration or the glycolic acid.

LIST OF SYMBOLS

A	Particles total interfacial area [L^2]
Bi	Biot number; $Bi = kR/D_L$ [-]
c	Concentrations, [$M \cdot L^{-3}$]
D_i	Diffusivity of the ith species, [$L^2 \cdot T^{-1}$]
d_p	Particle diameter, [L]
k_1	Rate constant of the lactose fermentation, Eqn. (1), [-]
k_2	Rate constant of lactic acid degradation, Eqn. (1), [$(M \cdot L^{-3})^{-1} . T^{-1}$]
k	Mass transfer coefficient, Eqn. ($Bi = kR/D_L$), [$L \cdot T^{-1}$]
K_S	Saturation constant for lactose in Monod Eqn. (7), [$M \cdot L^{-3}$]
K_i	Constant of substrate inhibition, Eqn. (2), [$(M \cdot L^{-3})^{-1}$]
K_P	Constant of product inhibition, Eqn. (2), [$M \cdot L^{-3}$]
L	Parameter taking into account the effect of specific particles area; $L = 3(1-\varepsilon)$, [-]
N_p	Number of gel particles, [-]
R	Radius of the particles, [L]
r	Radial co-ordinate, [L]
R_D	Ratio of diffusivities related to that of lactose, [-]
t	Time, [T]
T	Dimensionless time, $T = D_L t/R^2$, [-]
V	Total volume of the system, [L^3]
X	Living cells concentration, [$M \cdot L^{-3}$]
$Y_{P/X}$	Product yield coefficient, [-]

Greek Symbols

β	Apparent radius of the peripheral layer of the particles emitting viable cells from interface into the bulk, [L]
$\bar{\beta}$	Share of viable cells leaking from the particles interface into the bulk, $\bar{\beta} = \beta/R$, between 0 and 1, [-]
ε	Void fraction, [-]
μ	Specific microbial growth rate, Eqn. (7), [T^{-1}]
$\rho = r/R$	Dimensionless radial coordinate, [-]
Φ_S^2	Thiele modulus for lactose conversion, Eqn. (7), [-]
Φ_P^2	Thiele modulus for lactic acid degradation, Eqn. (7), [-]

Subscripts

S	Denotes quantities related to lactose (substrate)
P	Denotes quantities related to lactic acid (product)
i	Denotes quantities related to certain species in the system
im	Denotes values, related to immobilized cells
max	Denotes maximum values
∞	Denotes values, related to the bulk phase

Superscript

–	Denotes dimensionless quantities
0	Denotes initial concentrations

REFERENCES

1. D. B. Janssen, A. Scheper, B. Witholt, *Prog. Ind. Microbiol*., **20**, 169 (1985).
2. R. M. M. Diks, S. P. P. Ottengraf, *Bioprocess Eng*. **6**, 93 (1991).
3. R. M. M. Diks, S. P. P. Ottengraf, *Bioprocess Eng*. **6**, 131 (1991).
4. V. Beschkov, S. Velizarov, *Bioprocess Eng*., **22**, 233 (2000).
5. V. Beschkov, S. Velizarov, T. Georgieva, *Bulg. Chem. Commun*., **31**, 521(1999).
6. K. K. Petrov, D. S. Yankov, V. N. Beschkov, *World J. Microbiol. Biotechnol*., **22**, 337 (2006).

7. J. Lefebvre, J. C. Vincent, *Enzyme & Microb. Technol*. **17**, 276 (1995).
8. J. Gutenwik, B. Nilsson, A. Axelsson, *Biotechnol. Bioeng*., **79**, 664 (2002).
9. M. Torz, V. Beschkov, *Biodegradation*, **16**, 423 (2005).
10. V. Beschkov, Ts. Sapundzhiev, M. Torz, P. Wietzes, D. B. Janssen, *Chem. Biochem. Eng. Quart*., **22**, 339 (2008).
11. J. F. Andrews, *Biotechnol. Bioeng*., **10**, 707 (1968).
12. R. D.Martin, P. R. Unwin, *J. Electroanal. Chem.*, **397**, 325 (1995).
13. E. Vasileva, K. Petrov, V. Beschkov, *Biotechnol. & Biotechnol. Eq*., **23**, 788 (2009).

МАТЕМАТИЧНО МОДЕЛИРАНЕ НА БИОРАЗГРАЖДАНЕ НА МОНОХЛОРОЦЕТНА КИСЕЛИНА ОТ КЛЕТКИ НА ЩАМА *XANTHOBACTER AUTOTROPHICUS GJ10,* ИМОБИЛИЗИРАНИ В ПОЛИАКРИЛАМИДЕН ГЕЛ

Е. К. Василева*, К. К. Петров, В. Н. Бешков

Институт по инженерна химия, Българска академия на науките, ул. „Акад. Г. Бончев“, блок 103, 1113, София

Постъпила на 2 февруари 2009 г.; Преработена на 1 октомври 2009 г.

(Резюме)

Биологичните методи за пречистване на отпадни води се осъществяват чрез използване на специфични бактериални щамове, които са в състояние да използват халогенираните алифати като въглероден източник.

В настоящата статия е представен кинетичен модел на процеса на биоразграждане на монохлороцетна киселина с междинен продукт гликолова киселина. Този модел позволява оценката на ефекта от микробния растеж и дифузионните ограничения в гелните частици. Оценен е приносът на свободните и имобилизираните клетки в процеса на биоразграждане при многократно използване на гелните частици.

Резултатите от математичния модел са проверени експериментално с клетки на щама *Xanthobacter autotrophicus GJ10*, известен със способността си да разгражда токсичния 1,2-дихлоретан. Щамът е подходящ за обезвреждане на среди, замърсени с монохлорацетати.

Bulgarian Chemical Communications, Volume 42, Number 2 (pp. 180– 184) 2010

Sulphide ions heterogeneous catalytic oxidation by electrochemical methods

I. Mitov, A. Andreev, I. Nikolov, P. Andreev, E. Mladenova, K. Petrov*

Institute of Electrochemistry and Energy Systems, Bulgarian Academy of Sciences, Acad. G. Bonchev St., Block 10, 1113 Sofia, Bulgaria

Received: March 18, 2009

Additivity principle is employed to study heterogeneous redox catalytic process mechanisms by electrochemical means. The reaction mechanism of sulphide ions oxidation by air in alkaline medium is investigated. Assuming an electrochemically proceeding mechanism two partial reactions of sulphide oxidation and oxygen reduction are evaluated. Two highly active catalysts, suitable for industrial application, namely cobalt disulphophthalocyanine complex [$CoPc(SO_3H)_2$] and nickel hydroxide $Ni(OH)_2$ are studied. Hydrophobic gas diffusion carbon electrodes (GDE), are utilized.

The electrochemical mechanism of the process is proven by the good agreement between calculated by Faraday's law values and converted quantity of sulphide ions, measured analytically. The sulphide ions oxidation reaction by oxygen proceeds essentially on spread micro-galvanic elements created in the Carbon-Teflon structure of the electrodes. The carbon in the GDE exhibits its own catalytic activity. The electrodes modified with $CoPc(SO_3H)_2$ and $Ni(OH)_2$ possess considerably higher catalytic activity (about 5-fold).

The studied systems are quite promising for industrial purification of waste waters containing H_2S.

Key words: Electrocatalytic oxidation; sulphide ions.

INTRODUCTION

Sulphide ion catalytic oxidation to elemental sulfur [1–3] is one of the most effective methods for eliminating this hazardous pollutant from waste waters. They are highly toxic and biological methods for cleaning become problematic [4]. Chemical processes for sulphide oxidation are generally homogeneous and heterogeneous. Cobalt sulphophthalocyanine complexes, nickel, cobalt and iron salts [5–8] are used as catalysts in homogeneous media. Heterogeneous catalysts like Fe, Co and Pd salts as well as phthalocyanine and oxides of transition metals deposited on active carbon, silicagel or Al_2O_3 [9–12] have been studied. The mechanism of the sulphide oxidation process is complex and depending on the working conditions produces either colloidal sulphur or polysulphides.

Wagner and Traud [13] have proposed an additivity principle that was employed and developed [14] to study heterogeneous redox catalytic process mechanisms by electrochemical means. Applying the additivity principle, we have aimed at gaining information on the reaction mechanism of sulphide ions oxidation in alkaline medium:

$$S^{2-} + 1/2O_2 + H_2O \rightarrow S^0 + 2OH^- \quad (1)$$

The catalytic redox reaction (1) can be modelled by two partial reactions of oxidation and reduction [15, 16]. Assuming an electrochemically proceeding mechanism, the anodic and cathodic reactions may be presented as follows:

Anodic reaction

$$S^{2-} \rightarrow 1/2S_2 + 2e^- \quad (2)$$

Cathodic reaction

$$O_2 + H_2O + 2e^- \rightarrow HO_2^- + OH^- \quad (3)$$

Total:

$$S^{2-} + O_2 + H_2O \rightarrow 1/2S_2 + HO_2^- + OH^- \quad (4)$$

In this work two suitable for industrial application and highly active catalysts, namely cobalt disulphophthalocyanine complex [$CoPc(SO_3H)_2$] and nickel hydroxide $Ni(OH)_2$ have been studied.

EXPERIMENTAL

Hydrophobic gas diffusion carbon electrodes (GDE), developed in this laboratory (IEES, BAS) are utilized [17]. The electrodes are double layered and composed of gas diffusion and catalytic layers. The geometrical area of the GDE is 200 cm^2. The GDE's catalytic layer surfaces are modified by two catalytically active substances. The GDE is used as a wall of a reactor's cell as illustrated in Fig. 1.

The GDE is arranged in the reactor in such a way as to shape the reactor chamber (2) where the elec-

* To whom all correspondence should be sent:
E-mail: kpetrov@bas.bg

trolyte is supplied. The GDE catalyst surface faces the electrolyte while its other side is in direct contact with the surrounding air. The sulphide ions containing electrolyte is supplied from the tank (7) to the reactor chamber (2) by means of the peristaltic pump (6) *via* the electrolyte supply line (5). The waste solution is fed back to the tank (7) closing the cycle, where the electrolyte continually circulates with a defined flow rate. The waste electrolyte contains 10% Na_2S (15 g $S^{2-}{\cdot}l^{-1}$) and 1% NaOH (0.25 N NaOH). In the course of the experiment a sample is taken from the tank (7) for analysis at 1 hour intervals. Mercury oxide (Hg/HgO) reference electrode is used and all potentials in this paper are given in mV *vs*. E (Hg/HgO).

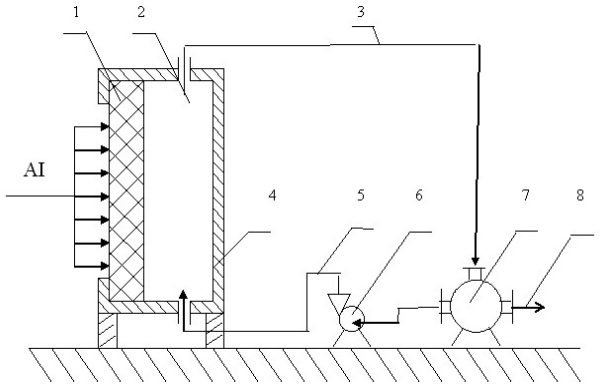

Fig. 1. Scheme of the reactor's cell: 1 - GDE.; 2 - reactor chamber; 3 - waste solution line; 4 - reactor; 5 - solution supply line; 6 - peristaltic pump; 7 - solution tank; 8 - sampling line.

The catalysts were deposited on the electrode surface. One of the substances, $[CoPc(SO_3H)_2]$, was deposited by impregnation on the GDE catalytic layer from an ethylenediamine hydrochloride solution. The surplus ethylenediamine was washed away and the electrode dried at 80ºC. Concentrated solution of $Ni(NO_3)_2$ was used for impregnation of the electrode with nickel nitrate solution, followed by precipitation of the hydroxide on the surface through 10% NaOH solution treatment and finishing wash with distilled water, and drying at 100ºC.

The catalytic activity was measured by transporting a solution of 15 g $S^{2-}{\cdot}l^{-1}$ and 0.25 N NaOH through the reactor cell. Under these conditions the sulphide ions were oxidized by air that has diffused through the GDE. The reaction rate (V) was evaluated by catalyst productivity expressed as equivalents of converted sulphide ions at 20ºC per unit time onto a specific geometric surface, equal for non-modified and modified electrodes, at identical flow rates. The converted amounts of sulphide ions were determined by analytical method [18], which is based on precipitation of Na_2S in $Cu(ClO_4)$ to CuS, which is titrated volumetrically with EDTA. The degree of conversion (Dc) of sulphide ions to elemental sulphur was used as criteria for the catalytic activity according to the Equation 5.

$$Dc = \frac{(Co - C)}{Co} \tag{5}$$

where D_c – degree of conversion; C_o – initial concentration of S^{2-} ions; C – current concentration of S^{2-} ions (measured after some working time). In agreement with the Faraday's law the reaction rate can be expressed as a current:

$$V = \Delta N S^{2-}/\Delta t = IF/nF \quad \text{or}$$

$$IF = V.nF = \Delta N S^{2-} nF/\Delta t \tag{6}$$

where: V ($mol{\cdot}sec^{-1}$) is the reaction rate; n is the number of electrons exchanged by the two half-reactions; F is the Faraday constant and $\Delta N S^{2-}$ are the gram equivalents of S_2, oxidized over the time interval Δt.

The GDE electrochemical characterization was carried out by plotting partial polarization curves on GDE with or without deposited catalysts. The sulphide ions polarization curves were plotted by isolating the cell from oxygen and by utilizing the above mentioned electrolyte. The oxygen polarization curves were plotted while admitting oxygen in the absence of sulphide ions. The electrolyte contains only 0.25 N NaOH. The E_{mix} values of the respective polarization curves for each electrode were compared with a measured value of the open circuit potential in the presence of both redox couples. The similarity between the values of mixed current I_{mix} (mA) and the reaction rate V (expressed as a current IF) as well as between mixed (E_{mix}) and open circuit (E_{0c}) potentials is an indication of the electrochemical mechanism of the process.

RESULTS AND DISCUSSION

The measurements of the sulphide oxidation reaction rate and the partial electrochemical curves commenced with the non modified GDE. In the first experiment the dependence of the reaction rate on the sulphide solution flow rate (v_r) has been studied. The results at 20ºC and various flow rates (between 14 and 53 $cm^3{\cdot}min^{-1}$) are depicted in Fig. 2. It is quite apparent that the degree of conversion increases with the solution flow rate. This is probably due to lower diffusion limitations and increase of circulation cycles. Flow rate of v_r = 24.15 $cm^3{\cdot}min^{-1}$ has been selected for next experiments.

With the chosen flow rate of solution, tests of the

catalytic activity on non modified GDE at different temperatures have been performed. Fig. 3 shows the relationships between the degree of conversion and time on stream for three operating temperatures. The D_c increases with temperature but reaches a plateau, which is lower than 100% conversion of sulphide ions.

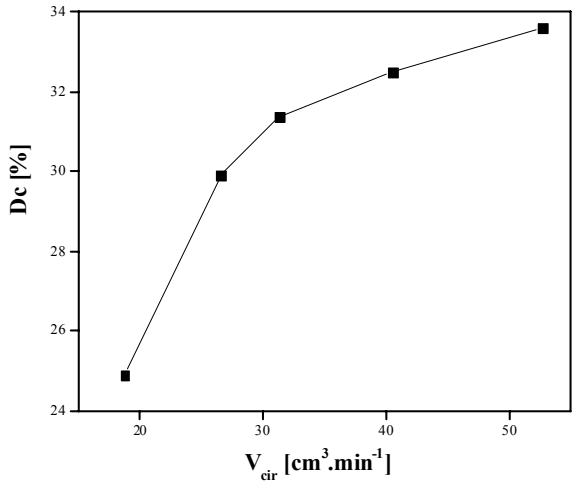

Fig. 2. Relationship between rate of sulphide oxidation by oxygen and flow rate of solution; T = 20ºC; electrolyte: 15 g $S^{2-}\cdot l^{-1}$ + 0.25 N NaOH; non-modified GDE SGDE = 200 cm^2.

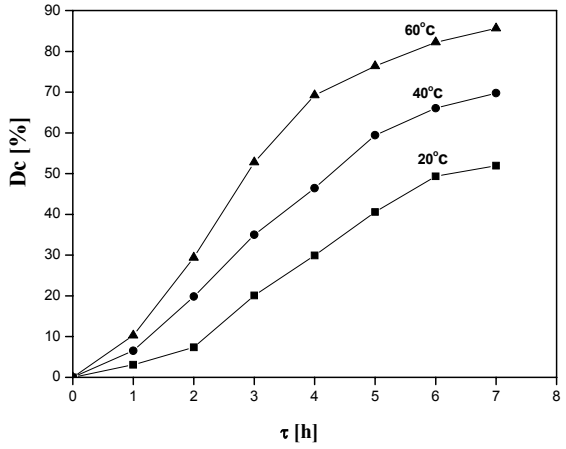

Fig. 3. Relationships between degree of conversion and time on stream at different temperatures: T = 20, 40 and 60ºC; electrolyte: 15 g $S^{2-}\cdot l^{-1}$ + 0.25 N NaOH + O_2 (Air); non-modified GDE; SGDE = 200 cm^2; flow rate v_r = 24.15 $cm^3\cdot min^{-1}$.

The electrochemical partial polarization curves on non-modified GDE were plotted at 20ºC and represented in Fig. 4. The nature of the curves indicates that the system can be regarded as a "poly-electrode" system. The anodic curve (oxidation of sulphide ions) was measured in absence of oxygen – the gas facing side of the GDE was covered. Argon gas was admitted through the electrolyte (15 g $S^{2-}\cdot l^{-1}$ + 0.25 N NaOH). The cathodic curve was measured with oxygen in 0.25 N NaOH electrolyte. The open circuit potential (E_{0c}) was measured on a GDE without external current, in the presence of oxygen in 15 g $S^{2-}\cdot l^{-1}$ +0.25 N NaOH electrolyte (i.e. in the presence of both oxidation-reduction couples S^{2-}/S and OH^-/O_2) and it is illustrated as a point in Fig. 4. The intercept of both curves determines the two values specific for the catalytic reaction: mixed current (I_{mix} = 125 mA) and mixed potential (E_{mix} = –295 mV). The analytically measured amount of sulphide ions oxidized for one hour at 20ºC (Fig. 3) is converted into current using Eqns. (5) and (6) and is found to be IF = 124 mA. The open circuit potential (E_{0c}) was measured in the presence of both oxidation-reduction couples S^{2-}/S and OH^-/O_2 in the electrolyte and it equals E_{0c} = –297 mV. The good agreement between the values of mixed and open circuit potentials and currents confirms the electrochemical mechanism of H_2S oxidation by atmospheric oxygen when no external current is applied.

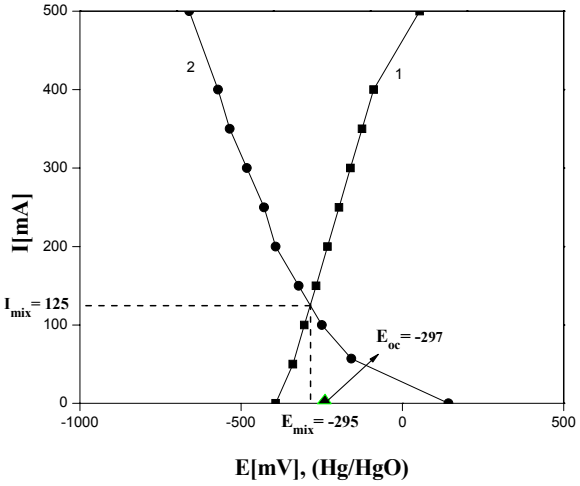

Fig. 4. Partial polarization curves: T = 20ºC; non-modified GDE; v_r = 24.15 $cm^3\cdot min^{-1}$; SGDE = 200 cm^2; cathodic curve (■) - 15 g $S^{2-}\cdot l^{-1}$ + 0.25 N NaOH + Ar; anodic curve (●) - 0.25 N NaOH + O_2 (Air); E_{0c} (▲) - 15 g $S^{2-}\cdot l^{-1}$ + 0.25 N NaOH + O_2 (Air).

The catalytic activity of a modified GDE at different temperatures has been measured, too. Fig. 5 and Fig. 6 show the relationships between the degree of conversion and time on stream for three operating temperatures. The Dc increases with temperature. It should be noted that due to the high catalytic activity of the catalyzed GDE's the complete sulphide ions conversion is achieved within a comparatively short period of time. The values calculated according to the Faraday's law for the currents corresponding to the converted quantity of sulphide ions at 20ºC are respectively IF1 = 556 mA and IF2 = 908 mA. Here IF1 is the Faraday

current of the modified with the [$CoPc(SO_3H)$] catalyst GDE, while *IF*2 is the Faraday current for the modified with the $Ni(OH)_2$ catalyst GDE.

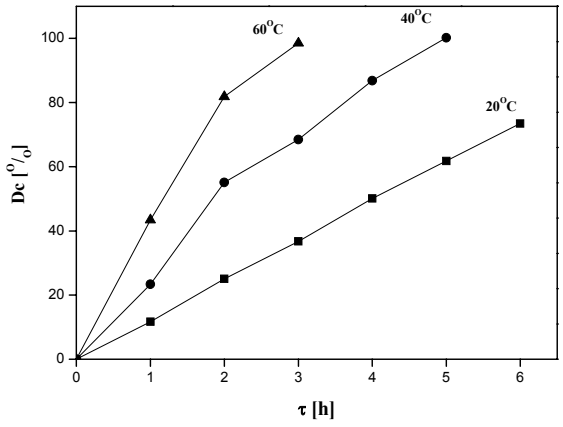

Fig. 5. Relationships between degree of conversion and time on stream at different temperatures for $CoPc(SO_3H)$] catalyst on GDE: SGDE = 200 cm^2; T = 20, 40 and 60ºC; electrolyte: 15 g $S^{2-}{\cdot}l^{-1}$ + 0.25 N NaOH + O_2 (Air); flow rate v_r = 24.15 $cm^3{\cdot}min^{-1}$.

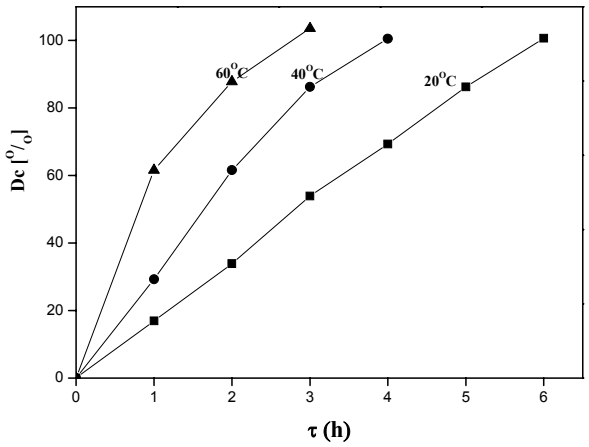

Fig. 6. Relationships between degree of conversion and time on stream at different temperatures for $Ni(OH)_2$ catalyst on GDE: SGDE = 200 cm^2; T = 20, 40 and 60ºC; electrolyte: 15 g $S^{2-}{\cdot}l^{-1}$ + 0.25 N NaOH + O_2 (Air); flow rate v_r = 24.15 $cm^3{\cdot}min^{-1}$.

Fig. 7 illustrates the partial polarization curves of anodic (') and cathodic (") reactions of sulphide ions oxidation and oxygen reduction, respectively, for GDE modified with [$CoPc(SO_3H)_2$] – 1', 1" and $Ni(OH)_2$ – 2', 2" catalysts. The nature of the curves (a steeper slope for the anodic curves) of shifting E_{mix} to cathodic values is a good reason to believe that the cathodic (oxygen) reaction is the rate-limiting step [15, 16].

The I_{mix} and E_{mix} values for the three catalysts studied on GDEs are given in Table 1. It is apparent that the modified electrodes exhibit considerably higher catalytic activity, about 5-fold, compared to the non-modified electrodes. The following order of catalytic activity: GDE < GDE/$CoPc(SO_3H)_2$ < GDE/$Ni(OH)_2$ corresponds to an increased rate of the rate-determining step of the oxygen cathodic reduction. Modification with a catalyst enhances the reversibility of both half-reactions and the polarization curves exhibit steeper slopes and higher I_{mix} values, which is an indication for higher catalytic activity.

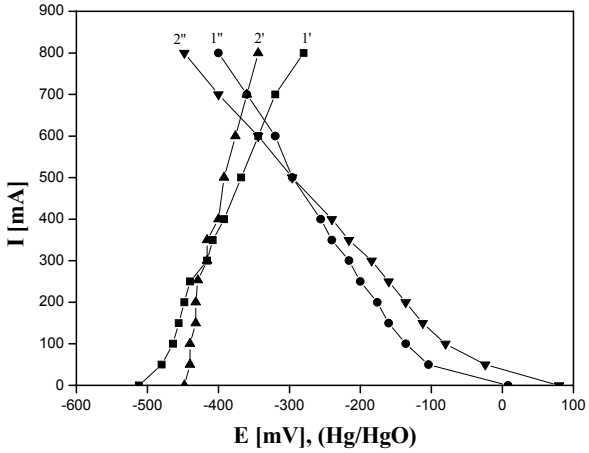

Fig. 7. Partial polarization curves: T = 20ºC; flow rate v_r = 24.15 $cm^3{\cdot}min^{-1}$; SGDE = 200 cm^2; cathodic curves: (15 g $S^{2-}{\cdot}l^{-1}$ + 0.25 N NaOH +Ar), (●) - [$CoPc(SO_3H)_2$] and (▼) - $Ni(OH)_2$; anodic curves (0.25 N NaOH +O_2 (Air)), (■) - [$CoPc(SO_3H)_2$] and (▲) - $Ni(OH)_2$;

Table 1. I_{mix} and E_{mix} values for the three studied catalyzed electrodes.

Catalyst	E_{mix} [mV]	E_{0c} [mV]	I_{mix} [mA]	*IF* [mA]
GDE	−295	−297	125	124
GDE/$CoPc(SO_3H)_2$	−348	−320	615	556
GDE/$Ni(OH)_2$	−385	−408	645	908

Table 1 points out to a good agreement between E_{mix} and E_{0c}, as well as between I_{mix} and *IF*, for non-modified GDE, which is coherent with a pure electrochemical mechanism. The GDE/$CoPc(SO_3H)_2$ couple manifested $I_{mix} > IF$ and more negative values of E_{mix} in comparison to E_{0c}. This evidences a deviation from the additivity principle. Most likely it is due to the adsorption of reaction products onto the catalyst. As for the second ($Ni(OH)_2$) catalyst, the observed yield of polysulphides (catalytic activity) is higher than predicted electrochemically. This fact implies the occurrence of two parallel reactions: electrochemical oxidation on the catalyzed electrode and homogeneous sulphide ions oxidation in solution [19, 20]:

$$S^{2-} + HO_2^- + H_2O \rightarrow S^0 + 3OH^- \qquad (6)$$

CONCLUSIONS

The sulphide ions oxidation reaction proceeds essentially *via* an electrochemical mechanism. The

carbon in the GDE exhibits its own catalytic activity. The electrodes modified with $CoPc(SO_3H)_2$ and $Ni(OH)_2$ possess considerably higher catalytic activity (about 5-fold). For these electrodes, the carbon behaves as a conductor in the electrochemical mechanism implementation. The studied systems are quite promising for industrial purification of waste waters containing H_2S.

REFERENCES

1. A. Mazgerov, V. Fomia, L Ovsyannikova, G. Ostroumova, I. Khrushcheva, *Khim. Promishl*., 281 (1985).
2. D. L. Stern, K. E. Nariman, J. S. Johnson, R. K. Grasselli, *Catal. Today*, **55**, 311 (2000).
3. G. Buska, C. Pistarino, *J. Loss Prev. Process Ind.*, **16**, 363 (2003).
4. A. Barona, A. Elias, A. Amurrio, I. Cano, R. Arias, *Biochem. Eng. J*., **24**, 79 (2005).
5. M. Hoffman, B. Lim, *Environ. Sci. Technol*., **13**, 1406 (1979).
6. K. Chan, J. Morris *Environ. Sci. Technol*., **6**, 529 (1972).
7. O. Weres, L. Tsao, R. Chatre, *Corrosion*, **41**, 307 (1985).
8. K. Chan, S. Gupta, *Environ. Lett*., **4**, 187 (1973).
9. K. Juergen, H. Klaus-Dirk, *Fuel*, **63**, 1064 (1984).
10. L. Meljac, L. Perier-Camby, G. Thomas, *Carbon*, **43**, 1407 (2005).
11. B. Lafit, J. Smith, *Powder Technol*., **27**, 143 (1980).
12. E. Laperdrix, G. Costentin, O. Saur, J. C. Lavalley, C. Nedez, S. Savin-Poncet, J. Nougayrede, *Carbon*, **38**, 1757 (2000).
13. C. Wagner, W. Traud, *Z. Electrochem*., **44**, 331 (1938).
14. M. Spiro, *Chem. Soc. Rev*., **15**, 141 (1986).
15. V. V. Skorcheletti, Theory of Metals Corrosion, Himiya, Leningrad, 1972 (in Russian).
16. I. Nikolov, K. Petrov, T. Vitanov, *J. Appl. Electrochem*., **26**, 703 (1996).
17. K. Petrov, I. Nikolov, T. Vitanov, *Int. J. Hydrogen Energy*, **10**, 245 (1985).
18. P. Kivalo, *Anal. Chem*., **27**, 1809 (1955).
19. M. Spiro, P. L. Freund, *J. Electroanal. Chem*., **144**, 293 (1983)
20. Y. Okinaka, *J. Electrochem. Soc*., **120**, 739 (1973).

ХЕТЕРОГЕННО КАТАЛИТИЧНО ОКИСЛЕНИЕ НА СУЛФИДНИ ЙОНИ ПО ЕЛЕКТРОХИМИЧЕН ПЪТ

И. Митов, А. Андреев, И. Николов, П. Андреев, Е. Младенова, К. Петров*

Институт по електрохимия и енергийни системи, Българска академия на науките, ул. „Акад. Г. Бончев“, блок 10, 1113 София

Постъпила на 18 март 2009 г.

(Резюме)

Принципът на адитивността е приложен за изясняване на механизма на хетерогенен каталитичен редокси процес по електрохимичен път. Изследван е реакционният механизъм на окислението на сулфидните йони от кислорода на въздуха в алкална среда. Предполагайки електрохимичен механизъм на процесите са измерени парциалните реакции на редукция на кислорода и окисление на сулфидните йони. Охарактеризирани са два високо активни катализатора приложими в промишлеността – кобалтов дисулфофталоцианинов комплекс $[CoPc(SO_3H)_2]$ и никелов хидроксид $Ni(OH)_2$. Използвани са въгленови хидрофобни газодифузионни електроди (ГДЕ).

Намереното добро съответствие между количеството превърнати сулфидни йони, определени аналитично и измерени електрохимично чрез „тока на късо“ е доказателство за електохимичния характер на процеса. Окислението на сулфидните йони от кислорода протича основно върху разпръснати микрогалванични елементи възникващи в порите на въглен-тефлоновата структура на електродите. Електродите модифицирани с $[CoPc(SO_3H)_2]$ и $Ni(OH)_2$ притежават около пет пъти по-висока каталитична активност в сравнение с тази на въглена.

Изследваната система е с възможно приложение за очистване на индустриални отпадни води от сероводород.

CONTENTS

СЪДЪРЖАНИЕ